BERGISCHE
UNIVERSITÄT
WUPPERTAL

JÜLICH
Forschungszentrum

Formation and fate of secondary organic aerosol components in the atmosphere: explicit modeling at global scale

Dissertation

zur Erlangung des Doktorgrades der Naturwissenschaft (Dr. rer. nat.)

der mathematisch-naturwissenschaftlichen Fakultät

der Bergischen Universität Wuppertal

vorgelegt von

Felix Wieser

aus Nettetal

Erstgutachter: Prof. Dr. Peter Wiesen

Zweitgutachter: Prof. Dr. Hendrik Fuchs

Tag der mündlichen Prüfung:

Abstract

The chemical processing of organic molecules in the multiphase system of the atmosphere has various implications for the formation and loss of organic aerosols. Gaseous compounds emitted at the Earth's surface undergo different oxidation reactions, depending on the chemical environment. In most cases, these reactions produce less volatile and more soluble gases. They can dissolve in available aqueous media or condense on pre-existing aerosols. This category of particulate matter is called secondary organic aerosol, in short SOA. The physical and chemical properties of secondary organic aerosols vary due to the wide range of different constituents. Differences in chemical composition adapt the radiative properties, the aerosol phase state (e.g. phase separation or glass-liquid transition) or the hygroscopicity of a specific organic aerosol particle. These properties, in turn, have far-reaching consequences for the atmosphere and human life. Secondary organic aerosols impact global warming, urban visibility, and human health. Assessing the present and future magnitude of these globally relevant topics requires a detailed knowledge of secondary organic aerosols.

The secondary organic aerosol yield of specific chemicals and their aging processes are investigated in lab experiments and theoretical calculations. Global atmospheric models are employed to analyze the global influences of new chemical kinetics and physical processes on secondary organic aerosols. This allows for efficient testing under a manifold of different atmospherically relevant conditions. However, the simulation results strongly depend on the complexity of the representation of organic aerosols in the model.

This work aims to improve the representation of secondary organic aerosols in the global atmospheric model MESSy. Secondary organic aerosols are separated into a hydrophilic and a hydrophobic mode in this model. Both modes are impacted by gas-phase chemistry. Although this chemistry is already rather detailed, it has never been analyzed with respect to secondary organic aerosols. In addition to the gas phase, the model simulates the chemical processing of reactants in secondary organic aerosols and cloud and rain droplets. This chemistry is essential for the simulation of secondary organic aerosols. However, in the current state of the model, only a small fraction of large oxidized organics partition to and react in these phases.

In this work, the shortcomings in the model concerning secondary organic aerosols are addressed by three adaptations: 1) the chemistry of key organic compounds in the gas

phase is revised, 2) the partitioning of organics (especially medium and large organics) is extended by new partitioning constants together with their thermal dependence, and 3) the construction of a mechanism generator for aqueous oxidation reactions and its application to the MESSy framework. The newly developed oxidation scheme and the adapted partitioning are tested in sensitivity simulations in a box model. The implications of all objectives are assessed in global model simulations.

Sensitivity simulations in a simplified box model revealed a strong increase in secondary organic aerosol mass due to the introduction of additional chemical processing of gas-phase organics. Isoprene-derived epoxy diols and the respective aqueous-phase products stand out as the most impactful new additions. Comparisons with field measurements displayed that the model overpredicts secondary organic aerosol formation from the new isoprene oxidation pathways. However, within the limited capabilities of the box model the produced concentrations are still comparable to the observations. The newly developed limonene oxidation mechanism and the revised oxidation of isoprene by nitrate radicals were compared with chamber experiments. Within the simplified box model, the simulated results were in reasonable agreement with the experiments. This comparison provides confidence that isoprene and limonene have realistic budgets and product concentrations in model simulations.

In the global model, a reference simulation was compared with two updated setups. One included the revised gas-phase oxidation of organics and the newly developed partitioning constants. The second setup additionally featured an extended aqueous-phase oxidation scheme based on the developed mechanism generator. Similar to the findings in the box model system, the new isoprene and limonene chemistry enhanced the global model secondary organic aerosol burden significantly, with an annual increase of 110 Gg. The introduction of additional aqueous-phase oxidation reactions reduced this enhancement to 70 Gg. Analysis of the oxygen-to-carbon ratio revealed that especially the updated partitioning scheme led to a strong reduction in the oxidative state of deliquescent organic aerosols. Due to the temperature dependence of the partitioning constant, wet deposition has larger impact at colder temperatures. Cloud droplets are affected in a similar way as the deliquescent aerosols. However, due to the shorter lifetime, the effects are weaker than expected. Finally, the implications of the updates on oxidant concentrations were assessed. Ozone and the OH radical display substantial differences between the simulations. Elucidating these changes and assessing the implications for the atmospheric oxidation capacity requires further sensitivity simulations with full chemical budgets.

Contents

Chapter 1

Introduction

1.1 Atmospheric aerosols

From the planetary boundary layer to the upper troposphere, under clean and polluted conditions, throughout the year, aerosols play a central role in numerous processes in the atmosphere [Huang et al., 2018, Andreae et al., 2018, Jeong and Sokolik, 2007, Sanap and Pandithurai, 2015]. While inorganic aerosols commonly consist of known ions or ion mixtures, organic aerosols are known to have a larger variety of constituents, complicating source contribution and the process understanding. Organic aerosols from primary sources (primary organic aerosol (POA)), meaning organics emitted directly in aerosol form, can be traced back to their emission sites. This helps to identify the sources and composition of primary organic aerosols. The composition of secondary organic aerosol (SOA) is more complex. This type of organic aerosol is formed by gas-phase oxidation of volatile organic compounds (VOCs) that are emitted and processed from biogenic and anthropogenic sources. Due to the wide range of different organic molecules, functional groups, reactive sites, and atmospheric oxidants (OH, O_3 and NO_3), secondary organic aerosols can consist of thousands of compounds [Aljawhary et al., 2013]. Aerosol aging (e.g. in-aerosol oxidation) and aerosol mixing lead to a changing aerosol composition over time [Lambe et al., 2011]. Together with secondary organic aerosol composition, the properties also vary. These circumstances make it challenging to reflect the measured or observed organic aerosols in theoretic models.

Unravelling the mechanisms and processes behind secondary organic aerosols remains a central task to investigate their effects on the atmosphere and all living organisms. Aerosols are known to have a significant impact on human life. In populated regions, urban visibility depends on the aerosol burden in the planetary boundary layer (PBL). Emissions from vehicles, households, and industry can lead to smog events, especially at low wind speeds. Similarly, aerosols affect the radiative forcing. Depending on the optical properties of the aerosol particles, they have a cooling or warming effect in the atmosphere. Organic

aerosols composed of nitrogen-containing aromatic compounds with large, conjugated π-electron systems are classified as brown carbon (BrC) and have a weak light absorption that increases at shorter wavelengths [Laskin et al., 2015]. In contrast, organic aerosols composed of small, non-photoactive molecules scatters radiation, resulting in a negative radiative effect. Secondary organic aerosols are known to have a cooling effect on the Earth's climate [Lin et al., 2014]. Moreover, aerosols can affect the formation and properties of clouds and thus the climate [Pöhlker et al., 2023]. Hygroscopic organic aerosols take up available water and thus act as cloud condensation nuclei (CCN) [Petters et al., 2017]. Aerosol pollution also impacts human health. Especially in urban areas, they increase the risk for respiratory diseases such as chronic obstructive pulmonary disease (COPD) [Lelieveld, 2017]. Air pollution has been estimated to cause a substantial number of premature deaths each year, with the highest share from ozone and aerosol pollution [Shiraiwa et al., 2017]. Based on different exposure-response functions, Pozzer et al. [2023] modeled the global mortality due to particular matter smaller than 2.5 μm. For the period between 1990 and 2020, they collected estimates ranging from 0.8 to 10.2 million premature deaths per year. It is therefore important to investigate and unravel the underlying processes determining the distribution and abundance of organic aerosols in the atmosphere.

1.2 Organic aerosol sources and sinks

Organic aerosols are emitted directly or formed by secondary chemistry. Depending on the region, the ratio between primary and secondary organic aerosols can vary substantially. About 90% of the global primary organic aerosol budget originates from biomass/biofuel combustion sources [Lu et al., 2015]. It can therefore be of natural and anthropogenic origin (e.g. domestic heating and natural wildfires) [Zhang et al., 2011]. Apart from the emissions, the primary organic aerosol concentration is controlled by aging processes and evaporation of volatile organic compounds inside the organic aerosols to the gas phase [Shrivastava et al., 2008, Palm et al., 2020]. Secondary organic aerosol levels, on the other hand, depend on the emission of volatile organic compounds and the available oxidants. These compounds are emitted by various processes around the globe. In the biosphere, isoprene, α/β-pinene, and limonene are among the most important emitted molecules. Anthropogenic emissions include the so-called volatile chemical products (VCPs) (e.g. cleaning agents and personal care products), organics from industrial activities and from road traffic. In the atmosphere, VOCs react with oxidants (OH, O_3 and NO_3) which can oxidize molecules. This oxidation process and the outcome depends on the molecular structure of the VOCs. Some of the molecules decompose into smaller compounds, eventually forming CO_2. However, oxidation may also lower the volatility of a given precursor species by increasing the molecular mass, oxygen content, and polarity. Low volatile compounds can effectively condense onto pre-existing aerosols and thus contribute to the secondary organic aerosol burden. Alternatively, oxidized, soluble gases dissolve in available water (cloud droplets, fog, and deliquescent

aerosols). In the aqueous phase, new reaction pathways become accessible. This leads to further oxidation of dissolved species yielding highly soluble and high molecular weight low volatile organic compounds (LVOC). Upon evaporation of cloud and rain droplets, the low volatile organic compounds remain in the condensed phase, contributing to the overall organic aerosol mass (see Fig. 1.1). Wet and dry deposition of secondary organic aerosols and of the gaseous precursors (e.g. by rain) are the main physical loss processes [Knote et al., 2015]. Dry deposition is estimated to be four times slower than wet deposition [Farmer et al., 2021]. The loss to chemical processes is often simplified or neglected in model simulations or in the interpretation of observations. Still, the aqueous-phase oxidation of compounds also increases the volatility until a product is sufficiently volatile to outgas. In the literature, more than 63% of the organic aerosol is estimated to be of secondary origin [Shilling et al., 2013]. This highlights the importance of understanding the complex sources and sinks of secondary organic aerosols.

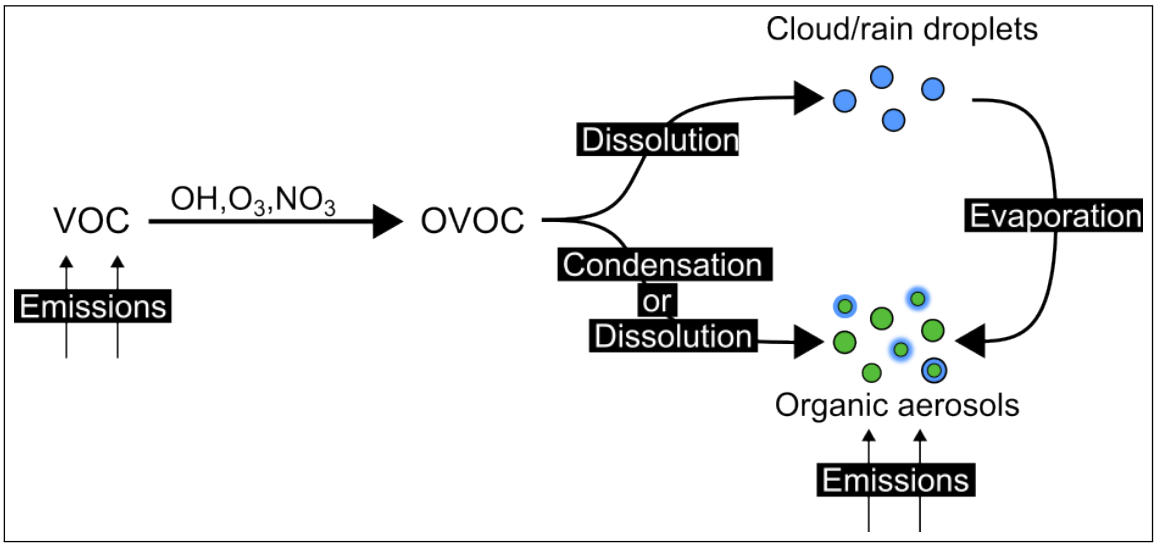

Figure 1.1: Schematic representation of the secondary organic aerosol formation processes. The coagulation of smaller aerosols in favor of large aerosols is not shown.

1.3 Phase partitioning

The processes shown in Figure 1.1 illustrate the importance of phase partitioning for secondary organic aerosols and organic aerosols in general. Organic compounds that are oxidized in the gas phase can condense on pre-existing aerosols. Alternatively, they may dissolve in cloud and rain droplets, fog or deliquescent aerosols. The description of these processes requires a mathematical basis, especially in theoretical investigations. In atmospheric science, condensation is commonly described by applying saturation vapor pressures. Assuming that a pure organic vapor is in equilibrium with the condensed phase of the same organic molecule, the vapor pressure provides the pressure of the given compound in the

gas phase. Molecules with a low vapor pressure, formed in gas-phase oxidation reactions, condense on pre-existing aerosols and contribute to the organic matter. The second partitioning process is the dissolution of gaseous organics into an aqueous phase and vice versa. The physics of this equilibrium is commonly described by utilizing Henry's law [Hodzic et al., 2014]. It describes the partitioning of organics between the gas and a pure aqueous phase. In the calculations, Henry's law constants are applied to estimate the fraction of a compound in both phases. Depending on the application, Henry's law constants are defined differently. Due to the application case in this work, the constants are defined as the concentration of a molecule dissolved in the aqueous solution per pressure of the same molecule in the gas phase [Sander et al., 2022]. This partitioning process is particularly important for soluble compounds of low or medium molecular mass. For high solubilities and molar masses, condensation and dissolution are compete (under sufficiently humid conditions).

1.4 Organic aerosols in models

The realistic simulation of organic aerosols in global atmospheric models, especially of secondary organic aerosols, remains a complex and unresolved problem. As highlighted above, the formation and aging of secondary organic aerosols involves numerous different processes, molecules, and oxidants. The physico-chemical processing of molecules must be applied in a multiphase framework in order to represent all key processes. Box and regional models can handle more explicit chemical mechanisms than global models. This is due to the difference in the number of grid boxes and the processes considered (e.g. global meteorology). Current air parcel models are able to use more than 20000 reactions [Zhu et al., 2020]. This, together with complex partitioning and microphysics, has been shown to result in an accurate simulation of organic aerosols on the regional scale [Simmel and Wurzler, 2006, Rusumdar et al., 2016, 2020, Zhu et al., 2020]. Simulations of such models show the potential that arises from using a large chemical mechanism and a sophisticated partitioning scheme. Multiphase chemistry is largely neglected in global models. This is also the case for the aqueous fraction of organic aerosols. Large chemical mechanisms are costly for multi-annual simulations as they require much more computational resources. Depending on the research question, advanced chemistry may not have a significant impact on the simulation results. For the modeling of secondary organic aerosols, the need for more complex chemical schemes has previously been assessed based on global model simulations [Hodzic et al., 2016]. Commonly, simplifications are applied to lower the computational demand while maintaining an intermediate level of detail. In some models, the complex secondary organic aerosol formation process is reduced to a set of organic precursors with previously measured secondary organic aerosol yields. This approach avoids the chemical calculations and simplifies the partitioning process. Other global models include a large inventory of gas-phase reactions but simplify the partitioning process. Both of these assumptions may yield correct secondary organic aerosol concentrations under certain boundary conditions

but lack the sensitivity to environmental influence factors. The most prominent approach to simplify the condensation of molecules onto pre-existing aerosols is called volatility basis set (VBS) [Donahue et al., 2012]. In this method, gas-phase molecules are grouped into volatility bins. After the binning, only the groups are further processed, reducing the number of partitioning compounds drastically. Finally, the groups form secondary organic aerosols based on the previously analyzed main contributors of the bin. Studies have been conducted to investigate the impact of the assumptions [Lane et al., 2008, Pye et al., 2020b]. However, the investigations are limited to specific atmospheric conditions, thus further research is needed. Furthermore, in the VBS framework oxidation in the condensed phase is largely neglected. This omission may lead to a significant overprediction of secondary organic aerosols under certain conditions [Daumit et al., 2016]. In light of future advances in computing power, chemistry, and partitioning can be progressively refined to reflect more complex environmental conditions and assumptions can be eliminated.

1.5 Thesis objective

The aim of this thesis is to improve the representation of secondary organic aerosols in the global atmospheric chemistry model EMAC which is based on the Modular Earth Submodel System (MESSy). The focus is on achieving a better simulation of the abundance, distribution, and physical properties of organic aerosols compared to a reference and field observations. These improvements are intended to be achieved by adding new formation and degradation pathways across phases for the main secondary organic aerosol precursors. The importance of specific volatile organics for SOA has to be assessed based on the secondary organic aerosol yield and the global abundance in the literature. For the selected volatile organic compounds, reaction mechanisms according to experimental and theoretical results have to be constructed. Gaps in literature knowledge have to be bridged by applying structure-activity relationships (SARs). They are used to estimate the required rate constants based on the molecule structure. Since secondary organic aerosol formation is a multiphase phenomenon, species and reactions have to be implemented in all relevant phases. Apart from the underlying chemistry, phase partitioning is of central importance for secondary organic aerosols. Thus, missing partitioning constants between the gas and aqueous phase need to be estimated and implemented. This includes the temperature dependence of the partitioning coefficients. Finally, a comprehensive evaluation of the novel developments is performed in global model simulations to assess improvements and future developments.
After a description of the tools used, the remainder of this thesis deals with:

- **Update and extension of VOC oxidation (see Sect. 3.1):** Models commonly struggle to reflect the global organic aerosol budget in various chemical environments. The secondary organic aerosol formation is strongly influenced by the volatile organic

compounds treated within the chemical scheme of the model. Thus, the model is updated to contain additional VOCs, but also mechanisms for previously included volatile organic compounds are refined. The effect of the additional formation mechanisms is analyzed in this thesis. In particular, the influence on SOA under various conditions (e.g. different oxidant concentrations) has to be assessed in box model simulations.

- **Estimation and evaluation of Henry's law coefficients (see Sect. 4):** Partitioning has a high significance for SOA. In global models, partitioning rates (e.g. Henry's law constants) are often estimated due to the compound quantity and the scarcity of available experimental data. With the extension of the chemical scheme, also the partitioning also needs to be implemented to model. The required Henry's law constants need to be added to the list of chemical properties of the model. Due to the potentially high temperature dependence of Henry's law constants, this needs to be considered in the implementation. The dependence of model results on the used Henry's law constants and their temperature dependence needs to be investigated in sensitivity simulations.

- **Evaluation of the kinetic model (see Sect. 3.3 and Sect. 3.2):** The comparison between model simulations and chamber experiments can be used to validate updated chemical mechanisms. Experimental work commonly focuses on a specific precursor-oxidant combination. Box model simulation can be used to describe such experiments. Within this work, a qualitative and quantitative comparison between newly implemented mechanisms in a simplified model and chamber experiment data is planned. In addition, the new kinetic model is compared to the previous chemical scheme.

- **Aqueous-phase oxidation of oxygenated VOCs (see Sect. 5.1):** In comparison to gas-phase reactions, reaction kinetics for condensed phase reactions are limited in the literature. Nevertheless, reactions in clouds, rain, and deliquescent aerosols are needed for a precise description of SOA. Due to the amount of missing reactions within the liquid phase of the MESSy model, a script has to be developed and applied, to close the gaps in aqueous-phase processing.

- **Global organic aerosol budget (see Sect. 5.2):** With updates to the chemical and physico-chemical processes involved in secondary organic aerosol formation and loss, an impact on SOA properties is expected. Important properties are the vertical distribution of SOA among the atmospheric levels and the oxygen-to-carbon ratio as a proxy for the degree of oxidation. Further, the refined secondary organic aerosol concentration have to be compared to measurement stations on a global scale. Within this thesis, the change to those properties will be assessed.

Chapter 2

Model introduction

2.1 Box model: CAABA/MECCA

CAABA/MECCA is the integrated box model of the global model MESSy (see Sect. 2.2), but it is also available and applicable as a standalone box model [Sander et al., 2011, 2019]. It simulates an air parcel in the atmosphere under predefined conditions. The gas and aqueous-phase chemistry is represented in the name-giving MECCA (Module Efficiently Calculating the Chemistry of the Atmosphere) module (see Sect. 2.3.1). Besides chemistry, processes such as emission and deposition are of central importance. The semidep subroutine is applied to simulate both fluxes. It is specifically designed to meet the needs of the box model. Furthermore, photo-chemical rate constants are calculated by the method by Landgraf and Crutzen [1998], which allows the photolysis of molecules in MECCA. Two separate aerosol modes can be used in the simulations. The aerosols have a predefined radius, liquid water content, and salt composition. The box model has two main applications: 1) efficient testing of novel chemical developments, and 2) analysis of field campaigns and chamber experiments [Rosanka et al., 2021b, Eger et al., 2021]. Both use cases gain additional value from the simple adaptation of the box chemistry to the global model. Both models share the same basic chemistry submodel (MECCA). Consequently, the testing of chemical mechanisms in CAABA/MECCA facilitates the application of new chemistry in MESSy. This is especially helpful for large chemical mechanisms that slow down the global model substantially. However, CAABA/MECCA reaches its limitations when applied to multiphase experiments with organic aerosols. CAABA/MECCA simplifies or completely neglects key processes. Aerosol dynamics and microphysics are not simulated. Similarly, new particle formation or aerosol loss processes are not included, and the partitioning is only described by Henry's law constants (only solubility-based partitioning, no condensation). Regardless of the limitations, CAABA/MECCA is applied in this work prior to more sophisticated global model simulations. The simplified box model provides a first assessment of the impact of adaptions to the chemistry and the partitioning. The results for organic aerosol (OA) are based on assumptions that are further elucidated in Section 3.2.1.

2.2 Global model: the Modular Earth Submodel System

The Modular Earth Submodel System, short MESSy, is a comprehensive Earth System Model (ESM) used to the simulate and analyze the biological, chemical, and physical processes that affect the atmosphere [Jöckel et al., 2005]. It stands out from other ESMs in its flexibility and the possible levels of detail. The flexibility is provided by the name-giving submodel system. In addition to the base model controls, the model consists of three main layers: the base model interface layer (BMIL), the submodel interface layer (SMIL), and the submodel core layer (SMCL). BMIL controls the data transfer between the base and the submodels, as well as the data exchange between submodels. A similar task is performed by SMIL. It collects all the data that is required for the execution of a specific submodel. In addition, it executes the routines of the core layer and exchanges the results with BMIL. Finally, SMCL includes all routines that are necessary for the execution of a submodel that are not covered by the base model. In the present setup, the general circulation model ECHAM5 is coupled to the MESSy model [Roeckner et al., 2003, Jöckel et al., 2006]. This combination is called EMAC (ECHAM5/MESSy for Atmospheric Chemistry) [De Meij et al., 2012]. This model combination allows the coupling of the chemistry in MESSy to the dynamics in ECHAM5. Before a simulation can be executed, a so-called namelist needs to be selected or created. A namelist includes all settings related to the submodels (List of active submodels; option within submodels). In a simulation, a specific predefined or self-constructed namelist is applied. Submodels can be activated or deactivated based on the user's needs, as long as the requirements of the submodels are met. Thus, simulations can be tailored to specific research questions. In addition to the level of detail, this also allows the control of the performance and runtime of the model. In this work, the multiphase chemistry setup MOM (Mainz Organic Mechanism) is adapted and applied. In terms of chemistry, it contains the highest level of detail of the predefined model setup. Chemistry calculations are performed in multiple phases (gas, deliquescent aerosols, and cloud and rain droplets). Dissolution and condensation of organics as well as the outgassing back to the gas phase is modeled. Table 2.1 lists the MOM submodels together with a short description. In the following sections, the submodels relevant to the chemical processing of organics and the formation and loss of SOA are presented. Before running the model, the user needs to select a grid resolution together with the number of vertical levels. Due to the coupling, the resolution setup refers to the given resolutions of ECHAM5 [Roeckner et al., 2003]. In this work, the model simulates at a grid resolution of T42. This resolution refers to a Gaussian grid with 2.8° x 2.8° in latitude and longitude. At the equator, this corresponds to a grid size of 310 km. The vertical resolution is set to 31 levels ranging from ground level up to 10 hPa. This rather coarse resolution is chosen due to the computational demands of the detailed chemistry.

Table 2.1: List of all submodels used in the present MOM setup. The second and third column give a short description of the submodels purpose within MESSy and the connected publications. Unfinished or small submodels have not been published. Submodels that are an active part of the developments in this work are written in bold text. Note that AERCHEM (see Sect. 2.3.3) is not listed as it is part of the GMXe submodel.

Submodel	**Description**	**Publications**
AEROPT	Aerosol optical properties	Dietmüller et al. [2016]
AIRSEA	Air-sea exchange	Pozzer et al. [2006]
ALBEDO	Radiation surface albedo	-
BIOBURN	Biomass burning	Kaiser et al. [2012]
CLOUD	Cloud cover and microphysics	Dietmüller et al. [2016]
CLOUDOPT	Cloud optical properties	Dietmüller et al. [2016]
CONVECT	Convection of tracers	-
CVTRANS	Further convection calculations	-
DDEP	Dry deposition	Kerkweg et al. [2006a]
GMXe-AERCHEM	Aerosol microphysical properties	Pringle et al. [2010]
GWAVE	Gravity waves	-
JVAL	Calculation of photolysis rates	Sander et al. [2014a]
LNOX	NO_x from lightning	Tost et al. [2007]
MECCA	Calculation of gas-phase chemistry	Sander et al. [2019]
MEGAN	biogenic emissions	Guenther et al. [2006]
OFFEMIS	offline emissions	Kerkweg et al. [2006b]
ONEMIS	online emissions	Kerkweg et al. [2006b]
ORACLE	Organic aerosol composition and evolution	Tsimpidi et al. [2014]
ORBIT	Calculation of orbital parameters	Dietmüller et al. [2016]
OROGW	Subgrid scale orography parameters	-
RAD	Calculation of radiative transfer	Dietmüller et al. [2016]
SCALC	Simple calculation during simulation	Jöckel et al. [2016]
SCAV	Wet deposition and liquid phase chemistry	Tost et al. [2006a]
SCOUT	Output data of stationary observatories	Jöckel et al. [2010]
SEDI	Sedimentation of aerosols	Kerkweg et al. [2006a]
SORBIT	Sampling along satellite orbits	Jöckel et al. [2010]
SURFACE	Caluclation of various surface properties	-
TNUDGE	Nudging of tracers towards tracer fields	Kerkweg et al. [2006b]
TROPOP	Tropopause characteristics	-
VERTEX	Land-atmosphere exchange	-

2.3 Chemistry submodels

The chemistry in MESSy is divided into three different media and submodels. In this work, MECCA controls the gas-phase chemistry, although it is also capable of simulating liquid phase chemistry [Sander et al., 2005]. The chemistry within rain and cloud droplets is represented by the submodel SCAV [Tost et al., 2006b]. In addition to the major aqueous phases, the chemistry within the aqueous fraction of organic aerosols has recently been added to MESSy's chemistry system. The subsubmodel AERCHEM, which is part of the submodel GMXe, describes the aqueous-phase chemistry in deliquescent aerosols [Rosanka et al., 2024].

2.3.1 MECCA

MECCA is the fundamental chemistry submodel of CAABA/MECCA and MESSy. It is capable of solving gas and aqueous-phase reaction mechanisms, depending on the model setup. However, the MESSy model offers more comprehensive options for aqueous-phase chemistry. The submodels SCAV and AERCHEM replace MECCA, but include the same or a similar mechanism. Available chemical mechanisms are the Mainz Organic Mechanism (MOM) and the Jülich Aqueous-phase Mechanism of Organic Chemistry (JAMOC) mechanisms. MOM covers a wide range of gas-phase oxidation reactions of VOCs ranging from small compounds such as glyoxal to reactions of monoterpenes. JAMOC is an extension of MOM and includes aqueous-phase oxidation reactions for organic molecules with up to four carbon atoms. It was created based on a subset of the CLEPS mechanism (for more see Sect. 2.5.2) [Mouchel-Vallon et al., 2017]. Photolysis reactions require photochemical rate constants that depend on the properties of the reactants. These rates are derived by coupling MECCA to the submodel JVAL. In JVAL, photolysis frequencies are calculated based on the absorption cross section of the molecule and the quantum yield of the process. For a class of molecules (e.g. *n*-alkanes), photolysis frequencies are determined for the smallest molecule in the class and then applied to all larger homologs. More information on JVAL is available in Sander et al. [2014b]. The chemistry is processed and solved by Kinetic PreProcessor (KPP) [Sandu and Sander, 2006]. In KPP, the differential equations are evaluated by the chemical solver RODAS3 [Sandu et al., 1997]. Recent developments by Dreger et al. [2025] have revealed a considerable improvement in solving the Jacobian matrix by applying an adaptive step size controller. The respective time step controller is applied in the global model simulation in this work. Within MECCA, species can partition between phases. This gas-to-aqueous partitioning is controlled by Henry's law solubility constants (see Sect. 2.4.2). Similar to large chemical mechanisms in the literature, such as the Master Chemical Mechanism (MCM), numerous rate constants of important reaction classes (e.g. OH reactions) are predefined in MECCA's kinetic scheme (see Tab. 2.2).

2.3.2 SCAV

The scavenging of trace gases and aerosols by clouds and precipitation is represented by the submodel SCAV. It also simulates the chemistry in cloud and rain droplets. Scavenging and chemistry are calculated for vertical columns referring to the impact of rainwater [Tost et al., 2006b]. Henry's law constants and accommodation coefficients describe the scavenging process. Molecules can be scavenged in four different modes: convective and large scale cloud and rain droplets (cloud and rain is treated separately). In MESSy, this results in the generation of four molecular tracers. Chemical and physico-chemical calculations are performed on the sum of the four initial tracers, which are combined to form a new tracer. The reactions can include the same variety as in MECCA, but can be fine-tuned to the user's needs. Similar to MECCA, KPP is applied to solve the Jacobian matrix. The differential equations are evaluated by the chemical solver RODAS3 [Sandu et al., 1997]. Reactions in the aqueous phase can span several orders of magnitude (e.g. OH-oxidation and acid-base equilibrium). This has a significant impact on the speed of chemical calculations. Due to the amount of the tracers generated and the complex chemistry, SCAV is computationally heavy.

2.3.3 AERCHEM

The subsubmodel AERCHEM is part of the the aerosol submodel Global Modal-aerosol eXtension (GMXe) (see Sect. 2.4.1)[Rosanka et al., 2024]. It simulates the chemistry in the aqueous fraction of secondary organic aerosols and also the partitioning involving this phase. Like MECCA and SCAV, the chemical calculations are performed with the combination of KPP and RODAS3. AERCHEM is only applied to organic aerosols with a liquid water content (LWC) $\geqslant 4.5 \times 10^{-18}$ g/m^3. To apply the chemical mechanism in the model, an ordinary differential equation (ODE) has to be solved. The time required to solve this ODE depends on the range of LWCs considered [Dreger et al., 2025]. This is due to the scaling of concentrations and rate constants with LWC. Simulations with a lower threshold are either very slow or not solvable by RODAS3. The threshold has a negligible effect on the forward simulations in Chapter 5 (see Fig. 7.5). Within AERCHEM, the level of chemical detail is similar to that of the SCAV submodel. However, the chemical mechanism is independent of the kinetic model applied to rain and cloud droplets.

2.4 Aerosol and partitioning submodels

2.4.1 GMXe

The Global Modal-aerosol eXtension (GMXe) calculates aerosol microphysics and gas-aerosol partitioning. Aerosol sizes are distributed into seven log-normal modes: four hydrophilic and three hydrophobic modes. This is necessary to control the computational demands of the model. They are defined by the number concentration, the number mean

radius, and the geometric standard deviation. The mean radius of the hydrophilic modes is in the nucleation mode (< 5 nm) and the coarse mode (> 500 nm). For the three hydrophobic modes, the nucleation mode is discarded. The size range is fixed, but the mean radius is variable. The geometric standard deviation is constant for each mode. The aerosol inorganic composition is uniform in a specific mode but can be different throughout modes. The number of species used in the aerosol composition can be changed to suit the required setup. The nucleation of new particles follows Vehkamäki et al. [2002] and is calculated as a function of temperature, relative humidity, and the sulfuric acid concentration. Coagulation is based on Vignati et al. [2004] and can result in the transfer of aerosol mass from smaller to larger modes. Hydrophilic/hydrophobic coagulation results in hydrophilic aerosol. The gas/aerosol partitioning is represented by the module ISORROPIA-II. The interaction of different species is considered (K, Ca, Mg, NH_4...). More about ISORROPIA can be found elsewhere Fountoukis and Nenes [2007]. Note that AERCHEM (see Sect. 2.3.3) is a subsubmodule of GMXe.

2.4.2 MECCA-aero

MECCA-aero is a subsubmodel within the MECCA framework. It is designed to calculate forward and backward mass transfer rates between the gas and the (aqueous) aerosol phase. The resulting rates are applied to MECCA, but the submodels SCAV and AERCHEM apply the mass accommodation similarly. MECCA-aero reads all required chemical properties from an internal list, which includes a selection of properties for all molecules in the chemistry scheme. For the mass transfer the molecular mass (M), the Henry's law constant (H_s), the temperature dependence of H_s (B), the mass accommodation coefficient (α_{T0}) and the temperature dependence of the mass accommodation coefficient (α_{Tdep}) are required. Further physical constants (temperature (T), pressure (p), aerosol radius (r_a)) and liquid water content (LWC) are initialized from the model.
First, the mean velocity v_{mean} is calculated as a function of the temperature and the molar mass of the selected molecule. Simultaneously, the H_s is calculated at the current temperature using Equation 4.3.

$$v_{mean} = \sqrt{\frac{8 \cdot R_{gas} \cdot T}{M \cdot \pi}} = 4.60138 \cdot \sqrt{\frac{T}{M}} \tag{2.1}$$

Like H_s, the accommodation coefficient is temperature dependent. The Equation 2.2 provides the applied correlation.

$$\alpha = \left[1 + \frac{1}{\alpha_{T0} - 1} \cdot \exp\left(\alpha_{Tdep}\right) \cdot \left(\frac{1}{T_0} - \frac{1}{T}\right)\right]^{-1} \tag{2.2}$$

At this point, all the necessary molecular and temperature dependent constants have been calculated. The mass transfer coefficient k_{mt} is defined and reformulated as follows. A mass

transfer coefficient always refers to a specific molecule under given physical conditions.

$$k_{mt} = \frac{1}{((r_a^2/(3 \cdot D_{gas})) + (4 \cdot r_a/(3 \cdot v_{mean} \cdot \alpha))} = \frac{v_{mean}}{(r_a \cdot (r_a/\lambda) + (4/(3 \cdot \alpha)))} \tag{2.3}$$

$$with\ D_{gas} = \frac{v_{mean} \cdot \lambda}{3}$$

The constant λ denotes the mean free path of a molecule in the gas phase. The relationship between the mean free path and the gas-phase diffusion constant (D_{gas}) was previously adapted from Atkins [2006]. The complete partitioning is described by the forward (gas to aerosol)(k_{exf}) and backward (aerosol to gas)($\mathrm{k_{exb}}$) partitioning rates. Partitioning to the aerosol phase is controlled by the liquid water content, whereas the partitioning to the gas phase is controlled by $H_\mathrm{s}(T)$ and thus the solubility of the molecule.

$$k_{exf} = k_{mt} \cdot LWC \tag{2.4}$$

$$k_{exb} = \frac{k_{mt}}{R_{gas} \cdot T \cdot H_\mathrm{s}(T)} \tag{2.5}$$

The presented procedure is calculated for every molecule in a grid cell. Note that salt effects (salting-in/salting-out) and other non-linear effects are not considered in this method.

2.4.3 ORACLE

The submodel Organic Aerosol Composition and Evolution in the Atmosphere (ORACLE) is used to describe the partitioning and aging of organic aerosols [Tsimpidi et al., 2014]. It estimates the contribution of primary and secondary organic aerosols to the total organic aerosol mass. SOA formation from different volatility classes (volatility basis set), e.g. semi volatile (semi volatile organic compounds (SVOC)), intermediate volatile (intermediate volatile organic compounds (IVOC)), and low volatile organic compounds (LVOC), is simulated as follows. The classes are divided into volatility bins based on the saturation concentration specifically relevant for a given class (more volatile = higher saturation concentration) in order to minimize the computational cost of the submodel. For this binning process, the volatility of a specific compound has to be estimated. This is done by applying the estimation scheme published in Li et al. [2016]. They proposed an estimation approach based on the elemental composition of the molecule to derive the saturation mass concentration (C^0).

$$log(C^0) = (n_C^0 - n_C) \cdot b_C - n_O \cdot b_O - 2 \cdot \frac{n_C \cdot n_O}{n_C + n_O} \cdot b_{CO} - n_N \cdot b_N - n_S \cdot b_S \tag{2.6}$$

In this calculation n_x (with $x = C, O, N, S$) denotes the occurrence count of the specific element, n_C^0 is the carbon number of the reference molecule and b_x (with $x = C, O, CO, N, S$) are the contribution factors of the atoms or atom combinations (e.g. b_{CO}) [Donahue et al.,

2011]. The contribution factors are obtained by fitting the function to measured saturation mass concentrations. After estimation, the molecules are sorted into logarithmically spaced bins ($C^* = 0.1, 10, 1000...$). At each model time step, the compounds in a bin are distributed into the gas and aerosol phase based on the volatility of the bin. This equilibrium is established instantaneously, neglecting the kinetics of the partitioning process.
ORACLE can also monitor the contribution of VOC from different sources and bins to SOA. AVOC and BVOC contributions are monitored separately. The OA itself is distributed into size modes, allowing the analysis of the PM2.5 and PM10 fractions. These size modes are congruent with the modes in MECCA-AERO. In the ORACLE namelist file, the described variables (i.e. number of bins) can be modified to refine the simulation to individual needs.

2.4.4 Secondary organic aerosol simulation

Two submodels are available to simulate processes concerning secondary organic aerosols in MESSy. The AERCHEM submodel (see Sect. 2.3.3) represents the aqueous fraction of SOA, the hydrophilic mode. ORACLE also simulates secondary organic aerosols. However, it focuses on the fraction dominated by organic molecules, the hydrophobic mode. When both submodels are used, SOA is a combination of the hydrophilic and hydrophobic modes. Both fractions are assumed to be internally mixed, but the modes are simulated separately. Partitioning to the hydrophilic SOA is simulated using Henry's law constants, while the partitioning to the hydrophobic mode is based on saturation concentrations. Figure 2.1 provides a schematic overview of the representation of SOA in the model.

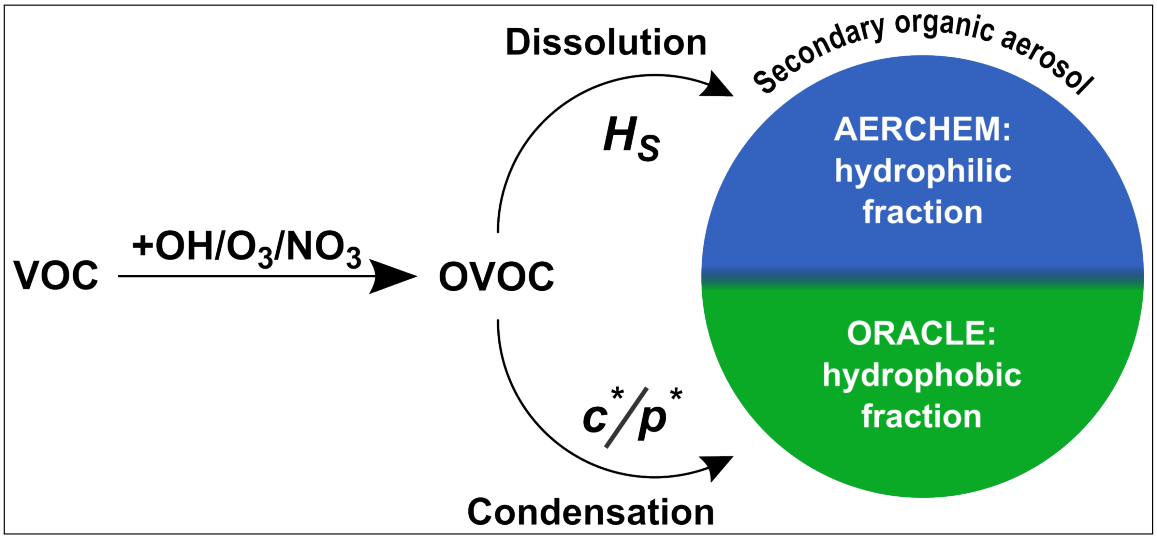

Figure 2.1: Schematic overview of the secondary organic aerosol representation in the model simulation. In the figure, the formula signs H_s, c^* and p^* describe the Henry's law constant, the saturation mass concentration and the saturation vapor pressure, respectively.

It has to be noted that the complex kinetic scheme is only applied to molecules in hydrophilic SOA. In hydrophobic SOA, only rudimentary aging reactions are considered. The present

work focuses is on the changes in hydrophilic SOA via chemistry and partitioning. The box CAABA/MECCA box model does not include the described SOA formation pathways and characteristics.

2.5 Chemical kinetics

In the applied global model setup, the chemistry scheme is divided into three submodels. MECCA represents the gas-phase chemistry, while SCAV and AERCHEM represent the various aqueous phases. The forward description is based on the MOM namelist. This setup contains the highest level of chemistry available in MESSy. The emitted VOCs and the available reaction schemes together with the general rules applied are described in the following sections.

2.5.1 Gas-phase reactions

The submodel MECCA includes gas-phase reactions for various molecules. It treats inorganic and organic molecules. Inorganic molecules include oxygen-, hydrogen-, nitrogen-, sulfur- and mercury-based compounds, as well as halogen molecules. The organic molecules in MECCA consist of 1 to 10 carbon atoms with various functional groups ranging from oxygen- and nitrogen-containing groups to sulfate. The emitted VOCs available in a simulation using the MOM setup are illustrated in Figure 2.2, subdivided into the nature of origin. It covers biogenic VOCs such as isoprene and a selection of monoterpenes (α-pinene, β-pinene, carene, sabinene, and camphene). Anthropogenic VOCs include a selection of alkanes (up to four carbons), alkenes and alkynes, and the major aromatics (benzene, toluene, and styrene). Due to the focus of the thesis on SOA and thus on organic molecules, the following description neglects the in-depth discussion of inorganic molecules.
Within the model, carbon-based molecules may undergo chemical and physico-chemical reactions. Chemical reactions include inter- and intramolecular processes (e.g. OH-addition and H-migration). Reactions between organic molecules and radicals are the main oxidation pathway. VOCs react with OH, NO_3, and O_3 depending on the reaction rate. OH and NO_3 can either abstract a hydrogen atom from the VOC or add to an existing double bond. Due to the high importance of the OH radical in the atmosphere, the related chemistry is implemented with a high level of detail. Both, abstraction and addition are treated by a predefined kinetic schemes within MECCA. These schemes were constructed in previous updates of the chemistry based on literature data [Kwok and Atkinson, 1995, Peeters et al., 2007]. It considers the degree of substitution of the reaction site and the temperature to calculate the rate constant. In addition, the chemical environment is taken into account by using so-called substituent factors. These factors are multiplied with the rate constant to yield the final rate. The main reaction pathway of O_3 is the addition to double bonds. The resulting ozonide cleaves at an O-O bond, forming a criegee intermediate. This forms the

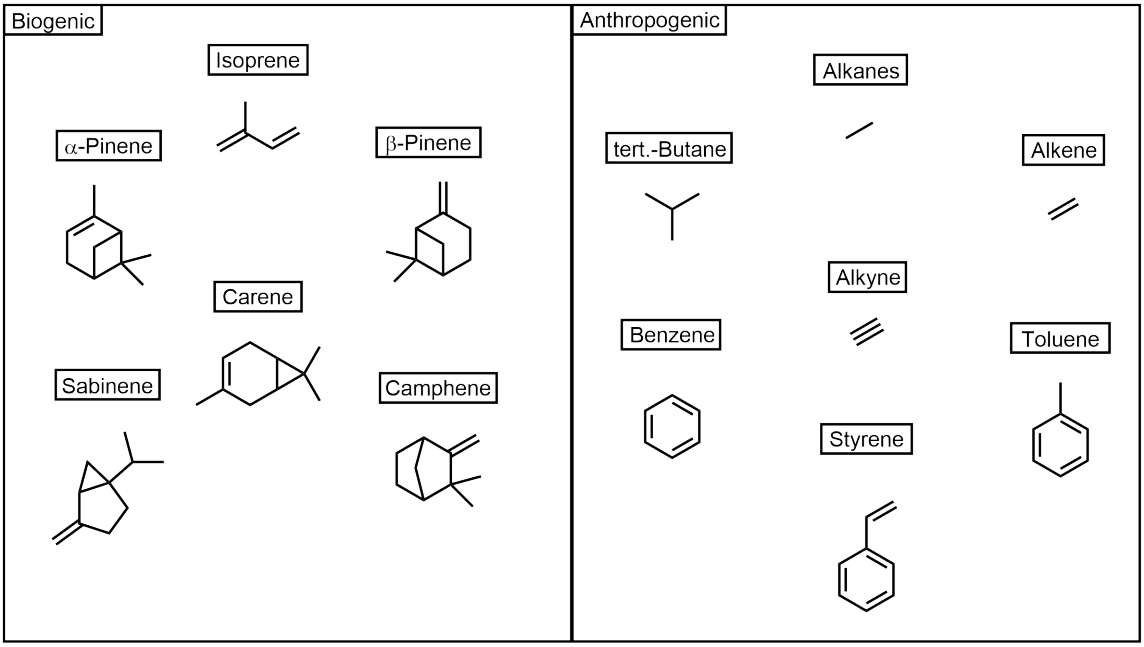

Figure 2.2: Overview of all emitted VOCs included in the MOM setup. Stereochemistry is neglected for improved structural visibility.

final product upon stabilization. MECCA does not include predefined kinetics for reactions of close-shelled VOCs with NO_3 and O_3.
Reactions of radicals with VOCs yield alkyl radicals, which are converted to peroxy radicals by the addition of molecular oxygen. The model generally considers the reaction of peroxy radicals with HO_2, NO and NO_3. Similar to the OH reactions, predefined schemes are available to ensure the consistency of the mechanism and to ease the implementation. The model implementation of the reaction of peroxy radicals with HO_2 refers to developments by Boyd et al. [2003] and Saunders et al. [2003]. It considers the dependence of the rate constants on temperature and the carbon number. The reactions with NO and NO_3 are based on temperature-dependent rate constants from the MCM [Jenkin et al., 1997]. Peroxy radicals can also react with other peroxy radicals. All peroxy radical concentrations are collected in a variable called RO_2. This is used to calculate the rate constants of peroxy cross reactions. For a specific alkyl peroxy radical, the rate depends on the degree of substitution of the radical site. The cross reaction rate of primary peroxy radicals refers to the 2-methylperoxypropane radical [Glover and Miller, 2005]. Secondary and tertiary peroxy radical cross reactions are based on isopropyl and tert-butyl peroxy radicals [Orlando and Tyndall, 2012]. Alkyl peroxy radicals with an oxygen-containing group in the β-position are treated with a similar level of detail. For acyl peroxy radicals, a separate predefined rate constant is available. Alkoxy radicals formed in the peroxy radical reactions result mainly in molecular decomposition. Table 2.2 lists the numbers and descriptions of the predefined rate constants outlined above. Further kinetics are available, but the table is limited to the

Table 2.2: Summary of the main predefined rate constants within the gas-phase scheme of MECCA. Further description is given in the text. The table is adapted from Sander et al. [2019], but extended with additional rates.

Variable	Rate constant / substituent factor	Description / substituent
H-abstraction by OH		
k_p	$4.49 \times 10^{-18} \times T^2 \times \exp(-320/T)$	Primary H-abstraction
k_s	$4.50 \times 10^{-18} \times T^2 \times \exp(253/T)$	Secondary H-abstraction
k_t	$2.12 \times 10^{-18} \times T^2 \times \exp(696/T)$	Tertiary H-abstraction
Substituent factor f		
f_{sOH}	3.44	OH at sec. carbon
f_{tOH}	2.68	OH at tert. carbon
f_{sOOH}	8.00	OOH at tert. carbon
f_{tOOH}	8.00	OOH at sec. carbon
f_{CHO}	0.55	aldehyde
f_{CO2H}	1.67	carbonic acid
f_O	8.15	double bond to O
OH-addition to double bonds		
k_{adp}	$4.5 \times 10^{-12} \times (T/300)^{-0.85}$	primary carbon of double bond
k_{ads}	$0.25 \times (1.1 \times 10^{-11} \times \exp(485/T)$ $+1.0 \times 10^{-11} \times \exp(553/T))$	secondary carbon of double bond
k_{adt}	$1.92 \times 10^{-11} \times \exp(450/T) - k_{ads}$	tertiary carbon of double bond
Substituent factor a		
a_{CHO}	0.31	aldehyde
a_{COCH3}	0.76	ketone
a_{CH2OH}	1.7	alcohol
a_{CH2OOH}	1.7	hydroperoxide
NO reaction with peroxy radicals		
k_{RO2NO}	$2.54 \times 10^{-12} \times \exp(360/T)$	all branches (NO-add. & O-abst.)
HO_2 reaction with peroxy radicals		
k_{RO2HO2}	$2.91 \times 10^{-13} \times \exp(1300/T) \times$ $(1 - \exp(-0.245 \times n_C))$	all branches (H-add. & O-abst.) n_C = number of carbon
NO_3 reaction with peroxy radicals		
k_{RO2NO3}	2.30×10^{-12}	O-abstraction
H abstraction to OOH by OH		
k_{ROOHRO}	$0.6 \times (5.3 \times 10^{-12} \times \exp(190/T))$	H-abstraction only OOH
Cross-reaction of alkyl peroxy radicals		
$k_{RO2pRO2}$	$2 \times \sqrt{(1 \times 10^{-12} \times k_{CH3O2})}$	Primary peroxy radicals
$k_{RO2sRO2}$	$2 \times \sqrt{1.6 \times 10^{-12} \times \exp(-2200/T) \times k_{CH3O2}}$	Secondary peroxy radicals
$k_{RO2tRO2}$	$2 \times 3.8 \times 10^{-13} \times \exp(-1430/T)$ With $k_{CH3O2} = 1.03 \times 10^{-13} \times \exp(365/T)$	Tertiary peroxy radicals
Cross reaction of alkyl peroxy radicals with oxygen-based functional group in β-position		
$k_{RO2pORO2}$	$2 \times 7.510^{-13} \times \exp(500/T)$	Primary peroxy radicals
$k_{RO2pORO2}$	$2 \times \sqrt{7.710^{-15} \times \exp(1330/T) \times k_{CH3O2}}$	Secondary peroxy radicals
$k_{RO2pORO2}$	$2 \times \sqrt{4.710^{-13} \times \exp(-1420/T) \times k_{CH3O2}}$	Tertiary peroxy radicals
Cross reaction of acyl peroxy radicals		
$k_{RO2RCO3}$	$2 \times 2 \times 10^{-12} \times \exp(500/T)$	acyl alkoxy radical formation

most important organic reactions.
Physico-chemical reactions are the result of the interaction of a molecule with radiation. In MECCA, the photolysis of predefined functional elements is treated. The required photochemical constants (e.g. absorption cross section) are collected in the submodel JVAL, which calculates the photolysis rates if applied within the gas-phase mechanism. Generally, the photolysis constant of a specific element is calculated for the smallest molecule and then used for all larger homologues. The photolyzed functional elements include glyoxal, methylglyoxal, hydroperoxy, isopropyl nitrate, acetol, and 2-hydroxyacetaldehyde functional elements. Further, photolysis reactions are specifically tailored for a single reaction and not used throughout the whole mechanism.

2.5.2 Aqueous-phase reactions

In the MOM setup, the chemistry in the aqueous phase is simulated by the SCAV and AERCHEM submodels. SCAV represents the chemistry in cloud and rain droplets, while AERCHEM simulates the chemistry in hydrophilic SOA. The modeled aqueous-phase chemistry is less refined than the gas-phase chemistry, similar to the general trend in the literature. In contrast to the gas phase, no predefined kinetic schemes are available. Nevertheless, the chemical scheme includes inorganic (oxygen, hydrogen, nitrogen, and halogen molecules) and organic molecules with various functional groups. Chemical reactions of organic molecules with up to four carbons are implemented in the aqueous phase. A large portion of the aqueous mechanism consists of JAMOC [Rosanka et al., 2021b]. This kinetic scheme has been constructed as an oxidation mechanism for oxidized volatile organic compounds (OVOC) in the aqueous phase and includes the oligomerization reactions of formaldehyde, glyoxal, and methylglyoxal. The chemical kinetics of the mechanism follow the CLEPS formalism [Mouchel-Vallon et al., 2017]. Furthermore, a small set of photolysis reactions is also included in JAMOC. These reactions use the same photolysis rate constants as in the gas phase. However, the rate constant is corrected by an enhancement factor based on literature experiments [Ruggaber et al., 1997]. JAMOC also includes equilibrium (e.g. acid/base or hydration reactions) and partitioning reactions. Both reaction types include a forward and a backward reaction enabling the formation of a kinetic equilibrium. While the oxidation scheme only extends to organics with up to four carbons, organics with up to ten carbons partition to the aqueous phase. This mismatch may lead to an overprediction of large organics in the aqueous phases. This issue is addressed in Chapter 5.

Chapter 3

Oxidation of gaseous secondary organic aerosol precursors

In this chapter, the oxidation scheme of gas-phase VOCs in CAABA/MECCA is adapted to improve the representation of SOA in model simulations. The focus is on the oxidation of isoprene, limonene, benzene, and *n*-alkanes. The isoprene and benzene mechanisms are no longer up to date with developments in the literature, while limonene and *n*-alkanes are missing in the chemical schemes of CAABA/MECCA and MESSy. The following sections provide an overview of the new and adapted chemical mechanisms, the changes in the model simulations due to the updated chemistry, and a comparison of model results with chamber experiments. Note that some of the results presented in this chapter have been published in Wieser et al. [2024].

3.1 Development of a chemical mechanism to improve secondary organic aerosol formation

Improving the concentrations and properties of SOA by adding or adapting chemical reactions requires detailed knowledge of the kinetic scheme of the model. In addition, a broad overview of theoretical and experimental work is essential to identify gaps in the current chemical mechanism. Due to the already large size of MESSy's kinetic model and the continuously growing literature data, this is a challenging task. In the first step, it was assessed if VOCs important for SOA are still missing. The chemical mechanism of the model already treats many monoterpenes, but limonene is not included. Considering the emissions and SOA yields of limonene, adding it to the chemical scheme is expected to enhance monoterpene-related SOA in regions with high biogenic emissions [Pye et al., 2010, Saathoff et al., 2009]. Similarly, *n*-alkanes larger than butane are not included in the mechanism. For a first assessment, *n*-alkanes up to octane are implemented in this work. The detailed analysis of the established VOCs highlighted the need for further refinement of the isoprene oxidation scheme. Chamber experiments and theoretical calculations have

revealed new mechanistic insights since the last update [Vereecken et al., 2021, Bates et al., 2014, D'Ambro et al., 2017]. The addition of isoprene-derived epoxides and the refinement of the isoprene-NO_3 mechanism have been identified as valuable extensions to the chemistry scheme. In particular, products of isoprene-derived epoxy diols (IEPOX) are expected to increase the SOA yield of isoprene [D'Ambro et al., 2019]. The benzene chemistry in the model is based on the oxidation mechanism in the MCM [Jenkin et al., 1997]. In recent investigations, alternative branching ratios and products were measured. Benzene is a global contributor to SOA due to the abundance, molecule size, and reactivity of the VOC [Ng et al., 2007]. Therefore, the benzene mechanism has been re-evaluated. Finally, some reaction schemes do not fulfill the quality of the remaining VOC oxidation scheme. They are simplified and yield products from related mechanisms. Thus, they were excluded, and the impact of the missing chemistry was assessed. Table 3.1 lists the newly implemented and extended mechanisms for the specific precursor molecules. In the upcoming sections, the new mechanisms and the main sources are described.

Table 3.1: List of all newly introduced and updated VOCs, together with the main reactants and main mechanism sources. Compounds are divided into biogenic and anthropogenic origin.

Precursor	Implementation type	Main reactant	Mechanism sources
Biogenic			
isoprene	update	NO_3	Vereecken et al. [2021]
isoprene	update	OH	St. Clair et al. [2016], Bates et al. [2014] D'Ambro et al. [2017]
IEPOX	new	OH	Petters et al. [2021], Riedel et al. [2016]
limonene	new	OH / ozone / NO_3	MCM, Pang et al. [2022], Carslaw [2013], Vereecken and Peeters [2012]
β-pinene	update	OH	Vereecken and Peeters [2012]
sabinene / carene / camphene	excluded	OH / ozone	
Anthropogenic			
benzene	update	OH	Xu et al. [2020], Wang et al. [2013]
pentane, hexane, heptane, octane	new	OH	Sivaramakrishnan and Michael [2009] Atkinson et al. [2008]

3.1.1 Applied gas and aqueous-phase structure-activity relationships

Reaction mechanisms in models are implemented and refined based on literature data and pre-defined assumptions that differ between models (e.g. treatment of peroxy radicals). Experimental and theoretical investigations usually relate to reactions under specific conditions. For some VOCs, branching ratios and rate constants are still unknown. However, the introduction of VOC mechanisms into global models requires closed reaction schemes that lead to realistic product yields. Otherwise, performed simulations may lead to false conclusions. New mechanistic developments often need additional reactions or are built completely from scratch. An essential tool in this process are structure-activity relation-

ships (SARs). SARs allow the estimation of rate constants based on the chemical structure of a molecule. A given SAR commonly estimates the rate constant of a particular type of reaction in various chemical environments (e.g. H-abstraction by OH at differently substituted carbon centers). In this work, different SARs are applied to refine the established chemistry and construct new reactions.
Two main SARs have been used in this work to construct gas-phase reaction mechanisms. The first SAR was published by Kwok and Atkinson [1995] and is based on earlier work by Atkinson [1986]. It estimates reaction rates for H-abstractions by OH and OH-additions to double bonds in the gas phase. A large set of contribution factors for neighboring functional groups is available to modulate the rate constant. Especially in older mechanisms, intramolecular H-migration is commonly not considered. The SAR of Vereecken and Nozière [2020] can determine whether H-migration reactions are competitive with bi-molecular reactions. This is particularly helpful for the implementation of new and complex mechanisms. It provides access to previously unknown reaction channels.
SARs also play an important role in closing the gaps in mechanisms in the aqueous-phase reaction. Due to the rather smaller amount of available experimental and theoretical work on large organics in the aqueous phase, SARs are often required. For aqueous-phase oxidation, the CLEPS formalism stands out as a comprehensive guideline for mechanism creation Mouchel-Vallon et al. [2017]. It includes assumptions that keep the mechanisms small in size (e.g. alkoxy radicals are not explicitly considered), but still considers the treatment of the important intermediates in detail. Rate constants for reactions of the H-abstraction by OH in the aqueous phase are estimated based on Monod and Doussin [2008b]. In 2013, Doussin and Monod [2013] extended the SAR to cover additional influence factors of neighboring functional groups. For further information and application of the aqueous-phase mechanism creation tools (SARs and assumptions) see Section 5.1.1.

3.1.2 Volatile organic compounds from biogenic origin

The chemical scheme of MESSy is already rather detailed for VOCs of biogenic origin. In particular, the kinetic scheme of isoprene and the main monoterpenes (α-pinene and β-pinene) has been refined in previous work [Taraborrelli, 2010]. However, since these major updates, new reaction channels have been published. The mechanism of isoprene, due to its large global emissions, requires revision to reflect the real SOA contributions of the biogenic volatile organic compounds (BVOC). Based on the developments in the literature, the isoprene OH mechanism under low NO_x and the isoprene oxidation by NO_3 are revised. The absence of limonene in the mechanism is also a potentially major omission concerning SOA. Sakulyanontvittaya et al. [2008] have estimated the monoterpene and sesquiterpene emissions from various trees in the US. They estimated a substantial emission of limonene, especially by shrub bushes. Fry et al. [2011] found a SOA yield between 25% and 40% for the limonene nitrate oxidation. In the present update, the mechanism of the model is extended to include the limonene oxidation by OH, NO_3, and O_3. Additionally, the aqueous-phase

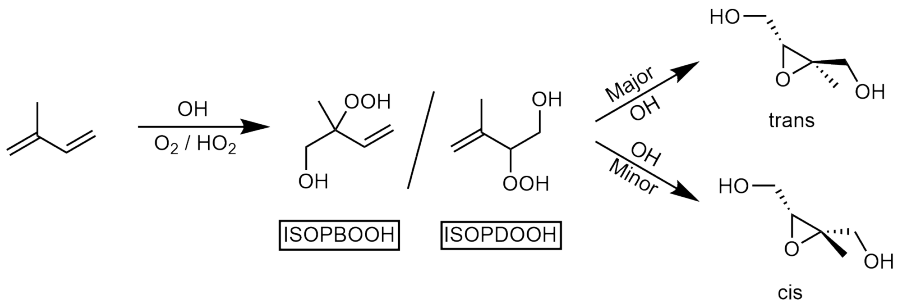

Figure 3.1: IEPOX formation from the OH-oxidation of isoprene. The OH radical adds to one of the terminal double bonds, forming a hydroxy group and an alkyl radical. After the addition of molecular oxygen to the alkyl radical, HO_2 reacts with the resulting peroxy radical. This reaction predominantly produces hydroperoxides. The epoxy diol is formed after the intramolecular ring-closure and the addition of the excess OH radical to the remaining alkyl radical. IEPOX is split into the main isomers: cis-β- and trans-β-IEPOX. Note that the δ-IEPOX isomer is also formed in small quantities.

oxidation of the major isoprene oxidation product IEPOX is implemented. The products are considerably less volatile and also remain largely in aqueous media. They are therefore expected to be essential for modeling SOA comparable to observations [Budisulistiorini et al., 2017].

Isoprene: gas phase

The implementation of isoprene-derived epoxydiols (IEPOX) and its oxidation products is expected to be one of the major factors influencing SOA by BVOCs. This reaction pathway was discovered by Paulot et al. [2009] while investigating the isoprene OH oxidation under low NO_x conditions. They already proposed large parts of the mechanism that was continuously developed in later years. St. Clair et al. [2016], Bates et al. [2014], D'Ambro et al. [2017] unravelled the complete underlying mechanisms, branching ratios, and rate constants in the gas and aqueous phases. Subsequent observational studies measured large amounts of IEPOX (and IEPOX oxidation products) in aerosols, highlighting the importance of this reaction channel [Schulz et al., 2018, Budisulistiorini et al., 2017, Hu et al., 2015]. Figure 3.1 displays the IEPOX formation mechanism for the main isomers (cis- and trans-β IEPOX). IEPOX isomers are efficiently formed from isoprene oxidation products containing a hydroperoxy moiety with an adjacent double bond. The update includes two main (trans-β-IEPOX, cis-β-IEPOX) and one minor IEPOX isomer (δ-IEPOX). The major isomers have a share of 67% and 33%, respectively. Bates et al. [2014] investigated the gas-phase oxidation of IEPOX under low NO_x conditions. Under these conditions, IEPOX is the main product, due to the efficient conversion of the peroxy radical to the hydroperoxide. At high NO_x concentrations, the nitrate formation competes with this process. Based on the results of Bates et al. [2014], the mechanism is divided into three initial reaction sites: H-abstraction by OH at C_1, C_3, or C_4. For all channels, ring-opening and decompo-

sition are among the main reaction pathways. This leads to various oxidized compounds with up to four carbons, including glyoxal, methylglyoxal, and acetol. H-migration reaction rates are reassessed based on Vereecken and Nozière [2020]. For the H-abstraction by OH at the non-ring carbons (C_1 and C_4), the epoxydiol is partially converted to a lumped epoxy-hydroxy aldehyde (LDIEPOXO). This compound does not react further in Bates et al. [2014]. Therefore, a mechanism has been developed based on the SARs presented above. The main oxidation products are still consistent with the products of the previously developed mechanisms [Taraborrelli, 2010]. Figure 3.2 displays a simplified representation of the adapted mechanism implemented in the model. A further adaptation of the classi-

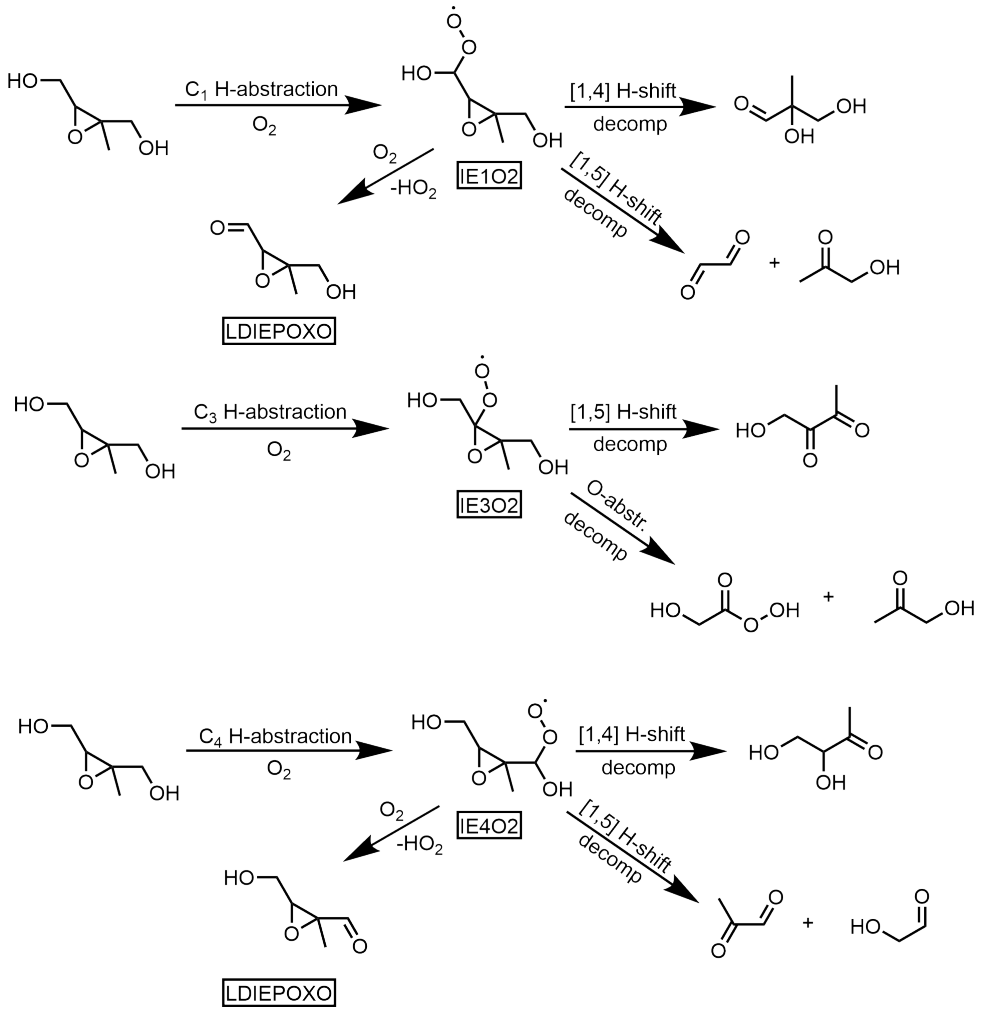

Figure 3.2: Schematic representation of the three main OH-oxidation pathways of gas-phase IEPOX under low NO_x conditions. The oxidation is initiated by an H-abstraction in the C_1, C_3 or C_4 position. At low NO concentrations, the conversion of the peroxy radical to an alkoxy radical is slow. The dominant reaction pathways are intramolecular H-shifts.

cal isoprene oxidation scheme is introduced following the investigations of D'Ambro et al. [2017]. They found that the 3,4 ring closure in isoprene hydroperoxides competes with the

1,2 ring closure after an additional H-migration step. In the new mechanism, the resulting molecule is called ISOPBEPX (epoxide of ISOPBOOH). Further mechanistic details are provided in the upcoming section.
In previous updates, a chemical mechanism for the reaction of isoprene with NO_3 was introduced as part of the chemical scheme of MOM. In the meantime, theoretical and experimental investigations by Vereecken et al. [2021] have further elucidated the reaction mechanism. Novel reaction channels and branching ratios have been revealed in addition to the established mechanism. However, it should be noted that chamber experiments have also shown that there are still considerable uncertainties in the mechanism [Carlsson et al., 2023].

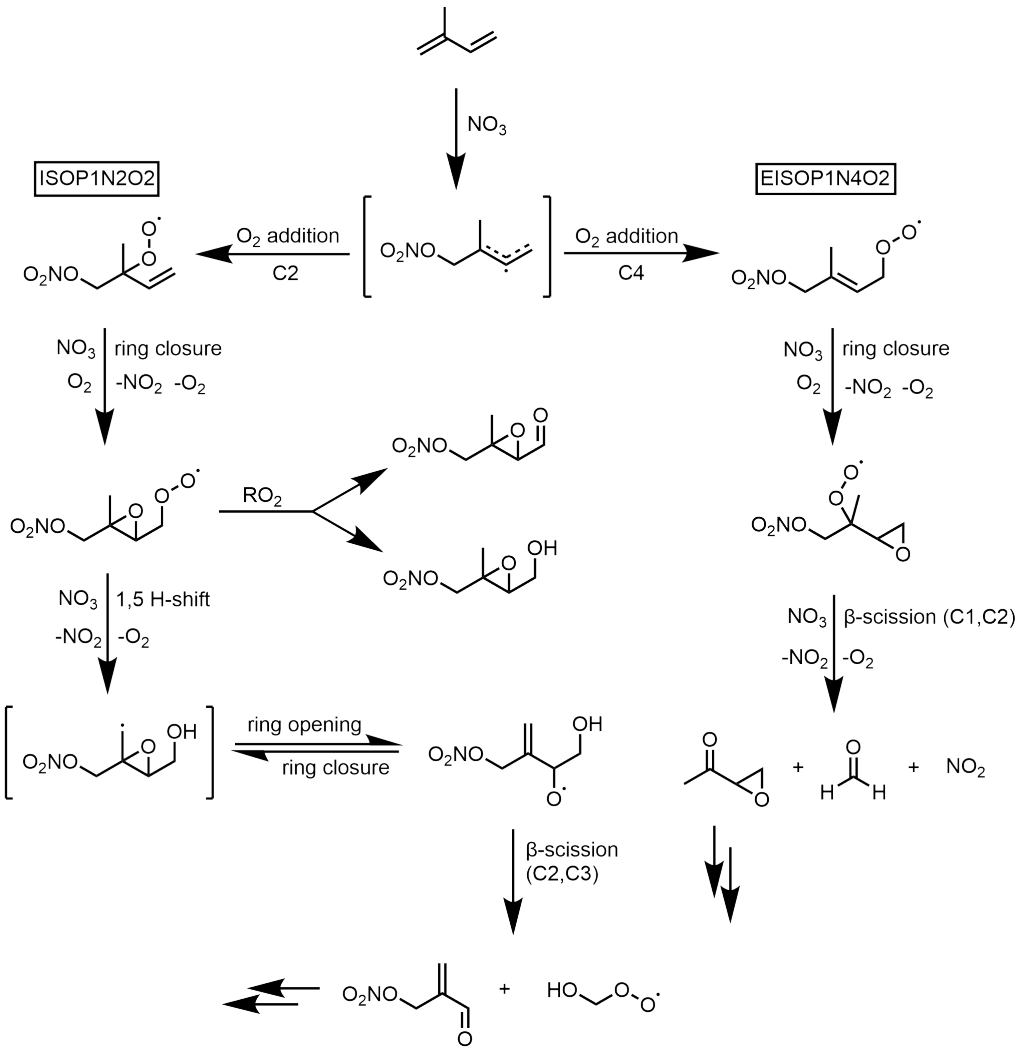

Figure 3.3: Representative subset of the isoprene-NO_3 oxidation mechanism implemented in the model.

The new kinetic scheme developed in this work restricts the addition of NO_3 to the C_1 site of isoprene (see Fig. 3.3). This is because it accounts for 87% of all initial addition

reactions. Once the nitrate radical is attached to the molecule, the radical electron is in resonance with the remaining double bond. With the double bond at C_2/C_3, the molecule exists in either cis or trans conformation. The following description focuses on the cis isomer (see Fig. 3.3). Upon O_2 addition, either a tertiary or a primary peroxy radical is formed. The in-chain peroxy radical favors the formation of an IEPOX-like epoxy nitrate, whereas the terminal peroxy radical leads to a less stabilized epoxide. Both decompose mainly in sequential oxidation reactions. Although isomers are commonly not explicitly treated in MESSy, the isoprene-NO_3 is strongly impacted by isomerization. Thus, all high-yield isomers are formed as in Vereecken et al. [2021]. The new mechanism is expected to introduce new nitrate-containing C5 compounds and additional hydroperoxides. At the same time, the concentrations of α-nitrooxyacetone, glyoxal, and methylglyoxal should be lower in regions with high isoprene and NO_3 mixing ratios.

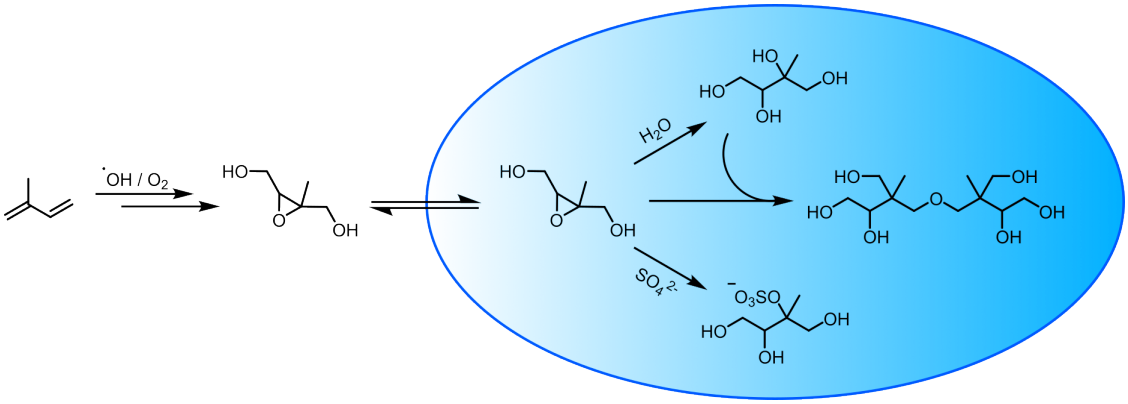

Figure 3.4: Oxidation mechanism of the main IEPOX isomers in the aqueous phase. Depending on the environmental conditions, either an organo sulfate or a tetrol is formed. Sufficiently high product concentrations may lead to oligomerization. The ring opening by water additionally forms triols and tetrahydrofuran derivatives.

Isoprene: Aqueous phase

The importance of the previously described isoprene oxidation products for SOA formation derives from their potential to partition into the aqueous phase. The Henry's law constant of IEPOX is greater than 1×10^6 M/atm, while ISOPBEPX even exceeds 1×10^{10} M/atm (estimated as described in Sect. 4.2). Thus, both molecules have a substantial concentration in the aqueous phase after efficient gas-phase production. Once partitioned into the aqueous phase, new oxidation pathways are available, leading to the formation of even more soluble, lower volatile compounds, as well as C-C bond cleavage and outgassing. Figure 3.4 displays the main reactions of IEPOX in aqueous media. The epoxy ring is opened as a result of the nucleophilic attack of water or sulfate at C_3. This reaction is acid-catalyzed and therefore reaches higher rates in deliquescent aerosols than in cloud droplets. Ring-opening by water yields a tetrol (methylbutane-1,2,3,4-tetrol (MEBUTETROL)), while the respec-

tive organic sulfate is formed with sulfate as the nucleophile. However, the ring-opening by water also produces other by-products (alkenetriols and methyltetrahydrofuran-3,4-diols). The branching ratios for the reaction are extracted from Riedel et al. [2016]. In the supplementary material of Petters et al. [2021] the reactive uptake of IEPOX is described in detail. The reactions are similarly implemented in the model.

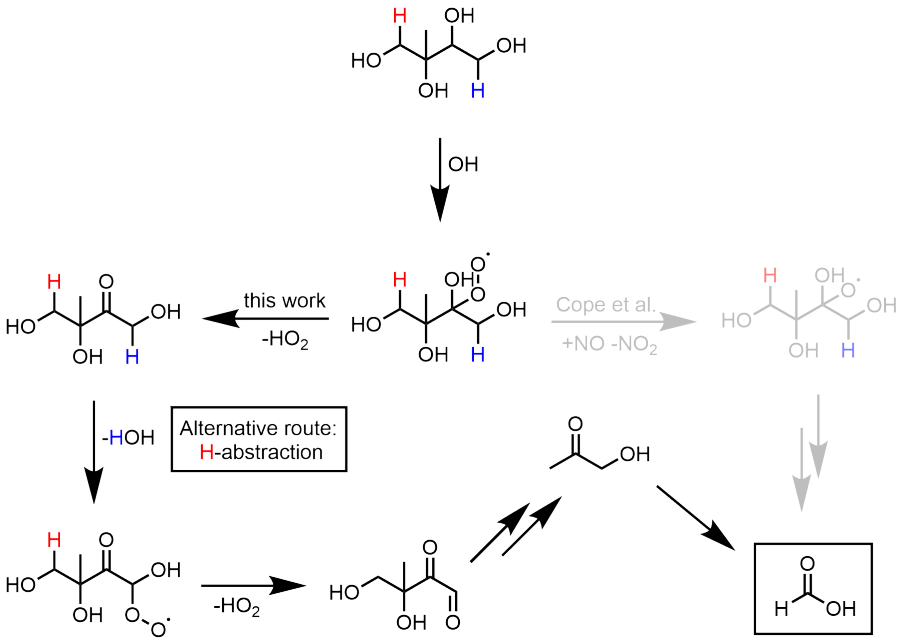

Figure 3.5: MEBUTETROL oxidation mechanism in the aqueous phase based on the results of Cope et al. [2021]. However, some pathways are replaced by reactions with faster kinetics. The original mechanistic explanation proposed in Cope et al. [2021] is displayed greyed out.

Cope et al. [2021] investigated the degradation of MEBUTETROL in the aqueous phase. In experiments, they revealed formic acid as the main oxidation product. Based on this information, they proposed a mechanism. Although it describes the formation of formic acid, the mechanism by Cope et al. [2021] prefers reactions with slower reaction rates over faster channels, thereby imposing unusual reaction kinetics. For the implementation in MESSy, the mechanism has been refined to agree with the reaction rates known from the literature (e.g. as in the CLEPS formalism [Mouchel-Vallon et al., 2017]). Figure 3.5 displays the revised scheme. The oxygen abstraction by NO is neglected and the HO_2-elimination channel is considered instead . The refined scheme still explains the formation of formic acid and is still in agreement with the experimental results. Due to the scarcity of literature data, the organic sulfate is treated as chemically stable and is only lost by deposition. Additional work on the organic sulfate removal is required in future projects.
ISOPBEPX, the alternative epoxide of isoprene, is even more soluble than IEPOX. In studies it was found to be a strong contributor to SOA D'Ambro et al. [2017]. The formation mechanism and reaction kinetics of ISOPBEPX have been investigated in the literature.

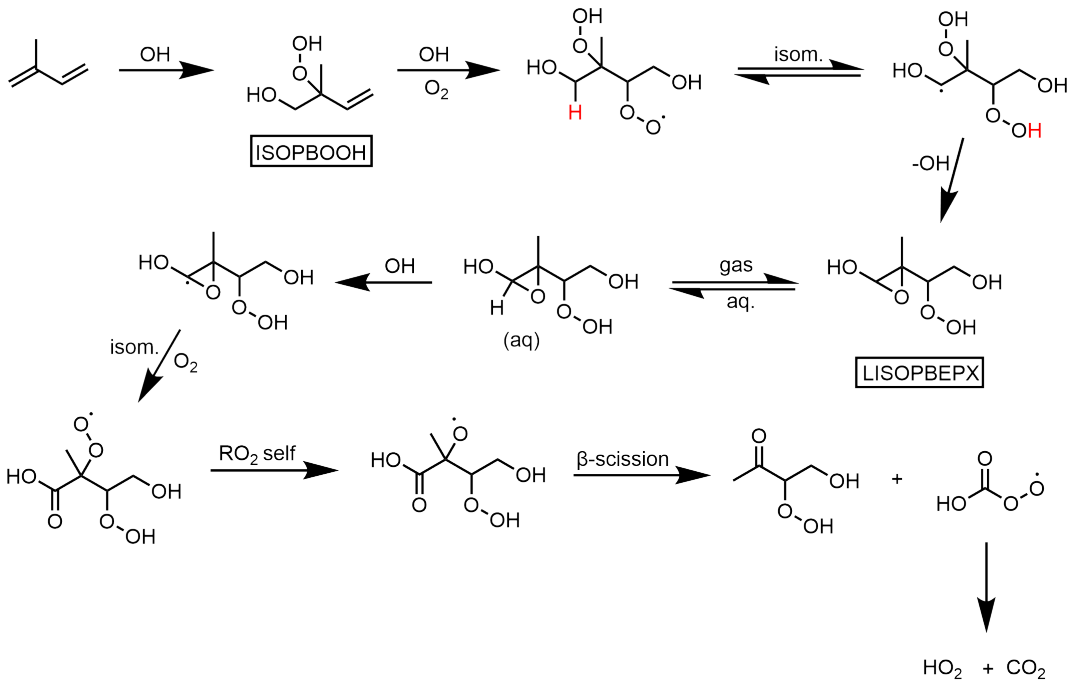

Figure 3.6: ISOPBEPX formation mechanism, partitioning and aqueous-phase oxidation/degradation. Note that this reactions pathway competes with the IEPOX formation.

However, removal processes such as aqueous-phase oxidation remain unknown. Due to the potential magnitude of formation, missing loss pathways lead to significant overpredictions in model simulations. Therefore, an aqueous-phase oxidation mechanism has been constructed as part of this update. Figure 3.6 displays a simplified representation of the mechanism. Once partitioned to the aqueous phase, ISOPBEPX is expected to undergo ring-opening similar to IEPOX, yielding a peroxy radical with large functional groups on the neighboring carbons. Following the CLEPS formalism the peroxy radical efficiently forms an alkoxy radical [Mouchel-Vallon et al., 2017]. This alkoxy radical performs a beta scission reaction, as the functional groups at C_1 stabilize the radical in the transition state. The main oxidation product of this mechanism is 3-hydroperoxy-4-hydroxybutan-2-one. Both, the aqueous degradation of IEPOX and ISOPBEPX, were implemented together with the gas-phase chemistry, to ensure the realistic formation of isoprene oxidation products for the box model comparison.

Limonene and further monoterpenes

The newly implemented limonene oxidation scheme contributes the largest number of reactions to the mechanism update. This is due to the fact, that limonene was previously not considered in MESSy's chemistry. Therefore, the mechanism can only utilize a limited set of pre-existing reactions. The basic structure and most of the reactions are based on the mechanism of the MCM [Jenkin et al., 1997]. Similar to the MCM, the new mechanism

covers the initial radical addition of OH, O_3 and NO_3. The products are oxidized until they form compounds already known to the MESSy model. Reaction kinetics are adapted to the predefined reaction rates within MECCA (see Tab. 2.2), if applicable. H-shift reactions are considered if the estimated reaction rates are competitive [Vereecken and Nozière, 2020]. Similar to the isoprene-NO_3 mechanism, chamber experiments have shown that the limonene oxidation mechanisms (e.g. from the MCM) are still uncertain and require further investigation [Pang et al., 2022].

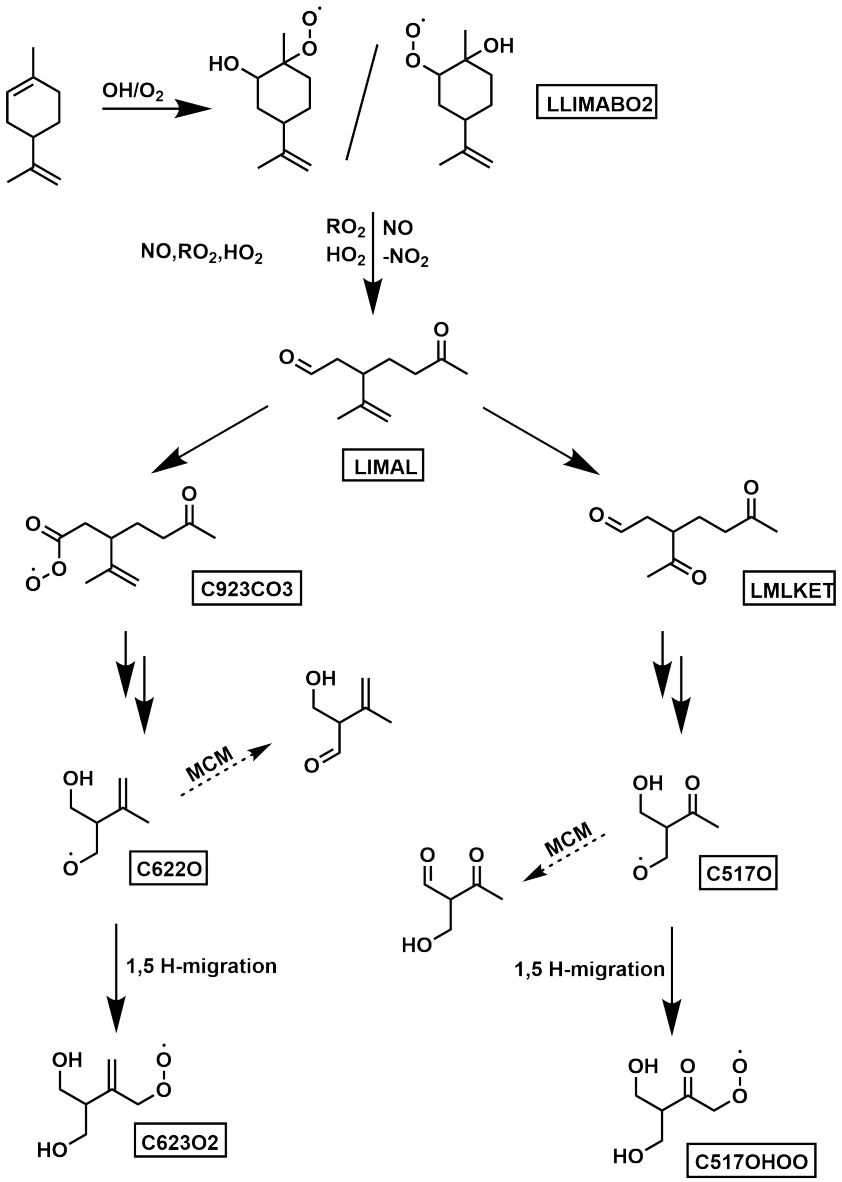

Figure 3.7: Schematic representation of the change in the LIMAL branch of the limonene-OH mechanism compared to the MCM. For a better comparison with the MCM, the molecule names are provided.

The limonene-OH reaction scheme is the most detailed of the limonene-oxidant mechanism.

The MCM mechanism forms three different peroxy radicals upon OH- and O_2-addition. In the developed scheme, those radicals are condensed into two lumped species (LLIMABO2, LABPINCO2), as the ring addition isomers (LLIMABO2) both lead to the same ring-opening product (LIMAL). After the formation of LIMAL (see Fig. 3.7), two large adaptions are applied to the reaction branch. A dominant pathway of LIMAL is the H-abstraction at the aldehyde reaction site. After O_2 addition this reaction branch yields a peroxidic acid (C923CO3). This acid decomposes in additional oxidation steps, producing an alkoxy radical (C622O). In the MCM this radical undergoes H-abstraction by O_2 forming an aldehyde. However, the comparison to SAR estimates shows that the 1,5 H-migration outcompetes the H-abstraction. Thus, the reaction yields a hydroxy moiety and a peroxy radical (C623O2) instead. Note that the molecule C623O2 has a different structure in MESSy and the MCM. A similar adaption was made to the LMLKET branch of LIMAL (see Fig. 3.7). In this branch, an alkoxy radical (C517O) is formed, which performs a 1,4 H-shift in the MCM. This channel is redirected to the available 1,5 H-shift yielding a peroxy radical. As LMLKET is also formed from the OH-addition to the non-ring double bond, the change to C517O impacts all branches in the limonene-OH mechanism. The novel reaction pathways lead to different final products. In theoretical investigations, Vereecken and Peeters [2004]

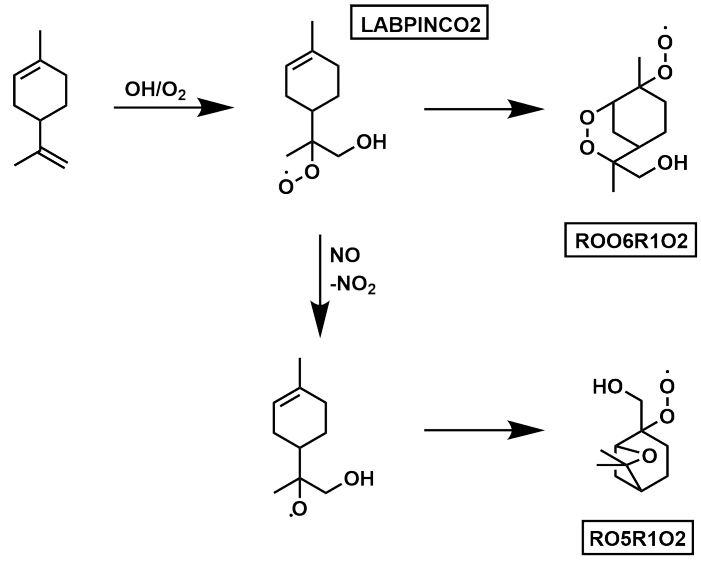

Figure 3.8: Formation pathways of bicyclic ring structures in the limonene OH mechanism. The ring closure reaction of the alkoxy radical competes with a beta scission yielding the corresponding ketone and a hydroxymethyl hydroperoxy radical.

discovered two ring-closure pathways in the α- and β-pinene reaction mechanisms. They also constructed the oxidation mechanism of the newly formed products. Later, Piletic and Kleindienst [2022] extended the application of this reaction mechanism to the limonene-OH oxidation. In this work, the developments of Vereecken and Peeters [2004] are applied to the first-generation products of the non-ring OH-addition (LABPINCO2). This leads to a

further distinction between the implemented and the original MCM scheme.
Figure 3.8 displays the mechanistic formation of both ring-closure products. The subsequent oxidation mechanism is taken from Vereecken and Peeters [2004], but extended to form final products already included in MESSy's chemical scheme. It has to be noted that the rate constants have been adapted from the theoretical calculations of Vereecken and Peeters [2004]. However, they investigated pinene products, which are isomers of the compound in the limonene mechanism. Therefore, a similar but not identical rate constant would be expected for LABPINCO2 and the later product oxidation. The rates should be reassessed when more data on the kinetics of the limonene oxidation is available. The

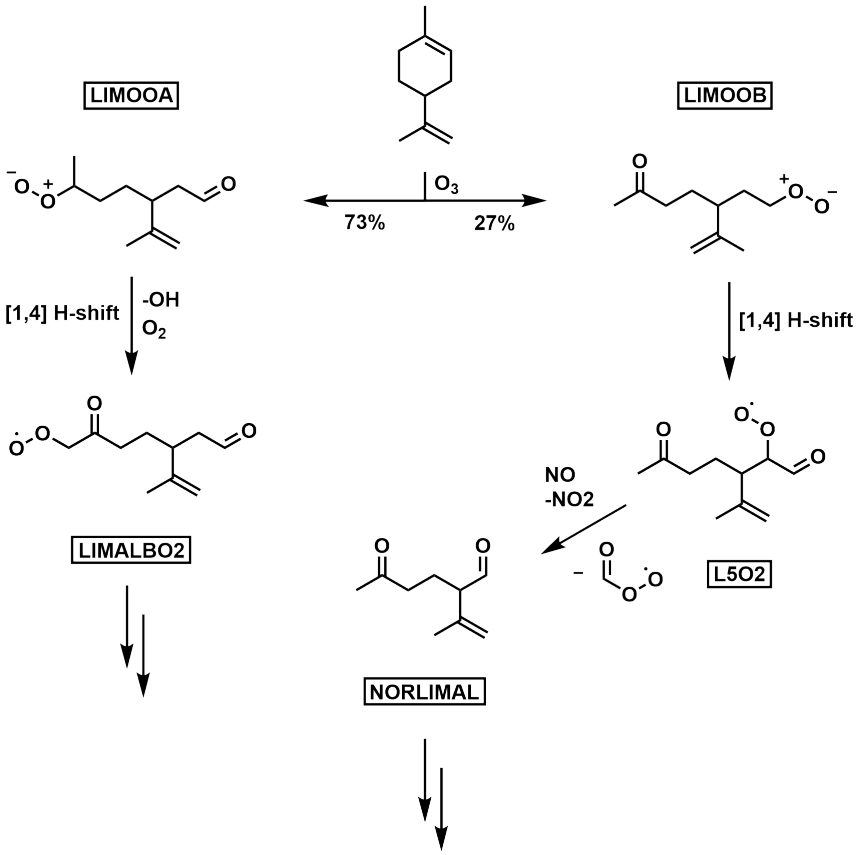

Figure 3.9: Simplified representation of the initial reaction of limonene with ozone. The processing of the criegee intermediate LIMOOA conforms with the MCM, while LIMOOB was adapted based on literature data [Pang et al., 2022, Rissanen et al., 2014].

reaction mechanism of limonene with ozone consists of mechanistic information from the MCM and available work by Pang et al. [2022], Rissanen et al. [2014], Carslaw [2013]. Only the addition of O_3 to the in-ring double bond is considered, similar to the MCM mechanism. After the formation of the molozonide, it decomposes into a carbonyl and a criegee intermediate moiety, opening the carbon ring. This results in either an aldehyde and an in-chain criegee intermediate, or a ketone and a terminal criegee intermediate (see Fig. 3.9).

The in-chain criegee intermediate (LIMOOA) is dominant with a 73% share. This first-generation product is implemented following the MCM with minor modifications based on Carslaw [2013]. The MCM chemistry of the minor product (LIMOOB), on the other hand, does not agree with the experimental and theoretical work in Pang et al. [2022], Rissanen et al. [2014]. The terminal criegee intermediate forms, after a series of fast reactions, an aldehyde at the former criegee position and a secondary peroxy radical at the neighboring carbon. This is supported by the ozonolysis behavior of cyclohexene and has been successfully applied in experimental studies. Data from Newland et al. [2018] were used to estimate the rate constants for the decomposition of the criegee intermediate.
The monoterpenes camphene, sabinene, and carene were excluded from the forward box model comparison. All three had simplified chemical mechanisms designed to yield α-pinene products. However, the structural differences between the monoterpenes would not lead to the formation of these products (at least not exclusively). Due to the lack of detail, they did not meet the same quality standards as the remaining mechanisms. Therefore, they were excluded (only in the box model study) and it was planned to reintroduce a revised mechanism in the future. This update is beyond of the scope of this work. In the global model study, the camphene, sabinene, and carene mechanisms are still applied as the exclusion has more implications than in the box model. The potential influence of the missing monoterpenes on the box model results is assessed in the model-model comparison.

3.1.3 Volatile organic compounds from anthropogenic origin

Anthropogenic VOCs make a significant contribution to the SOA budget in certain areas. It has been estimated that aromatics accounted for over 20% of the non methane volatile organic compound (NMVOC) in China in 2005 [Wei et al., 2008]. Aromatics and alkanes have been identified as the main substituents in vehicle exhaust gas emissions [Schmitz et al., 2000]. Ng et al. [2007] investigated the SOA yield of xylene, benzene, and toluene. In chamber experiments with ammonium sulfate seeds, they found a benzene SOA yield of more than 25%. For C8-C20 n-alkanes, Aumont et al. [2012] found an increasing OA yield with increasing OA concentration. In particular, large n-alkanes depicted a high OA yield. Because of these potential implications for SOA and the overall gas-phase chemistry, both classes of compounds were investigated further.

Benzene

The chemistry of benzene and toluene in MESSy was previously derived from the MCM. Some reductions are applied to control the computational demand within the global model [Cabrera-Perez et al., 2016]. Nevertheless, the level of detail is comparable to that of the MCM. In this mechanism, benzene is oxidized by an OH radical, yielding phenol, bicyclic peroxy radicals (BZBIPERO2), and epoxides. The chemistry of the epoxide was simplified in the model. Due to the developments on IEPOX in the present work, it was hypothesised

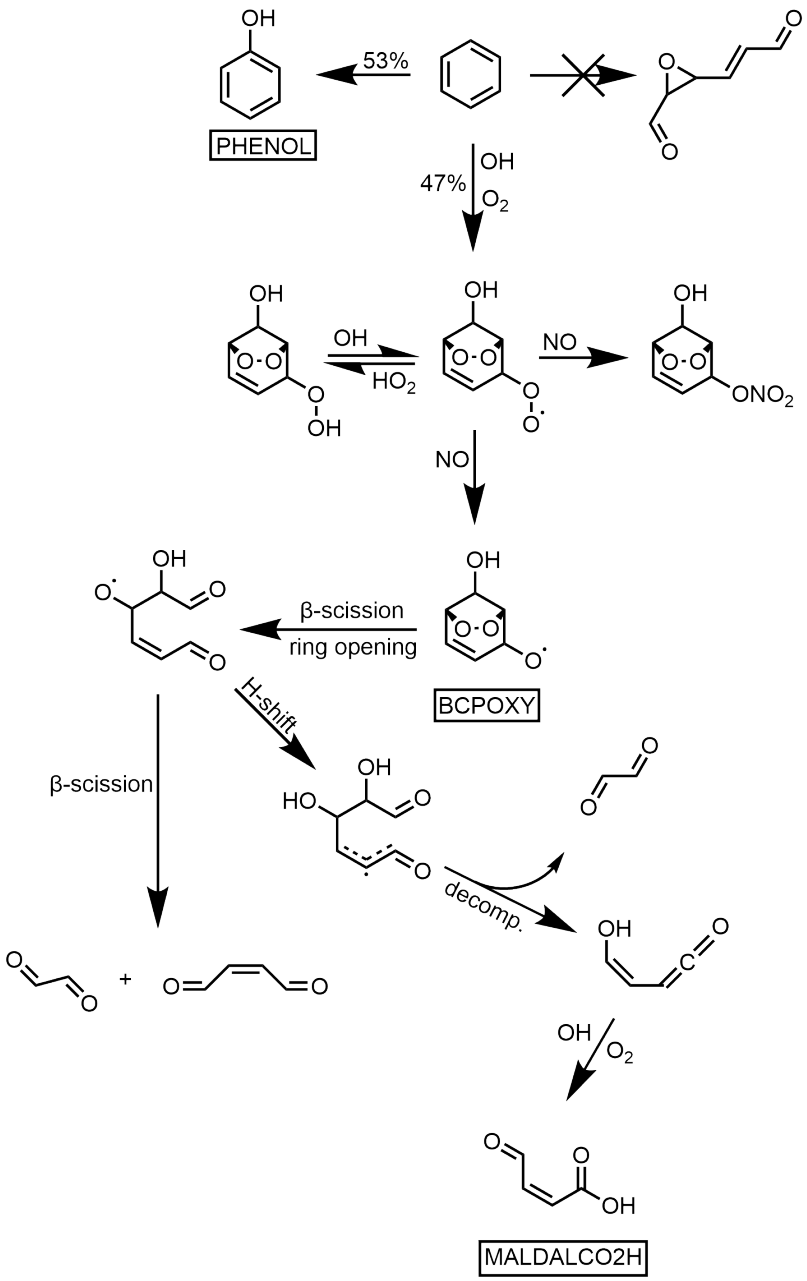

Figure 3.10: Adapted Benzene OH-oxidation mechanism. The epoxide formation is excluded and the branching ratio of the peroxy ring-closure enhanced.

that the epoxide could also be ring-opened, resulting in a highly oxidized product. This product could have a significant impact on benzene SOA yields. However, the formation of the epoxide in high yields could not be demonstrated in recent theoretical and experimental investigations (under 1% yield) [Xu et al., 2020, Vereecken, 2019]. Instead, Xu et al. [2020] neglected the epoxide pathway and increased the branching ratio of the ring-closure reaction branch. This mechanistic reassessment increases the importance of BZBIPERO2, which in turn requires more detail for further oxidation. In this work, the benzene mechanism is modified following Xu et al. [2020] and Wang et al. [2013]. Xu et al. [2020] elucidated the mechanism in experiments, while Wang et al. [2013] investigated rate constants in theoretical calculations. This update is expected to result in a more realistic product composition from the benzene oxidation. Note that the MCM (and the previous kinetic model of MESSy) includes an epoxide yield of 10%.
Figure 3.10 displays the adapted and the novel pathways. In the novel mechanism, the OH-addition to benzene forms phenol and BZBIPERO2. The epoxide pathway is neglected. The oxidation of BZBIPERO2 has an increased level of detail, rather than reducing the mechanism to the end products. Instead, the peroxy radical is converted to an alkoxy radical. The molecule undergoes two beta-scission reactions, in rapid succession. The first scission opens the carbon ring structure. The remaining alkoxy radical then leads to the cleavage of the peroxy bond. The alkoxy radical moiety is retained. In the newly formed molecule, a further beta-scission reaction and an H-shift reaction is accessible. The beta scission yields glyoxal and but-2-ene-1,4-dione (both known to the model). In the H-shift reaction branch, glyoxal is also one of the main products, together with beta-formylacrylic acid. Therefore, the new mechanism can still explain the high glyoxal yields measured in benzene experiments [Xu et al., 2020]. Concerning SOA, the new mechanism is expected to reduce the SOA yield from benzene. Nevertheless, under cloudy conditions, glyoxal oligomer formation efficiently yields SOA [Rosanka et al., 2021b].

n-Alkanes

The chemical scheme of MESSy covers the oxidation of *n*-alkanes by OH ranging from methane up to butane. However, the SOA yield from *n*-alkanes increases with the alkane size [Aumont et al., 2012]. At the same time, the complexity of the mechanism also increases with size. Large unfunctionalized molecules have more reactive sites and a wider range of possible products. Implementing all emitted *n*-alkanes in the chemical scheme of a global model is not feasible due to computational constraints. Therefore, the medium and large *n*-alkanes have so far only been treated in a simplified way in the insoluble mode (ORACLE). For a first assessment of the impact of new *n*-alkanes on SOA (hydrophobic and hydrophilic SOA) and further chemistry, the new *n*-alkane mechanism is restricted to *n*-alkanes from *n*-pentane to *n*-octane. Furthermore, only the addition of one secondary reactive site is covered. This reduced mechanism is a first step towards a comprehensive alkane scheme in the future.

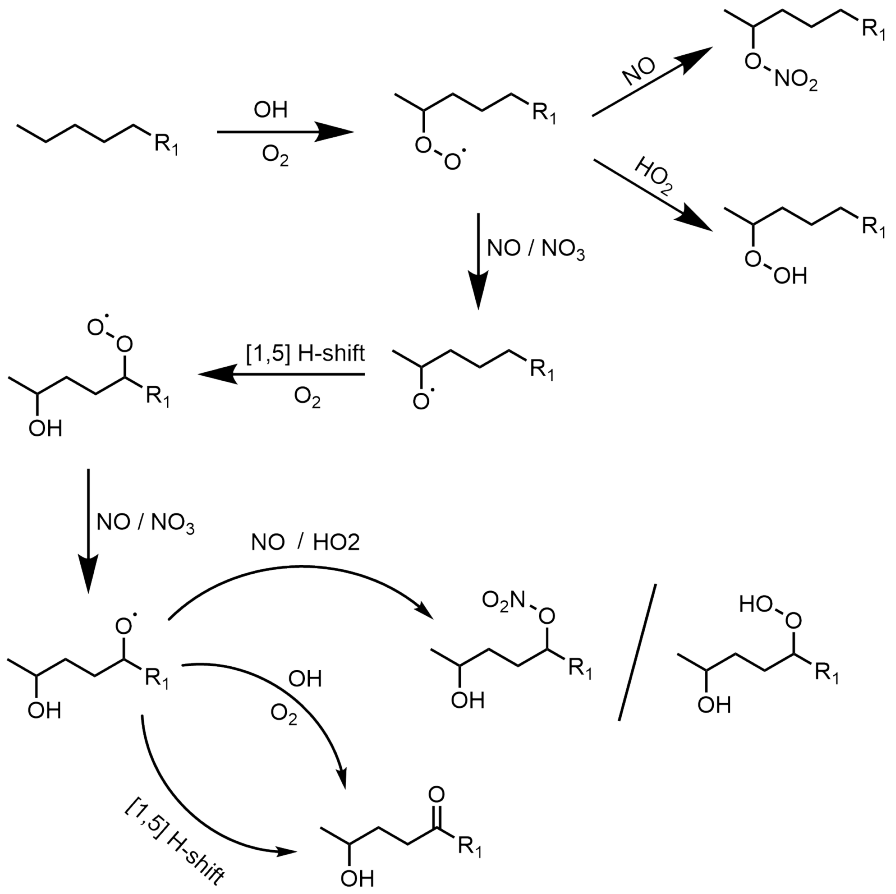

Figure 3.11: Novel *n*-hexane oxidation mechanism after Atkinson et al. [2008]. This mechanism is similarly implemented for *n*-pentane, *n*-heptane and *n*-octane.

Figure 3.11 displays the reduced mechanism for *n*-hexane. The mechanism design and reaction order are representative of all *n*-alkanes. The mechanism development was guided by the work of Atkinson et al. [2008]. The H-abstraction by OH is reduced to the secondary carbon site adjacent to the terminal carbon, neglecting the oxidation sites with equal rates. After the typical peroxy radical addition and radical reactions including NO or HO_2, an alkoxy radical is obtained. Due to the slow β-scission rate constant, the dominant pathway is the 1,5 H-migration yielding a hydroxyl group and a peroxy radical. The RO_2 moiety is once again converted to an alkoxy radical. Similar to the first alkoxy radical, the chemical environment favors an H-migration over the scission reaction. The main final product, besides the intermediate nitrates and hydroperoxides, is a hydroxy ketone (or a hydroxy aldehyde for pentane). This product has a moderate solubility. Therefore, it only affects hydrophilic SOA under cold conditions.

Table 3.2: Collection of aerosol chemical composition, liquid water content, ambient ($T_{ambient,SOAS}$) and aerosol water temperature ($T_{aerosol,SOAS}$).

Chemical composition						
NH_4^+ / $\frac{\mu g}{m^3}$	NO_3^- / $\frac{\mu g}{m^3}$	SO_4^{2-} / $\frac{\mu g}{m^3}$	LWC / $\frac{\mu g}{m^3}$	$r_{aerosol}$ / μm	$T_{ambient,SOAS}$ / K	$T_{aerosol,SOAS}$ / K
0.9	0.7	2.4	3.0	1.0	295.2-301.2	300.6

3.2 Model-Model comparison and IEPOX concentrations against observations

In this section, the updated mechanism is compared to the previous version of the mechanism. The CAABA/MECCA box model is imployed for this comparison. Two setups are constructed, one with the old and one with the updated mechanism. Several sensitivity simulations are performed under different physical and chemical conditions. The comparison focuses on LVOC concentrations and the influence of environmental variables on LVOC formation. LVOCs replace SOA due to the limitations of CAABA/MECCA concerning SOA formation and aerosol microphysics (see Sect. 2.1). LVOCs are used as a proxy for SOA. In CAABA/MECCA, only gas-aqueous partitioning is applied, and condensation of organics onto pre-existing particles is neglected. However, it is assumed that all LVOC in the gas and aqueous phase are converted to SOA. This assumption provides an upper bound on the SOA concentration. In addition to the model-to-model comparison, observational data are used to evaluate the new IEPOX mechanism.

3.2.1 Simulation setup model-model comparison

Model-model comparisons are highly dependent on the details of the simulation setup. In this study, the boundary conditions of the CAABA/MECCA box model are modified to represent the conditions during the SOAS campaign. This campaign was conducted in the southeastern US during summer. The observation scenario is representative of a mildly polluted (from anthropogenic sources) deciduous forest in summer. One of the objectives of the observation campaign was to investigate the formation of SOA, especially from isoprene [Budisulistiorini et al., 2015]. Due to the large changes in the isoprene chemistry in this work, the campaign data can be used to investigate the product concentrations. Further details of the SOAS campaign can be found in Budisulistiorini et al. [2015], Ayres et al. [2015], Sareen et al. [2016]. Organic mixing ratios (isoprene and IEPOX), radical concentrations, and physical constants were measured during the campaign. The isoprene concentration is constrained to the mean measured mixing ratio during the campaign (4 nmol/mol) [Hu et al., 2015]. This ensures that the modeled IEPOX SOA tracers are comparable to the observations. Limonene, α-pinene and β-pinene mixing ratios are set to 0.6 ppb. Compared to the observed concentrations, this is realistic for α-pinene and β-pinene [Qin et al., 2018]. However, limonene combines the measured concentrations of limonene and the remaining

Table 3.3: Model initial mixing ratios of the major chemical compounds. More information about the selected numbers is given in the text.

Species	**mixing ratio / nmol/mol**	**Species**	**mixing ratio / [nmol/mol]**
H_2O_2	7	MGLYOX	0.5
O_3	25	C_5H_8	4
O_2	2.1×10^{8}	PAN	0.1
NH_3	1	NO_3	3.15×10^{-3}
NO	2×10^{-2}	APINENE	0.6
NO_2	4×10^{-2}	BPINENE	0.6
HNO_3	5×10^{-3}	HCOOH	0.35
N_2	7.8×10^{8}	LIMONENE	0.6
CH_4	1.86×10^{3}	BENZENE	0.1
HCHO	5	ACETOL	4
CO	100	C_5H_{12}	0.4
CO_2	3.5×10^{5}	C_6H_{14}	0.4
CH_3CO_2H	2	C_7H_{16}	0.4
CH_3CO_3H	1.5	C_8H_{18}	0.4
CH_3OH	0.5	CH_3OOH	4
HONO	4×10^{-5}	TOLUENE	0.1

monoterpenes. The limonene concentration is still a factor of three higher than measured in the campaign. Otherwise, the influence of monoterpenes would be covered by the isoprene oxidation results. Similarly, anthropogenic emissions are elevated to compensate for missing sources of OH-reactivity. Nevertheless, the modeled and measured oxidant mixing ratios are in the same order of magnitude and isoprene remains the dominant VOC [Qin et al., 2018]. Other initial concentrations of chemical species are set to values that were previously applied in Taraborrelli et al. [2009].

Aerosol concentrations, properties, and physical constants have been set to values measured during the SOAS campaign (see Tab. 3.2). The composition of inorganic aerosols is adapted from Xu et al. [2015]. The liquid water content plays an important role in the model simulation, as only partitioning based on Henry's law constants is accessible. Consequently, the liquid water content is constrained to the mean value of the SOAS campaign [Nguyen et al., 2014]. Table 3.2 additionally displays the ambient and aerosol water temperature during the SOAS measurements. Both temperatures are close to the standard conditions applied in the model (298 K). Table 3.4 provides a list of the abbreviations used for the performed sensitivity simulations. It also contains a description of each setup. The comparison covers the different chemical mechanisms at varying temperatures. Moreover, the impact of NO_x on LVOC formation is investigated.

Table 3.4: Abbreviations and descriptions of the sensitivity simulation of the model-model comparison.

Abbreviation	Description
BASE	base run with the updated mechanism
OLD	model run with CAABA/MECCA 4.5.5
BASE-278K	low temperature run with the updated mechanism
OLD-278K	low temperature run with CAABA/MECCA 4.5.5
High-NO_x	model run with the updated mechanism at high NO_x
Medium-NO_x	model run with the updated mechanism at medium NO_x
Low-NO_x	model run with the updated mechanism at low NO_x

3.2.2 Low-volatile organic compound mixing ratio

The impact of the new chemistry on SOA is assessed by comparing LVOC concentrations throughout sensitivity simulations. All LVOCs are assumed to be SOA precursors. This assumption is applied to gaseous and aqueous-phase LVOC, to approximate the SOA formation. This is necessary because of the missing processes in CAABA/MECCA. In the box model, only Henry's law constants are applied for partitioning with pure water as reference. However, condensation would require saturation mass concentrations or Henry's law constant referenced to organic liquids. Hodzic et al. [2014] investigated the correlation between saturation concentration and Henry's law coefficients. Donahue et al. [2012] defined an upper limit for LVOC at > 0.3 $\mu g/m^3$. Applying the correlation published by Hodzic et al. [2014], this corresponds to a Henry's law constant of $\sim 1 \times 10^8$ M/atm. Therefore, to account for condensation and dissolution, LVOCs are defined as compounds with $H_s \geqslant 1 \times 10^8$ M/atm. LVOCs are additionally divided into four categories to facilitate the analysis. The categories relate to the carbon count of the included molecules. Small-LVOCs include molecules with up to four carbons, medium-LVOC with five and six carbons, large-LVOC with more than six carbons, and total LVOC includes all categories. This simplified the assignment of LVOC mixing ratio changes to a precursor molecule. In the analysis, the small-LVOC category is neglected, as no significant change is observed for this size range.

BASE vs OLD comparison

Figure 3.12 displays the LVOC mixing ratios for the BASE and OLD simulations of all categories. In addition to the runs at standard conditions, the figures depict the LVOC at 278 K. The medium-sized LVOC category shows the most significant change. Before sunrise, the medium-LVOC concentration is negligible. During the night the O_3 and NO_3 chemistry is dominates. The low medium-LVOC mixin ratio implies that the isoprene NO_3 mechanism shows little influence on LVOC. Due to the low initial concentration of NO_3, a large contribution from this mechanism was not expected. The isoprene NO_3 mechanism is analyzed in detail in Section 3.3.3. At sunrise, OH is formed and medium-LVOC continuously increases. The maximum mixing ratio is reached at 5 pm. This maximum mixing ratio is a

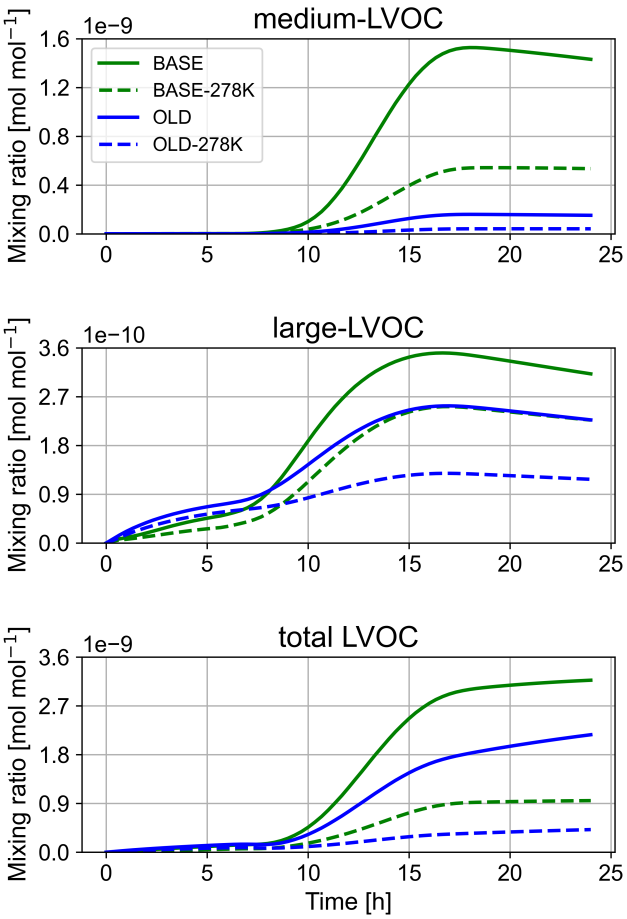

Figure 3.12: LVOC mixing ratios for the three main LVOC categories and a set of two temperatures (278 K and 298 K). Note that the LVOC include both gas and aqueous phase species.

factor of 10 higher in BASE than in OLD. The strong increase in LVOC mixing ratio after sunrise can be attributed to the formation of LISOPBEPX ($H_s = 1.3 \times 10^{10}$ M/atm) and the IEPOX products. In particular, the tetrol (MEBUTETROL) and the organic sulfate (IDOS) have a considerable contribution. The LVOC formation is temperature-dependent and decreases with falling temperature. In light of the chemical kinetics, this is expected. The reaction rates correlate with temperature, resulting for instance in a lower OH concentration (see Fig. 3.13d). At the same time, the acidity of the aqueous phase is lower at higher temperatures (see Fig. 7.1b). As described in section 3.1.2, MEBUTETROL and also the corresponding organic sulfate (IDOS) are formed in an acid-catalyzed ring-opening reaction. However, Henry's law constants increase with decreasing temperature. At higher temperatures, the increase in reaction rates is higher than the decrease in solubility. This dependence is not generally expected on a global scale. The large LVOCs depict a similar dependence on temperature, but a different LVOC change between BASE and OLD, especially before sunrise. During this period, the OLD outcompetes the BASE simulation. Here

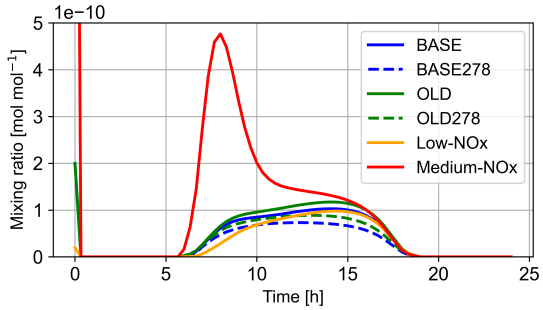

(a) NO mixing ratio

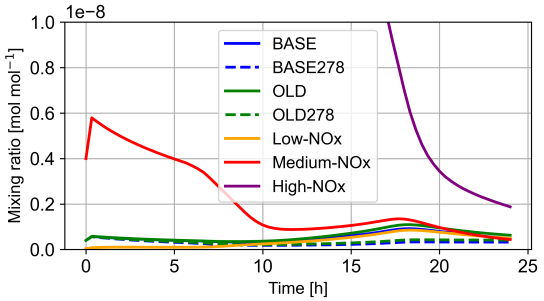

(b) NO_2 mixing ratio

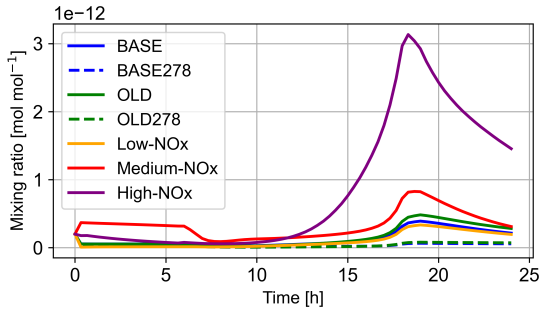

(c) NO_3 mixing ratio

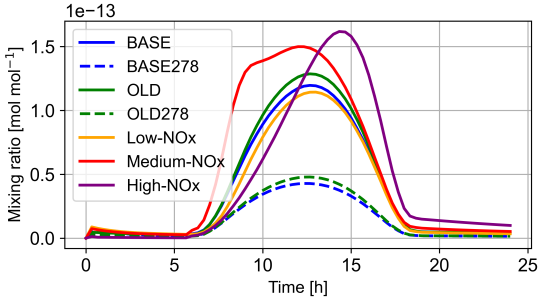

(d) OH mixing ratio

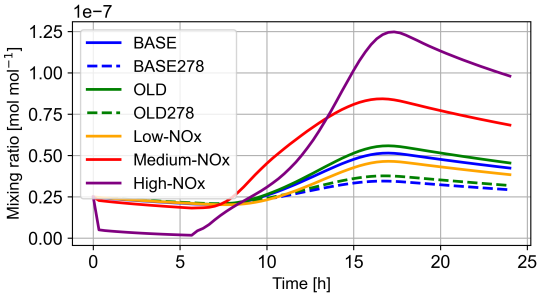

(e) O_3 mixing ratio

Figure 3.13: Oxidant concentrations for all sensitivity simulations. In the figure for NO, the High-NO_x scenario is not shown, due to its significant difference to the remaining simulations. Note that NO is converted to NO_2 and NO_3 during the night (reaction with RO_2 and ozone). At daytime, the photolysis of NO_2 enhances the NO concentration. These processes explain the strong NO_x concentration variations.

it can be assumed that the new limonene mechanism does not form a substantial amount of LVOCs under the given conditions. However, it may influence the radical concentrations (e.g. ozone and nitrate) so that other processes produce less LVOC. In the BASE run, the monoterpenes carene, sabinene, and camphene were excluded as their mechanisms are highly simplified and predominantly yield α-pinene and β-pinene (see Sect. 3.1.2). The results suggest that the LVOC yields of the excluded monoterpenes dominate the LVOC of limonene at night. However, test runs with carene, sabinene, and camphene in the mechanisms do not support this hypothesis (see Fig. 7.1a). During the day, the OH concentration increases by a factor of ten, enabling the limonene-OH mechanism. This results in an increase of up to 50% in large-LVOC. Nevertheless, the ratio between large-LVOC and medium-LVOC changes from ∼1:1 in the OLD run to ∼1:5 in the BASE run. The total LVOCs show a similar trend as seen for the other categories, but the total LVOC mixing ratio does not decline at the end of the day. This is due to the formation of small-LVOC from medium- and large-LVOC, which retains LVOC molecules in the total LVOC category. Small-LVOC (not shown) are minorly impacted by the updated chemistry.
Note that in this section LVOCs are used as a proxy for SOA. Although LVOC formation increases with temperature, the evaporation of species also increases and Henry's law constants decrease. Thus, the equilibrium between organic species in the gas and aqueous/aerosol phases is shifted towards the gas phase. In simulations considering the complete SOA formation process into account, an anti-correlation between SOA concentration and temperature is expected.

BASE vs OLD impact of NO_x

The NO_x concentration plays an important role in the LVOC formation mechanisms. IEPOX is efficiently formed under high OH and HO_2 conditions but low NO_x mixing ratios. Other mechanisms require the formation of nitrate moieties or alkoxy radicals to yield LVOC, which is favored under high NO_x conditions. In the scope of the CAABA/MECCA analysis, there is a bias towards low NO_x LVOC formation. This is due to the fact that hydroperoxides are in general more soluble than nitrates, while nitrates are less volatile (higher molecular mass) [Li et al., 2016]. CAABA/MECCA does not model the condensation of gas-phase species on available aerosols. However, the aqueous-phase partitioning is modeled. As the gas-phase oxidation is more sophisticated than the aqueous-phase oxidation scheme, molecules have a longer lifetime in the aqueous phase. Thus, soluble LVOCs retain a higher concentration than less soluble LVOCs. It is expected that this behavior is different in global model simulations in which condensation is modeled (cf. Sect. 5.2.2). In the NO_x sensitivity simulations, the initial concentrations of NO are set to remote (Low-NO_x; 20 pmol/mol), mildly polluted (Medium-NO_x; 2 nmol/mol), and highly polluted (High-NO_x; 20 nmol/mol) levels. NO_2 is initialized with twice the NO mixing ratio. Figures 3.13a and 3.13b show that the radical levels for the low-NO_x case are similar to the levels of the previous analysis. In the medium-NO_x and high-NO_x sensitivity runs,

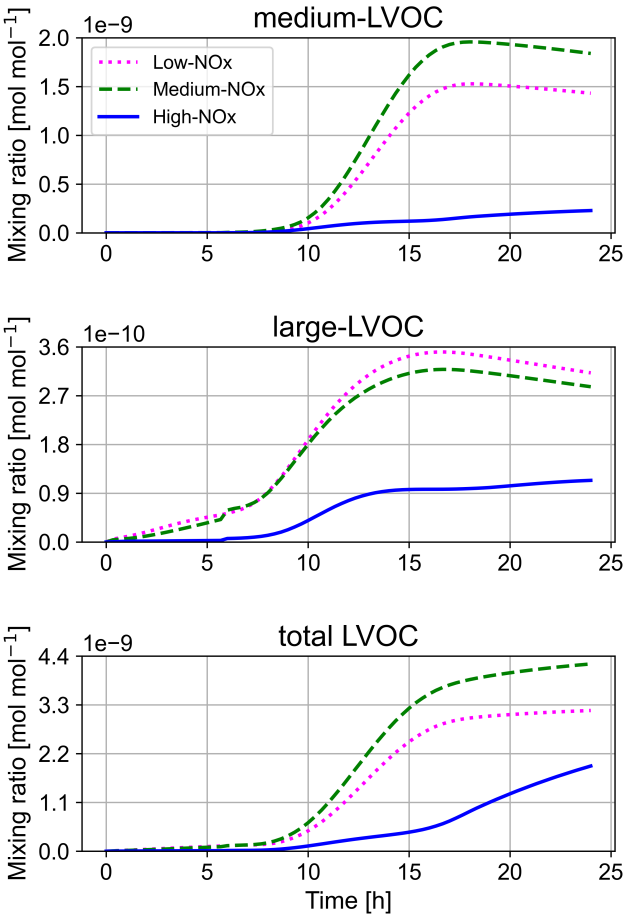

Figure 3.14: LVOC mixing ratios for the three main LVOC categories at varying NO_x concentrations. Note that the LVOC include both gas and aqueous phase species.

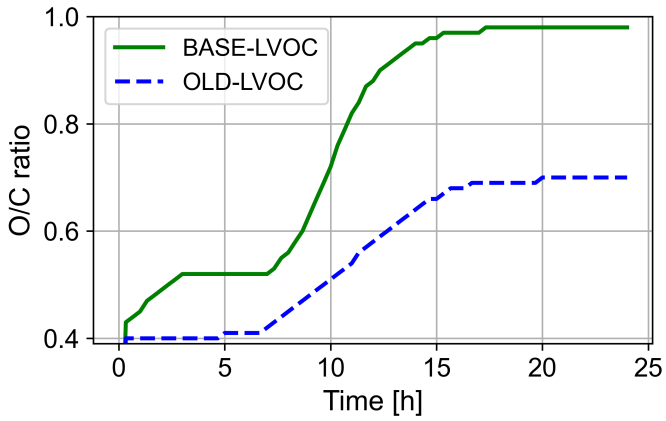

Figure 3.15: O/C ratio of the total LVOC in the OLD and BASE sensitivity simulations. In the SOAS campaign an average O/C ratio of 0.91 was measured.

NO, NO_2, NO_3 and O_3 are strongly elevated during most periods of the modeled day. Figure 3.14 illustrates the LVOC mixing ratios for medium-LVOC, large-LVOC, and total LVOC under varying NO_x concentrations. The medium-LVOC display a rather complex NO_x dependency. At low NO_x, the medium-LVOC is already high, but it increases further in the medium-NO_x simulation. At high NO_x mixing ratios, the medium-LVOC yield is low. This observation can be explained by the dependence of IEPOX and other LVOCs on the OH and HO_2 concentrations. With increasing NO_x, the OH mixing ratio also rises. At the same time, the HO_2 mixing ratio decreases. IEPOX is formed from an intermediate hydroperoxy molecule (see Fig. 3.1). This in turn requires the reaction of isoprene with OH and the conversion of the resulting peroxy radical to the hydroperoxide by HO_2. At medium NO_x concentrations, the hydroperoxide formation is rapid and the isoprene OH reaction is the dominant oxidation during daytime. At higher NO_x mixing ratios, the hydroperoxide formation from peroxy radicals is slower due to the lower HO_2 concentration. Other pathways of the RO_2 radicals gain more importance. The dependence of the large LVOC on NO_x is different for day and night. In the first 10 hours of the modelled day, the low- and medium-NO_x simulations show a similar LVOC yield. At later times, the low-NO_x simulation starts to outperform the medium-NO_x sensitivity run. Similar to the medium LVOC, this can be explained by the dependence of LVOC on OH and HO_2. Under high NO_x conditions the LVOC yield is always the lowest. Similar to the total LVOC in the previous analysis, the mixing ratios do not decrease at the end of the modelled day. As before, this is due to the small LVOC that is modelled but not represented.

3.2.3 Low-volatile organic compound O/C ratio

The oxygen-to-carbon (O/C) ratio gives a first assessment of the chemical composition. The comparison against observational or experimental data under similar conditions indicates the quality of the applied chemical mechanism. Global models commonly under-predict the

Table 3.5: Modeled and measured MEBUTETROL and organic sulfate concentrations during the SOAS campaign. The model values were extracted after a full modeled day. Measured data is acquired from Hu et al. [2015].

Compound	Measured / $\frac{\mu g}{m^3}$	Modeled / $\frac{\mu g}{m^3}$	Modeled no MEBUTETROL degrad. / $\frac{\mu g}{m^3}$
	Hu et al. [2015]	**This work**	
MEBUTETROL	0.3	4.4	6.6
OS	0.6	5.3	4.4
total IEPOX-SOA	0.9	9.7	11.0

degree of oxidation in hydrophilic SOA, and cloud and rain droplets. The implementation of IEPOX chemistry and the aqueous-phase oxidation products is expected to increase the O/C ratio due to the high degree of oxidation of the products. MEBUTETROL and IDOS exhibit an O/C ratio of 1.0 and 1.6, respectively. Only small oxidized organic compounds like formic acid or methyl sulfonate reach higher O/C ratios.
Figure 3.15 displays the O/C ratio of the summed-up LVOC during the full modeled day. The O/C ratio of the BASE run shows a higher value in all time instances. At the end of the day, the LVOCs in the OLD run have a mean O/C ratio of 0.70, while the BASE run simulates a value of 0.98. In the SOAS campaign an average O/C ratio of 0.91 was measured, with an O/C range of detected compounds from 0.5 to 1.4 [Massoli et al., 2018]. This comparison is perturbed by the differences in initial VOC concentrations in the model. However, isoprene products are the main source of LVOC and SOA. The isoprene mixing ratio is constrained to the mean measured value and the radical concentrations are in a similar magnitude in the model and during the campaign. Therefore, it can be concluded that the observations are in good agreement with the results of the BASE run.

3.2.4 Measured and modeled IEPOX secondary organic aerosol tracers

The results of the LVOC concentration and the O/C ratio suggest that the aqueous-phase oxidation products of IEPOX dominate the LVOC mixing ratio and the SOA concentration in regions with high isoprene emissions under low and medium NO_x conditions. Due to the potentially large contribution of these products in global model simulation, it is central that they are formed in a realistic magnitude. Hu et al. [2015] reported IEPOX SOA tracer concentrations during the SOAS campaign. They measured the concentrations of MEBUTETROL, isoprene-derived organic sulfate, and the total IEPOX SOA contribution in organic aerosol particles. The relevant concentrations in the simulations are fine-tuned towards the SOAS campaign conditions. Nevertheless, the SOA formation is not modeled. Instead, it is assumed that all highly soluble IEPOX products in the gas and aqueous phase contribute to SOA. Due to this simplification, an overprediction of the model is expected.
Table 3.5 lists the modeled and measured IEPOX SOA tracer mass concentrations. The last column shows the modeled concentrations of the IEPOX products, excluding the novel MEBUTETROL oxidation scheme (see Fig. 3.5). Thereby, the importance of the aqueous-

phase oxidation of MEBUTETROL can be assessed. The model results are extracted after the full modeled day. In general, the modeled tracer mass concentrations are one order of magnitude higher than the measured results. The exclusion of the aqueous-phase oxidation of MEBUTETROL increases the mass concentration by 50%. Considering the given assumptions and unknown influence factors such as the aqueous-phase pH, the results are in reasonable agreement with the measurements. The ratio between MEBUTETROL and the organic sulfate is in particularly good agreement.

3.3 Model-chamber comparison

In chamber experiments, the reaction mechanisms of specific compounds are investigated. In particular, large new mechanistic additions to the model require validation before they can be applied on a global scale. Comparison with chamber experiments can be used to identify potential problems in the mechanism. The CAABA/MECCA box model is equipped to simulate simple chamber experiments that depend mainly on gas-phase reactions. For the modeling of more complex multiphase experiments, assumptions need to be applied. Nevertheless, this comparison can show the quality and possible weaknesses of the new mechanism.

3.3.1 Experiment description

The applied chamber results originate from experiments in the SAPHIR (Simulation of Atmospheric PHotochemistry in a large Reaction chamber) chamber Gkatzelis et al. [2018], Vereecken et al. [2021]. The chamber has a volume of 270 m^3 and has a two-layered wall made up of fluorine-ethen-propene [Schlosser et al., 2007]. It is located outside to use natural light to perform photochemical reactions under realistic conditions. Next to the in-house measurement devices, it provides enough space and connectivity for instruments provided by guests. Further information concerning the SAPHIR chamber can be found in Rohrer et al. [2005], Karl et al. [2006], Schlosser et al. [2007].

Limonene ozonolysis

The limonene ozonolysis experiment was conducted in 2015. It is part of a campaign investigating the aerosol formation of different BVOCs and BVOC mixtures [Gkatzelis et al., 2018]. Due to the precursor-oxidant combination, the experiment on 27. June 2015 is best suited to investigate the new limonene oxidation scheme. In this experiment, limonene was oxidized by ozone under dark conditions and the formed aerosols were aged by NO_3. Before the injection of limonene, the relative humidity was set to 50%. In the chamber, a temperature between 20°C and 26°C was measured throughout the experiment. The SAPHIR chamber has a high volume-to-surface ratio. Therefore, wall losses are minimized in the experiment. In the simulation, no wall loss is applied, but a second model simulation is

performed to investigate the potential impact of wall losses. The loss rate was adapted from Schmitt [2018]. In all simulations a dilution rate of 4.8%/h was applied, representing the mean total flow during the experiment. The LWC has a large impact on the model results as soluble gas-phase molecules can be taken up by deliquescent aerosols. Therefore, aerosol mass spectrometer (AMS) data for the high resolution H_2O signal is used to estimate the LWC. It has to be noted, that this signal is perturbed by oxygen-containing organic compounds and is expected to be the upper limit of LWC. The estimation yields a lower LWC of 6 $\mu g/m^3$. Thus, it is unlikely that the uncertainty of LWC induces a large perturbation to the model results. The injections of the experiment are listed in table 3.6. OA and O/C are both analyzed based on AMS data. For O/C the data is corrected as presented in Canagaratna et al. [2015]. The modeled organic aerosol concentration is represented by the sum of all species with an H_s larger than 4×10^6 M/atm in both gas and aqueous phase.

Isoprene oxidation by NO_3

The isoprene experiment used in the comparison is part of the isoprene-NO_3 campaign and was performed in 2018 [Brownwood et al., 2021, Carlsson et al., 2023]. The analysis in Vereecken et al. [2021] includes a comparison with the experiment on 13. August of the campaign. The presented mechanism in Section 3.1.2 is developed following Vereecken et al. [2021]. In large parts, it is a condensed subset for global model application. Selecting the same experiment for the model-chamber comparison provides more information than the differences between the model and the experiment. Additionally, the influence of the mechanism reduction can be analyzed. The original data of the chamber experiment are available at Fuchs et al. [2018] in the Eurochamp database. The experiment was conducted under dark conditions, with temperatures between 20°C and 27°C. No seed aerosols or water were injected into the chamber. Thus, model simulations are restricted to gas-phase chemistry. New particle formation is not modeled. Potential new particle formation is outside the limitations of CAABA/MECCA. Radical concentrations of NO_3 and HO_2 are constrained to the measurements. This ensures that the chemical mechanism is studied, regardless of the model's ability to reflect the radical concentration. Similar to the limonene experiment, wall losses are neglected, but a dilution of 5.6%/h is applied. The isoprene concentration is initiated based on measurements of the VOCUS instrument [Brownwood et al., 2021]. The raw data is corrected by a factor of 0.7 to account for the VOCUS dependency on water. The alkylnitrate (AN) and RO_2 concentrations are compared between the old mechanism, the new mechanism, and the experiment. The RO_2 data from the model simulations need further refinement before they can be compared to the experimental results. This is due to the applied measurement technique. The RO_2 radical is not measured directly. Instead, HO_2 radicals are measured by a laser-induced fluorescence (LIF) device. It is assumed that the RO_2 radicals undergo the reactions shown in part (a) of Figure 3.16.

In the presence of NO, peroxy radicals are converted to alkoxy radicals and NO_2. Alkoxy

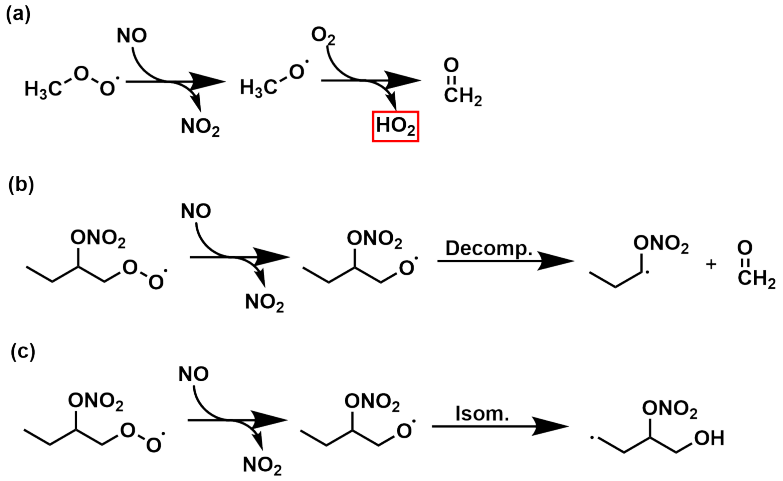

Figure 3.16: Reactions branch of the RO_2-NO kinetic scheme. LIF measurement detect the HO_2 formed in reaction (a). Depending on the chemical structure of the molecules, reactions (b) and (c) are competitive to (a).

radicals are then expected to undergo H-abstraction by O_2 forming a carbonyl group (aldehyde or ketone). In the H-abstraction process, O_2 is converted to HO_2. This molecule is detected by the LIF. Consequently, the RO_2 measurements depend on the efficiency of the RO_2 radical to form HO_2 by this mechanism. It has been shown that the efficiency is close to 100% for simple RO_2 molecules such as the methylperoxy radical [Novelli et al., 2021, Vereecken et al., 2021]. However, more complex nitrate-containing RO_2 molecules display a lower efficiency, depending on the chemical structure. Novelli et al. [2021] revealed that both decomposition and isomerization may compete with the assumed mechanism (see Fig. 3.16,(b) and (c)). Therefore, model results need to be corrected for the fraction of the pathways that do not generate HO_2. In the previous comparison by Vereecken et al. [2021], the branching ratios were estimated. Within this work, the same ratios are applied. For lumped species in the model, an even distribution among all species collected in the lumped group is assumed.

3.3.2 Comparison between modeled and measured limonene secondary organic aerosols

Figure 3.17 displays the organic mass concentration measured during the experiment, compared to the modeled secondary organic aerosol mass. Similar to the model-model analysis, the organic mass concentration in Figure 3.17 is the combined LVOC from the gas and aqueous phase, assuming that the LVOC are fully converted to SOA. Thus, the depicted model SOA is an upper limit of the SOA concentration. At the start of the experiment, limonene and ozone are injected into the chamber. This leads to a rapid increase in modeled SOA concentration. After one hour the measured SOA mass concentration displays a maximum at $\sim$50 $\mu g/m^3$ and then declines over the course of the following hours. The

Table 3.6: List of injections in both chamber experiments. In the model, the species are injected within one timestep.

Limonene + Ozone				
Injection No.	**Limonene [ppb]**	**Ozone [ppb]**	**NO [ppb]**	**Time since start [min]**
1	23.6	140	-	0
2	-	-	30	450
Isoprene + NO_3				
Injection No.	**Isoprene [ppb]**	**Ozone [ppb]**	**NO_2 [ppb]**	**Time since start [min]**
1	-	105	24	0
2	5.1	-	-	5
3	8.0	108	23	117
4	7.0	102	25	202
5	-	111	23	360

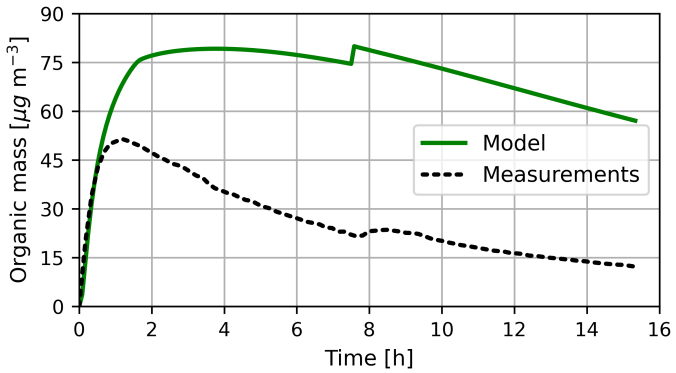

Figure 3.17: Organic mass concentration modeled and measured in the limonene oxidation experiment. In the model simulation chamber wall losses is neglected.

model predicts an increasing SOA mass concentration over the first four hours, reaching a maximum at ∼80 $\mu g/m^3$. There is also a decline in the model simulation, but only to a small extent. The NO injection after 7.5 h leads to a sharp increase in the modeled SOA. In the chamber, the SOA mass also increases. However, the chamber shows a slower response time to the injection. This stronger response by the model can be attributed to the method of injection. In a real experiment, a compound is injected and distributes in the chamber in up to 30 minutes. In the model, this is an instantaneous process, which favors the strong response as seen in the results. During the remainder of the experiment, both SOA mass concentrations continue to fall off. Although it could be demonstrated that the new limonene oxidation scheme yields LVOCs and thus SOA mass, the model results suggest that a loss process is missing for a realistic representation of the SOA mass.
The model simulation in Figure 3.17 only considers the loss by dilution. Wall loss processes are neglected. The displayed results indicate that wall losses play an important role in

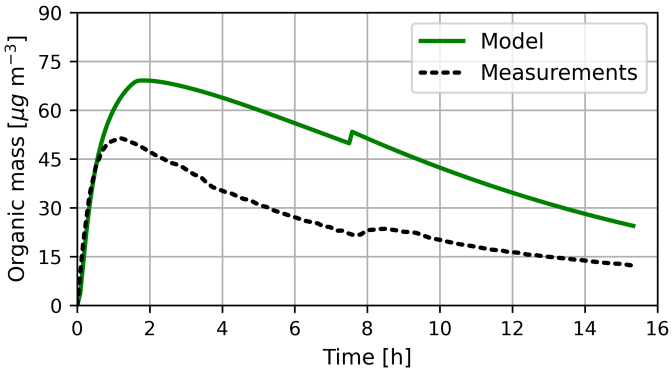

Figure 3.18: Organic mass concentration modeled for and measured in the limonene oxidation experiment. The model simulation includes an estimated wall loss based on Schmitt [2018].

describing the experiment. As wall losses were not measured in the particular experiment, they have to be estimated based on older data. Schmitt [2018] investigated the influence of wall losses on SAPHIR chamber experiments. They found that especially the loss of aerosols to the wall is a significant process. Particle wall loss was estimated with a rate constant of 1.5×10^{-5} s^{-1}. In Figure 3.18, this loss rate is applied to the model results in a simplified manner. LVOC concentrations are continuously lowered by the given rate constant. This comparison displays a closer agreement between the model and chamber results. Considering the incomplete SOA formation process in the model, the modeled concentrations reasonably agree with the chamber results. Nevertheless, the organic mass concentration is overpredicted by more than 10 μg/m^3.
Alternatively, the overprediction can be attributed to incorrect radical concentrations in the model. Radicals are not constrained in the model simulation as they were not measured during the experiment. If limonene reacts with different radicals, it produces products with potentially higher solubility or lower volatility. Thus, the results are altered and may be incorrect. The main oxidants in the mechanism are OH, ozone, and NO_3. Unfortunately, only ozone was directly measured. The influence of the hydroxy radical can be estimated based on the measurements of the OH-reactivity.
Figures 3.19a-3.19c display the modeled and measured values of the OH-reactivity and the ozone and NO_2 concentrations. Prior to the injection of NO, only the OH-reactivity and O_3 concentrations are relevant. The OH-reactivity is underpredicted, indicating that the model lacks oxidation products from limonene-OH-oxidation and proper oxidation of the intermediates in the limonene-O_3 mechanism. Nevertheless, the O_3 concentration shows a similar trend in both, the model and the measurements. After the NO injection, ozone decreases faster in the chamber experiment than in the model. This is due to the reaction of ozone with NO, yielding NO_2. At the same time, the OH reactivities approach each other. In the simulations, the injected NO is nearly completely converted to NO_2 upon

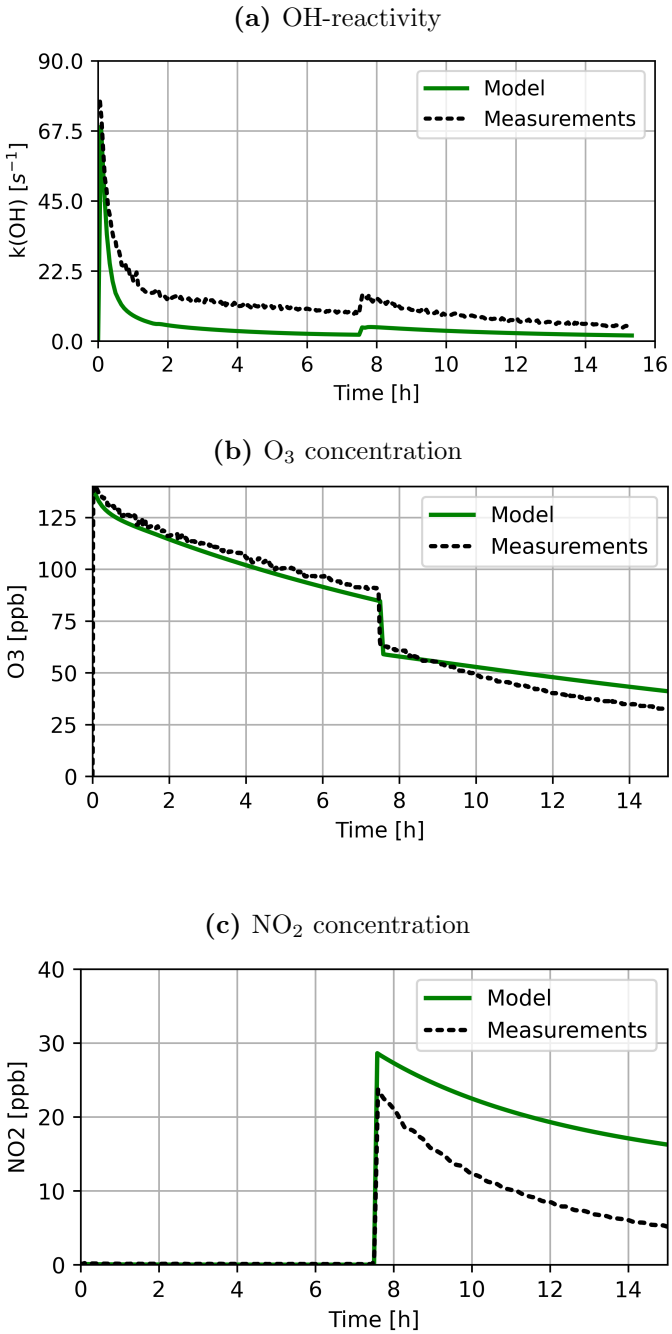

Figure 3.19: Modeled and measured OH-reactivity (a), ozone (b) and NO_2 concentration (c) in the limonene ozone experiment. The model results refer to the simulation with neglected wall losses.

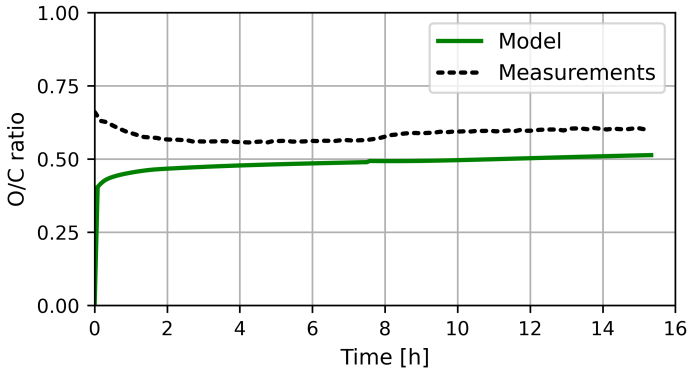

Figure 3.20: Modeled and measured O/C ratio of the OA in the limonene ozonolysis. In the model simulation, chamber wall losses was neglected.

injection, while the measurements show lower NO_2 concentrations. During the remaining experiment, NO_2 decays faster in the measurement than in the model. These differences indicate, that the model only describes the measurements up to the second injection. After that, most trends in radical concentration diverge. The model results after the second injection are strongly impacted by its capabilities to reflect aerosol processes, but also by the limonene NO_3 mechanism. This reaction branch requires further refinement as new mechanistic information becomes available.
It has been shown that the SOA is overpredicted by the model for the given assumptions and that mainly the first 7.5 h can be used to analyze the mechanism. Figure 3.20 provides further indications of the accuracy of the oxidation mechanism. It displays the O/C ratio comparison between model and measurement results. In the chamber experiment an O/C ratio of ∼0.58 is measured after the first two hours. In the same time frame, the modeled O/C ratio increases to ∼0.50. For ring-opening products of limonene that retain all carbon atoms, this refers to a difference of less than one oxygen per molecule. Within the uncertainty of the measurements and model simulations, both results show a good agreement. In flow tube experiments by Liu et al. [2022], an O/C ratio of 0.36-0.39 was measured for limonene-ozone SOA. More detailed tests of the multiphase chemistry will be accessible in future simulations by applying the recently developed MESSy DWARF [Kerkweg et al., 2024].

3.3.3 Comparison between modeled and measured products in the isoprene oxidation by the nitrate radical

The adaptations to the kinetic model in the isoprene-NO_3 oxidation mechanism are compared with experimental data of the SAPHIR chamber. In contrast to the limonene experiment, the isoprene oxidation experiment is conducted without seed and water injection. As a result, the mechanism can be investigated without aerosol-related assumptions. Vereecken et al. [2021] previously used the same experiment to examine the complex mechanism on

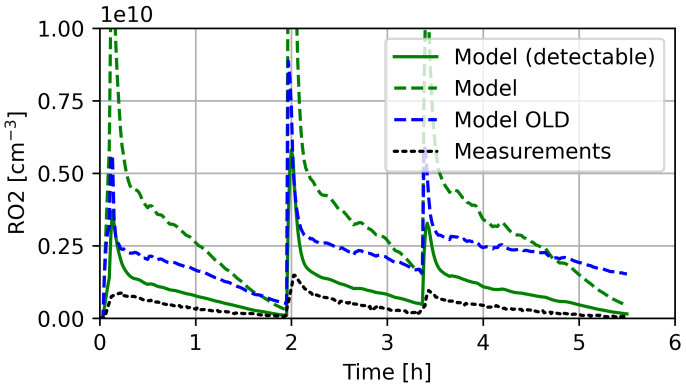

Figure 3.21: Development of the RO_2 concentration during the isoprene-NO_3 experiment and simulated by the model. The solid model line includes the corrections for the alkoxy formation efficiency.

which the new mechanism in the model is based on (see Sect. 3.1.2). The focus of this section is therefore on the comparison with the experiment, but also on the comparison with the results presented in Vereecken et al. [2021]. Thereby, possible deviations induced by the applied simplifications can be assessed. Similar to the discussion in Vereecken et al. [2021], the RO_2 concentration and alkyl nitrate yields are evaluated. The analyzed variables are also depicted for the previous model mechanism.

Figure 3.21 displays the RO_2 concentration simulated using the OLD and reworked mechanism, and measured during the chamber experiment. The model results of the new reaction mechanism are displayed with corrected and non-corrected RO_2 concentrations (see Sect. 3.3.1 and Fig. 3.16). Unfortunately, this correction cannot be applied to the old mechanism, as the correction factors were estimated for the novel compounds in Vereecken et al. [2021].

The highest RO_2 concentrations are displayed for the uncorrected new mechanism, although the RO_2 concentrations for the old mechanism are also uncorrected. This trend is observed after all isoprene and oxidant injections. However, this is consistent with the findings in Vereecken et al. [2021]. The OLD mechanism is the next closest to the measurements, but the RO_2 concentration declines differ in the OLD and new mechanisms. Especially after the last injection, the OLD mechanism retains a high RO_2 concentration until the end of the sampling. The reworked reaction scheme declines considerably faster. The RO_2 concentration of the corrected new mechanism is the closest to the experiment. It shows a similar RO_2 development, but still overpredicts the concentration by a factor of two. This observation indicates a higher RO_2 production or a smaller loss in the model simulation. The model results by Vereecken et al. [2021] show a slightly closer fit to the measurements than the current best fit. Due to the reduction of the mechanism, this is expected. Nevertheless, with respect to RO_2, the new mechanism is a good compromise between the mechanism size and the accuracy of the results. Considering the corrections to

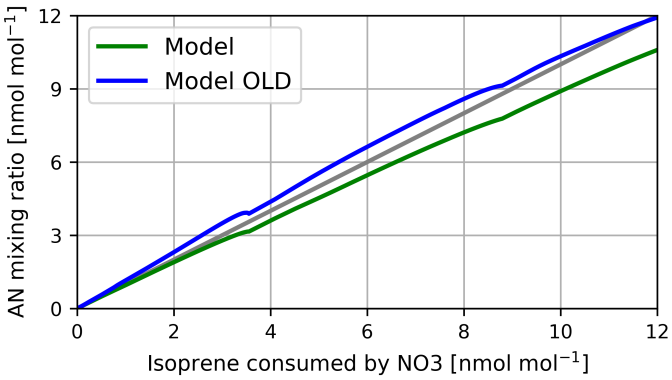

Figure 3.22: Alkylnitrate against the proportion of isoprene that was consumed by NO_3 during the chamber experiment. The grey line indicates where the consumption of isoprene by NO_3 has a 100% yield of AN. The portion of isoprene that was consumed by NO_3 was calculated as total consumed isoprene, subtracted by the isoprene consumed by OH and ozone.

the RO_2 concentrations, both the old and the new mechanism show a reasonable agreement with the experiment.

The final box model test of the novel mechanism is the direct comparison between modeled and measured alkyl nitrate mixing ratios. Throughout the isoprene-NO_3 campaign, an average of $108 \pm 15\%$ of ANs was derived. Consequently, a nitrate molecule that reacts with isoprene yields one AN molecule that can be detected. Figure 3.22 illustrates the modeled AN mixing ratios against the isoprene consumed by the NO_3 radical for the OLD and new mechanisms. The isoprene consumption was calculated based on the total consumption of isoprene minus the consumption by OH and O_3. The new mechanism lowers the AN yield by 10-20% depending on the isoprene reacted. However, the application of both mechanisms result in a reasonable agreement with the experiment. The high AN concentration in the OLD mechanism include a large fraction of 2-propanone nitrate. This molecule and other compounds solely reacts with the OH radical in the model. Under low OH conditions, these compounds have an unnaturally long lifetime. This incomplete degradation is adapted in the new mechanism so that less AN is retained. Despite the decrease in AN yield, the new products are expected to have different properties. Among those are lower volatilities and higher solubilities.

Chapter 4

Phase partitioning between gas and aqueous phase

Together with gas and aqueous-phase oxidation reactions, partitioning is one of the main factors influencing secondary organic aerosols. Two partitioning approaches are commonly applied in global models. Partitioning based on the solubility (Henry's law constants) or partitioning based on the volatility (saturation concentration). These two approaches describe different physico-chemical processes. Therefore, only when both methods are applied, the partitioning scheme provides realistic amounts of secondary organic aerosols. This work focuses on hydrophilic SOA. Consequently, the partitioning by dissolution of gases in aqueous media is of central importance. Note that partial results of this chapter have been published in Wieser et al. [2024].

4.1 General

4.1.1 Henry's law

Henry's law describes the partitioning of species between the gas phase and pure water [Henry, 1803]. Due to its long history, the term "Henry's law constants" refers to measured and estimated values that follow different definitions and naming conventions [Sander, 2015]. In the context of this thesis, Henry's law constants are defined as the amount concentration (c) of a species in water divided by the partial pressure (p) of the same species in the gas phase. According to the IUPAC definition, this specific constant is associated with the formula sign H_{s}^{cp}. In the following, the abbreviation H_{s} is applied for the described Henry's law constant, which is defined by the formula below.

$$H_{\mathrm{s}} = \lim_{c \to 0} \frac{c}{p} \tag{4.1}$$

Measured values of H_{s} are (in most cases) only valid for the specific temperature range. For a more general application (e.g. in global models), the temperature dependence of

the constant is also required. H_s can vary by orders of magnitude in different regions and altitudes. The van't Hoff equation is used to account for the temperature dependence of H_s.

$$B = \frac{dln(H_s)}{d(1/T)} = -\frac{\Delta_{sol}H}{R} \tag{4.2}$$

B is the temperature dependence coefficient. It can be calculated by dividing the solvation enthalpy ($\Delta_{sol}H$) by the ideal gas constant (R). Integrating and solving the equation for H_s gives the Equation 4.3.

$$H_s(T) = H_s^0 \cdot \exp(B \cdot (\frac{1}{T} - \frac{1}{T^0})) \tag{4.3}$$

Since $\Delta_{sol}H$ is also temperature dependent, Equation 4.3 is valid within a certain temperature range [Sander, 2015]. The temperature dependence is largely unknown and therefore neglected in most applications. Depending on the compounds of interest, this can introduce a significant error in the model results or in the analysis of an experiment [Kühne et al., 2005].

H_s also changes with the salt concentration (ionic strength) in the aqueous phase (perturbation from pure water). This phenomenon is called salting-in or salting-out effect, for increasing and decreasing H_s, respectively [Schumpe, 1993]. This behavior was first discovered by Setschenow in 1889 based on the solubility of CO_2 in water [Setschenow, 1889].

$$\log 10 \frac{H_{s,0}}{H_{s,salt}} = K_s \cdot c_{salt} \tag{4.4}$$

According to Setschenow, the decadic logarithm of the Henry's law constant in pure water ($H_{s,0}$) divided by the Henry's law constant in the salt solution ($H_{s,salt}$) equals a constant (K_s) multiplied by the salt concentration. K_s is called the Setschenow constant and is specific to a solute/salt combination [Ni and Yalkowsky, 2003]. Due to the large number of different organic gases in the atmosphere, a Setschenow constant for every possible combination would require an extensive database, coupled with systematic measurements. An alternative approach is the prediction of Setschenow constants from known solute/salt combinations [Ni and Yalkowsky, 2003]. Most systems remain unexplored, making the large-scale application of salting-in and salting-out effects in global models difficult. In atmospheric science, Henry's law is commonly used to describe the concentrations of species that are dissolved in cloud or rain droplets [Mao et al., 2014]. Given the abundance of trace gases and the LWC in clouds the applicability of Henry's law to dilute solutions is valid.

4.1.2 Estimation of Henry's law constants

Similar to the Setschenow constants, also the H_s data are not complete. For well-known compounds, the partitioning has been studied and H_s is known. In contrast, reaction intermediates or novel compounds have unknown solubility parameters. In order to operate a global model with a large number of molecules, missing H_s can be estimated from available data. Typically, bond/group contribution methods such as HenryWIN or GROMHE are applied [US-EPA, 2012, Raventos-Duran et al., 2010]. In these methods, data on H_s from a training set and the molecular structure are correlated to estimate the individual contribution of a predefined group to H_s. For a compound with an unknown H_s, the molecule is analyzed for these groups. The H_s is then estimated based on the linear combination of the contribution of the recognized groups. This methodology can produce a large H_s inventory with a level of detail that relates to the training set. Group contribution methods are a good compromise between complexity and precision.

4.1.3 Estimation of the temperature dependence of Henry's law constants

It has been shown that the H_s can depend considerably on temperature and moderately on pressure [Lau et al., 2010]. These dependencies are often neglected due to the scarcity of literature data, although this might lead to systematic errors depending on the compounds under consideration. A general overview and a collection of data is presented by Staudinger and Roberts [2001]. They found that on average H_s values double for a temperature decrease of 10 K, but many atmospherically relevant compounds exceed this average value. Temperature dependence has similar pitfalls as H_s: data for intermediates or novel compounds are only available from estimations. Thus, atmospheric models with a detailed reaction mechanism, combined with a sophisticated partitioning scheme rely on the accuracy of the available estimation schemes. Kühne et al. [2005] developed an estimation approach for the temperature dependence (B) of H_s. Similar to the $H_{s,0}$, B is estimated based on the chemical structure of the compound. This estimation approach is restricted to molecules containing functional groups covered by the training set. Figure 4.1 illustrates the dependence of H_s for six example compounds (alcohols and aldehydes). The dashed lines are calculated with estimated values according to Kühne et al. [2005]. The solid colored lines are based on literature data. The black line indicates H_s neglecting temperature dependence. The figure illustrates how much the solubility varies in different temperature regimes in the atmosphere.

4.1.4 Henry's law constants for non-water solvents

Traditionally, Henry's law constants refer to the partitioning of organic vapors into a pure aqueous phase. However, also organic aerosols with low LWC are also abundant in the Earth's atmosphere. Additionally, under certain conditions, a phase separation of the

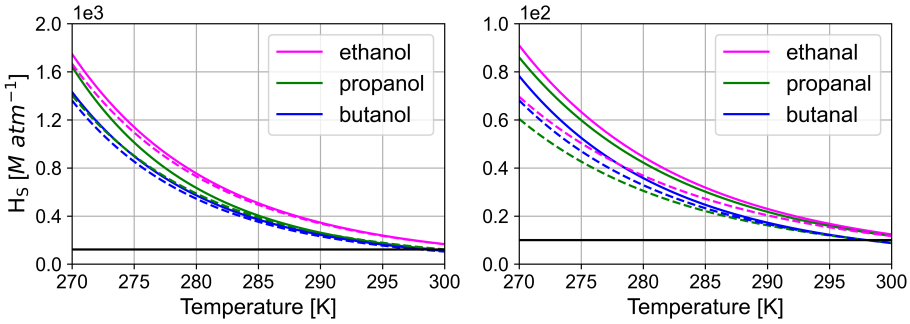

Figure 4.1: Dependency of Henry's law constant on temperature. The Henry's law constants at 298 K are taken from Sander [2015]. The colored solid line denotes H_s after literature data Sander [2015] and the dashed lines denote the temperature dependency as estimated by Kühne et al. [2005]. The black solid line neglects the temperature dependency.

organic and aqueous phases has been found [Pye et al., 2017, Anttila et al., 2006]. The simulation of organic aerosol formation and loss requires a more sophisticated partitioning scheme than the traditional Henry's law constants. The use of Henry's law can be extended in two main ways to allow additional partitioning to an organic phase in a model. The partitioning scheme can be extended by a second phase transfer based on the saturation vapor pressure of a compound. This requires an additional computational framework for complete schemes like the Volatility Basis Set [Donahue et al., 2006]. However, this approach often neglects the kinetics behind the process. The second option is to extend the already existing Henry's law partitioning scheme by partitioning to non-water solvents. Henry's law constants are related to the saturation vapor pressure (p^*) by the infinite dilution activity coefficient (γ) [Sander, 1999]. Equation 4.5 illustrates the relationship between H_s and γ.

$$H_s = \frac{\rho_{H_2O}/M_{H_2O}}{p^* \cdot \gamma^\infty} \tag{4.5}$$

H_s are inversely proportional to the saturation vapor pressure and γ. The saturation vapor pressure (p^*) refers to the pressure of an organic compound in the gas phase. H_s refers to a concentration in water and a pressure in the gas phase. Thus, the density (ρ_{H_2O}) and the molar mass (M_{H_2O}) of water are required for the unit conversion. The infinite dilution activity coefficient (γ) refers to a solvent or solvent mixture, thus solvents other than water can be selected. In the literature, laboratory experiments and estimation schemes for γ for different solvents are available. Consequently, a so-called $H_{s,org}$ can be derived, which describes the partitioning of an organic molecule into an organic phase. Alternatively, the relationship between saturation vapor and H_s can be used to derive H_s from p^*. Anttila et al. [2006] and Gaston et al. [2014b] successfully tested the application of this calculation scheme for chamber experiments on N_2O_5 uptake by aerosols with organic coatings. Other studies have used $H_{s,org}$ to model chamber experiments on the reactive uptake of epoxydiols [Gaston et al., 2014a, Octaviani et al., 2021].

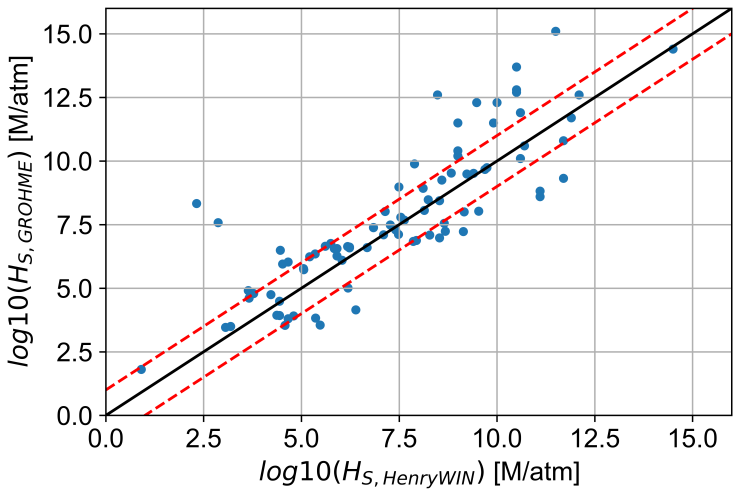

Figure 4.2: H_s of the newly created limonene oxidation products estimated by GROMHE against the same compounds estimated by HenryWIN. The black solid and red dashed lines indicate a perfect agreement and a difference by one order of magnitude, respectively.

4.2 Estimation of Henry's law constants

In a multiphase system, it is essential, that the partitioning constants are updated together with the chemical reactions. This step ensures that new soluble/low volatile gases can partition to all available phases. Otherwise, the new chemistry would only affect the phase in which it is applied in the first place. In the kinetic framework of CAABA/MECCA, Henry's law coefficients are utilized to simulate phase partitioning to aqueous media. The outgassing is simulated based on Equation 2.5. Literature data on partitioning coefficients are generally not available for all compounds in a kinetic model. In particular, data on reaction intermediates that are part of novel mechanisms are very scarce [Raventos-Duran et al., 2010]. As a result, model simulations require estimates of the physical properties of the compounds involved. The HenryWIN and GROMHE estimation methods are well-known, freely available prediction schemes for scientific applications. In the scope of this work, it is necessary to decide which method is most appropriate for the mechanism update. The US Environmental Protection Agency (EPA) provides the code of the HenryWIN method within the EPI Suite software [US-EPA, 2012]. Estimations are based on preset molecular descriptors in a bond contribution method that are calculated from experimental results [Meylan and Howard, 1991]. The alternative method, GROMHE, estimates H_s using a group contribution method [Raventos-Duran et al., 2010]. In both schemes, the descriptors of a single molecule are combined in a multiple linear regression to obtain the final Henry's law constant. The training sets are equal in size (345 species), but HernyWIN has 90 additional compounds for subsequent regression. However, GROMHE has a larger validation set including 143 compounds (HenryWIN uses data from 72 compounds). The amount of literature data used gives a first indication of the quality of the resulting H_s.

Table 4.1: Representative cutout of complete table listing the estimated molecules together with the respective values. Molecules are represented by the MESSy name, the SMILES string and the InChI-Key. The full table is available in the appendix (see Tab. 7.1)

compound	**SMILES**	**InChI-Key**	H_s / M/atm	$d \ln H_s / d(1/T)$ / K
Large Alkanes + OH				
C7H15ONO2	CC(ON(=O)(=O))CCCCC	HHXLSUKHLTZWKR	2.3E-1	6600
C7H15O2H	CC(OO)CCCCC	FWELUXZVATZEMI	7.8E1	7600
C7OHONO2	CCC(ON(=O)(=O))CCC(O)C	MZJHMUSTUUJGSJ	1.2E3	10600
C7OHOOH	CCC(OO)CCC(O)C	KHWIBANUCNWWGW	4.2E5	11600
C72CO5OH (LC7OHCO)	CCC(O)CCC(=O)C	MQRALIJAASQPNT	2.1E5	10500
C8H17ONO2	CC(ON(=O)(=O))CCCCCC	QCOKASLKYUXYJH	6.9E2	7000
C8H17O2H	CC(OO)CCCCCC	NAXZMRYIZGEALQ	5.9E1	8000
C8OHONO2	CCCC(ON(=O)(=O))CCC(O)C	UEQWMROPIQKFIM	9.1E2	10900
C8OHOOH	CCCC(OO)CCC(O)C	QQTSMKQYSKGCOU	3.2E5	11900
C82CO5OH (LC8OHCO)	CCCC(O)CCC(=O)C	KZPPEBIAPHLFQD	1.6E5	10800
Limonene				
HOC2H4CHO	O=CCCO	AKXKFZDCRYJKTF	3.6E3	9900
C517OOH	CC(=O)C(CO)COO	OAFCGFSFCVGKSH	1.1E8	13400
HMVKBCHO	CC(=O)C(C=O)CO	XYGGNMZYIGPNCC	3.6E7	10800
CO2C4CHO	CC(=O)CCC=O	KEHNRUNQZGRQHU	5.6E4	8400
C519OOH	CC(=O)C(CCO)OO	RDSFTYTWLRHJGZ	1.7E7	13400
C517CHO	CC(=O)C(CO)CC=O	JGHPNZFTVGSLKF	9.6E4	12700
C622OOH	C=C(C)C(CO)COO	GWTGWFHICNOSTQ	1.3E6	12000
C519CHO	CC(=O)C(C=O)CCO	PVAHQKAVPKMXGV	2.8E8	11100
C622ONO2	C=C(C)C(CO)CON(=O)=O	UCAFMJJTBHTENA	3.5E3	11000
C622CHO	C=C(C)C(CO)CC=O	JWVBPJJNIHELFZ	5.9E5	11300
C728OOH	CC(CO)(OO)C(CO)CC=O	WJYXJQPIZCIBJO	5.4E12	18100
C727OOH	CC(=O)CCC(OO)C(C)=O	IMCLYNFQESJQRO	2.0E7	12700
C624CHO	C=C(C)C(C=O)CCO	AIMYSSDKEKDSEU	5.9E5	11300
C730OOH	CC(CO)(OO)C(C=O)CCO	YXKHJQXHKYJCPI	6.2E12	18100
C728ONO2	CC(CO)(ON(=O)=O)C(CO)CC=O	CDBHNFBQKSTCON	1.5E10	17100
C622CONO2	C=C(C)C(CO)CC(=O)ON(=O)=O	DJCVHBPUJHAWIU	1.0E5	13900
C730ONO2	CC(CO)(ON(=O)=O)C(C=O)CCO	RVWIAVBELSCRER	3.5E11	17100
C818CO	CC(=O)C(=O)CC(CO)C(C)=O	CRQAGKNTHDNGEW	6.6E8	15900
C816CO	C=C(C)C(=O)CCC(C)=O	FXXXYZSMIIVJDG	3.1E4	10200
C819OOH	CC(=O)CCC(=O)C(C)(CO)OO	JRXMSSDNDAZISI	2.1E9	17000
C817CO	CC(=O)CCC(C=O)C(C)=O	WSCYQCAMZDXSLH	3.1E7	12000
C817OOH	CC(=O)CCC(COO)C(C)=O	WQMXPSRLZZCZTO	1.2E8	13000
C818OOH	CC(=O)C(CO)CC(OO)C(C)=O	DLMBPALZQHFDOH	5.8E10	17000
C729CHO	C=C(C)C(CC=O)CC=O	MEGRLTONSLAOOM	8.1E4	10200
C822OOH	C=C(C)C(CC=O)CCOO	XWYULULFGKWPMD	8.9E5	11300

The datasets are required to cover a wide range of chemical structures. Thereby, most molecule structures or substructures can be constructed based on the data. In the first publication of the GROMHE method, Raventos-Duran et al. [2010] compared GROMHE with the previously established HenryWIN. The application of the GROMHE validation set to the HenryWIN estimation results revealed that HenryWIN struggles to estimate H_s for multifunctional molecules. This problem is expected to cause a potentially large bias for products in reaction mechanisms, as compounds formed in later reaction generations typically have more than one functional group. Nevertheless, Raventos-Duran et al. [2010] also showed that the error is most likely related to the training set of HenryWIN. Using the GROMHE training set, HenryWIN estimated H_s close to the validation set.
In order to get a clear picture of which estimation method is better suited to the new mechanism, the H_s of the compounds in the new limonene mechanism were estimated and compared between the two methods (see Fig. 4.2). Most of the estimates (61%) deviate by less than one order of magnitude between the two methods, displaying a generally good agreement between the two methods. The deviation is similar to the comparison of HenryWIN estimates with experimental values in Raventos-Duran et al. [2010]. Further analysis of the compounds with the largest deviations shows an overprediction of H_s by GROMHE for molecules containing hydroxyl together with carbonyl groups. On the other hand, Henry's law constants of nitrate-containing compounds are often overpredicted by HenryWIN. The comparison of all estimates against published data obtained with the commercially available COSMOtherm software was inconclusive [Wang et al., 2017]. Both estimation methods considered here have individual advantages and disadvantages. Based on the previous analysis by Raventos-Duran et al. [2010] and the larger validation set, GROMHE is applied to estimate H_s in this work. A representative subset of all estimated Henry's law coefficients is displayed in Table 4.1. All estimation results are included in the appendix.

4.3 Henry's law constants for non-ideal solutions

4.3.1 Calculation of Henry's law constants based on saturation vapor pressure and infinity dilution activity coefficients

The Henry's law constant estimates described above follow the assumption that the solvent is pure water. The calculation based on the saturation vapor pressure and γ (see Eq. 4.5) is an alternative to the direct estimation of H_s. Further, it can be used to extend the Henry's law framework to non-water solvents. It allows estimations that take into account the non-ideal effects of concentrated solutions and solvent mixtures. This is useful for modeling organic aerosols, which are are expected to contain a complex mixture of solvents. Here, the alternative H_s estimation route is used to generate an additional/independent set of Henry's law constants, calculated by invoking different assumptions. This derivation route requires the estimation of the saturation vapor pressure (p^*) and the infinite dilution activity

coefficient (γ) and therefore still requires the application of estimation schemes. However, unlike the Henry's law constants, p^* refers to the gas/liquid partitioning of the pure organic component (not a pure aqueous phase). Both frameworks are connected by γ, which in turn is based on Raoult's law [Sander, 1999]. This relationship (see Eq. 4.5) allows the estimation of Henry's law constants that relate to variable solvents or solvent mixtures. In the forward analysis, this relation is used to validate the derived water referenced H_s. However, this ensemble of estimation methods can be a valuable tool for future developments. The range of application of H_s can be extended to pure organic liquids or mixtures. The γ constant is derived by various measurement techniques, but the application in models requires the estimation of a wider variety of constants [Kojima et al., 1997a].

4.3.2 Estimation of saturation vapor pressures

The literature offers different estimation methods for the saturation vapor pressure due to the importance of the constant in atmospheric science [Pankow, 1994, Odum, 1998]. The following discussion is limited to freely available estimation methods. Methods such as the recently published COSMOtherm extension are not considered [Hyttinen et al., 2024].
Within the MESSy model, the ORACLE submodel uses the approach published in Li et al. [2016] within its VBS partitioning scheme (see Sect. 2.4.3) to derive the required saturation vapor pressures. This scheme provides a good compromise between complexity and accuracy. Nevertheless, it uses only the elemental composition, neglecting details about the structural information of the molecule (e.g. functional groups). This simplification complicates the comparability of final H_s to the GROMHE estimation approach (see Sect. 4.2). Differences in the estimation results would always be attributed to the lack of detail in the estimation approach. The estimation schemes for p^* included in the UManSysProp suite [Topping et al., 2016] have several similarities with GROMHE. Both schemes use SMILES as input format and the desired physical properties are derived using a group contribution method. Thus, the input information is the same in both approaches. Besides the saturation vapor pressure, the UManSysProp is able to estimate further constants like the sub-cooled liquid density and various critical properties of a compound. These options are not applied in this work.
The developers of the UManSysProp used to host a website that could be utilized to estimate all the properties it contains. This website is no longer accessible, but the code behind the website is stored in a GitLab repository (see `https://github.com/loftytopping/UManSysProp_public/tree/master/umansysprop`). For the application in this work, the code was migrated to JURECA, one of the Jülich supercomputers [Krause and Thörnig, 2016]. A working setup was developed, including a custom Python required file. For the estimation of the saturation vapor pressure, different method combinations are available in the UManSysProp. The accurate estimation of the saturation vapor pressure requires the knowledge of the boiling temperature of the compound. In this work, the boiling temperature and saturation vapor pressure methods of Nannoolal et al. [2004] and Nannoolal et al.

[2008] are applied, respectively. This combination was found to be among the most accurate saturation vaor pressure estimation methods [Barley and McFiggans, 2010]. However, it has to be noted that the author describes a large deviation between the estimated and measured boiling temperatures of small compounds [Nannoolal et al., 2004]. Table 4.2 lists a subset of the estimated p^* against experimental data [Hyttinen et al., 2024, 2022]. All estimated saturation vapor pressures are collected in Table 7.2 in the appendix.

4.3.3 Estimation of activity coefficient at infinite dilution

The selection of simple and free to use estimation schemes to derive infinite dilution activity coefficients is rather small. COSMO-RS and UNIFAC are the two most widely used, but commercial options (see Brouwer and Schuur [2019], Fig.1). Both derive the constants using a group contribution method. Alternative methods are mainly solvent models with varying levels of detail [Brouwer and Schuur, 2019]. Recently, Winter et al. [2022] published a so-called SMILES-to-properties-transformer. This software estimates γ using a machine learning approach that is trained and fine-tuned on pre-existing data. The training set consists of sampled data obtained with COSMO-RS [Klamt, 1995]. The accuracy of the approach is increased by using experimental data to fine-tune the algorithm. Winter et al. [2022] found a higher accuracy of the machine learning approach compared to the conventional prediction methods. Another advantage is the comparably simple setup and application of the method. Similar to the estimation of p^*, the input of molecular structures in SMILES format is required. The infinite dilution activity coefficients in this work are based on this method. Table 7.2 lists a subset of the estimated γ and the corresponding experimentally-derived constants. Note that the estimated constants always refer to a temperature of 298 K.

4.4 Estimation of the temperature dependency of Henry's law constants

In Section 4.1.3 the importance of the temperature dependence of Henry's law constants is assessed. Henry's law partitioning is sensitive to temperature. The partitioning to aqueous media therefore depends on the tropospheric region. Therefore, a temperature dependence coefficient is required for the newly estimated Henry's law constants. Additionally, numerous large compounds, integrated in previous updates, have unknown temperature dependence values (B) in MESSy. Kühne et al. [2005] developed an approach to estimate the temperature dependency constant, known as the B-value (see Eq. 4.3). This approach is similar to the methods described above for estimating Henry's law constants. Molecules are divided into molecular fragments. These fragments have predefined contributions to the temperature dependence. The sum of all fragments yields the B-value (see Fig. 4.3). The problem with this estimation approach is that molecular fragments have the same

Table 4.2: Collection of saturation vapor pressures and activity coefficients at infinite dilution-derived by estimation and measured in the literature. The estimated values are based on the UManSysProp [Topping et al., 2016] and the machine learning approach on Winter et al. [2022]. Experimental data are taken from Kojima et al. [1997b] (*), Hyttinen et al. [2024] (†) and Hyttinen et al. [2022] (§).

Compound	$\mathbf{p^*_{est}}$ / Pa	$\mathbf{p^*_{exp}}$ / Pa	$\gamma_{\mathbf{est}}$	$\gamma_{\mathbf{exp}}$ (T)
Hexane	2.16E4	-	5.54E3	2940* (293)
Heptane	7.08E3	-	9.41E3	8050* (293)
Octane	2.32E3	-	2.20E4	9.08E6* (298)
Methanol	2.96E4	-	1.28	1.65* (298)
Ethanol	9.70E3	-	2.72	3.74* (298)
Isopropanol	1.09E4	-	4.39	7.47* (298)
1,2-Ethanediol	2.46E1	1.17E1† (298)	0.51	0.8* (297)
Formaldehyde	3.68E5	-	2.86	2.8* (298)
Acetone	3.95E4	3.08E4† (298)	1.85	7.01* (298)
Benzene	1.37E4	-	5.18E2	2.68E3* (298)
Toluene	4.47E3	-	1.56E3	9.70E3* (298)
Oxalic acid	2.97E-2	2.9E-2†	0.26	-
Pinic acid	2.97E-4	3.2E-5§	3.60	-
Pinonic acid	9.61E-2	7.05E-5§	8.58	-

contribution in all molecules and fragment combinations. For an OH fragment, one would expect a different contribution when attached to an otherwise non-functionalized carbon compared to a carboxy element, forming an acid. For these cases Kühne et al. [2005] proposed correction factors to replace the alternatively used molecular fragments.
As part of this work, a code routine was developed following the estimation scheme of Kühne et al. [2005]. The molecular fragments and correction factors used within this code framework are listed in Table 4.3. The hydroperoxy functional group is not covered by Kühne et al. [2005]. However, hydroperoxides are an essential functional group in atmospheric reaction mechanisms. For the application to compounds within MESSy, the contribution

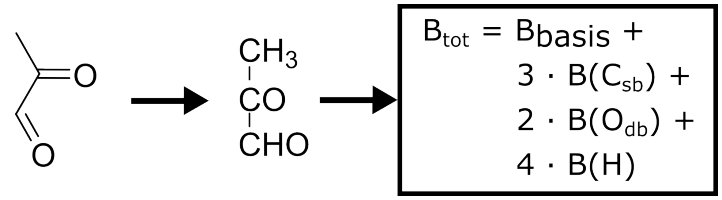

Figure 4.3: Schematic representation of the estimation approach by Kühne et al. [2005] for methylglyoxal.

Table 4.3: Molecular fragments of the Kühne et al. [2005] estimation scheme and the referring B-factors for the B-value estimation. The fragment and correction factor for the hydroperoxy group were extended within this work.

Fragment	**B-factor / K**
basis	1202
Csb / single bond	-60
Cdb / double bond	541
H	203
OH	4145
O / double bond	2931
-O-	1966
ONO2	-811
OOH	3625
correction factors	
C(=O)CO	-1538
COCCO	-1538
COC(OO)	-1538
C(=O)O	-3009
C(=O)OO	-3009

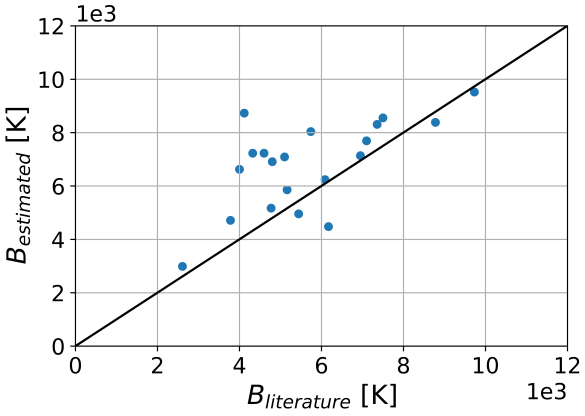

Figure 4.4: Comparison of estimated and measurement-based temperature dependencies of H_s. Literature data was taken from the supplement of Kühne et al. [2005] and Sander [2023]

Table 4.4: Abbreviations and descriptions of the sensitivity simulation performed to investigate the influence of partitioning on model results.

Abbreviation	Description
BASE	base run with the updated mechanism
BASE-psat	base run with adapted H_s based on p^* and γ
BASE-278K	low temperature run with the updated mechanism
BASE-Tdep	low temperature run with the updated mechanism, but excluded B-values

of the hydroperoxy molecular fraction has been estimated based on the difference between the literature B-value of alkanes and the B-value of hydroperoxy alkanes. The correction factor for hydroperoxidic acids is set to the correction factor for carboxylic acids. The data required for the estimation and extension are obtained from the supplement of Kühne et al. [2005] and Sander [2023].

Figure 4.4 displays a comparison between the estimated B-values and the temperature dependencies derived from experimental work. On average B-values are overpredicted by the estimation scheme. The compounds with overpredicted B-values are multi-functionalized molecules with a variety of different functional groups. This finding suggests the need for additional correction factors. For a more refined estimation scheme and further correction factors, more experimental data on B-values for multifunctional molecules are required. Additionally, not all molecules are covered by the estimation scheme. Organic sulfate molecules are known to contribute a significant fraction to SOA, while peroxy acetyl nitrate (PAN) is frequently observed in polluted regions [Brueggemann et al., 2020, Zheng et al., 2011]. Both molecule classes are not included in the estimation scheme, showing the need for further development. Nevertheless, the estimation scheme provides a first assessment of the impact of the temperature dependence of Henry's law constants.

4.5 Dependence of model results on partitioning coefficients

The previous and following model simulations include the basic CAABA/MECCA partitioning coefficients, combined with the new coefficients presented in Section 4. Phase partitioning can influence simulation results, but is commonly not analyzed in detail. In this section, the influence of the estimated coefficients on the simulation results is evaluated. In Section 1.3 and 2.4.2 the general principles and application of Henry's law constants in the model are described in detail. The constant that is used at a given temperature consists of a H_s at a reference temperature (298 K) and a temperature dependence term, which is combined in a so-called B-value. The new H_s at the reference temperature are estimated with the GROMHE scheme. The B-values were derived based on the method by Kühne et al. [2005], which was extended to include the hydroperoxy moiety. Both methods use experimental results as a training set to build up an inventory of contribution factors containing different functional groups. Henry's law constant measurements are performed with

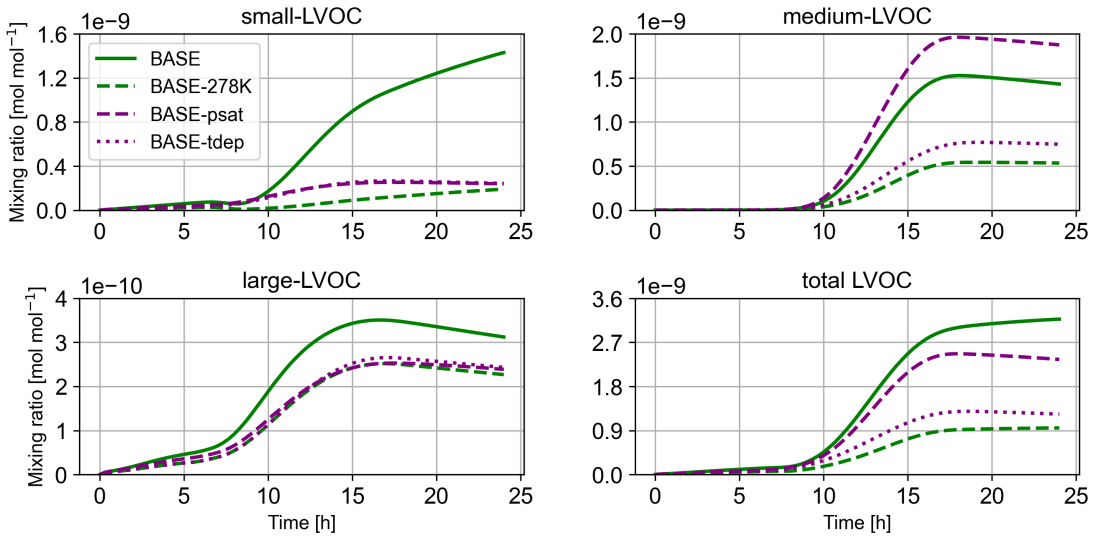

Figure 4.5: Comparison of the LVOC simulation results above with those obtained using different sets of partitioning coefficients. In BASE-psat, all H_s are replaced by H_s calculated on the basis of p^* and γ. BASE-tdep, on the other hand, does not include the novel temperature dependencies. Unlike the remaining figures, small-LVOC are shown as well, due to the large influence of the H_s replacement in BASE-psat.

an aqueous solution at near infinite dilution to fulfil the basic assumption of Henry's law. However, H_s can be alternatively derived based on saturation vapor pressures and activity coefficients at infinite dilution (see Sect. 4.3.1). The comparison of the results of the model simulation based on the different estimation approaches displays the changes induced by the estimation methods and the dependence of the model on the partitioning coefficients. At the same time, the effect of the temperature dependence on the simulation can be similarly assessed. The influence of the salt concentration and other factors cannot be evaluated within the CAABA/MECCA and MESSy models, as only the temperature dependence is considered in the both. Figure 4.5 illustrates the results of box model simulations following the basic setup of the model-model comparison (same emissions and aerosols) described in Section 3.2.1. Isoprene concentrations and aerosol characteristics refer to the SOAS campaign [Hu et al., 2015]. The comparison includes four simulations (see Tab. 4.4) BASE and BASE-278K reflect the results previously shown in Figure 3.12. They include the H_s and B-values estimated according to Sections 4.2and 4.4. The BASE-tdep simulation utilizes the same H_s, but the new B-values are excluded and the temperature is fixed to 278 K. The change in temperature is needed to review the thermal response of the partitioning. BASE-psat includes H_s based on the estimation in Section 4.3 and Equation 4.5. The BASE-psat simulation is performed at room temperature.
BASE and BASE-psat show similar results for to the total LVOC for large parts of the modeled day. However, the LVOC concentrations at the end of the day display considerable deviations. This is mainly due to large differences in the small LVOC concentrations. As

described in Section 4.3.2, Nannoolal et al. [2004] noted that the boiling point estimation method, required for the saturation vapor pressure estimation, shows large differences to the measurements. The results of the simulation agree with their findings. Medium- and Large-LVOC are predicted higher and lower by BASE-psat, respectively. The medium-LVOCs consist mainly of isoprene-derived tetrols and organic sulfates. Organic sulfates are not adapted in the current comparison due to limitations in the estimation scheme. However, the Henry's law constant of IEPOX (the tetrol and organic sulfate precursor) and the tetrol are adjusted. The partitioning constant of IEPOX is changed from 2.7×10^6 M/atm to 8.0×10^6 M/atm, while the constant of the tetrol is adjusted from 6.2×10^{12} M/atm to 3.6×10^9 M/atm. The adjustment of the IEPOX partitioning has a strong influence on the simulation results. In the medium partitioning range, smaller adaptions to the Henry's law constant have a significant effect on the fraction of the respective molecule in the gas and aqueous phase. Although the change in the tetrol is larger than three orders of magnitude, it is highly soluble according to both estimates. Therefore, this does not lead to a large change in the results. As a result, the medium LVOC concentration in BASE-psat is increased. The experimental results in Gaston et al. [2014a] suggest a Henry's law constant of 1.7×10^8 M/atm for IEPOX, in contrast to previous lower estimations/measurements. This suggests that the IEPOX partitioning should be re-evaluated as more experimental results become available.

The total LVOC increases by approximately 30% between BASE-278K and BASE-tdep. This change can be attributed to the increase in Henry's law constants of less soluble compounds. LVOCs have been used as a proxy for SOA (see Sect. 3.2.2). Thus, only compounds with a Henry's law constant greater than 1×10^8 M/atm at room temperature are considered to simulate a realistic SOA yield. At lower temperatures the proportion of soluble organics increases, but only the previously defined organics are considered LVOC. However, in return the amount of highly soluble organics decreases as the necessary gas-phase reactions are performed less. Thus, the simulation gives the false impression that LVOC yield decreases by implementing temperature dependencies. In future box model and global model simulations, this is expected to lead to a change in the SOA constituent mixture.

Chapter 5

Aqueous-phase oxidation

The oxidation of soluble organic gases in the various aqueous phases has far-reaching effects within the troposphere. It can affect radical and VOC concentrations, or change the properties of particles [Herrmann et al., 2005]. Consequently, aqueous-phase chemistry is required in models that attempt to capture the chemical state of the atmosphere. It is essential for investigating clouds and aerosols. As a result, efforts have been made over the last decades to improve the aqueous chemistry within MESSy and other atmospheric models. The most recent development concerning MESSy is the introduction of JAMOC [Rosanka et al., 2021b]. This major addition to the chemical scheme of MESSy contains a wide variety of different aqueous-phase reactions. Among those are new oxidation, partitioning, and acid/base equilibrium reactions. Due to this mechanism, the oxidation of organics up to four carbons is covered in the aqueous phases of MESSy. The oligomerization reactions of glyoxal and methylglyoxal products are potentially important for SOA [Rosanka et al., 2021b]. However, the partitioning of soluble gases to hydrophilic SOA, cloud and rain droplets may also lead to new challenges that need to be addressed.
Most tests of the updated chemical mechanism and the partitioning scheme prior to this chapter displayed an increased budget of organic molecules in the aqueous phase. With the exception of MEBUTETROL, the large and oxidized organic molecules remain non-reactive in the aqueous phase, because the corresponding chemical reactions are not included in MESSy's chemical scheme. This omission leads to an overprediction of organic molecules in the aqueous phases of an unknown magnitude. The O/C ratio as well as the vertical distribution of organic compounds in aqueous media, is expected to be similarly affected. Accordingly, the model requires a sophisticated aqueous-phase oxidation scheme to simulate of aqueous phases comparable to the real atmosphere. This task is complicated by the fact, that aqueous-phase oxidation is less researched than the gas-phase counterpart. The literature contains few ready-to-use mechanisms such that most mechanism construction needs to be done by hand, mostly from available SARs. MESSy's gas-phase reaction scheme is large and rather detailed. It yields hundreds of oxidized compounds that are soluble in aqueous media. The construction of sufficiently detailed aqueous-phase mechanisms is time-

consuming and leads to an increase in simulation time. It is therefore important to maintain a good balance between the length and comprehensiveness of the mechanism.

5.1 Development of an aqueous-phase oxidation mechanism routine

In recent years, the application of reaction generation scripts has taken rise, especially in the regional modeling community [Herrmann et al., 2005, Bräuer et al., 2019]. These scripts reduce human error (e.g. spelling or typing errors) in reaction mechanisms. They also greatly reduce the amount of time a developer or user has to spend on creating mechanisms decreases substantially. For gas-phase oxidation, SAPRC and GECKO-A are well-established mechanism generation tools [Aumont et al., 2005, Carter et al., 2023]. In the aqueous phase, CAPRAM-GECKO-A is the most widely used mechanism autogenerator [Bräuer et al., 2019]. Through the application of recent SARs, these methods have been shown to improve the chemical scheme of atmospheric models [Bräuer et al., 2019]. However, the application of the generated mechanisms in global models, similar to the MESSy framework, differs from previous use cases. The variety of aqueous phases (cloud and rain droplets, and deliquescent aerosols) requires the generation of a reduced, but self-contained mechanism. For this purpose, a new mechanism generator has to be constructed, containing adapted generation routines.

5.1.1 The aqueous-phase oxidation mechanism generator

In the scope of this work, an automatic mechanism generator has been constructed and its impact on global model simulations has been assessed. The whole generator is written in Python code and stored in a private GitLab repository. The code can be review in a zenodo repository with restricted access. Although it is mainly built to be applied to the MESSy model, the application to further models and more is possible. In the following subsections, the structure, assumptions, and limitations of the generator are presented.

5.1.2 Initial setup

Before the generation script starts, the user has to select options from an initial query. This helps to set up and customize the mechanism generation process to the user's needs. The generator can be used in two different ways. Either it is used in conjunction with the MESSy model. This option reads and writes data from and to MESSy files, simplifying the application to the model. Alternatively, an input molecule in SMILES notation can be inserted by user input. In this case a mechanism is generated for the given molecule. Note that all SMILES need to be readable by Openbabel [O'Boyle et al., 2011], otherwise they cannot be read by the generator. The forward description focuses on the application of the generator in conjunction with the MESSy model.

Table 5.1: Initial queries of the mechanism generator. The bold string inside the brackets has to be entered by the user to chose the option.

Query	**Options**
Select a molecule input type:	Single SMILES (**SMI**) Read SMILES from MESSy (**M**) Read SMILES with nitrates from MESSy (**N**)
Select the reactions/reaction combinations of interest:	H-abstraction by OH (**OH-abs**) OH-addition (**OH-add**) H-abstraction by OH and OH-addition (**OH**) tert.-nitrate hydrolysis (**NH**) photolysis reactions (**photo**) all reactions (**all**)
Choose prefered output format of unknown species:	InChi-Key strings (**I**) SMILES strings (**S**)

Table 5.1 lists all queries and the available options. First, the molecule input type has to be selected. In conjunction with MESSy, all or all nitrate-containing molecules can be selected as input. In both cases, the generator will only read in molecules that meet a certain set of requirements. The Henry's law constant of a compound is read from MESSy's chemical properties table ("chemprop.tbl"). If the Henry's law constant of a compound is below the threshold of 1×10^5 M/atm (at 298 K), or if the model does not contain a H_s for a certain species, it is neglected from the input list. Enforcing this threshold ensures that at least one third of the compound is partitioning to the aqueous phase under typical conditions (LWC = 0.15 g/m^3) [Gultepe and Isaac, 1997]. This procedure minimizes the reactions that are generated for non-soluble, volatile species. Further, molecules that are out of the scope of the estimation scheme are not considered. These include aromatics and sulfates. Before selecting the desired input type, the user can choose a reaction or multiple reaction types (see Sect. 5.1.6) of interest. The options include OH, hydrolysis, and photolysis reactions. All available reaction types are applied in the forward discussion. Finally, an output format for compounds, that are newly created by the generator, must be selected. For the application to MESSy, only the representation by InChi-Key strings is viable. The representation of compounds by SMILES strings contains symbols that are not allowed in MESSy (e.g. "="). Nevertheless, SMILES strings retain the chemical structure of a compound in its name, simplifying the analysis of a mechanism. The generator does not consider the stereochemical properties of a molecule. Thus, the output InChi-Key strings do not contain the stereo information of the molecules.

5.1.3 Input handling

The list of SMILES strings that are created in the initial setup needs further refinement to be usable by the generator. In SMILES strings there are different ways to describe the same molecule, which complicates the application within a script. Molecular representations with a clear definition of the functional groups that are bound to a specific carbon center are easier to apply. The generator uses bond matrices. The SMILES strings are first converted to mol files using the Openbabel library [O'Boyle et al., 2011]. This notation includes a label number for each atom and a bond list between labelled atoms. An additional script converts the mol file notation to the bond matrix notation. Figure 5.1 displays a schematic conversion of methylglyoxal between SMILES and bond matrix notation.

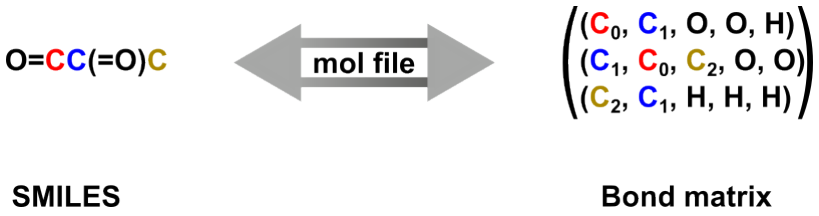

Figure 5.1: Schematic representation of the conversion of methylglyoxal between SMILES and bond matrix notation. The carbons are color coded.

In the bond matrix notation, each row is corresponds to one carbon center within the molecule. The first element in every row is the current carbon center (e.g. C_0, C_1, ...). All other elements in a row are the collection of bonded atoms or functional groups. Since only the bonds to carbon centers are described, bonds between oxygen, nitrogen, and hydrogen are summarized in functional groups. Available functional groups are peroxy radicals (OO), hydroperoxides (OOH), alcohols (OH), and nitrate groups (ONO_2). The oxygen in carbonyl groups is described by two oxygen bonds (O) to the carbon center. Double bonds between carbon centers have a similar description.

5.1.4 Reaction generation process

In this step, the generator applies the reactions selected in the initial setup and the necessary radical reactions. Here we assume that all reaction types have been selected. The OH reactions are the main source of oxidation in the generator. Therefore, molecules are first screened for possible OH-addition or H-abstraction reactions. Only one OH reaction is applied in each iteration. This restriction reduces the number of generated reactions. Furthermore, addition reactions are always preferred over abstraction reactions, to save estimation and simulation time. This assumption is based on the higher average rate constant of the addition reactions. Table 5.2 lists the mean reaction rates of the H-abstraction by OH and OH-addition based on the number of substituents. The comparison displays that the mean addition rate is at least one order of magnitude larger than the H-abstraction throughout all numbers of functional groups. Both reactions yield a peroxy radical. This

radical has two different reaction channels, as defined in the CLEPS protocol [Mouchel-Vallon et al., 2017]. The first channel is an intramolecular reaction, forming a ketone and an aldehyde with the release of HO_2. This reaction is carried out for peroxy radicals with a hydroxy group in the β-position. For molecules that do not fulfil this criterion, the only remaining channel is the RO_2-RO_2 self-reaction. RO_2-RO_2 cross reactions are not performed because the total aqueous phase RO_2 is unknown in the aqueous phases of MESSy. Alkoxy radicals are assumed to react instantaneously due to their shot lifetime. The β-scission reaction is the dominant fate of alkoxy radicals. In molecules with unstable scission products (slow reaction rate), alkoxy radicals perform H-shift reactions.
Once the OH-reaction cycle is constructed and new, stable (non-radical) products have been formed, the hydrolysis and photolysis reactions are investigated. Radicals formed in these reactions are treated in a similar way to those from OH-reactions. Further details on specific reaction kinetics are given in Section 5.1.6. During the reaction generation process, all molecules and reactions are written in SMILES notation.

5.1.5 Data post-processing

The raw output of the generator includes reactions in a non-MESSy readable, unsorted structure and also duplicate reactions. In general, the generator prints the molecules in SMILES string format. For the development of new mechanisms, SMILES strings are favorable as they are human-readable. However, SMILES strings have several problems when used in programs and scripts. Within MESSy, molecule names are not allowed to contain certain characters and should not exceed a predefined length. SMILES include "=" to represent double bonds and they can be of variable lengths. In the generator, this problem is solved by converting of the SMILES string into an InChI-Key. Without the stereo information, InChI-Keys contain only letters and always have a fixed length. This makes them safe to use in MESSy. In addition, all duplicate reactions are deleted and the reactions are sorted into size bins (short to long carbon chains of the reactants). In the final step, the reactions are labelled according to the MESSy reaction labelling convention.

5.1.6 Reaction types

Addition and H-abstraction by OH

The generator considers two different types of reactions between OH and organics, the H-abstraction by OH and the OH-addition to double bonds. In the generator, only one of the two reactions is performed per reactant and the OH-addition is always preferred. This assumption is based on the higher average rate constant of the OH-addition. Reducing the number of OH-reactions results in fewer product compounds. The reduction in the mechanism accuracy in turn gives a significant reduction in simulation time and computational demand. The H-abstraction is estimated by applying the SARs of Monod and Doussin [2008a], Doussin and Monod [2013]. Both, the basic estimation in [Monod and Doussin,

2008a] together with the update [Doussin and Monod, 2013] cover over 20 adjacency factors for neighbouring functional groups. Nitrogen- and sulfur-containing functional groups are not considered. The generation of OH-addition reactions is based on Minakata et al. [2009] and includes four of the seven published group contribution factors. The group contribution of Cl, F, and CN is not considered in the generator (halogen-containing molecules are not allowed as reactants).

Table 5.2: Comparison of the (geometric) mean reaction rates for all H-abstraction and OH-addition combinations, depending on the amount of functional groups in the molecules. For the H-abstraction by OH, the first functional group is assumed to be in the alpha position and the second in the beta position.

$N_{Funct.\ groups}$	Mean H-abstraction rate / $M^{-1}s^{-1}$	Mean OH-addition rate / $M^{-1}s^{-1}$
0	4.2×10^8	1.4×10^{10}
1	2.7×10^8	4.7×10^9
2	2.6×10^8	1.6×10^9

Nitrate hydrolysis

The hydrolysis of nitrates is limited to tertiary nitrates. Although other nitrates can also be hydrolyzed, the rate constant is considerably slower. Boyd et al. [2015] found that non-tertiary nitrates can be considered stable against hydrolysis under various conditions (e.g. different temperatures and pH). For tertiary nitrates, Zare et al. [2019] collected literature data for the hydrolysis in different chemical environments [Hu et al., 2011, Jacobs et al., 2014, Darer et al., 2011]. They applied hydrolysis rate constants in the CMAQ model based on the number of hydroxyl groups that are adjacent to the nitrate moiety. The rate constants of the tertiary nitrates collected by Zare et al. [2019] are adapted to the generation script. Nitrates are generally only read into the generator if they contain one tertiary nitrate and no subsequent nitrates. Table 4.4 lists the applied hydrolysis rate constants.

Table 5.3: Rate constants of the three different types of tertiary nitrate hydrolysis reactions. Other nitrates are not considered by the generator.

N_{OH} adjacent to tertiary nitrate	Hydrolysis rate constant / s^{-1}
0	9.3×10^{-3}
1	1.6×10^{-2}
$\geqslant 2$	4.1×10^{-4}

Photolysis of organics

The photolysis of compounds in aqueous media depends on the radiation properties in the different phases (aerosols, clouds and rain droplets). Previously, Ruggaber et al. [1997] investigated the differences in photolysis reactions in the gas and the aqueous phase. In

water droplets, they found an enhancement of the actinic flux associated with a change in droplet size and wavelength. Adapting such findings to global models is challenging due to the variety of aqueous media, physical conditions, and the amount of different molecules. However, Bateman et al. [2011], Zawadowicz et al. [2020] have demonstrated the need for an aqueous-phase photolysis scheme to reflect global concentrations of SOA and O/C ratios. The implementation of a comprehensive molecule and medium-dependent multiphase photolysis scheme is outside of the scope of this work. In previous MESSy updates, an enhancement factor of 2.33 was applied to the reaction rates that were adapted from the gas phase to the aqueous phase. Considering the measurements of Ruggaber et al. [1997], this factor corresponds to the mean enhancement between a solution of pure water and a solution with a mole fraction of 1×10^{-3} mol/mol of absorbers in a droplet with a radius of 1 μm. These conditions are commonly found in clouds and fogs. In the model, the reactions are also applied to deliquescent organic aerosols. This adaption has to be re-evaluated in future developments.

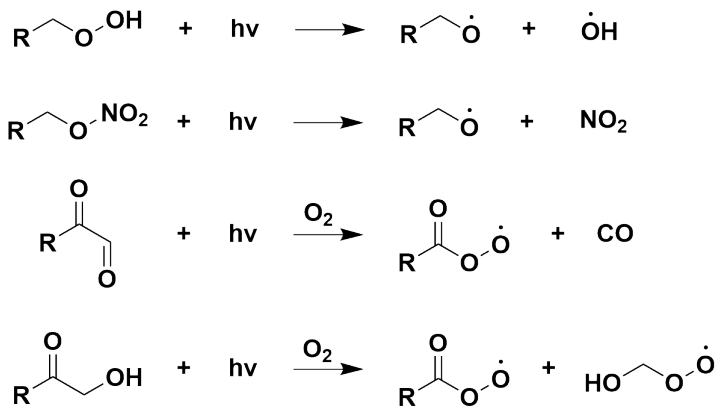

Figure 5.2: Schematic representations of all considered photolysis reactions.

The generator estimates photolysis reactions for a distinct set of predefined reaction classes. These classes are defined by the functional element that is photolyzed. A given molecule must contain a methylglyoxal-like or acetol-like functional element, a hydroperoxide, or a nitrate group for photolysis reactions to be generated. These classes represent the most important molecules to be photolyzed that were adapted from the gas-phase reaction scheme of MESSy. Photolysis rates depend on the composition of linked absorbing groups (e.g. a hydroperoxide and a neighbouring carbonyl) in a molecule [Wang et al., 2023]. This enhancement of the absorption cross section is considered for nitrates and hydroperoxides with adjacent carbonyl groups. Figure 5.2 gives a schematic overview of the included photolysis reactions.

Table 5.4: Collection of peroxy radical reactions in the mechanism generator. The faster reaction that fits to a molecule is applied in the mechanism generator. The reaction classes are based on measurements of small oxidized compounds, but are used in the mechanism for all larger homologues. Considering the low concentration of single peroxy radicals ($\sim 1 \times 10^{-10}$ M) in the aqueous phase, the hydroperoxide elimination generally outcompetes the tetroxide formation [Mouchel-Vallon et al., 2017].

Reaction class	**Chemical environment**	**Reaction rate / $M^{-1}s^{-1}$**
Tetroxide formation/decomposition	$RCH(OH)CH_2O_2$	1E8
	$RCOCH_2O_2$	4E8
	RCH_2O_2	1.6E8
Reaction class	**Chemical environment**	**Reaction rate / s^{-1}**
Hydroperoxide elimination	RCH_2OHO_2	10
	$RCH(CH_3)OHO_2$	52
	$RCH(CH_2OH)OHO_2$	190
	$RC(CH_3)(CH_3)OHO_2$	665

Reactions of organic radicals

The generation of self-contained mechanisms requires a comprehensive set of radical reactions. Alkoxy and peroxy radicals need to be processed on the correct time scales, or the whole mechanism will be affected. Previously, Mouchel-Vallon et al. [2017] constructed a set of assumptions and reactions for radicals in the aqueous phase. The generated radical reactions mostly follow this scheme.

The formation of alkoxy radicals is not explicitly considered due to their short lifetime. Instead, alkoxy radical decompose by the cleavage of the carbon-carbon bond with the lowest hybridization next to the radical (e.g. β-scission). If two bonds are similar in hybridization the first bond found is cleaved. In some molecules, bond cleavage is either slow or not possible. These molecules undergo an intramolecular H-shift, forming a hydroxy group and a peroxy radical.

The reaction pathways of peroxy radicals are more complex and therefore require more reactions. In the generator, the main reaction routes are tetroxide formation/decomposition and HO_2-elimination. For a given molecule, only one peroxy radical reaction is generated. Tetroxide formation is an intermolecular reaction of two peroxy radicals. Therefore, the reaction rate depends on the peroxy radical concentration. The aqueous-phase chemistry scheme of the MESSy model does not include information on the total concentration of all peroxy radicals. Similar to the CLEPS protocol, the tetroxide formation only considers self-reaction (reaction of a molecule with a second equal molecule). This assumption decelerates the processing of peroxy radicals. The decomposition of the tetroxide depends on the structure of the molecule. Three of the four different decomposition pathways that are discussed in Mouchel-Vallon et al. [2017] are applied in the generator. The fourth reaction

route involves the formation of charged molecules. This class of molecules is not considered in the generator. In a particular pathway, the decomposition branches into different products. Branches with less than 20% yield are not considered, while the remaining branches are scaled to 100%. This measure prevents follow-up reactions of low-yield products and thus conserves computational resources. If none of the decomposition pathways can be applied to a tetroxide, it decomposes into two alkoxy radicals. For α-hydroxyperoxides, the HO_2-elimination is accessible in addition to the tetroxide formation. Due to the magnitude and concentration-independent reaction rate of the hydroperoxide elimination it is preferred over the tetroxide formation. The reaction rate depends only on the chemical environment of the carbon center of the radical. Unlike the tetroxide decomposition, the chemical environment does not change the composition of the products. Table 5.4 provides an overview of the included peroxy radical reactions.

5.1.7 Comparison to literature mechanism generators

The automatic generation of chemical mechanisms following a predefined protocol and a set of available SARs is not a new approach. In the gas phase, mechanisms such as SAPRC and the gas phase of GECKO-A are well-known examples of the application of mechanism generators [Aumont et al., 2005, Carter et al., 2023]. For the aqueous phase, the range of generators is considerably smaller and mostly tied to the specific application. The most well-known example of aqueous-phase mechanisms is CAPRAM-GECKO-A. It generates reactions for precursors with up to four carbons. Similar to the presented generator it considers OH, nitrate, radical, and further reactions. It generally makes fewer assumptions than the presented approach. As a result, CAPRAM generates thousands of reactions and builds very detailed mechanisms. Another advantage of CAPRAM is the application together with GECKO-A's gas-phase generator and the estimation of partitioning coefficients. This combination allows compounds to partition between both phases while having comprehensive mechanisms independent of the phase. Although this level of detail is desirable in all models, as of today global models do not have the capabilities to use such large mechanisms. Simulation times scale with the size of the mechanism, especially for multiphase setups. In addition, on a global scale, many molecules are larger than four carbons. Extending CAPRAM would inflate the final mechanism even further. The mechanism generator presented in this work is a trade off between computational efficiency, the number of oxidized precursors, and the mechanism detail. Compared to CAPRAM, the level of detail is lower, but the scheme is still feasible for global models. Additionally, it is built to be used in conjunction with the MESSy model, simplifying the application in future MESSy-related research. Nevertheless, in the novel generator intermediate species do not partition between the phases due to missing reactions in the gas phase. This necessary assumption hinders intermediates from outgassing and might lead to an overprediction of organics in the aqueous phase compared to GECKO-A. Further and more detailed mechanisms require dynamic mechanism reduction techniques in global models.

5.1.8 Comparison between generated mechanisms and literature mechanisms proposed based on measurements

In this section, mechanisms constructed by the mechanism generator are compared with mechanisms found in the literature. Typically, mechanisms proposed in experimental work are based on the measured product species and concentrations. Alternatively, theoretical calculations (e.g. density functional theory (DFT)) are used to investigate the energetic barriers of a reaction and the stability of intermediates and products. This approach can also provide a detailed mechanism. As mentioned above, these mechanisms are scarce and often less sophisticated than required. Especially for large compounds (more than five carbons), the available mechanistic data is limited. It should be noted that the generator does not provide mechanisms for all input molecules. Certain structural elements are not allowed. This is due to the possible side effects of these elements. In particular, aromatic compounds may have different branching ratios and rate constants than non-aromatic compounds.
There are several studies in the literature proposing aqueous-phase mechanisms for small- and medium-sized organics [Lim et al., 2013]. The only applicable mechanism for large organics was published by Aljawhary et al. [2016]. They analyzed the aqueous-phase OH-oxidation chemistry of large α-pinene products. However, the chosen compounds are outside of the current generator limitations. The first version of the generator was designed to be used in conjunction with MESSy. It was therefore necessary to ensure that the aqueous-phase oxidation of the model remains self-contained. This means that the generator is currently unable to oxidize compounds with end products unknown to MESSy. Otherwise, the end products would accumulate in the aqueous phase of the model as partitioning is not possible. This limitation is planned to be a selectable option in the future but is hardcoded in the current version. As a result, the generator cannot construct mechanisms for the α-pinene product given in Aljawhary et al. [2016].
Otto et al. [2017] investigated the aqueous-phase oxidation of two isoprene oxidation products in photoreactor experiments. They analyzed the molecules 3,4-dihydroxy-2-butanone (DHBO) and 2,3-dihydroxy-2-methylpropanal (DHMP). These molecules are possibly important to SOA because of their high Henry's law constants. Otto et al. [2017] proposed a mechanism to explain the formation of the measured product compounds. Figures 5.3 and 5.4 compare the mechanisms proposed by Otto et al. [2017] and the alternative mechanism of the generator. The comparison is restricted to the fastest pathway. This restriction is applied as the generator only constructs the fastest OH-oxidation route. Thereby, the generation of small yield pathways is prevented and simulation time is saved. Measured compounds are marked by a red box. The first figure illustrates the oxidation pathway of DHBO. Initially, DHBO is oxidized to hydroxy-3-oxobutanal (HOBA). This is consistent in both mechanisms. In the second step, Otto et al. propose an H-abstraction in C_1, which is carried out by the generator. However, the products of the reaction chains are different. Otto et al. convert the aldehyde group to a stable carboxylic acid. Unfortunately, the given reactant molecules cannot yield the product (the atoms do not add up) and this step is not

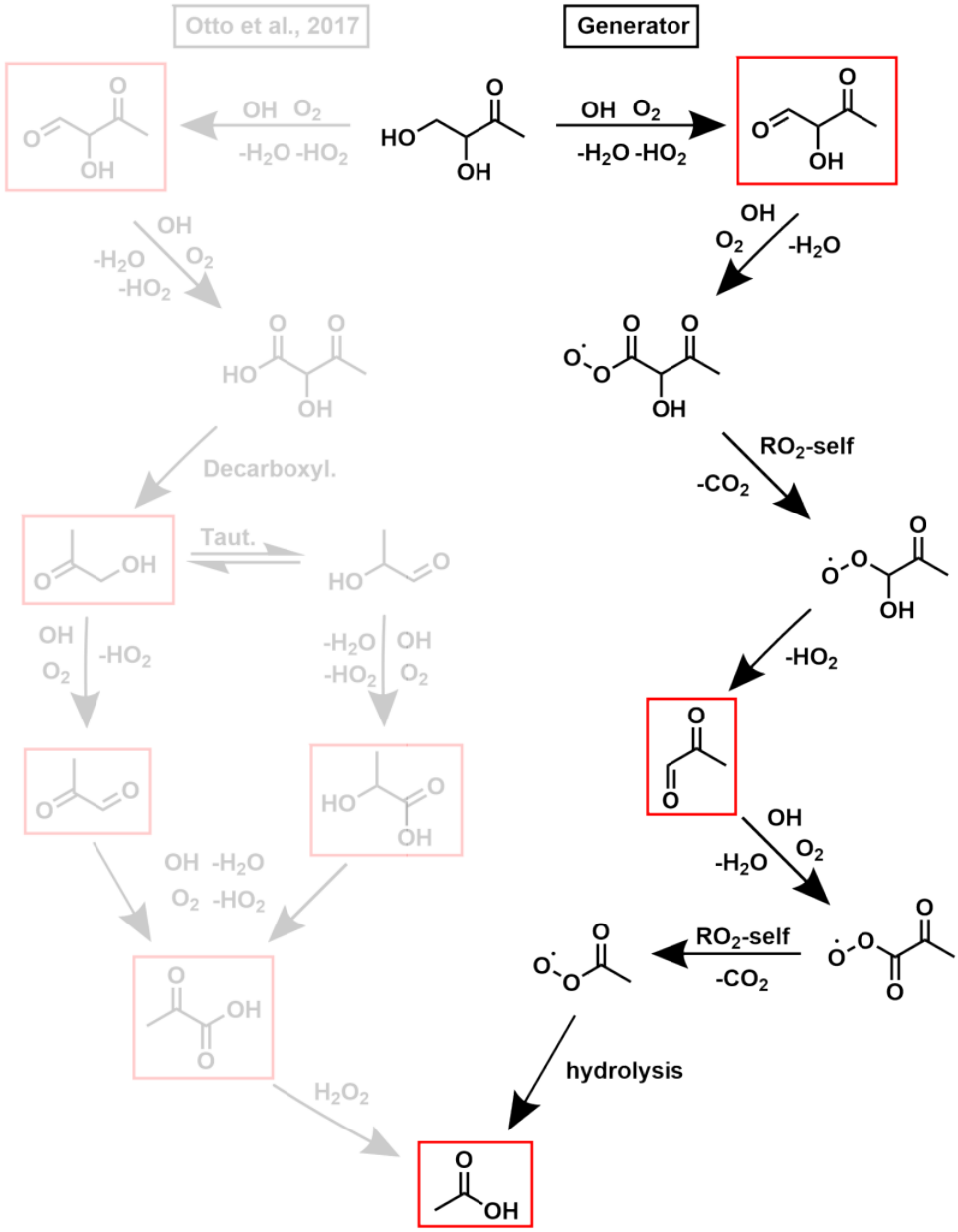

Figure 5.3: Main oxidation pathway of 3,4-dihydroxy-2-butanone (DHBO) generated by the script. The grey part shows a cutout of the mechanism as proposed by Otto et al. [2017]. It is reduced to the main first generation oxidation product (HOBA). Red boxes mark compounds that were measured in Otto et al. [2017]. Note that the final hydrolysis step in the generator mechanism is part of the default aqueous-phase mechanism of MESSy (original source Villalta et al. [1996]). The generator does not consider this hydrolysis reaction.

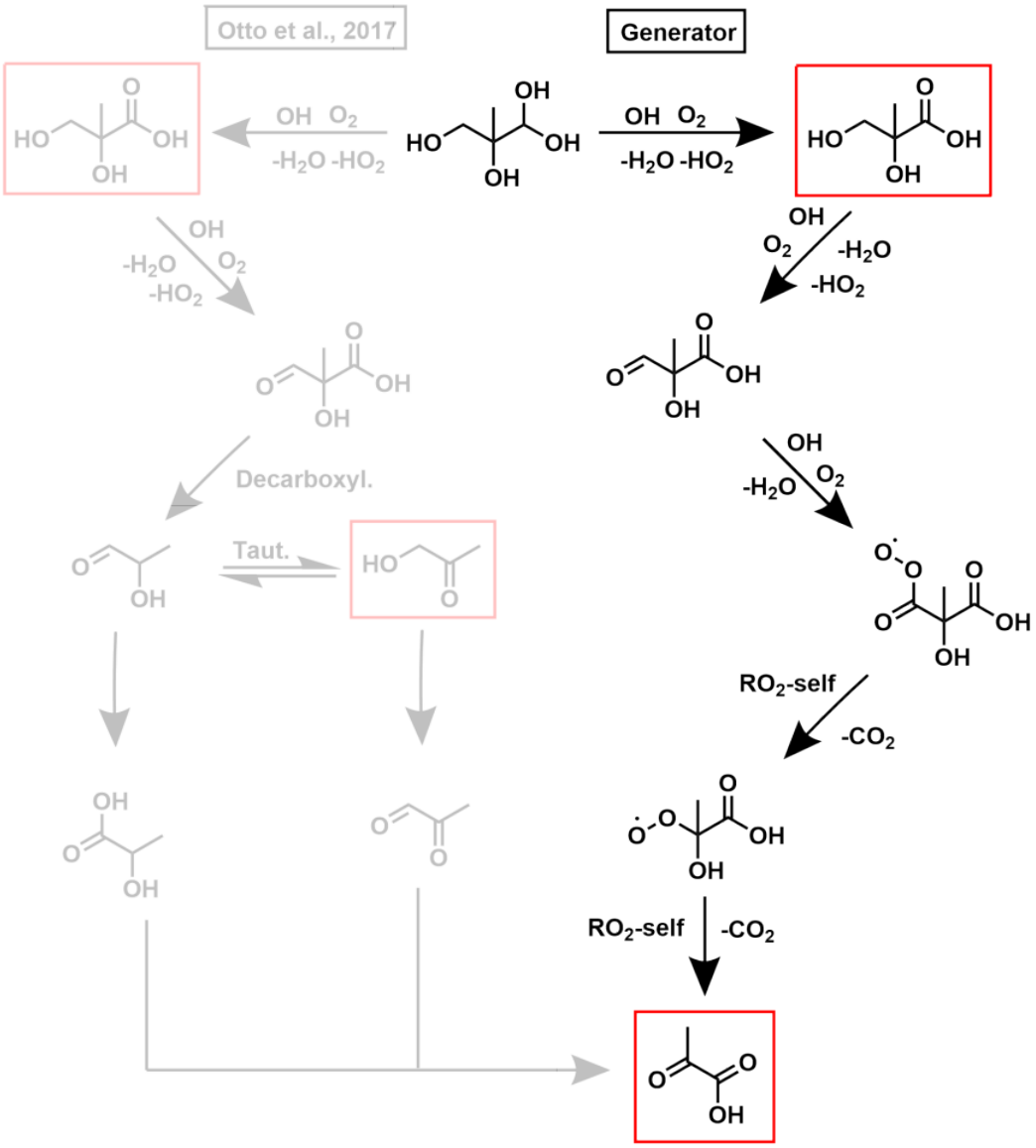

Figure 5.4: Main oxidation pathway of 2-methylpropane-1,1,2,3-tetrol (MPT) as generated by the script. The grey part shows a cutout of the mechanism as proposed by Otto et al. [2017]. The first generation product is selected based on the results of the generator. Otto et al. [2017] propose a different main first generation product. However, the displayed mechanism is the described alternative and leads to the same products. Red boxes mark compounds that were measured in Otto et al. [2017].

explained in detail. The intermediate acetylperoxy radical can react with OH as described in Chen et al. [2024] to give the carboxylic acid. However, this novel pathway is not mentioned in the description. Due to the availability of an alternative route and the limited set of reactions considered by the generator, the mechanisms diverge at this point. It forms a tetroxide, which mainly converts the peroxy to an alkoxy radical. The CO_2 element is then abstracted, leaving an acetol derivative with a peroxy group at C_1. In an HO_2-elimination this yields methylglyoxal. Otto et al. similarly propose the formation of methylglyoxal. In their mechanism, the stable carboxylic acid undergoes a decarboxylation. This yields acetol, which tautomerizes to a hydroxyaldehyde. Decarboxylation commonly requires heat or a catalyst to overcome the energy barrier [Kluger, 2015]. Both are rarely available in the various aqueous phases of the atmosphere. Nevertheless, Otto et al. propose decarboxylation and tautomerization, which splits the products into methylglyoxal and lactic acid. The methylglyoxal molecule is formed similarly to the generator. Lactic acid requires similar kinetics as described for the previous acetyl peroxy radical to be formed [Chen et al., 2024]. In the final steps, both methylglyoxal and lactic acid form pyruvic acid. This is oxidized by H_2O_2 following the reaction scheme by Stefan and Bolton [1999], Schöne and Herrmann [2014] to obtain acetic acid as the end product. In the generator, methylglyoxal reacts with OH/O_2 to form an acetyl peroxide. This is the final product of the generator. However, in the model, it is converted to acetic acid by hydrolysis. Thus, in the oxidation of DHBO, the generated mechanism confirms most of the proposed and measured molecules.
In contrast to the oxidation of DHBO, the dominant proposed and generated first generation products in the oxidation of DHMP are different. Otto et al. [2017] postulate an equilibrium constant of 9.77 between the hydrated and dehydrated forms. The equilibrium is on the hydrated side. Consequently, the mechanism by the generator is based on the hydrated form, 2-methylpropane-1,1,2,3-tetrol (MPT) (see Fig. 5.4), and not on DHMP. Otto et al. calculated the branching ratio based on DHMP. As a result, they propose 2-hydroxy-2-methylpropanedial (HMPD) as the main product, while the generator yields 2,3-hydroxy-2-methylpropanoic acid (HMPA). However, both first generation products yield the same product compound. Consequently, the analysis is limited to the HMPA pathway.
Figure 5.4 depicts both mechanisms. After the formation of HMPA, the generated and the proposed mechanisms convert the hydroxy group at C_3 to an aldehyde via H-abstraction by OH and HO_2-elimination. At this point, Otto et al. propose a decarboxylation and a tautomerization, similar to the first scheme. Again, this is not considered by the generator. Alternatively, the aldehyde in C_3 is oxidized by OH, leading to a series of two tetroxide formations and decompositions. The final product is pyruvic acid. In contrast, the proposed mechanism yields methylglyoxal and lactic acid as a result of the tautomerization. However, both are converted to pyruvic acid. Similar to the first comparison, the generator yields similar products and intermediates as measured by Otto et al. [2017]. For the intermediates that are not formed by the generator, the differences to the proposed mechanism are consistent with those of DHBO.

Finally, the generator results were compared with a mechanism proposed by Zhang et al. [2010]. They investigated the in-cloud chemistry of methyl vinyl ketone and methacrolein, and the importance of this chemistry for in-cloud SOA. The study included five experiments in which the intermediate and product compounds were measured. Based on these measurements, they propose a mechanism. Here, the proposed methacrolein mechanism is compared with the results of the generator.
Figure 5.5 displays both (proposed and generated) pathways with the highest yields in the methacrolein oxidation. Unlike the previous initial VOCs, methacrolein contains a double bond. The generator always prefers the OH-addition over the H-abstraction by OH. This addition is also one of the main pathways in Zhang et al. [2010]. This step yields a peroxy radical after O_2 addition to the tertiary radical site. The next step is a tetroxide formation in both mechanisms. However, the mechanism generator converts the peroxy radical into a hydroxy group, whereas Zhang et al. [2010] propose the formation of an alkoxy radical. According to Mouchel-Vallon et al. [2017], a β-hydroxy peroxy radical forming a tetroxide dimer, decomposes into three different products. Zhang et al. [2010] consider different decomposition products (only the dominant one is shown in Fig. 5.5), but they do not include the OH group in the estimation. As a result, the mechanisms diverge. The alkoxy radical proposed by Zhang et al. [2010] decomposes in two routes. Either a methylglyoxal or an acetol molecule and formic acid are obtained. Methylglyoxal can be further oxidized to form acetic acid. The generator, on the other hand, performs a series of H-abstraction reactions after the formation of the dihydroxy aldehyde species. After the abstraction of CO_2 and a HO_2-elimination, acetol is formed. This is converted to methylglyoxal by further H-abstraction and HO_2-elimination. Similarly to Fig 5.3, the oxidation of methylglyoxal gives acetic acid.
The three comparisons reveal the advantages and disadvantages of the mechanism generation scheme. The products proposed by the experimentalists and those estimated products by the generator are generally similar. Nevertheless, the proposed mechanisms in the literature differ from the results of the generator. This could lead to different product yields compared to the measurements. Due to the aim of the generator to construct mechanisms for global model simulations, only the OH pathway with the highest yield is generated. Although this saves simulation time, it also simplifies the mechanism so that not all measured compounds are found. This shows that for box or regional model applications an individual mode would be required for full mechanism construction. However, for compounds up to four carbons, this can already be done with CAPRAM-GECKO-A. All comparisons did also show that the generator produces mechanisms that are consistent with the underlying rules and SARs. As illustrated in the comparison with the mechanism proposed by Zhang et al. [2010], the generator can even yield improved mechanisms (compared to the SAR). However, the comparison does not analyze the evolution of concentrations in an the actual experiment, but focuses only on the mechanism. For a quantitative comparison, the generator needs to be validated against the concentrations in chamber experiments.

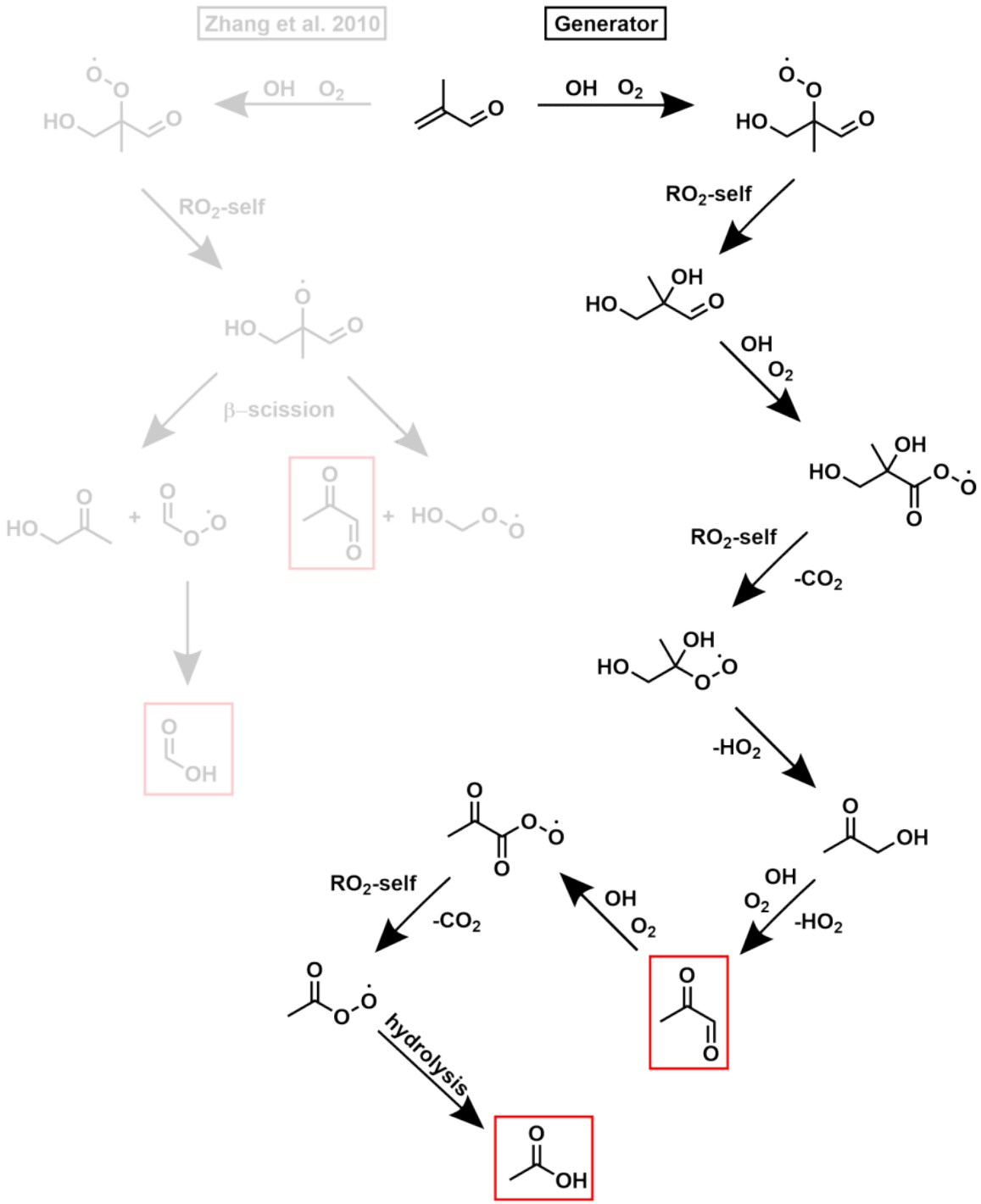

Figure 5.5: Main oxidation pathway of methacrolein as generated by the script. The grey part shows a cutout of the same mechanism pathway as proposed by Zhang et al. [2010]. The proposed reaction scheme does not show the formation of acetic acid (main product in the experiment). However, methylglyoxal can be converted to acetic acid by hydrolysis [Villalta et al., 1996]. Measured compounds are marked with a red box.

5.2 Application of the extended mechanisms to MESSy

The newly developed chemistry, the handcrafted VOC oxidation mechanism, and the automatically generated aqueous-phase mechanism have been incorporated into the chemistry scheme of the MESSy model to conduct the following sensitivity simulations. In accordance with the objectives of the thesis, the influence of the novel chemical processing on SOA and more generally on OA is evaluated. Due to the continuous development of the MESSy infrastructure and the introduction of new submodels, the exact reconstruction of simulation setups used in earlier publications is rather difficult and error-prone. Additionally, the application of an earlier code might influence the conclusions drawn about the chemical mechanism under evaluation. Hence, the application focuses on a model-model (current model version) and a model-observation comparison with a fixed model configuration.

5.2.1 Model configuration

Three simulation setups (POZ, MOM, and MOM+) are employed for the evaluation. Each setup is based on the same namelist configuration. This includes the choice of MESSy submodels, emissions, and the extent of the output data. Only the emissions of medium-sized alkanes and limonene are adjusted between the setups. Limonene and alkanes larger than butane previously only affected the bulk organic aerosol mass (neither chemistry nor partitioning to the aqueous phase). In the MOM and MOM+ setups (see Tab. 5.6), limonene and the alkanes are included in the multiphase chemistry scheme, impacting all available phases. Aerosol chemistry and microphysics are represented in the GMXe submodel. Within the latter, the subsubmodel AERCHEM calculates the phase partitioning and oxidation kinetics in hydrophilic SOA (see Fig. 2.1). ORACLE represents the formation and evolution of organic aerosols using the VBS framework. Wet scavenging of gases and aerosols is part of the SCAV submodel, which also includes the aqueous-phase chemistry in rain and cloud droplets.
The gas-phase chemistry of MESSy is represented by the submodel MECCA. The emission factors of biogenic and anthropogenic VOCs are controlled by the offline and online emission submodels OFFEMIS and ONEMIS, but also by the MEGAN submodel to estimate specific plant emissions. In MEGAN, the composition and magnitude of the emissions are estimated based on temperature, light intensity, and one of four plant types (broadleaf, needleleaf, shrub, and the combination of herb, grass, and crop) that are dominant in an area. Further information on the listed submodels can be found in Chapter 2 or accessible on the MESSy website (`https://messy-interface.org/`). The three setups differ in the choice of the chemical mechanisms and the associated physico-chemical properties. Table 5.6 lists a description and the chemical composition of the setups. The basis of the chemistry in all setups is the chemistry of the Mainz Organic Mechanism (MOM). The reference setup contains the chemistry that was present in MESSy before the publication of Wieser et al. [2024]. This mechanism is largely similar to the chemical mechanism used in Pozzer et al.

Table 5.5: Primary emitted compounds/compound classes in all model setups. Note that limonene and the alkanes (pentane and larger) are only emitted to the chemical system in the MOM and MOM+ simulations. In POZ, both are only considered in ORACLE and the medium to large alkanes are combined in LALK5.

Variable name	**Description**	**Emission** / Tg/yr
BENZENE	Benzene	7.2
TOLUENE	Toluene	8.9
LXYL	Lumped xylenes	7.5
STYRENE	Styrene	2.0
LALK4	Lumped small alkanes	15.1
C5H12	Pentane	5.3
C6H14	Hexane	5.3
C7H16	Heptane	5.3
C8H18	Octane	5.3
C5H8	Isoprene	462.0
APINENE	α-pinene	22.0
BPINENE	α-pinene	12.6
LIMONENE	Limonene	5.5
CARENE	Carene	4.9
SABINENE	Sabinene	4.6
CAMPHENE	Camphene	2.15
LTERP	Remaining other terpenes	26.4

Table 5.6: Overview of the sensitivity runs. The POZ setup is used as reference in the later comparison. MOM and MOM+ reflect the two steps of chemical development that have been developed throughout this thesis. Note that the number of species accounts for the occurrence of a species in different phases separately. A chemical that partitions in all phases (gas phase, the three aerosol phases and the aqueous phase) refers to four species as they are treated individually in the model.

Setup name	**Reaction set**	**Gas-phase reactions**	**Aq.-phase reactions**	**# species**
POZ	kinetic model as in Pozzer et al. [2022]	2210	440	3800
MOM	POZ + developments in Wieser et al. [2024]	2700	470	5640
MOM+	MOM + generated reactions in this study	2700	1100	7440

[2022] and is therefore called POZ. The second setup is labelled MOM as it reflects the current MOM (Mainz Organic Mechanism) chemistry in the MESSy model. This includes the developments made in Wieser et al. [2024]. Finally, MOM+ is the MOM setup with extended aqueous-phase oxidation of organics by the mechanism generator (see Sect. 5.1). Table 5.5 lists the annual emissions of selected molecules in the model. Anthropogenic emissions align with the emissions in Pozzer et al. [2022]. However, biogenic emissions are different, especially concerning monoterpenes. This is caused by the nudging in Pozzer et al. [2022]. The simulations in this work are not nudged and represent the internal meteorology of MESSy.

5.2.2 Secondary organic aerosol burden

The annual cycle of the global SOA burden provides a first assessment of the total change induced. Although it is difficult to attribute changes in the global burden to a specific compound, pollutant, or source region, it does indicate the periode in which large changes occur. In the MESSy model, organics partition into two organic aerosol fractions, one hydrophilic and one hydrophobic. They dissolve in the aqueous organic (hydrophilic) aerosol fraction and condense in parallel on the organic (hydrophobic) aerosol fraction (see Sect. 2.3 and Sect. 2.4).

Figure 5.6 illustrates the difference in global SOA burden between the MOM/MOM+ and the POZ simulations in three panels. Panel A displays the change in the total SOA burden. Panels B and C focus on the changes in hydrophilic and hydrophobic SOA, respectively. The grey bars in each panel show the difference between the MOM and the MOM+ simulations. Based on the first panel it becomes clear that the MOM and MOM+ setups induce a net increase in the total simulated SOA burden. The minimum at the end of March stands out as the only clear negative influence of both setups with more refined chemistry. Panel B demonstrates that the increase in total SOA burden is related to the strong enhancement in hydrophilic SOA mass. On the other hand, the mass change in hydrophobic SOA overall dampens the increase in total SOA mass. The difference between MOM and MOM+ chemistry is located in the hydrophilic SOA and also in the cloud and rain droplets. Thus, the grey area in Panel B provides a first indication of how the increase in the aqueous-phase oxidation mechanism affects the SOA mass in the respective phase. The hydrophobic SOA is only indirectly influenced by the uptake and outgassing associated with the hydrophilic SOA. Panel B illustrates a decline in SOA mass during summer and winter due to the addition of the MOM+ reactions. This is in line with the expectations. Dissolved compounds in the hydrophilic phase are oxidized, eventually leading to a scission reaction. Smaller compounds are commonly more volatile and thus also less soluble [Hodzic et al., 2014]. Once a hydrophobic compound of the established MESSy mechanisms is formed, it outgasses and thus reduces the SOA mass. Compounds that do not undergo a scission reaction may also increase the SOA mass by incorporating additional functional groups. Oligomerization would also increase the total SOA mass by preventing the outgassing of

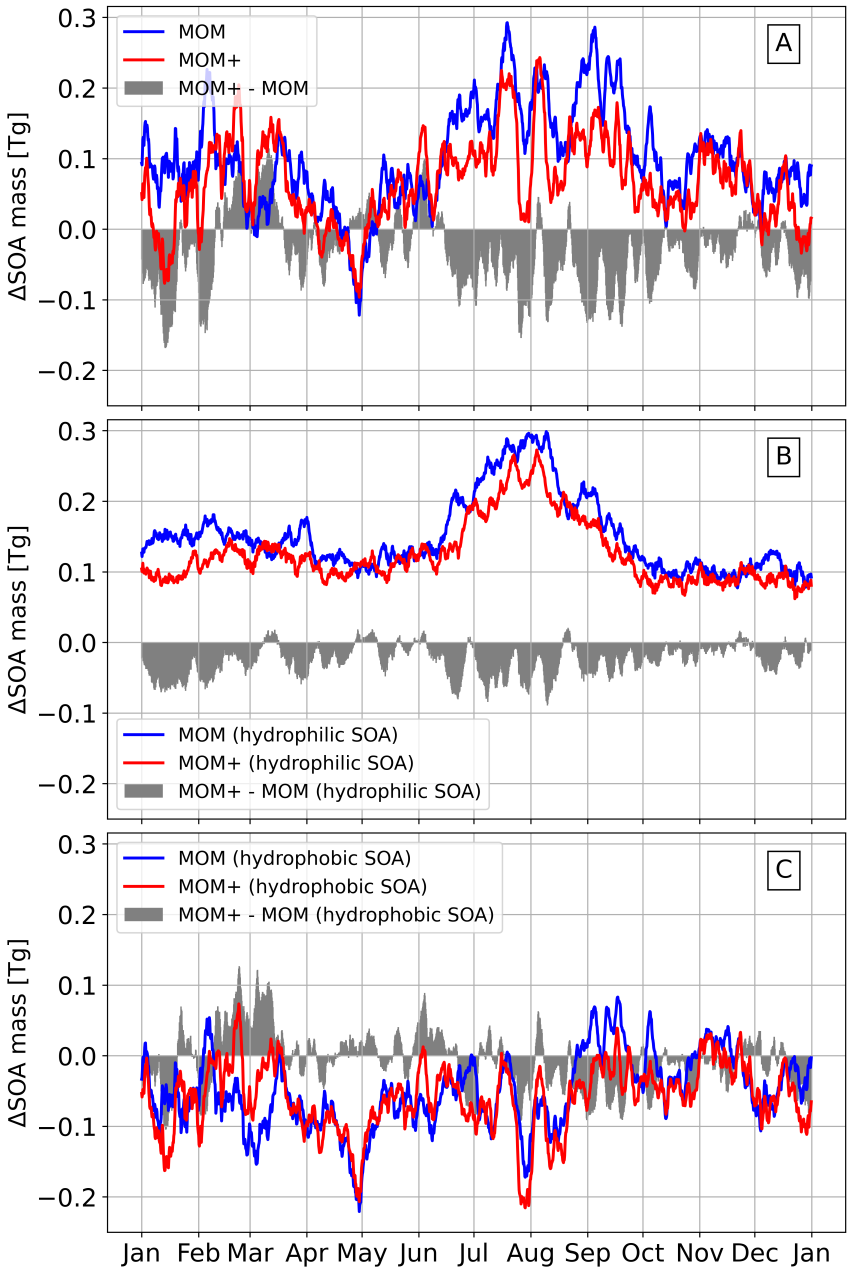

Figure 5.6: Difference between the SOA burden of the MOM (blue) and MOM+ (red) setups and the POZ setup. The deviation between MOM and MOM+ is indicated by the grey area. Panel A displays the development of the total SOA burden. Panel B and Panel C illustrate the progression of the SOA burden in hydrophilic and hydrophobic SOA (see Sect. 2.4.4), respectively.

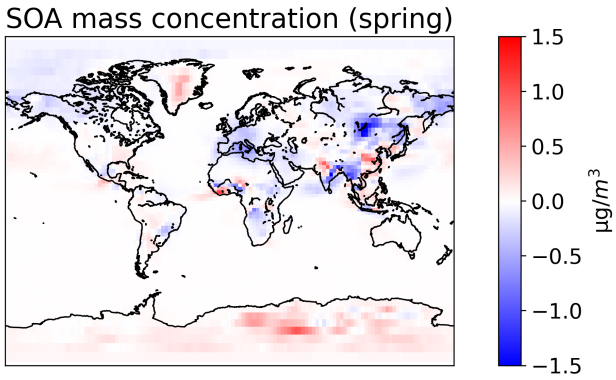

Figure 5.7: Difference in mean hydrophobic SOA (ORACLE) concentration between MOM and POZ during spring (March, April and May).

the monomers. However, oligomerization is not covered by the mechanism generator.
The detailed analysis of the evolution of the SOA burden reveals some interesting periods that require further explanation. In Panel B the increase is most dominant between early June and late September. This can be explained by the combination of two novel developments. In the northern continental summer, the global isoprene emissions are at a minimum, while monoterpene emissions are at their maximum extent [Sindelarova et al., 2014]. Intuitively, one would expect that monoterpene SOA (e.g. from the new limonene scheme) increases, while isoprene SOA declines. However, the newly introduced SOA precursor IPOEX only forms under low NO_x conditions. Due to its high solubility, but moderate volatility, it will only impact SOA concentrations if the aerosol liquid water content (LWC) is sufficiently high. Similar to the investigations of Hodzic et al. [2016] IEPOX-SOA increases during summer. Thus, the total SOA burden increase peaks around 300 Gg in July and early autumn in the MOM simulation. MOM+ includes further aqueous-phase oxidation for the various monoterpene products, leading to degradation and outgassing. This results in a reduced peak in the value of the MOM+ SOA mass. Another notable period is the sharp minimum of the SOA mass difference at the end of March (Panel A). This decrease can be attributed to the hydrophobic SOA. Figure 5.7 illustrates the mean difference in hydrophobic SOA concentration between MOM and POZ during spring on a global scale. The largest decline is observed in southeastern Russia near Lake Baikal. The model predicts lower oxidant concentrations in this area in the simulations with more comprehensive chemistry. As a consequence, the ORACLE submodel produces less biomass burning SOA, resulting in the observed minimum. The reduction in oxidant concentration can be attributed to the enhanced oxidant consumption by additional VOC reactions (and the entirely new limonene mechanism). This is reflected in the simulated levels of other VOCs, such as benzene, which shows high mixing ratios in the same region during this time period.
Table 5.7 lists the mean absolute burdens of all runs and the relative differences between

Table 5.7: Absolute and relative increase in SOA burden between the simulation results of the different setups. The POZ run is used as reference for the calculation of the relative increase. The columns are divided into the total, the hydrophilic and the hydrophobic SOA.

Differences in SOA burden	POZ / Tg	MOM / Tg (%)	MOM+ / Tg (%)
Total SOA	0.80	0.91 (12.5)	0.87 (8.3)
Hydrophilic SOA	0.11	0.26 (136)	0.24 (113)
Hydrophobic SOA	0.69	0.64 (-7.4)	0.63 (-8.5)

the MOM/MOM+ and the POZ simulations. On average, the MOM chemistry and partitioning increases the total SOA burden from 0.8 Tg to 0.91 Tg, corresponding to a relative increase of 12.5%. The extended chemistry in MOM+ reduces the change relative to the total SOA gain (8.3%), but still yields an increase of 70 Gg over the POZ simulation. The hydrophilic and hydrophobic columns display that the increase is exclusively in the hydrophilic SOA, while the hydrophobic SOA decreases in mean mass. With an increase of 136%, the developments in MOM strongly influence the hydrophilic SOA mass. Although still significant, MOM+ displays a smaller increase than MOM. In the hydrophobic SOA, the MOM and MOM+ SOA masses decrease by -7.4 and -8.5% respectively. These results further illustrate the implications for the MOM and MOM+ setups described above. The hydrophilic SOA increases while the hydrophobic SOA decreases, but in a smaller magnitude. Thus, in MOM and MOM+, more gas-phase molecules have an active role in the aqueous partitioning. However, the aqueous-phase oxidation in MOM+ shifts the equilibrium between the gas and aqueous phase towards the gas phase. This is analyzed in further detail in the following sections.

5.2.3 Secondary organic aerosol mass concentrations

The course of the SOA burden shows time periods where large global changes to the SOA mass occur between the three setups. In contrast, the global SOA concentration can be used as a tool to investigate the regions with the most dominant absolute changes. This allows for the source contribution between precursors and SOA. Furthermore, in the calculation of the SOA burden positive and negative changes may compensate each other. The global SOA concentration can reveal this hidden information. This section focuses on the analysis of ground-level SOA concentrations. This limitation simplifies the connection to the precursor emission sites. The difference in the vertical distribution is discussed in upcoming sections. Figure 5.8 displays the mean seasonal ground-level SOA concentration (hydrophilic and hydrophobic SOA) between the MOM and POZ simulations. With respect to the results shown in Figure 5.6, it is expected that the SOA concentration illustrates a net increase during all seasons. These expectations hold true but especially during spring and winter, the positive and negative changes are of similar magnitude. For spring, this is consistent with the previous results. The minimum at the end of April compensates for the sum of the

SOA mass increases during the rest of the spring (cf. Fig. 5.7). In the SOA burden during winter, the MOM chemistry leads to a substantial increase, while the ground-level SOA concentration displays a minor increase. This indicates that the mean absolute difference of the SOA concentration increases with higher levels during this time period.

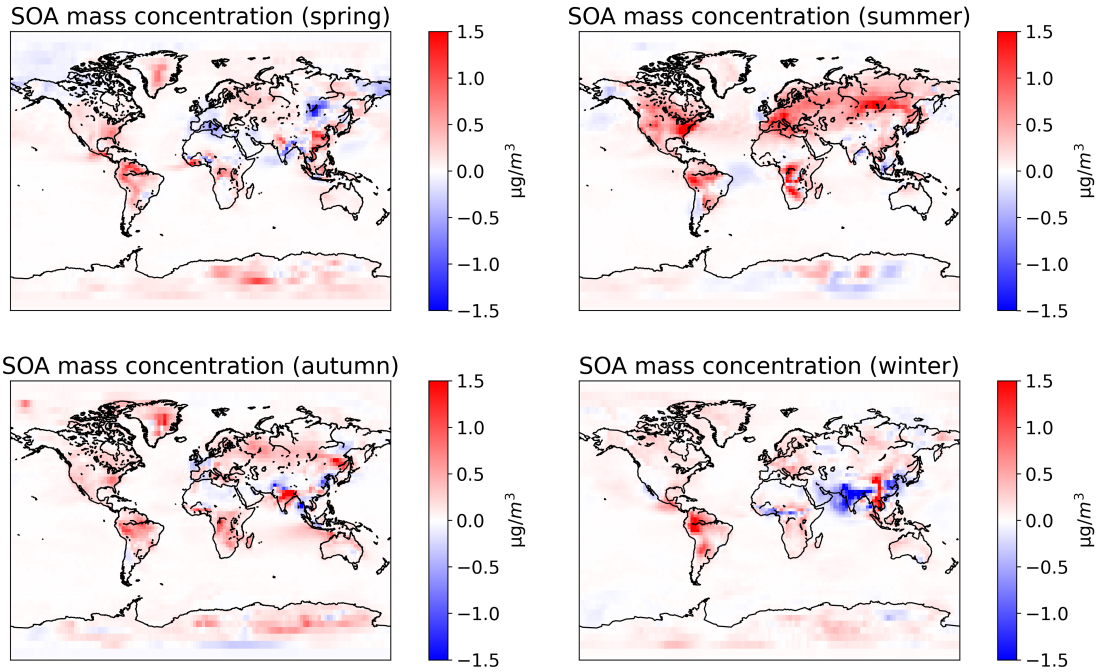

Figure 5.8: Seasonal absolute difference in surface level SOA concentration between MOM and POZ as simulated by the model.

The detailed changes can be attributed to different chemical and emission adjustments. The emission pattern of limonene is similar to that of isoprene (see Fig. 7.3 and Fig. 7.2). Both VOCs can account for the increase in SOA concentrations in northern South America and Russia during summer. The increase in SOA concentration in northern China during most times of the year can be attributed to the formation of isoprene-derived organic sulfates (IDOS) or tetrols. Similarly, elevated concentrations of the tetrol are simulated near the east coast of the United States. During summer, isoprene has elevated mixing ratios over North America. In autumn, concentrations decrease, especially along the east coast. This trend is also observed for the SOA concentration. Over central and southern Europe, SOA concentrations similarly increase during the summer. This can be also be attributed to biogenic emissions. Changes over Greenland are due to long-range transport of VOCs and aerosols. This is a result of the updated partitioning coefficients. Enhanced dissolution of LVOCs leads to an increase in long-range transport (see discussion in Sect. 5.2.6). The increased SOA concentration in the Antarctic can be attributed to the SOA condensation process in the ORACLE submodel. Figure 5.7 displays the organic mass in hydrophobic SOA (only spring), while Figure 5.8 combines hydrophilic and hydrophobic SOA. This

comparison suggests that the increase in SOA concentration in Antarctica is dominated by condensation and long-range transport. The MOM chemistry introduces new condensable gases that are transported to Antarctica. During winter, SOA concentrations decrease in northern India and some parts of China. In northern India, anthropogenic emissions such as benzene are high during this time window (see Fig. 7.4), while biogenic emissions are low (see Fig. 7.3 and Fig. 7.2). This is in line with observations [Jain et al., 2022]. Therefore, the stronger decrease of SOA concentrations in this region can be explained by the changes of anthropogenic VOCs (e.g. benzene chemistry) in winter, which are not compensated by the increases due to the new biogenic SOA sources. The exclusion of the n-alkanes from the lumped emission scheme of ORACLE further reduces the SOA yield. The chemical mechanism of the new n-alkanes, in its current state, is not capable of producing similar amounts of SOA. This can be improved by implementing more oxidation reactions and the consideration of branched alkanes.

Figure 5.9 illustrates the seasonal mean surface level SOA concentration between the MOM+ and MOM simulations. The source contribution of the SOA concentration changes by the generated aqueous-phase oxidation reaction in MOM+ is more complicated than the previous analysis between the MOM and POZ simulations. The black box nature of a generated mechanism leaves room for interpretation, as newly generated compounds are only described by an InChI-Key and are difficult to track thourgh in hundreds of reactions. This is one of the disadvantages of mechanism generation methods. However, general trends in the simulations can be found and interpreted without analysis of the generated reactions.

The direct comparison of Figure 5.8 and Figure 5.9 reveals that the generator compensates the changes induced by the MOM update. This trend is evident in several regions and seasons. In summer, on the east coast of the US and central Africa; in autumn in northeastern China and northern India; and in eastern China during winter. Considering that these are the areas with high emissions and overall high SOA precursor concentrations, this observation is in line with the expectations. The generator can influence the organic loading in hydrophilic SOA in two ways. In the first case, compounds with intermediate solubility are further oxidized. This increases the molecular mass and also the solubility of the reactants. As a result, a greater proportion of these compounds remain in the aqueous phase with a higher molecular mass. Even if scission reactions occur in the mechanism sequence, the gases may still be sufficiently soluble in the aqueous medium. The second case concerns highly soluble species. Without oxidation in the aqueous phase, these compounds remain in the aerosols until they are removed by a physical process. However, if chemical oxidation pathways are available, they may lose organic mass by scission reactions. Alternatively, the products formed are more volatile and outgas to the gas phase. Both pathways can be observed in Figure 5.9.

These two processes are responsible for the counteracting of the MOM and MOM+ chemistry. In regions where MOM increases the total amount of SOA in the hydrophilic phase, more highly soluble organics are oxidized in the aqueous phase. Thus, the total mass that

is removed by the aqueous oxidation process is greater. In the opposite case, the MOM chemistry and partitioning will result in a reduction in soluble SOA mass. Here the first process applies and less soluble organic mass is oxidized. This can increase the solubility and the molecular mass. In areas where there is no correlation between the two updates, the MOM+ chemistry does not include the necessary oxidation reactions or MOM-unrelated products are dominant.

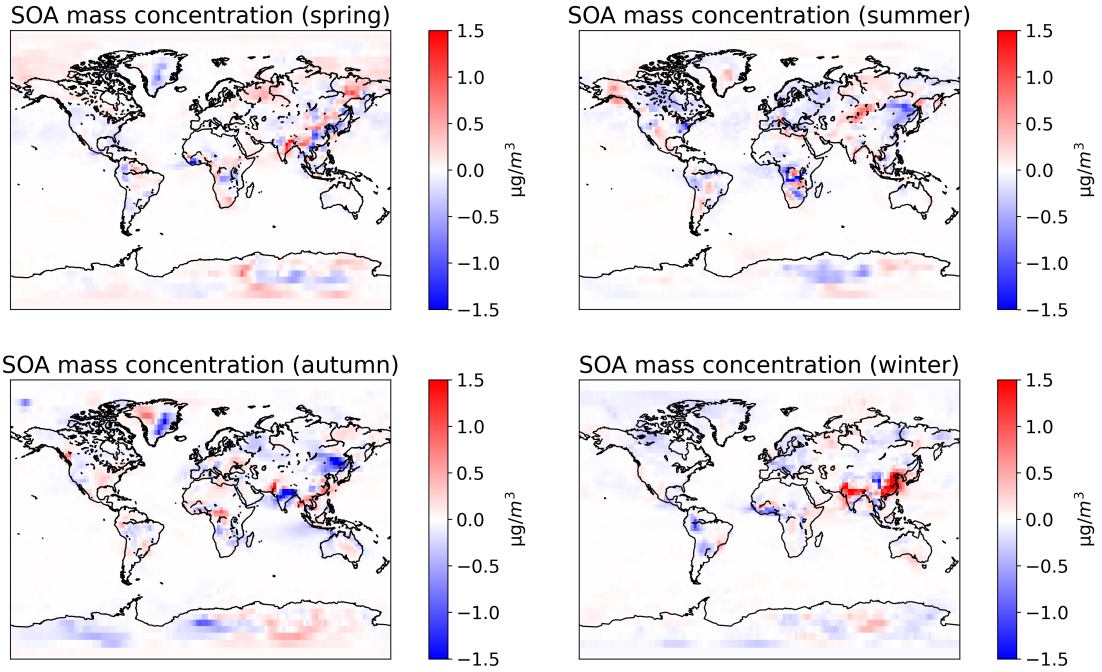

Figure 5.9: Seasonal absolute difference in surface level SOA concentration between MOM+ and MOM as simulated by the model.

5.2.4 Organic aerosol mass versus station data of the EPA/IMPROVE, EMEP and EANET networks

Comparing model results from different model generations is useful to evaluate the impact of a particular update. Further analysis requires real world data to assess whether model data yields correct absolute values. Model results at ground level can be validated using data from ground station. In general, ground stations provide data over several years, which facilitates the comparison with the modeled year. Furthermore, measured data from observation networks allow for a large-scale comparison, ranging over several countries. In the following comparison, three station networks are used. For the US, data from the Environmental Protection Agency (EPA) provide site measurements distributed over all states. The networks CASTNET (Clean Air Status and Trends Network) EPA (81 sites) and IMROVE (Interagency Monitoring of PROtected Visual Environments) (38 sites) both include PM2.5 (particulate matter with a diameter below 2.5 μm) data of organics. To-

gether they comprise more than 100 sites, providing a dense network across the US. The observations are evaluated annually by EPA scientists to assess the data quality. The European Monitoring and Evaluation Programme (EMEP) network is used to compare PM2.5 concentrations across Europe. In this thesis, 39 of the available stations are used. They provide one measurement per day in different European countries. Similar to the US measurements, the Chemical Coordinating Centre of EMEP publishes regular reports on their measurements. Data for China, Japan, and South Korea are taken from the EANET (acid deposition and air quality management from data to policy) network. The respective program is coordinated by the United Nations Environment Programme Asia and the Pacific Office. The present work uses PM2.5 data from 20 of the EANET stations. The following figures (Fig. 5.10 and Fig. 5.11) include the model results of the present work, but are based on the plotting script provided by the authors of Pozzer et al. [2022]. The station data mentioned above is also provided and used as in Pozzer et al. [2022].
Figure 5.10 displays the annual mean organic PM2.5 concentration as simulated by the model in three different regions: North America (left), Europe (middle), and East Asia (right). Each row in the figure corresponds to one of the three simulations. The results of the POZ simulation are shown in row a, MOM and MOM+ in rows b and c, respectively. The cycles in the figures depict the annual mean concentration from the ground stations of the monitoring networks described above.
The most pronounced changes are depicted in North America. The POZ simulation underpredicts PM2.5 concentrations over the central and eastern US. Stations on the east coast have significantly higher concentrations than the simulations. The additional chemistry and phase partitioning in MOM and MOM+ mitigate this underprediction. However, due to the coarse resolution of the model, small-scale effects are not resolved. Increases and decreases between cities and the west and east coasts are averaged. Changes between MOM and MOM+ are not strong enough over the US to cause a significant change in PM2.5. The figure also shows an increase in PM2.5 in the northern of South America, but this cannot be confirmed by measurement stations. In Europe, all three simulation setups show PM2.5 concentrations comparable to the monitoring stations. However, the concentrations in western Russia are higher in MOM and MOM+. The rather low emissions of BVOCs such as isoprene and monoterpenes prevent a strong increase in OA mass due to the introduction of IEPOX and limonene chemistry. The simulation results and observations in East Asia show a similar trend, but the model underpredicts the PM2.5 concentration, especially in the vicinity of megacities (e.g. Beijing). This is related to the resolution, but also to the fact that the updates self-compensate over the simulated year. The missing nudging also affects emissions and leads to less comparable results. Concentration changes between nearby cities can be larger than 10 $\mu g/m^3$, which is beyond the scope of the current simulation resolution. In addition, the seasonal development in Figure 5.8 displays that the impact in the East Asian region is time-dependent. In the vicinity of Beijing, enhancements in OA concentration in spring and summer are compensated by decreases in autumn and winter.

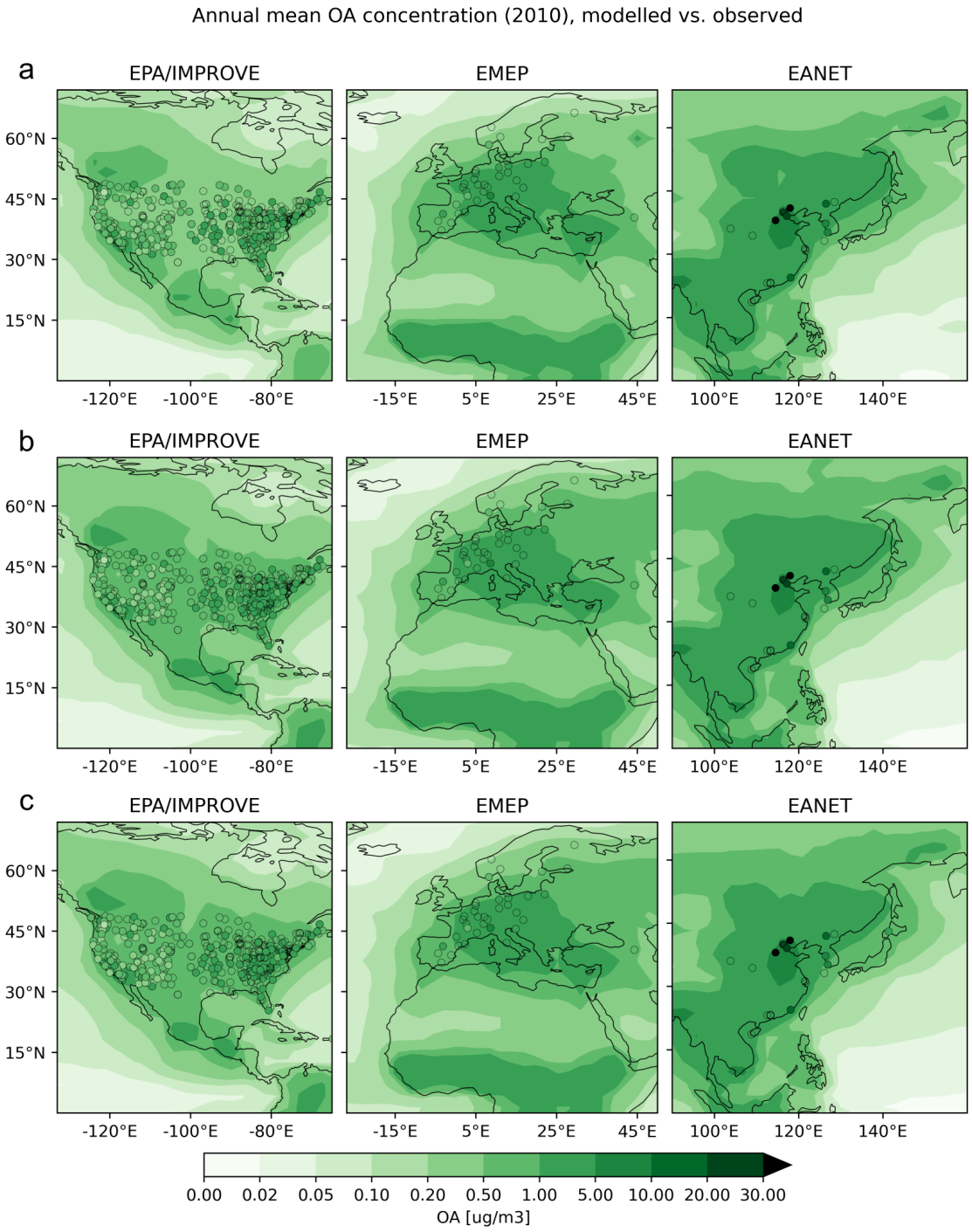

Figure 5.10: Contour plot of the annual mean surface level PM2.5 concentrations in the different simulations in North America, Europe and East Asia. The panels in a row correspond to one of the simulation setups (a = POZ, b = MOM and c = MOM+). The cycles mark the observation stations. The color inside the cycles refers to the annual mean measured value of the station. From left to right, the concentrations in Europe, the USA and East Asia are depicted. Note that the colorbar is non-linear to show the strong gradient of PM2.5 in the different regions. The plotting routine and station data is based on Pozzer et al. [2022].

The MOM update improves the PM2.5 concentration in regions with high biogenic emissions. This leads to corrections of the data in the eastern US, making the predicted concentrations more consistent with the observations. The changes in Europe and East Asia occur away from the monitoring stations. With the current limited set of observation stations, these changes in concentrations cannot be validated. The aqueous oxidation does not change the concentrations substantially. This suggests that the SOA composition is adapted rather than the SOA concentration.
Figure 5.11 shows a collection of scatterplots of the seasonal PM2.5 concentration of the stations against the model results. Similar to Figure 5.10, the different rows contain the results of one of the sensitivity simulations. The color code is divided into spring (orange), summer (red), autumn (light blue) and winter (dark blue). The seasonal mean is depicted as large circles filled with the corresponding color. The one-to-one line is shown as a solid black line. The dashed lines indicate a change of one order of magnitude.
Between POZ and the updated setups, the agreement between the modeled and observed PM2.5 of the IMPROVE network improves. While most seasonal means show an underprediction of more than one order of magnitude in the POZ simulation, the MOM and MOM+ results are above this threshold. The adjustments in the MOM setup have a strong influence on the results in spring and summer. The PM2.5 concentration in autumn increases less, but still noticeable. The mean concentration in winter increases to a minor extent. MOM+ induces a small decrease in spring, but also an increase in winter. In Europe (EMEP) Figure 5.10 does not depict strong changes close to the observation station by MOM and MOM+. However, the seasonal mean PM2.5 concentrations show that the picture is more complex. MOM shows a strong increase in concentrations during summer. This is partly compensated by decreases in spring and autumn. The aqueous oxidation in MOM+ causes a small increase in summer and autumn. In all simulations, the model underpredicts the concentrations. However, MOM and MOM+ show a clear improvement over POZ. The comparison of the model results against the station measurements in EASIA shows a similar trend as pointed out in the previous analysis. The model shows an underprediction, which is partly corrected in MOM and MOM+. In contrast to the other comparisons, these corrections are less pronounced. MOM improves the PM2.5 concentrations in spring and winter. The results of MOM+ show slightly better results in winter.
In the northern hemisphere, the chemistry in MOM is most active during summer. Biogenic emissions are highest during this period [Sindelarova et al., 2014]. All monitoring networks are located in the northern hemisphere, thus the strong increases in the results of MOM during summer are not surprising. The additional chemical processing in MOM+ shows a more ambiguous behaviour. It does not selectively affect a specific season, but shows a weak effect in most of the seasons. A detailed analysis of the comparison between individual stations and the model shows that single grid boxes are impacted by the generated reactions of MOM+. However, the mean seasonal concentration does not change significantly. This is again an indication that the composition of SOA changes with more aqueous oxidation

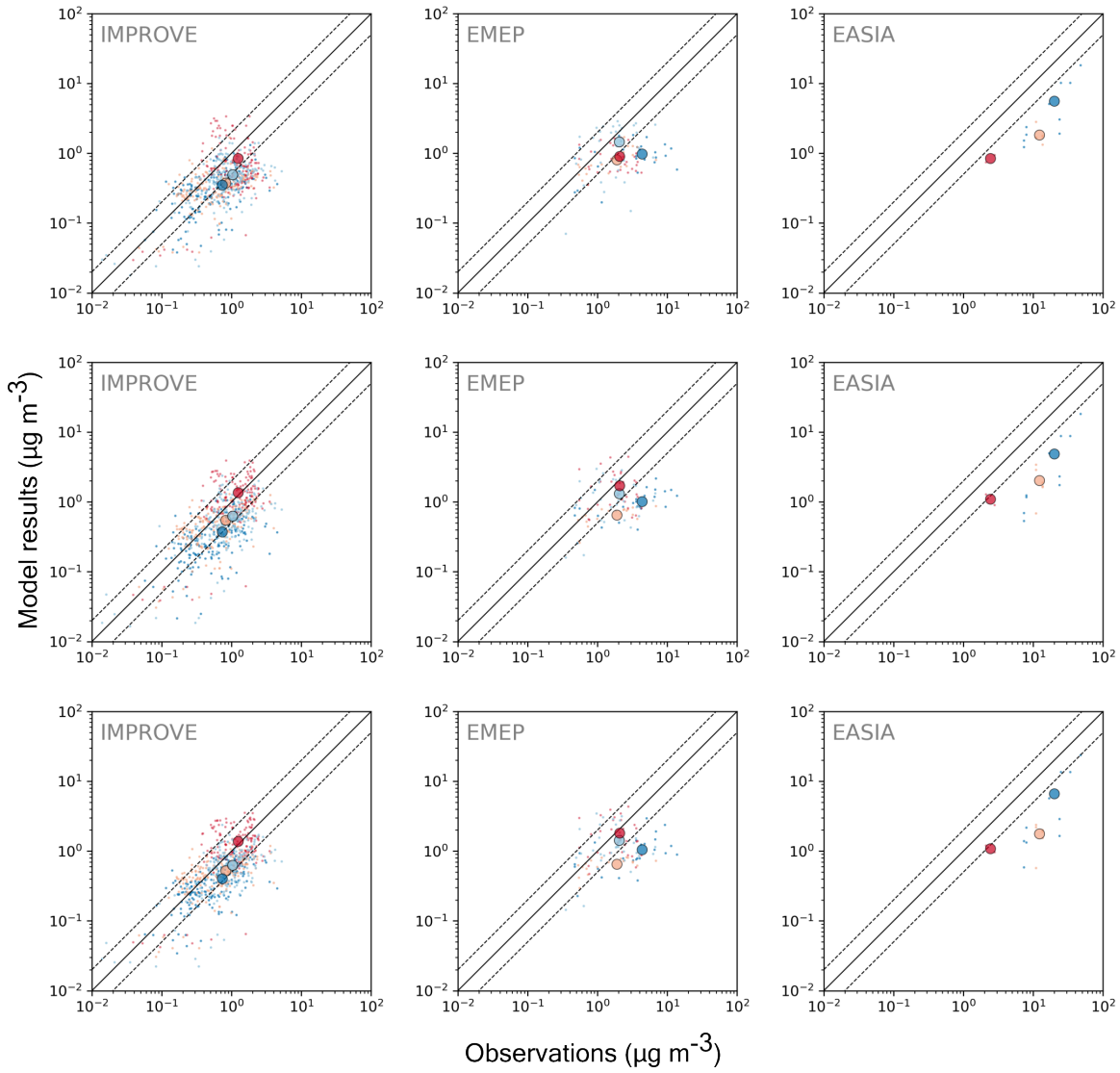

Figure 5.11: Scatterplot of the modeled against the observed PM2.5 concentrations. The rows correspond to the POZ, MOM and MOM+ simulation results, respectively. The colors of the points indicate the different seasons (spring = orange, summer = red, autumn = light blue and winter = dark blue). The large colored circles represent the seasonal means. The solid black line indicates a perfect agreement, while the dashed lines show a deviation of one order of magnitude. The plotting routine and station data is based on Pozzer et al. [2022].

reactions, without a clear effect on the PM2.5 concentration. Overall, it can be noted that SOA sources during spring and winter are currently not sufficiently represented in the model.
The figures shown are similarly displayed in Pozzer et al. [2022]. A comparison between both might reveal further changes in the model. The POZ setup and the Pozzer et al. [2022] chemistry are very similar. However, further model adjustments have been made between the two simulations. The recent additions of plant water stress and stomatal deposition affect the abundance of VOCs and oxidants in the atmosphere. Also the emissions of lumped n-alkanes with more than four carbons are no longer available in the ORACLE submodel. Another major influence factor is the new AERCHEM subsubmodel. In Pozzer et al. [2022] OA is only modeled using of ORACLE. SOA is therefore limited to the organic condensed phase. The influence of AERCHEM on SOA in the model was tested in this work. Figure 7.7 in the appendix illustrates the SOA development in POZ compared to POZ with deactivated AERCHEM. It shows that AERCHEM increases the SOA burden during all months. Another difference between the prior simulations and the simulations in this work is the nudging. In the presented simulations nudging is switched off, resulting in lower emissions. The comparison makes it obvious that these combined changes reduce the amount of PM2.5 in the model simulations. Thus, the introduction of AERCHEM is less significant than the remaining changes. MOM and MOM+ partly compensate for the differences. While most trends are less similar to the observations, the summer PM2.5 concentrations are improved in the MOM and MOM+ setups compared to Pozzer et al. [2022].

5.2.5 Vertical distribution of secondary organic aerosol

The analysis of the SOA burden and the ground-level SOA concentration does not show a clear correlation in all seasons. This finding suggests that the effect of the new developments may depend on the altitude. Thus, counter-intuitive correlations between the total SOA burden and the surface level SOA may be compensated by SOA changes at higher atmospheric levels. In addition, the vertical SOA concentration analysis provides an overview of the main domains in which aqueous-phase oxidation influences SOA concentrations.
Figure 5.12 displays the SOA concentration (hydrophilic and hydrophobic) in all simulations performed from the ground level up to 8 km. The vertical analysis is divided into seasonal means, with a figure of the absolute SOA concentration on the left and a figure of the relative changes on the right. For each season, the difference between the MOM and POZ simulations (navy) and the MOM+ and MOM simulations (green) is displayed. The grey bars illustrates the combined difference (MOM/POZ and MOM+/MOM).
The absolute SOA concentrations and the changes induced by both chemical updates are greatest at ground level. This is due to the proximity to the emission sites and the fast kinetics of the oxidation reactions. This trend is reasonably consistent with the average OA distribution in flight campaigns [Heald et al., 2011]. In the POZ simulation, the mean

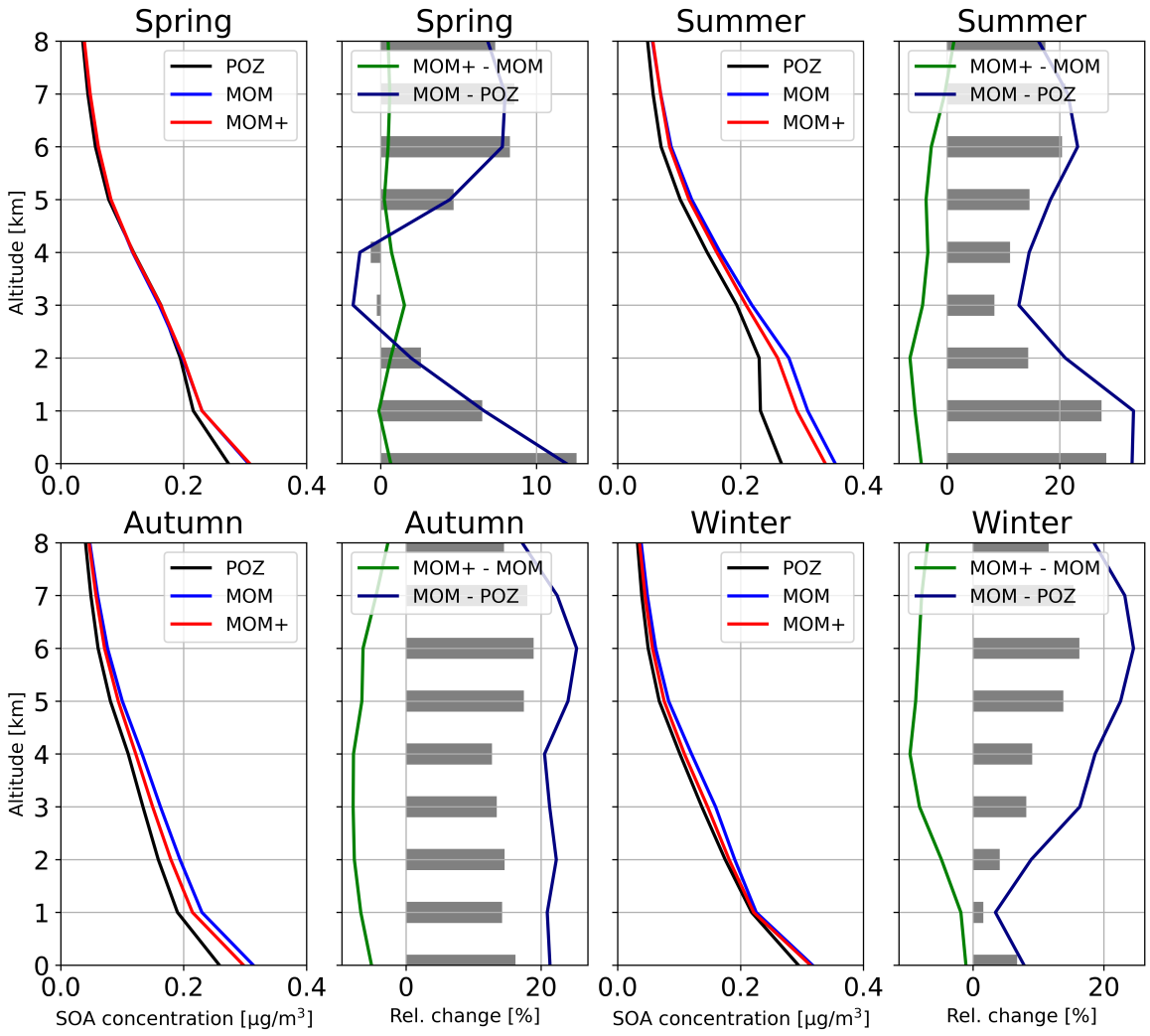

Figure 5.12: Seasonal mean SOA concentration of the lowest 8 km of the atmosphere of all three simulations. The plots next to the SOA concentrations illustrate the relative change induced by the MOM and MOM+ updates. The grey horizontal bars display the combined relative change of the MOM and MOM+ simulations with respect to the POZ simulation. Note that the figure shows the combined SOA concentration of hydrophilic and hydrophobic SOA, whereas it is mainly the hydrophilic aerosol phase that is affected by aqueous-phase oxidation.

ground-level SOA has the largest extent between 0.25 and 0.3 $\mu g/m^3$. In spring and summer, the concentration remains above ≥ 0.2 $\mu g/m^3$ up to an altitude of 2 km. Above this threshold, it gradually decreases with height. In autumn and winter, the SOA concentration decreases gradually at all altitudes. Despite the increase in the SOA concentrations, MOM and MOM+ display a similar vertical development as POZ. MOM increases SOA formation, especially in summer, while MOM+ counteracts this increase. The absolute SOA concentration does not indicate a strong change in the vertical distribution.
The relative impact of MOM is the highest close to the ground and at an altitude of six kilometers. As highlighted above, the changes close to the ground are related to the distance to the emission sources. At medium altitudes, many processes compete. Enhanced partitioning due to colder temperatures, dry deposition due to precipitation and the increased formation of low volatile organic compounds. At high altitudes the partitioning constant is increased even further, organic mass from evaporated clouds is transported to higher altitudes and is processed in multiphase chemical reactions. At this altitude, warm clouds also facilitate the hydrolysis of IEPOX in the aqueous phase. The relative contribution of the MOM simulation indicates that changes in chemical and physico-chemical processing impact SOA formation differently, depending on the tropospheric levels.
In contrast to MOM, the relative influence of MOM+ is the highest between two and four kilometers altitude. Instead of the water concentration, MOM+ correlates with the mixing ratios of oxidants and organic molecules in secondary organic aerosols. Figures 5.14 and 5.13 illustrate the OH and glyoxal concentrations in hydrophilic SOA. Glyoxal acts as a proxy for the abundance of organic molecule concentrations in hydrophilic SOA at the specific altitude. The OH concentration is highest at a height of 5 km in all seasons. Concentrations are particularly high in summer and comparatively low in winter. From this vertical trend one would expect the strongest effect of MOM+ at an altitude of 5 km. However, for a strong change due to aqueous oxidation, the oxidant and also the reactant concentrations must be high. The glyoxal concentration in hydrophilic SOA is highest on ground level and gradually decreases with heights. Consequently, the highest turnover rates of organics are between ground level and 5 km altitude. This can also explain the high impact of MOM+ (relative change, green line) at low altitudes in summer and, conversely, the low impact in winter. In summer, the high OH concentrations at low altitudes already oxidize the organics, so that the glyoxal concentrations diminish before reaching higher levels. In contrast, the OH radical concentrations are low in winter. Therefore, the concentration of organics remains higher at all altitudes.
Overall, the MOM+ chemistry reduces the SOA concentration. However, in spring it induces a slight decrease in at all altitudes. This is due to an increase in the hydrophobic SOA mass. Due to the limited mechanistic insight into the processing and condensation process of ORACLE, the reason is currently unknown, but needs to be investigated in future developments.
Hodzic et al. [2016] conducted a comparable analysis of the average vertical distribution

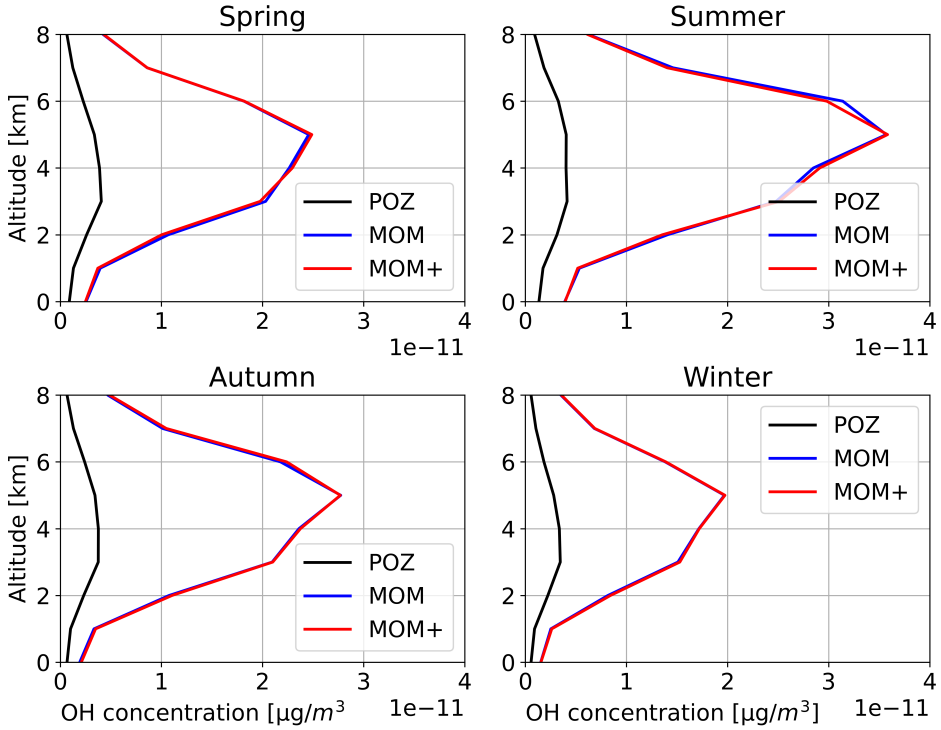

Figure 5.13: Seasonal global vertical distribution of the OH radical concentration in hydrophilic SOA.

of the SOA concentration between 2005 and 2008. The MOM+ simulation is the most comparable to the NY_DPH and NY_DP simulation of the study due to the similar level of detail. In these simulations, Hodzic et al. [2016] estimated ∼0.4 μg/m^3 SOA at ground level. This concentration declined with increasing altitude, reaching ∼0.03 μg/m^3 at an altitude of eight kilometers. These results are in good agreement with the results presented in Figure 5.12. At the ground level, the MOM+ simulation yields an SOA concentration of $\geqslant$ 0.3 μg/m^3 depending on the season. At an altitude of eight kilometers, the concentration drops to ∼0.03 μg/m^3. Consequently, the burden and distribution of SOA in the study by Hodzic et al. [2016] and the simulations in this work are comparable. However, both model simulations are on the lower side of the predicted global SOA concentration/burden spectrum [Lou et al., 2020].

5.2.6 Secondary organic aerosol O/C ratio

SOA formed in the aqueous fraction of deliquescent aerosols, is expected to have higher O/C ratios than SOA from the condensation of gas-phase LVOCs [Waxman et al., 2013, Ervens et al., 2011]. After the recent introduction of AERCHEM to the MESSy model, the O/C ratio of organics in hydrophilic and hydrophobic SOA can now be assessed for the first time. Previously, Tsimpidi et al. [2018] analyzed the O/C ratio of the molecules in the organic fraction. Here, the focus is on investigating the effect of physico-chemical processing

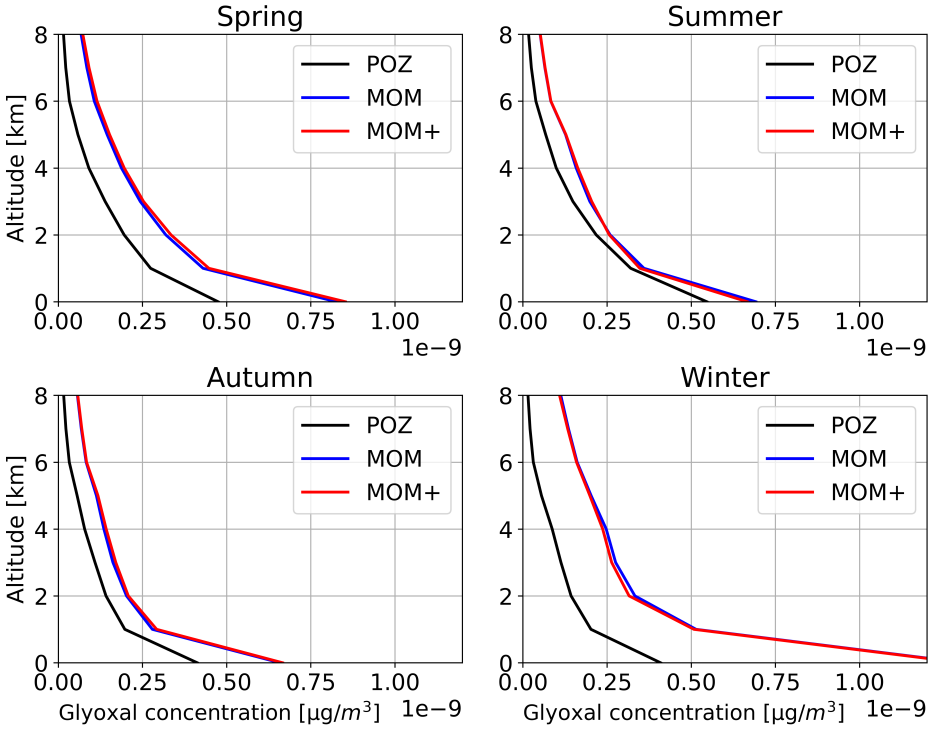

Figure 5.14: Seasonal global vertical distribution of the glyoxal concentration in hydrophilic SOA.

in the hydrophilic SOA on the O/C ratio. Section 5.2.2 revealed that the hydrophilic SOA constitutes a fraction of up to 30% of the total OA mass. Therefore, including this fraction in the O/C calculation can significantly affect the results.

In the scope of this analysis, some corrections are applied to ensure that the O/C calculations are comparable to measured O/C ratios. The atomic oxygen-to-carbon ratio is commonly measured based on the CO_2^+, CO^+ and H_2O^+ fragments [Rickards et al., 2013, Canagaratna et al., 2015]. When the AMS measurement is performed in the positive ion mode, the organic sulfate anion fragments are difficult to categorize [Schueneman et al., 2021]. This is due to the attribution of the sulfate-containing fragment to the inorganic mass [Moch et al., 2018]. Thus, they are not included in the calculations. Calibration techniques can be used to estimate the contribution of organic sulfate to the measured fragments (e.g. H_xO^+) [Aiken et al., 2008]. However, this is not done in all O/C measurements. Therefore, the oxygen atoms in the sulfate group of organic sulfate molecules are excluded from the average O/C ratio calculations.

Figure 5.15 illustrates the ground-level annual mean difference in O/C of the hydrophilic fraction of SOA between MOM and POZ (a) and between MOM+ and MOM (b). Note that the panels are not directly comparable to Figs. 5.8 and 5.9, as this section is restricted to organics in hydrophilic SOA, summing up the accumulation and the coarse modes. The hydrophobic SOA is divided into six volatility bins. In this step, the individual character-

istics of the molecules are partially lost. This complicates the analysis of properties such as the O/C ratio. Therefore, the investigations are limited to the hydrophilic SOA.
The following analysis is divided into two parts. The first section examines the changes in the regions with the highest differences. The second section examines the areas with a less pronounced influence (compared to the regions in the first section) are investigated. This is favorable for a clear visual representation of the results. Further, this measure separates the analysis of remote regions and regions close to emission sites.
Panel A depicts the changes induced by the MOM update. It shows strong O/C changes in Antarctica, over the tropical ocean regions (Indian Ocean and southern Pacific), and in Greenland. Between MOM and POZ, the chemistry of medium and large organics, and the partitioning constants have been adjusted. The mechanistic update in MOM includes mechanisms for new VOCs and additional oxidation pathways for already established compounds. The resulting enhanced production of highly oxygenated species is expected to increase the O/C ratio. The new oxidation pathways in the aqueous phase (IEPOX ring-opening, see Fig. 3.4) and the box model sensitivity simulations suggest this idea. Instead, the regions with the largest changes show a strong decrease in the O/C ratio.
The reasons for this misconception can be assessed by analyzing the aerosol constituents in the respective regions. Table 5.8 lists the five most abundant organics in hydrophilic SOA for all simulations but is restricted to the three regions of interest. Organic sulfates, except isoprene-derived organic sulfates, are not listed, as these compounds are not included in the previous O/C calculations. Sulfates from isoprene have been added in the MOM update and are therefore interesting for the analysis. A closer look at the SOA constituents in Antarctica shows solely oxygenated methyl derivatives in the POZ simulation. Due to low carbon numbers, but high degrees of oxidation, all molecules have an O/C ratio ≥ 2. The SOA composition changes significantly with the MOM update far from the source regions. Small organics are replaced by larger organics such as functionalized epoxides and isoprene oxidation products. These compounds were not introduced with the MOM update, but their partitioning constants are adjusted. With higher Henry's law coefficients, they partition to available aqueous media and remain in this phase until they are removed by deposition. They do not undergo any chemical removal in the aqueous phase. Additionally, Henry's law constants have an inverse dependence on the ambient temperature. As a result, the concentration of organic molecules increases in hydrophilic SOA in colder regions. The new SOA constituents exhibit an O/C ratio of 1, decreasing the mean value. Measurements of SOA components in remote areas have shown that isoprene and monoterpene products are transported over long distances to regions far from the emission sites [Cui et al., 2019, Yttri et al., 2024, Hu et al., 2013]. It has to be noted that the AERCHEM submodel currently assumes that organic aerosols with a sufficient amount of water are always liquid. This simplification is often applied in aerosol modeling. Observations have shown that organic aerosols retain properties of liquids, even under cold conditions [Cappa et al., 2008, Marcolli et al., 2004]. Thus, the organic aerosol composition in colder regions is still impacted by

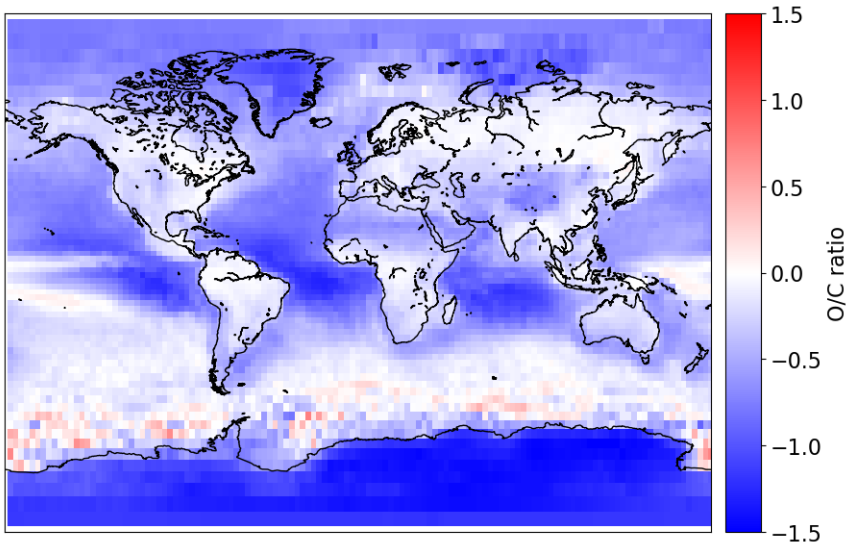

(a) MOM - POZ

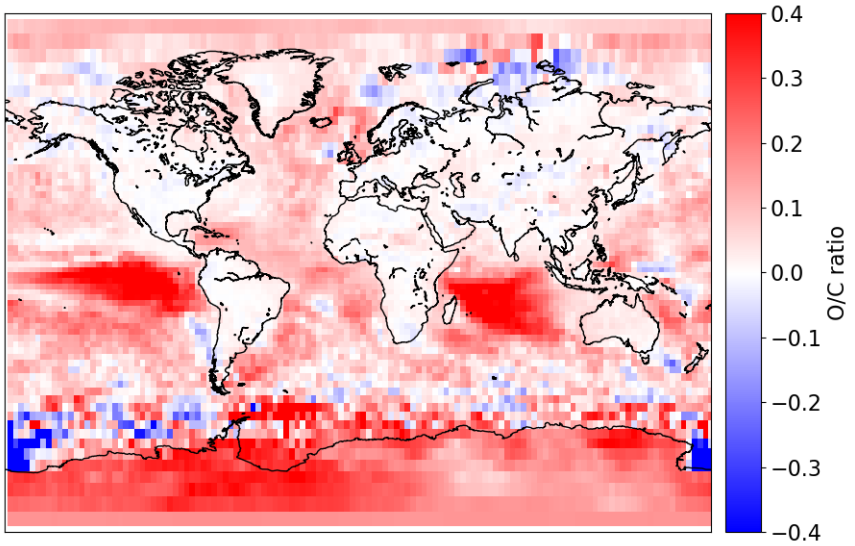

(b) MOM+ - MOM

Figure 5.15: Absolute change in the annual mean ground-level hydrophilic SOA O/C ratio between (a) MOM and POZ, and (b) between MOM+ and MOM. The seasonal changes for both panels can be found in the appendix (Figure 7.8 and Figure 7.9).

gas-to-aqueous partitioning. The magnitude on which this affects the organic loading of SOA is unknown.

Similar observations found for the Antarctic also apply to the dominant SOA tracers in the Indian Ocean and the south-eastern Pacific. Rather small oxidized compounds are replaced by larger low volatile, soluble organics. However, in these regions not only established compounds with enhanced aqueous-phase uptake are dominant, but also new highly soluble molecules in hydrophilic SOA. The secondary organic aerosol constituents are a mixture of isoprene, monoterpene, and toluene products. Enhancements in the tropical Pacific are associated with continental SOA precursor products. VOCs and aerosols over central and southern Africa are transported over the Indian Ocean by atmospheric circulation. This phenomenon was captured in observations and model simulations for January and February [Rajeev et al., 2000]. It was found that this enhanced accumulation of organic aerosols dissipated in March. Figure 7.8 in the appendix displays the seasonal change in the O/C ratio between MOM and POZ. It also shows the strongest O/C decrease over the Indian Ocean during winter. The decrease in spring is much less pronounced. This indicates that the model also transports less organics from the continental areas over the ocean during this period. Unlike the SOA mass concentration, the O/C ratio analysis is a relative, not an absolute comparison. The OA concentrations over the oceans are low. Therefore, this trend cannot be observed in the absolute change in SOA mass concentrations. However, the strong negative change in O/C over the southern Pacific is considered a model overprediction. Aerosols and gases are transported from South American emission regions to the tropical Pacific [Bourgeois et al., 2015]. The Andes are expected to act as an effective transport barrier. However, their orography is much shallower in the simulations at low spatial resolution. As a result, the transport from the Amazon basin to the southeast Pacific is overpredicted. This was clearly shown in previous MESSy simulations for formic acid [Franco et al., 2021].

The ground-level O/C ratio over Greenland is strongly influenced by toluene, benzene, and monoterpene products. Field observations show that biomass burning and fossil fuel plumes from Canada and the US east coast can reach Greenland [Schmale et al., 2011]. The scarcity of literature data on SOA composition in Greenland makes comparison with measurements difficult. However, von Schneidemesser et al. [2009] found very low concentrations of anthropogenic (alkane) and biogenic (levoglucosan) concentrations in Summit, Greenland. This indicates the efficiency of multiphase oxidation in the long-range transport of an aging plume.

The aqueous-phase oxidation in MOM+ leads predominantly to an increase in the O/C ratio over the ocean and Antarctica. It displays the opposite effect of the MOM update, affecting similar regions. This is consistent with the observations made in Section 5.2.3. The strong decreases induced by MOM in the southern Pacific and the Indian Ocean are compensated in large parts by the MOM+ chemistry. This can be explained by an interaction between the two updates. In the MOM simulation, large, organics with high Henry's law constants are

Table 5.8: Collection of the dominant SOA tracer in different regions with the highest O/C change in the three simulations. The molecules are sorted from highest to lowest concentration. Note that sulfates are not considered in the O/C calculation for Figure 5.15.

Location	Species POZ	Species MOM	Species MOM+
Antarctic	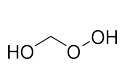		
		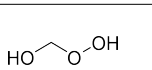	
		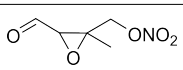	
		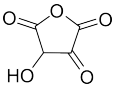	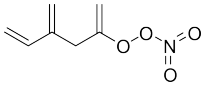
		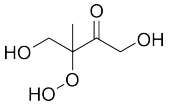	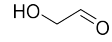
Indian Ocean			
		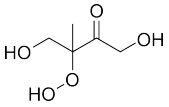	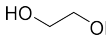
		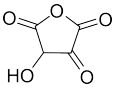	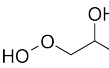
		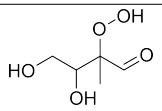	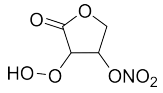
	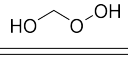	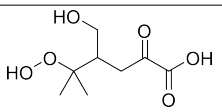	
Greenland	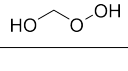	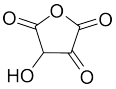	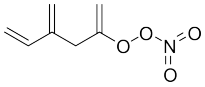
		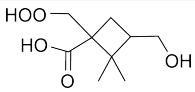	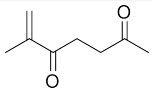
	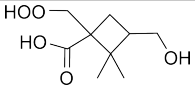		
		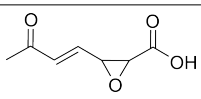	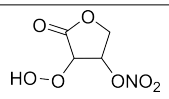
		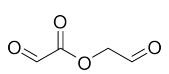	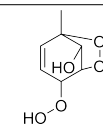

added to the organic aerosol mass. Although they are highly oxidized, they exhibit a lower O/C ratio than the small organics that dominate the hydrophilic SOA in POZ. Aqueous-phase oxidation in MOM+ increases the oxygen content in the new large molecules and breaks them down into smaller compounds. Thus, chemical processing has a large effect on the O/C ratio, especially in these regions. The absence of this effect in some areas may be related to the current limitations of the aqueous oxidation scheme. Depending on the molecular structure, some compounds are not included in the generated mechanism. For example, non-tertiary organic nitrates, aromatics, ethers, and esters are currently not considered.

In Antarctica and the Indian Ocean, the patterns agree with the expectations. Large organics are no longer dominant in hydrophilic SOA, but are replaced by small soluble compounds such as formic acid, acetic acid, glyoxal, glycol aldehyde, and ethylene glycol. The product collection of experimental results that investigated aqueous SOA in [Ervens et al., 2011] contains similar components, but also the corresponding oligomers. Real world observations of the SOA constituent distribution are scarce for Antarctica and over the ocean. Paglione et al. [2024] investigated the functional groups in Antarctic organic aerosols with H-NMR and found a considerable contribution of aliphatic carbons, poly-aliphatic chains, and hydroxy/alkoxy groups among the water soluble organic compounds. The oxygen-containing groups show a similar contribution to SOA as the aliphatic groups. This is in good agreement with the model results of the MOM+ simulation. The organic tracers in hydrophilic aerosols also show an equal contribution between carbon and oxygen-containing groups. However, a more detailed analysis is required to assess the SOA constituents in remote areas.

In Greenland, the effect of the additional aqueous-phase oxidation is different. The O/C ratio of the SOA tracer is only slightly affected. The dominant tracers are epoxides, peroxy nitrates, and heterocycles. These molecule types are not affected by the mechanism generator due to the limitations of the SAR methods and parameters for each functional group. For example, the unsaturated diketone is expected to yield end products that are not contained in the basic chemical mechanism. Thus, the mechanism is neglected. Generally, only previous MESSy products are found in the tracer analysis, and no intermediates of the mechanism generator. This indicates that the reaction kinetics in the aqueous phase are considerably faster than the SOA lifetime. Figure 7.6 in the appendix display the absolute O/C ratio by hydrophilic SOA in MOM+. The O/C ratio of the total SOA can be acquired by correlating the result in the present work with the hydrophobic SOA.

Due to the strong O/C variations over the ocean, changes over the continents are barely visible. Commonly, organic loadings are higher close to emission sources than in remote regions. Therefore, changes in the O/C ratio require a more pronounced absolute change in tracer mixing ratios. However, the products of the emitted VOCs are already dominant over the continents. Adjustments in chemistry and partitioning changes the product proportions or introduce new compounds. However, if the overall size of the products is not greatly

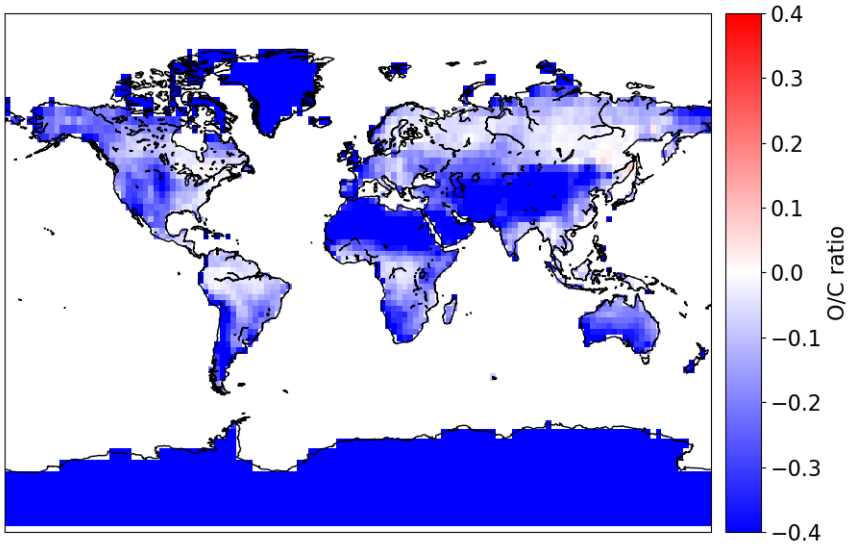

(a) MOM-POZ

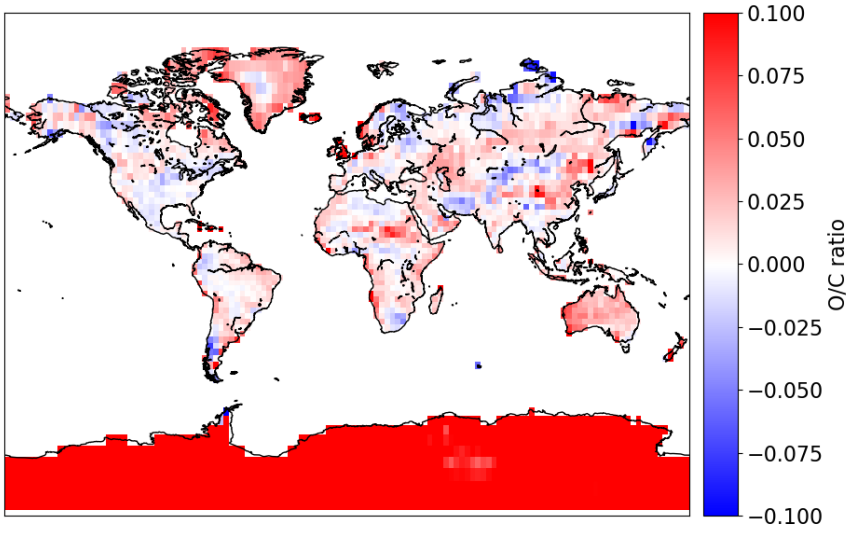

(b) MOM+ - MOM

Figure 5.16: Absolute change in the continental annual mean ground-level hydrophilic SOA O/C ratio between (a) MOM and POZ, and (b) between MOM+ and MOM. The ocean is excluded to improve the visibility of the continental changes.

affected, the O/C ratio remains similar.
In Figure 5.16a, the ground-level annual mean hydrophilic SOA O/C ratio between MOM and POZ is shown with a focus on the continents. Changes in O/C ratio over the ocean are masked. The overall trend is similar to the analysis of the changes in remote regions. The O/C ratio is largely lower in the MOM than in the POZ simulation. Nevertheless, there are areas where no change or a slightly positive change is depicted. In the following discussion, the focus is on the areas showing little change in O/C. Only the aqueous SOA constituents in North Africa are investigated to assess whether the tracer concentrations are similar to the ocean/Antarctic regions.
The MOM simulation induces no or slight increases in the annual mean ground-level O/C in three regions: on the North American east coast, in the north of South America, and in eastern Russia near the Sea of Japan. These regions have high VOC emissions and therefore it has to be assessed why the O/C changes are small. Due to strong similarities in the SOA tracer changes, eastern Russia is neglected in the following analysis. Instead, the SOA concentration over a less polluted continental area, central Algeria, is discussed.
Table 5.9 lists the dominant aqueous SOA tracers on the US east coast, in western Brazil, and in central Algeria. In both, the US and Brazil, the POZ simulation mostly shows the strongest contribution from monoterpene oxidation products. Among the five dominant tracers, four are α- and/or β-pinene products. Only one is formed in the isoprene oxidation mechanism (the C5 compound). In the MOM simulation, this observation shifts. Isoprene products such as tetrols and large organic sulfate replace prior monoterpene compounds. Xu et al. [2015] analyzed the constituents of OA in the southeastern US. They found that isoprene-derived OA is formed mainly during the warm months (May-August). In winter, the concentrations are very low. In July and March, they found a contribution of approximately one-third to total OA. However, in May and June, the contribution is around 20%. During the summer period, SOA dominates OA. The contribution can therefore be extrapolated from OA to SOA. In the colder months, the share of SOA to total OA also decreases. Nevertheless, the dominant contribution of isoprene SOA in the MOM simulation on an annual mean basis can be considered as an overprediction compared to the measurements.
In central Algeria, biogenic emissions of VOCs such as isoprene and monoterpenes are particularly low. This is reflected in the POZ simulation. Small SOA tracers similar to those over the ocean, and compounds from the oxidation of aromatic compounds are dominant. However, monoterpene-derived compounds are also found in this region. In the MOM simulation, non-biogenic compounds are replaced by isoprene and monoterpene products. Due to the low biogenic emissions, these molecules can be linked to long-range transport. SOA tracers of both VOCs have previously been found in particulate matter in the Saharan air layer [García et al., 2017].
The simulation results of MOM+ show the versatile effect of the aqueous oxidation chemistry on hydrophilic SOA. The O/C ratio difference between MOM+ and MOM is overall

Table 5.9: Collection of the dominant SOA tracer in selected continental regions in the three simulations. Note that sulfates are not included in the O/C calculation for Figure 5.15. The SOA tracers in Algeria and Brazil are reduced to four to improve the layout of the table.

Location	Species POZ	Species MOM	Species MOM+
US east coast	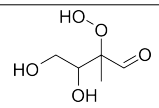	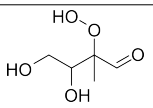	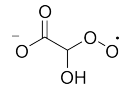
	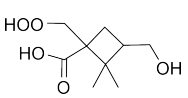	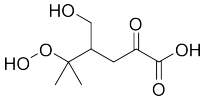	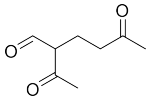
	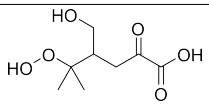	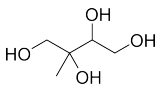	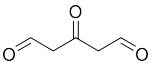
	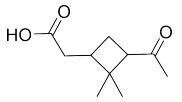	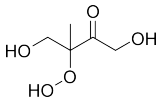	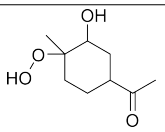
	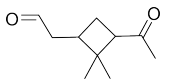	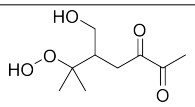	
West Brazil	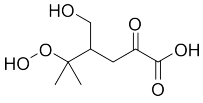	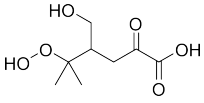	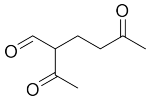
	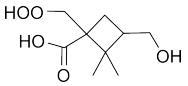	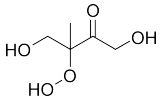	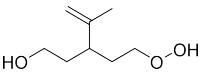
	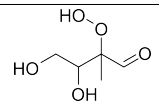	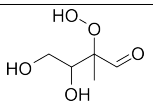	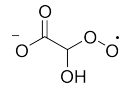
	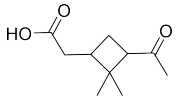	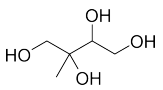	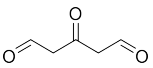
Central Algeria		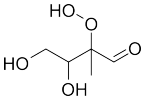	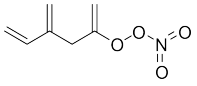
		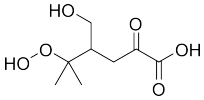	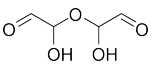
	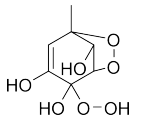	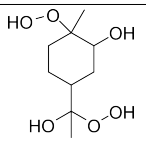	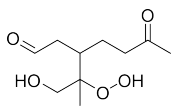
	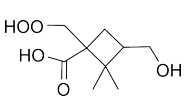	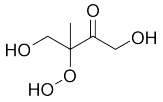	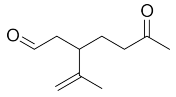

Table 5.10: Total mean organic mass in all aqueous phases (large clouds and rain droplets) simulated by SCAV and absolute/relative difference between the updated setups and the reference.

Sensitivity run	SOA burden / Gg	Abs. (rel.) Difference / Tg (%)
MESSy-POZ	150	-
MESSy-MOM	196	46 (30.7)
MESSy-MOM+	187	37 (24.4)

positive. Nevertheless, it also shows multiple areas that are negatively impacted. Overall, the change ranges from a small decrease (-0.05) to a moderate increase (0.1). Similar to the adaptation of the O/C ratio between the different simulations in remote areas, MOM induces up to four times larger changes than MOM+. However, the changes due to the additions to the chemical mechanism are of comparable magnitude. As seen before, MOM+ often counteracts the changes induced by MOM.

The hydrophilic SOA tracers shown for the US east coast and western Brazil show the main effects of the aqueous oxidation. The isoprene oxidation products are less dominant than before. This applies to the tetrol, but also the organic sulfate. Since sulfate-containing molecules are not included in the new aqueous oxidation scheme, the precursor compounds or alternative products need to be oxidized in the aqueous phase. This inhibits the strong formation of IEPOX products. Isoprene products generally exhibit rather high Henry's law constants larger than 1×10^6 M/atm. Hence, they efficiently partition to the aqueous phase. Similarly, monoterpene products are further oxidized yielding product compounds of later reaction generations. The high tracer concentration of dihydroxy methane oligomer in Brazil further indicates that larger compounds are oxidized, yielding smaller product compounds. All these processes lead to a slight decrease in the O/C ratio due to the abstraction of oxidized functional groups in the mechanism.

In central Algeria, the dominant contribution of biogenic VOC oxidation products remains. However, α- and β-pinene products are replaced by limonene-derived compounds. Additionally, glyoxal oligomers are efficiently formed. Although the tracer distribution changes, the O/C ratio remains fairly constant.

5.2.7 Organics in cloud and rain droplets

The new partitioning and gas-/aqueous-phase chemistry does not solely influence hydrophilic SOA. An even more pronounced effect is expected for other aqueous phases in the atmosphere, such as cloud and rain droplets. In contrast to the aerosols, these phases contain a higher proportion of water, which favors the partitioning of soluble organics. In particular, the aqueous-phase oxidation scheme is expected to show an even larger influence in these phases.

Figure 5.17 displays the organic mass inside all aqueous phases simulated by the SCAV

submodel (cloud and rain droplets). Similarly to Figure 5.6 the organic mass is illustrated as the absolute difference between the MOM and POZ (blue) and the MOM+ and MOM (red) simulations. The grey bars indicate the difference between the two updates. The MOM update shows the largest changes in summer and winter. This trend is consistent with the previous analysis. Nevertheless, the changes during summer are smaller than for SOA. This can be explained by the difference in pH values. In cloud droplets, the H^+ concentration is lower than in aerosols [Pye et al., 2020a]. The aqueous-phase oxidation of IEPOX, discussed in Section 3.1.2, is an acid-catalyzed process. Therefore, the chemical processing is likely to be slower than in the previous analysis. Due to the intermediate Henry's law constant of IEPOX, it remains partly in the gas phase. This lowers the impact of isoprene on cloud SOA during summer. In the southern hemisphere, isoprene emissions are strong during winter. Therefore, the same analysis also applies to the changes in winter. The aqueous-phase oxidation in MOM+ has overall a small effect on the organic mass in clouds. Only in winter, the increase depicted for MOM is partially compensated. During this period, isoprene emissions are strong in the southern hemisphere. Isoprene oxidation products contribute a large fraction of the cloud OA mass. The previous analysis has shown that the concentrations of IEPOX precursors and alternative isoprene oxidation products are lower in the MOM+ simulation. Therefore, fewer tetrols and isoprene-derived organic sulfates are formed. Smaller changes during summer indicate that monoterpenes are also less affected by aqueous-phase oxidation. Due to the higher liquid water content compared to hydrophilic SOA, cloud and rain droplets were expected to be strongly influenced by the generated reactions. However, the total organic mass in SOA is four times higher in SOA than in the remaining aqueous phases. This limits the overall change, especially with the current restrictions of the generator (not all compounds are oxidized yet). Additionally, gains in organic mass due to aqueous oxidation could also compensate for some of the losses. It also has to be noted that the lifetimes of SOA and cloud droplets are different. In model simulations, Kanakidou et al. [2005] found an organic aerosol lifetime between 4 and 11 days. The sampling time of the model simulation in the present work is five hours. Thus, several output values are calculated during the organic aerosol lifetime and the organic molecules are efficiently processed. Cloud and fog droplets, on the other hand, have a lifetime of a few minutes [Ervens, 2015]. This limits the processing time within clouds.

Table 5.10 lists the mean total aqueous-phase (SCAV only) SOA burdens in all simulations and the absolute/relative difference to the POZ run. The new chemistry included in the MOM simulation increases the SOA mass by 46 Gg, while the aqueous-phase oxidation reduces this enhancement to 37 Gg. These differences correspond to a 30.7 and 24.4% increase in OA mass, respectively. The new chemistry introduced in the MOM setup has a more pronounced effect on hydrophilic SOA than on the remaining aqueous phases. In the reference, the organic mass in cloud and rain droplets is higher than in hydrophilic SOA. This relationship shifts with the introduction of the new chemistry and the trend

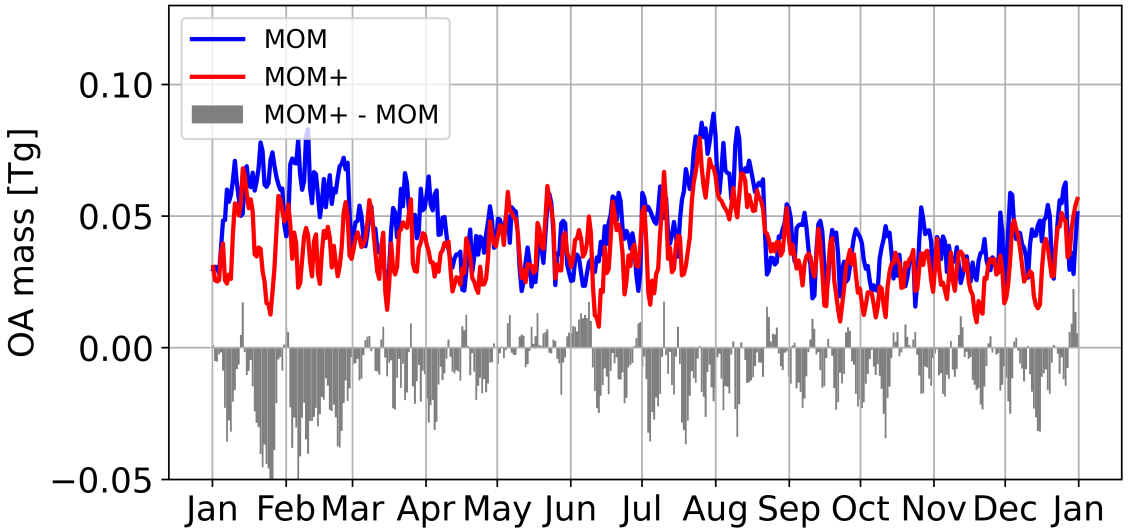

Figure 5.17: Modeled organic mass in the aqueous phase simulated within the SCAV submodel. The figure is based on averages over a 20 hour time period. This is due to the strong oscillation of the data on short time scales. Hence, averaging over a longer time period improves the visibility of the differences in organic mass.

remains with the introduction of further aqueous-phase oxidation. Due to the lack of literature on model simulations and experiments in which clouds and hydrophilic SOA are analyzed at the same time, a comparison with prior scientific results is complicated. Ervens et al. [2011] applied a simplified parcel model at varying meteorological parameters to investigate the amount of aqueous-phase SOA in clouds and hydrophilic SOA. The results show a higher cloud aqSOA by a factor of approximately two. However, the concentration strongly depends on the conditions and the simulations only include a certain of different VOCs. This highlights the importance of the hydrophilic SOA in model simulations and the interpretation of observations. Based on the model results hydrophilic SOA are more important for the analysis of atmospheric organic mass than previously expected. Finally, the change in the O/C ratio of organics in clouds and rain droplets is analyzed. This gives an overview of the change in the composition of the organic load. Figure 5.18 (a) and (b) illustrate the absolute change in annual mean O/C ratio of MOM against POZ, and MOM+ against MOM, respectively. The cloud and rain droplets are analyzed at level 20 of the model. This altitude is more representative of clouds.

The displayed characteristics differ from the analysis of hydrophilic SOA (see Sect. 5.2.6). The changes in O/C ratio induced by both updates are of similar magnitude. However, the additions in MOM mostly lead to a decrease in the O/C ratio. The MOM+ simulation shows varying impacts depending on the region. As shown before, the aqueous oxidation in MOM+ tends to counteract the changes in MOM. Table 5.11 lists the dominant cloud SOA tracers in three regions of interest: northern South America, western US, and central Russia. In northern South America, the opposing nature of both updates is depicted.

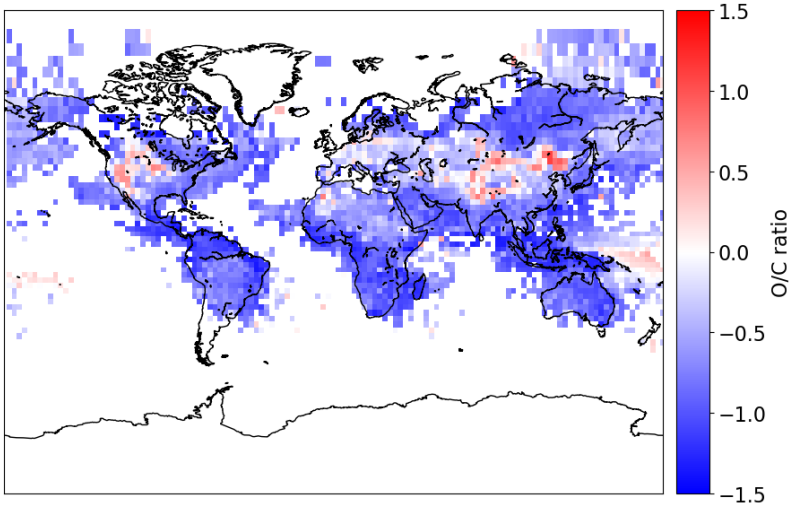

(a) MOM - POZ

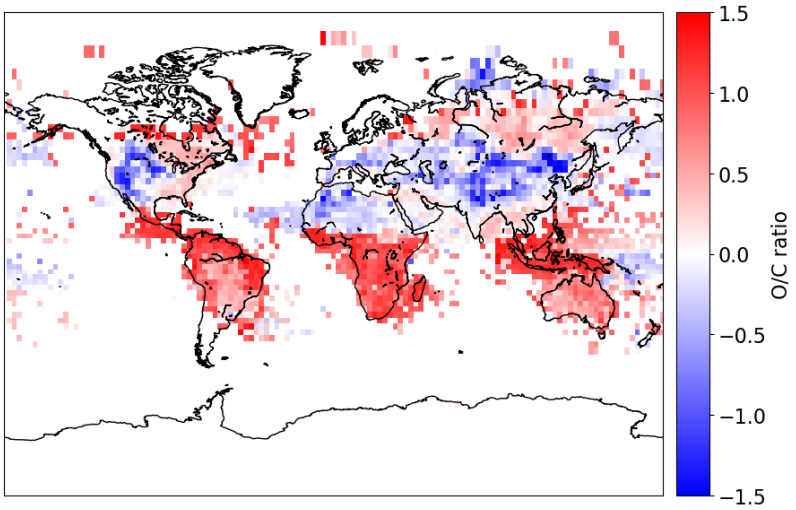

(b) MOM+ - MOM

Figure 5.18: Absolute change in the annual mean O/C ratio of OA in clouds and rain droplets between (a) MOM and POZ, and (b) MOM+ and MOM.

Table 5.11: Collection of the dominant SOA tracers in the regions with the highest O/C change in the three simulations. Note that sulfates are not considered in the O/C calculation for Figure 5.15.

Location	Species POZ	Species MOM	Species MOM+
North South America		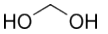	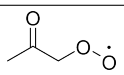
	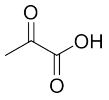	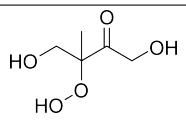	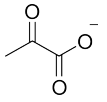
		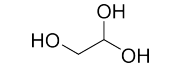	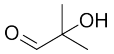
		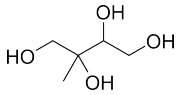	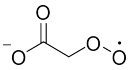
	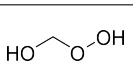	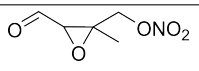	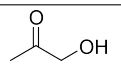
Western US		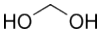	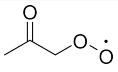
		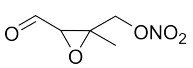	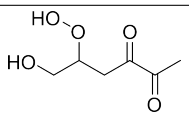
			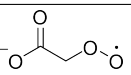
	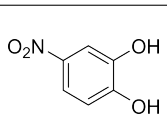	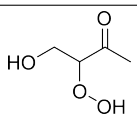	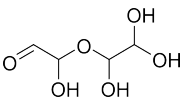
	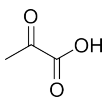	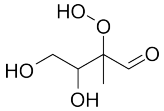	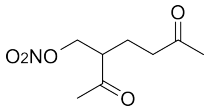
Central Russia		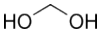	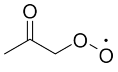
			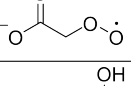
			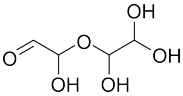
	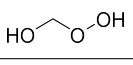	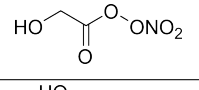	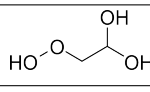
	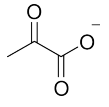	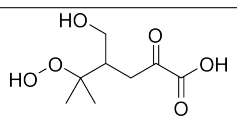	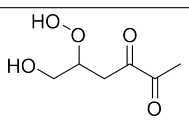

The cloud droplets in POZ contain organics up to three carbons and O/C ratios equal to or greater than one. In the MOM simulation, mainly isoprene-derived tracers replace smaller organics. Especially the organic nitrates, which are part of the revised isoprene-NO_3 mechanism, lead to a strong decrease in O/C. The introduction of the aqueous oxidation in MOM+ reverts this change. Cloud droplets in MOM+ are again dominated by small oxidized compounds such as methylglyoxal and acetol derivatives. This increases the O/C ratio. This trend is also occurs in the western United States, albeit in reverse. The POZ simulation has mainly small acids, but also a nitrate derivative of catechol in the cloud droplets in this region. Catechol is a product of the oxidation of benzene and phenol. Both precursors are emitted by anthropogenic and biomass burning sources. At sufficiently low temperatures, the Henry's law coefficient of the catechol nitrate is high enough to partition to the aqueous phase. It has a considerable impact on the O/C due to its high molecular mass. In MOM, the isoprene oxidation products make up the majority of cloud SOA tracers. However, in this environment, they have a higher O/C ratio than their counterparts in POZ. The total O/C ratio increases. In contrast, the tracers in MOM+ are limonene oxidation products and glyoxal oligomerization products. Due to the length of the carbon chains, the O/C ratio decreases. The changes in central Russia give an overview of the impacts in regions with rather low isoprene emissions. In all three simulations, small oxidized compounds are dominant in cloud droplets. MOM and MOM+ additionally show rather high concentrations of monoterpene products. It is noticeable once again that MOM+ shows high concentrations of glyoxal oligomer. This indicates that glyoxal is frequently formed in the aqueous-phase oxidation mechanism.

5.2.8 Oxidant concentrations

Adjustments to the kinetic scheme and the partitioning have implications beyond the presented gas and aqueous-phase concentrations of VOCs and oxidation products. Most reactions consume or produce oxidants, which in turn facilitate or slow down further reactions. This feedback effect may lead to unexpected results. Figure 5.19 displays four panels with different oxidant concentrations. The first three show the differences in ground-level OH concentration between the MOM and POZ simulations in all phases. The last panel focuses on the ground-level changes in gas-phase ozone concentration. In the gas phase, annual mean OH concentrations are simulated between 1×10^5 molecule/cm^3 and $\sim 1.7 \times 10^6$ molecule/cm^3 in global models [Zhang et al., 2018]. Lawrence et al. [2001] have simulated the annual mean OH concentrations in four different global models, divided into different atmospheric levels. At the lowest level (below 750 hPa) they found the lowest number concentration in the southern hemisphere (90°S-30°S; 3.5×10^5 molecule/cm^3) and the highest concentrations between the equator and 30°N (1.86×10^6 molecule/cm^3). In the Antarctic region, mean OH concentrations of 3.9×10^5 molecule/cm^3 were measured in January/February [Bloss et al., 2007]. In tropical regions, observations show values above the average, reaching up to 1×10^7 molecule/cm^3 [Kuhn et al., 2007, Martinez et al., 2010].

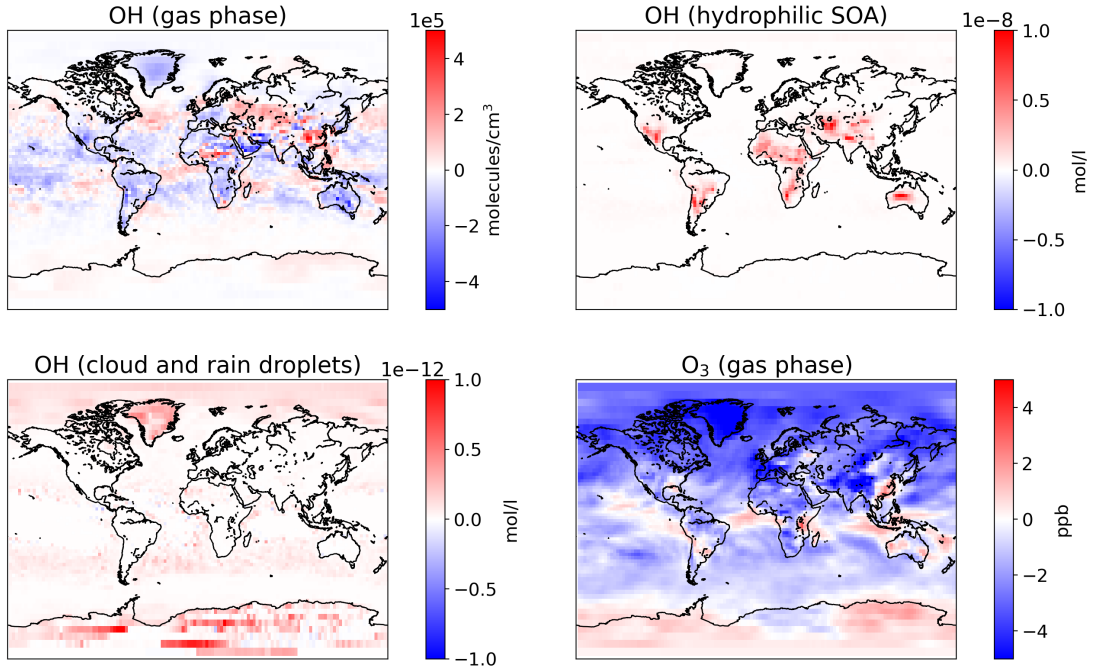

Figure 5.19: Ground-level OH concentration changes between MOM and POZ in the gas and all aqueous phases. The last panel displays the ground-level ozone concentrations in the gas phase.

The MOM update induces OH concentration changes up to 5×10^5 molecule/cm^3. Measurements of OH concentrations in clouds and aerosols that are generally representative of atmospheric conditions, are not available in the literature. In model studies, concentrations of the order of 1×10^{-12} M are often inferred in aqueous media [Ervens et al., 2014]. The change in cloud and rain droplets fits this literature model result. It shows that the aqueous-phase OH concentration is enhanced in remote, cold regions. In the hydrophilic SOA, the change in OH concentration is several orders of magnitude higher. However, these changes all occur in continental regions. Considering the short distance to the emission sites and the low water content compared to hydrophilic SOA over the ocean, the pattern fits the expectations. Further experiments are needed to improve the estimation of OH in aqueous solutions. In the last panel of Figure 5.19, the ozone concentration changes are displayed. Annual background measurements range from 35 to 50 ppb at mid-latitudes in the northern hemisphere [Sicard, 2021]. The differences between MOM and POZ range up to 5 ppb. Especially in the northern hemisphere there are strong negative changes. Figure 5.20 displays a similar comparison as shown in Figure 5.19 but for the differences between MOM+ and MOM. The OH concentrations in the gas phase change in a similar magnitude, but the distribution is different. The OH concentration in the aqueous phases shows a mixed pattern. Nevertheless, the most dominant changes in cloud and rain droplet OH are in the remote cold regions, while hydrophilic SOA illustrates the highest differences over the continents. This is observed in both updated simulations. In the gas phase,

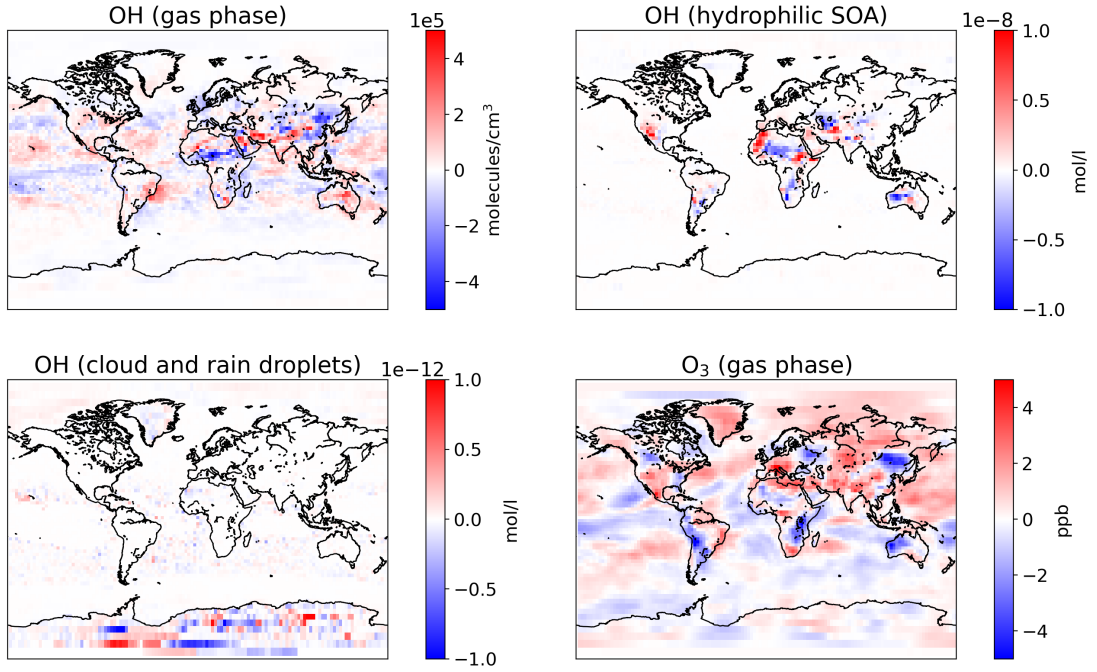

Figure 5.20: Ground-level OH concentration changes between MOM+ and MOM in the gas and all aqueous phases. The last panel displays the ground-level ozone concentrations in the gas phase.

ozone changes induced by the MOM update are partly reversed by the mechanistic additions in MOM+. However, the ozone concentration is still reduced compared to the POZ simulation. Previous investigations revealed that global models tend to overestimate the tropospheric ozone in the Northern Hemisphere [Young et al., 2013, 2018]. Thus, especially the presented partitioning updates may help to correct this bias. Oxidant concentrations in the atmosphere are influenced by a complex combination of sources and sinks. This makes it difficult to assess the dominant processes leading to variations in the oxidant levels. In the gas phase, OH is lost through the reactions with VOCs, CO and NO_2. The update in MOM introduces revised partitioning coefficients to the model, enhancing the concentrations of organic compounds in the aqueous phases (see Tab. 5.15). These compounds are less abundant in the gas phase, leading to an increase in OH concentrations. The correlation between the ozone and OH levels is apparent in several regions, particularly over the ocean at mid-latitudes. However, the reaction of HO_2 with NO also influences the OH budget [Rosanka et al., 2021a].

The changes in the gas-phase mixing ratios of ozone can be attributed to OVOC-related processes. The oxidation of organic molecules is a source of HO_2 in the gas and the aqueous phase. Gaseous HO_2 is a source of ozone, due to the reaction with NO and the subsequent photolysis of NO_2. In the aqueous phase, HO_2 is also formed by the oxidation of organics. Although, here it reacts with O_3, contributing to ozone loss (see Fig. 5.21 (adapted from Rosanka et al. [2021a])). As a result, the increased partitioning of organics into the aqueous

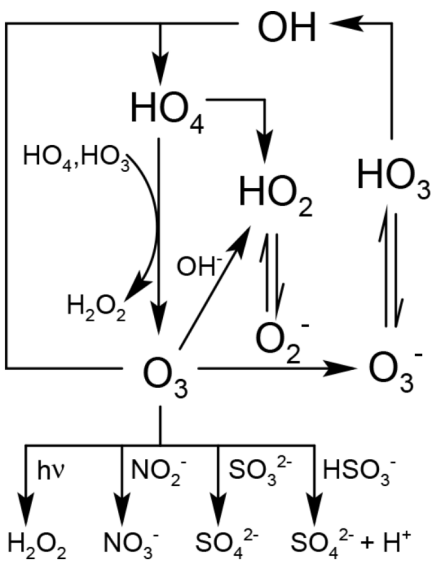

Figure 5.21: Inorganic reaction cycle of ozone in the aqueous phase. The figure is adapted from Rosanka et al. [2021a].

phase leads to a strong reduction in ozone concentrations (see chemical budgets in Rosanka et al. [2021a]).

The increase in aqueous OH can also be related to the production of HO_2 by oxidation in aqueous media. The effect of the HO_2 molecule on the ozone cycle is depicted in Figure 5.21 (adapted from Rosanka et al. [2021a]). Aqueous-phase HO_2 is in equilibrium with O_2^-. This anion promotes the production of O_3^-, which is in equilibrium with HO_3. This radical is unstable and decomposes to OH. If the organic loading in aqueous media decreases, this effect is reversed and the OH concentration decreases.

These processes explain some of the reasons for the changes between MOM and POZ. The same relationships apply to the differences between oxidant levels in MOM+ and MOM. However, the patterns are more complex, suggesting additional influence factors. Aqueous oxidation affects the outgassing of organics. Therefore, OVOC concentrations in both phases are influenced by the update, depending on the organics and oxidants available in a given grid box. Additionally, the mechanism generator includes the aqueous-phase photolysis of large organic hydroperoxides. This reaction produces OH radicals. On the other hand, OH reacts with OVOCs in the aqueous phase. Thus, a detailed examination of the influence of the mechanism generator requires knowledge of the chemical budgets for both the gas and the aqueous phase. This analysis is beyond the scope of the present work. The unexpected and unintended perturbation of the oxidant concentration should be evaluated in future investigations, due to the significant magnitude of the changes.

Chapter 6

Summary and outlook

In this work, the formation and loss of secondary organic aerosol was re-evaluated within the framework of the MESSy model. The main focus was on the hydrophilic SOA simulated by the model and the remaining aqueous phases (cloud and rain droplets). Among the various processes that affect secondary organic aerosols, three major chemical/physico-chemical influence factors were adapted: the chemical processing of selected volatile organic compounds, the partitioning of organics between the gas and the aqueous phase, and the extension of the aqueous-phase oxidation of organics MESSy by mechanism generation. Box model simulations in CAABA/MECCA and global model simulations in MESSy were performed to investigate the implications of the individual updates. The evaluation includes the analysis of the global secondary organic aerosol burden, the organic aerosol (SOA and PM2.5) mass concentration, the vertical distribution of organic aerosols, and the O/C ratio of organics in the tropospheric aqueous phases. The following sections summarize the results and implications of the adapted processes.

6.1 Secondary organic aerosols from gaseous precursors

The chemistry of volatile organic compounds of biogenic and anthropogenic origin has been adapted to improve the representation of secondary organic aerosols in the model. The most important changes have been made to the chemistry of isoprene and limonene. In previous updates, the formation of isoprene-derived epoxy diols (IEPOX) was added to the model. However, IEPOX was a lumped species with no further chemistry. In this work, IEPOX has been divided into the three main isomers, and the subsequent gas- and aqueous-phase chemistry has been added. The main products are tetrols and organics sulfates. The global isoprene burden is high and the new oxidation products are soluble in aqueous media. Therefore, this addition was expected to have a considerable impact on hydrophilic secondary organic aerosols. To ensure that the IEPOX products are formed in realistic quantities, degradation reactions have been adapted from the literature and re-evaluated. Due to recent developments in the isoprene-NO_3 mechanism, this scheme has

also been revised in the model. It has an indirect effect on secondary organic aerosols as the isoprene concentrations are controlled by the oxidation mechanisms. The addition of limonene, together with the corresponding gas-phase oxidation mechanism, further extends the range of organics from the biosphere. It was expected to add secondary organic aerosol mass in monoterpene-dominated regions. Adjustments for anthropogenic volatile organic compounds are rather small and show little effect in the analysis. Box model simulations revealed that the IEPOX and limonene chemistry strongly enhance the formation of low volatile organic compounds during the day. The new isoprene-NO_3 mechanism shows no obvious effect on LVOC concentrations.
Global model simulations confirm the expectations. In particular, the tetrols and organic sulfates of IEPOX are abundant in hydrophilic secondary organic aerosols, cloud and rain droplets. PM2.5 concentrations in the eastern US show an improved correlation to data of observation stations. However, the model underpredicts total organic aerosols as well as secondary organic aerosols in all simulations. This can be attributed to the emissions (no nudging), the model resolution, but also to VOCs from biomass burning, which are not yet considered in the chemical scheme. Overall, the mechanistic update was successful in influencing not only the secondary organic aerosol mass and constituents, but also the gas-phase mixing ratios.

6.2 Phase partitioning between gas and aqueous phase

The partitioning of gas-phase species to hydrophilic and hydrophobic phases is of central importance for secondary organic aerosols. The addition of new compounds to MESSy's chemical scheme requires knowledge not only of the chemical processing but also of the phase behavior of the compounds. For the condensation of organics on hydrophobic organic aerosols, MESSy includes an estimation scheme to assess the saturation mass concentrations of a given compound based on the elemental composition. On the other hand, partitioning to hydrophilic phases requires Henry's law constants, which must be obtained from sources outside of the model. Considering the size of the added chemical mechanism ($\sim$ 300 reactions) and new products, collecting the required partitioning constants is demanding. These Henry's law constants cannot be obtained from literature measurements because lesser known or intermediate species have not been examined. Therefore, estimation methods are applied to obtain the constants. In this work, the GROMHE and HenryWIN methods have been compared. No clear preference for one of the estimation schemes was found. Due to the advantages of the GROHME method found in the literature, it was selected to be applied in this work. Henry's law constants were estimated for all new and a selection of established compounds.
Depending on the chemical structure of the molecule, Henry's law constants may show little to strong variation with temperature. For some organics, this behavior has already been considered in MESSy. Given the importance of the partitioning constants for hydrophilic

secondary organic aerosols, cloud and rain droplets, the temperature dependence has been extended to cover all organics. Similar to Henry's law constants, this requires a reasonably accurate estimation method. Kühne et al. [2005] developed a group contribution method to predict the thermal changes in the gas-aqueous partitioning. This method was extended in this work to cover the hydroperoxide moiety and then applied to the molecules in the model.
The effects of the new Henry's law constants and temperature dependencies were assessed in box model tests and global model simulations. The box model simulations demonstrated the magnitude of the dependence of model results on partitioning coefficients. The application of an alternative estimation approach based on saturation vapor pressure and infinite dilution activity coefficients resulted in a significant reduction of the organic concentration in the aqueous phase. The exclusion of the inferred temperature dependency resulted in a change in the product distribution in low volatile organic compounds. In global simulation, the analysis of the global annual O/C ratio of hydrophilic secondary organic aerosol displayed further effects of the updated partitioning. O/C ratios are strongly decreased, especially in rural areas far from the emission sites. This is due to the new temperature dependence of the Henry's law constants. In particular small organics are strongly affected. This in turn affects the oxidant concentrations, leading to a significant correction of the ozone mixing ratios.

6.3 Aqueous-phase oxidation

The processing of organics in deliquescent aerosols, cloud and rain droplets is expected to impact the secondary organic aerosol mass and composition. To improve the aqueous-phase oxidation in the MESSy model, an aqueous-phase oxidation mechanism generator has been built in this work. It is capable of reading molecules from MESSy's kinetic model and automatically generates a collection of mechanisms based on the input. Alternatively, mechanisms can be generated by the input of SMILES strings. The generator considers H-abstractions by OH, OH-additions, hydrolysis of tertiary nitrates, photolysis of predefined molecular fragments, and radical reactions of peroxy radicals (alkoxy radicals are not explicitly considered). The information required for the reaction classes is taken from literature SARs, experimental data, or previously used rate constants in MESSy. Currently, the generator is limited to mechanisms that start and end with molecules that are established in the model and have a partitioning constant. This ensures the correct partitioning in the model and prevents accumulation. Nevertheless, the current setup can be applied to compounds that are implemented in future adaptations of the kinetic model. As a result, the generator not only influences the aqueous-phase chemistry of the current, but can also be applied to future simulations.
Global model simulations display a decrease in secondary organic aerosol mass with the additional aqueous oxidation reactions from the generator. This result confirms the ex-

pectations, although it has a smaller influence compared to the newly implemented VOC reactions. In contrast, the differences in chemical composition induced by the aqueous oxidation in hydrophilic secondary organic aerosols and also in cloud and rain droplets are larger than previously expected. The O/C ratio of the all organics in hydrophilic SOA displays changes by up to one O/C unit. In the simulation without the aqueous oxidation (MOM), isoprene oxidation products (tetrols and organic sulfates) were among the dominant contributors to hydrophilic secondary organic aerosols in continental regions. The introduction of the aqueous oxidation mechanism led to a strong decline in isoprene products. Monoterpene oxidation products of later generations increase in importance. Organic aerosol properties such as hygroscopicity and the aerosol phase state are influenced by the chemical composition. However, the analysis of these properties is beyond the scope of this work. The results of the PM2.5 station comparison are not significantly affected by the generated reactions.

6.4 Outlook

The results of this work indicate that significant progress has been made in the representation of hydrophilic SOA, but further investigation is needed to improve the representation of secondary organic aerosol in the model. Volatile organic compounds emitted during biomass burning events are still missing in the kinetic scheme. Studies have shown that they contribute to the secondary organic aerosol burden. This includes the chemical processing of levoglucosan, but also of large aromatics. The oxidation of n-alkanes needs to be extended to obtain realistic secondary organic aerosol concentrations. This will help to improve the secondary organic aerosol yield from emissions of diesel vehicles. Additionally, the oxidant levels in global model simulations need to be evaluated with a detailed formation and loss budget. Realistic oxidant levels are important for all chemical processes in the model.

Phase partitioning remains to be a relevant issue in the formation and loss of secondary organic aerosols. In this work, the partitioning between gas and aqueous phase was the main focus. However, the modeled organic mass in hydrophobic secondary organic aerosol is two times larger than in hydrophilic SOA. The Henry's law partitioning scheme operates on a kinetic basis and contains temperature-dependent partitioning constants. The partitioning to the organic phase, e.g. by condensation, is simplified and only considers the elemental composition of a specific molecule. It is also assumed that the thermodynamic equilibrium between the gas and the organic phase is established within one time step. The kinetics behind this process are neglected. In future developments, both partitioning schemes should be adapted to a comparable degree of complexity. Henry's law constants based on vapor pressure and infinity dilution activity coefficients have already been applied in this study. This lays the foundation for the application of Henry's law constants in more than just the aqueous phase. If the partitioning is sufficiently detailed, issues such as phase separation

can also be addressed. The potential impact of partitioning on organic aerosols, oxidant concentrations, and the oxidation of volatile organic compounds has been demonstrated in this work.

In the final part of this thesis, a mechanism generator for aqueous-phase oxidation reactions has been developed and applied. It already displays a remarkable impact on the aqueous-phase constituent mixture. Nevertheless, limitations in the generator scheme affect the results. Currently, compounds such as organic sulfates and ethers/esters are not considered by the generator. This is due to knowledge gaps in their contribution to rate constants. These molecule classes have significant concentrations in the aqueous phase, indicating the need for chemical processing. In addition, the dynamic estimation of Henry's law constants is required in the generator script, to ensure the correct partitioning of products and intermediates. This circumstance currently restricts the generated mechanisms to reaction schemes that start and end with molecules that already have a partitioning constant in MESSy. Furthermore, the generated reactions and the MESSy kinetic scheme in general would benefit from dynamic mechanism reduction techniques.

Chapter 7

Appendix

7.1 Additional simulation results

7.1.1 Box model

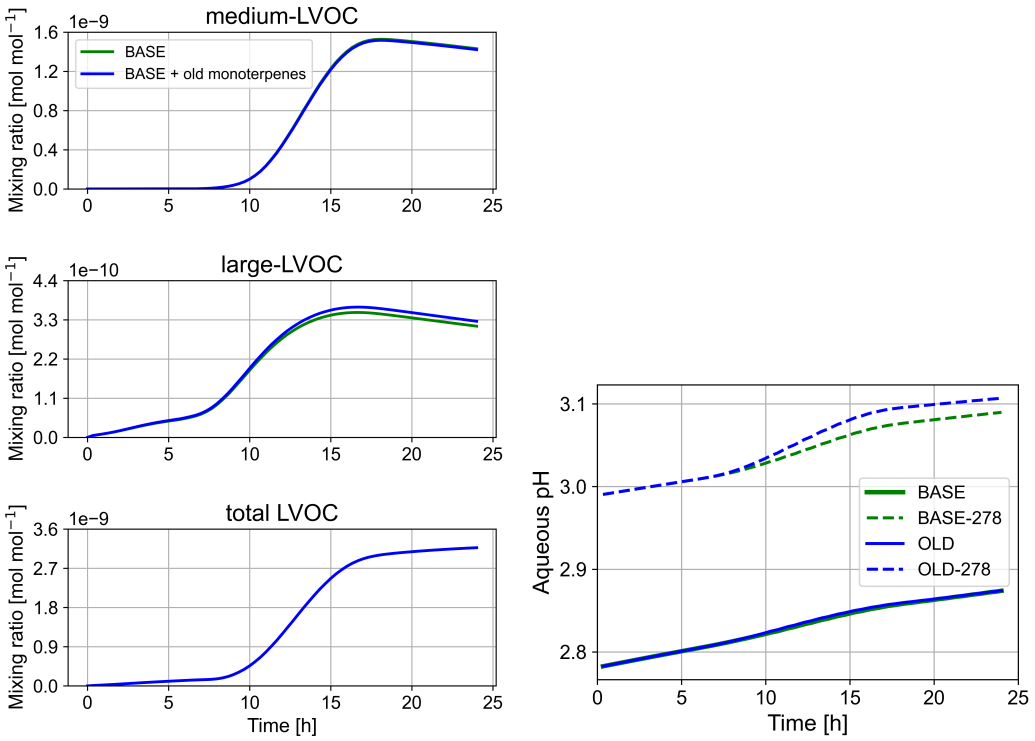

(a) OA with old monoterpenes **(b)** pH aqueous phase

Figure 7.1: Potential effect of the excluded monoterpenes (a) and change in the liquid phase pH in the OLD and BASE simulations (b).

7.1.2 Global model

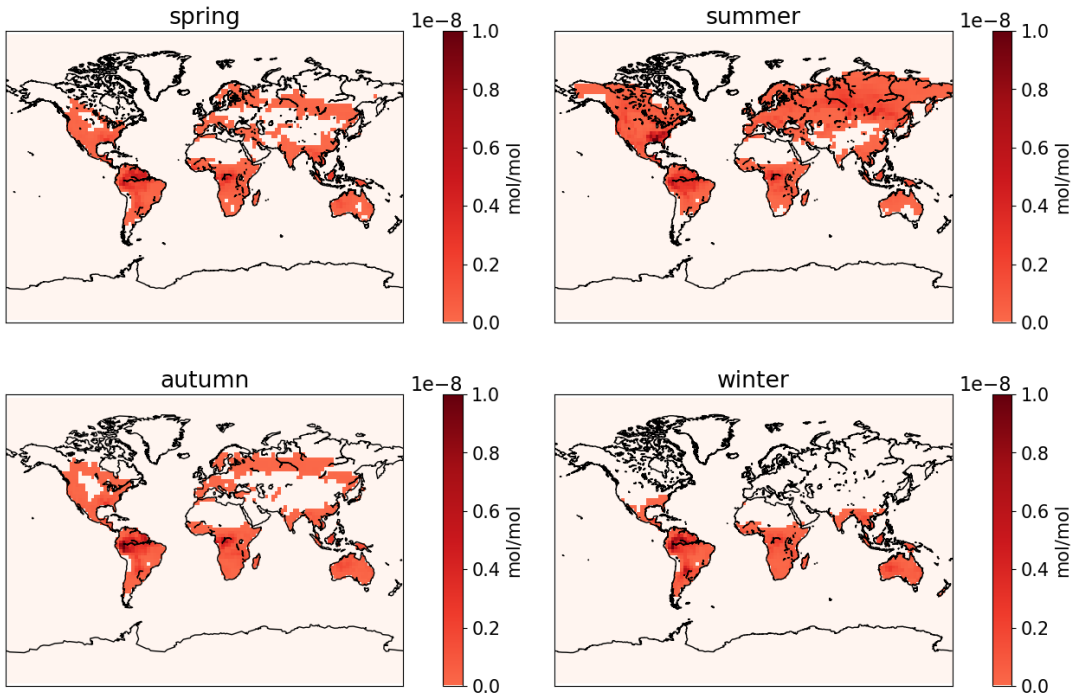

Figure 7.2: Mean seasonal ground-level isoprene concentration in the MOM simulation.

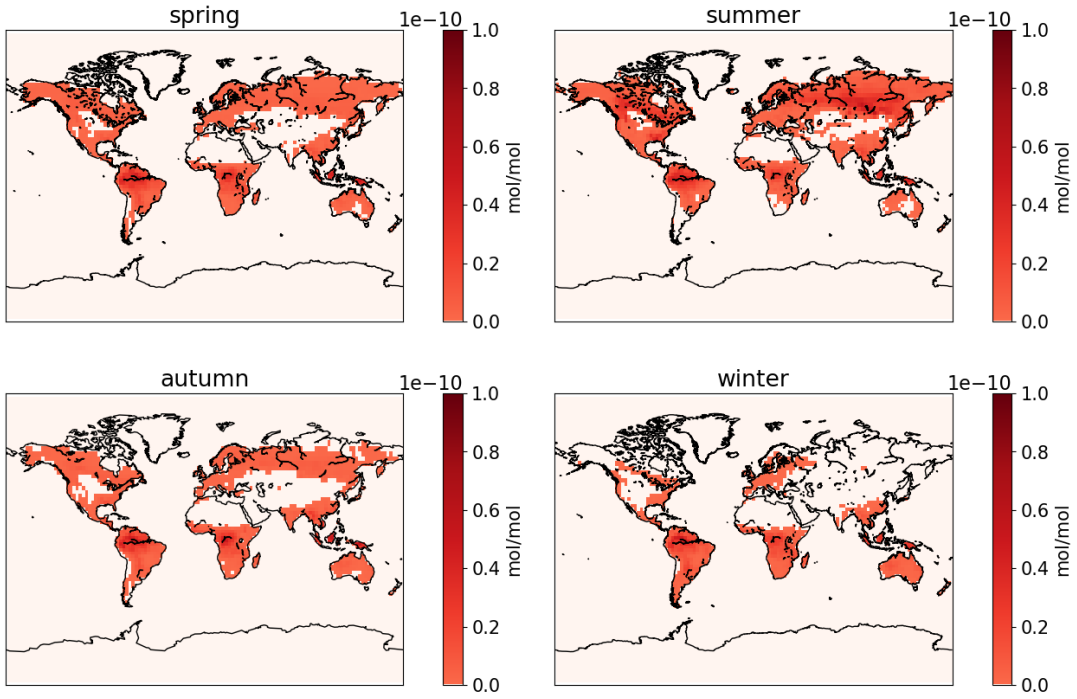

Figure 7.3: Mean seasonal ground-level limonene concentration in the MOM simulation.

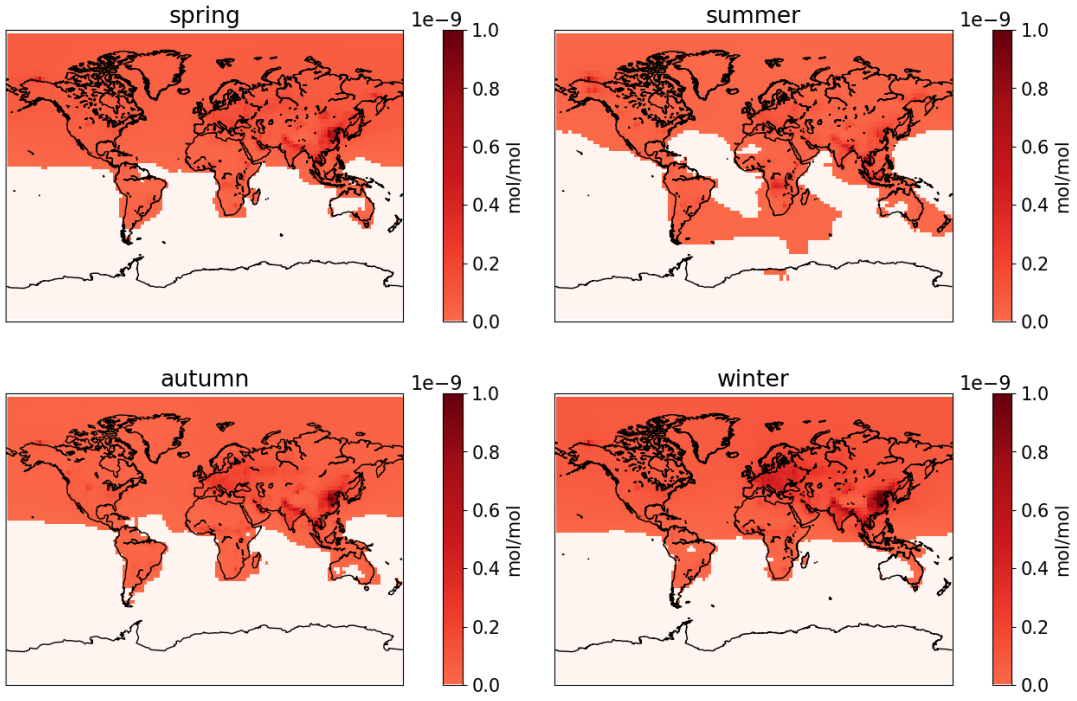

Figure 7.4: Mean seasonal ground-level benzene concentration in the MOM simulation.

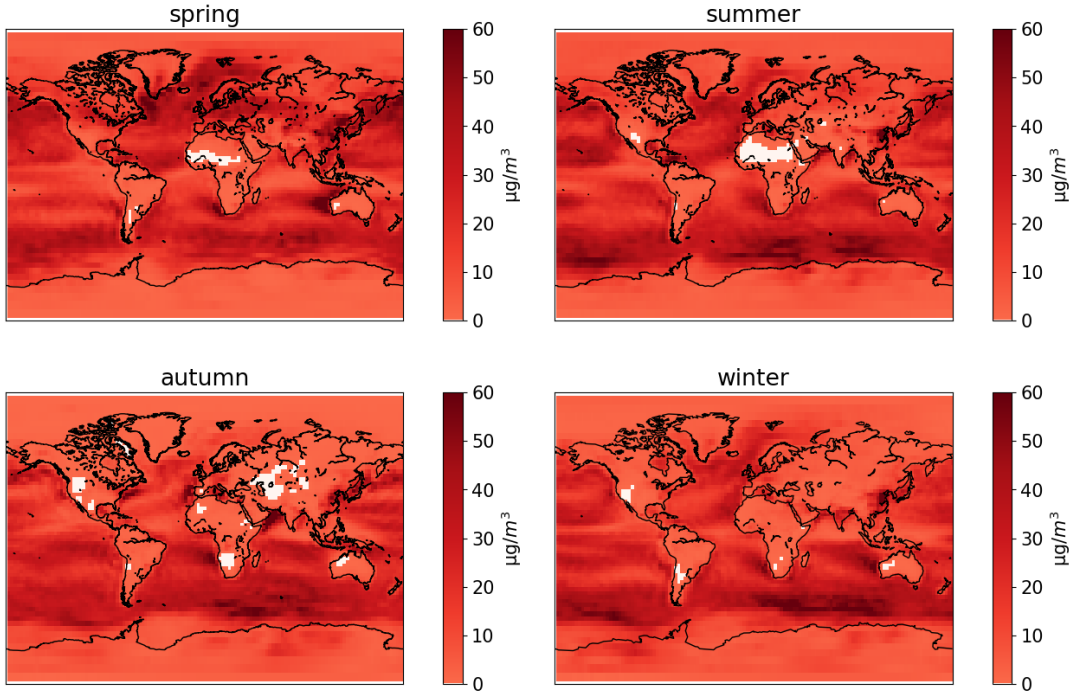

Figure 7.5: Mean seasonal ground-level organic aerosol water concentration in the POZ simulation.

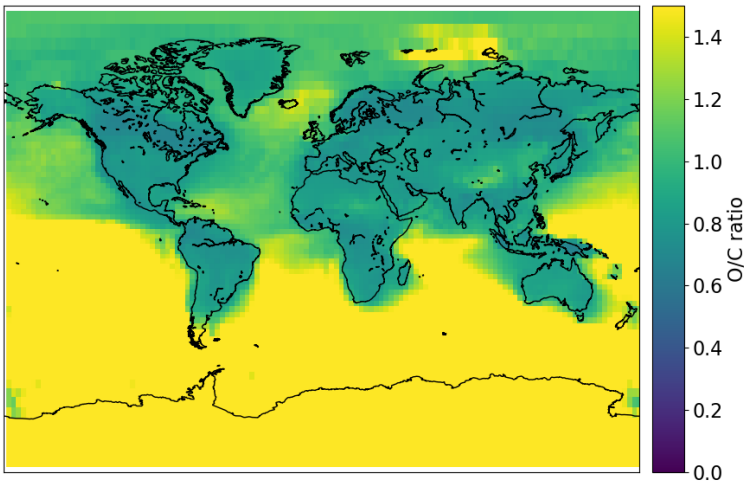

Figure 7.6: Annual average ground-level O/C ratio in hydrophilic SOA in the MOM+ simulation. Note that organic sulfates are not considered in the O/C ratio calculation.

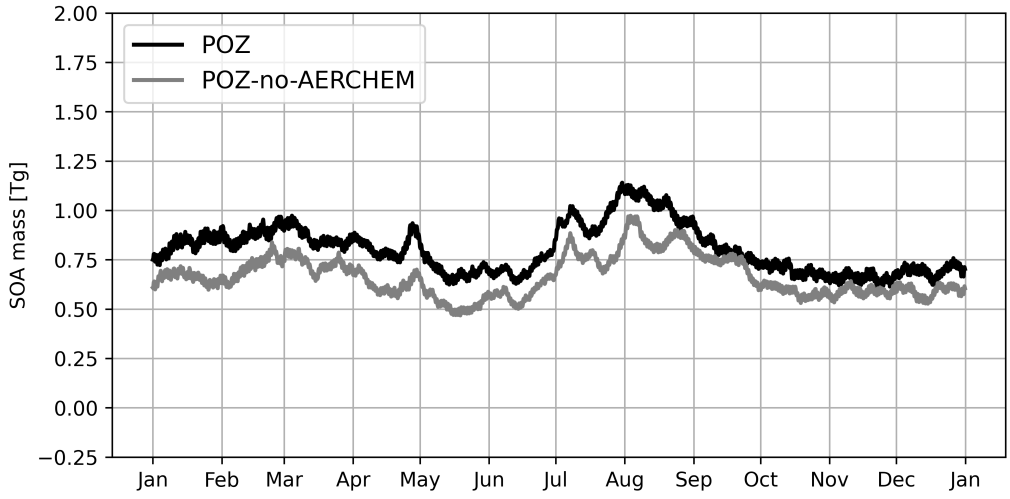

Figure 7.7: SOA burden in the POZ simulation compared to the same simulations setup with deactivated AERCHEM subsubmodel.

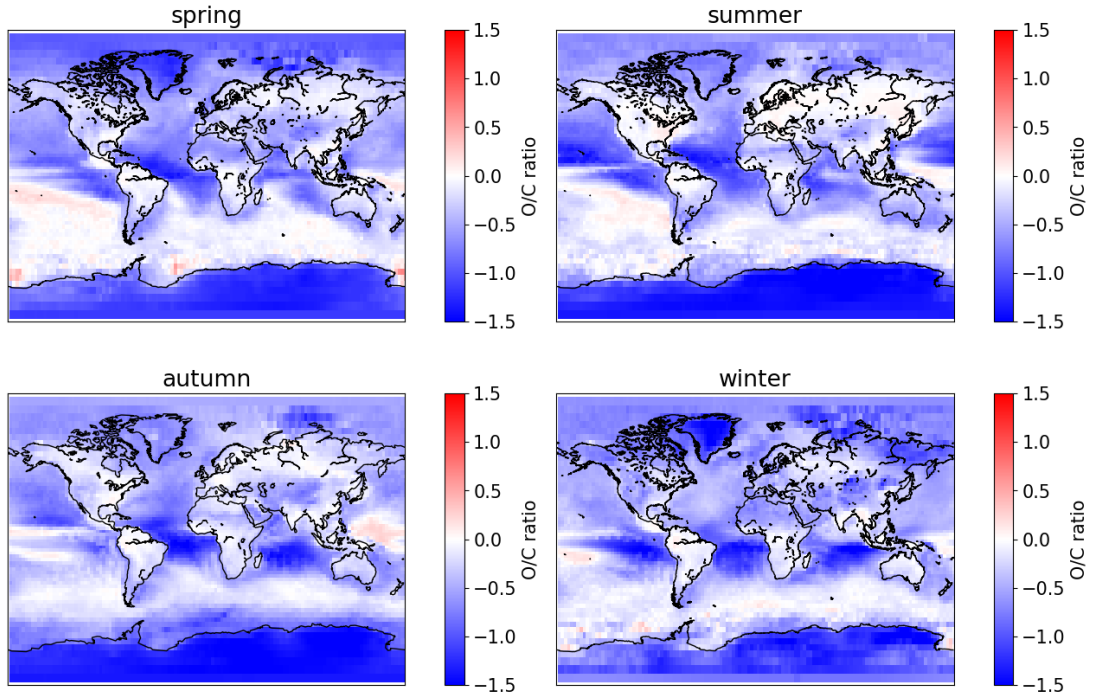

Figure 7.8: Seasonal difference between the ground-level O/C ratio in hydrophilic SOA between the MOM and POZ simulation

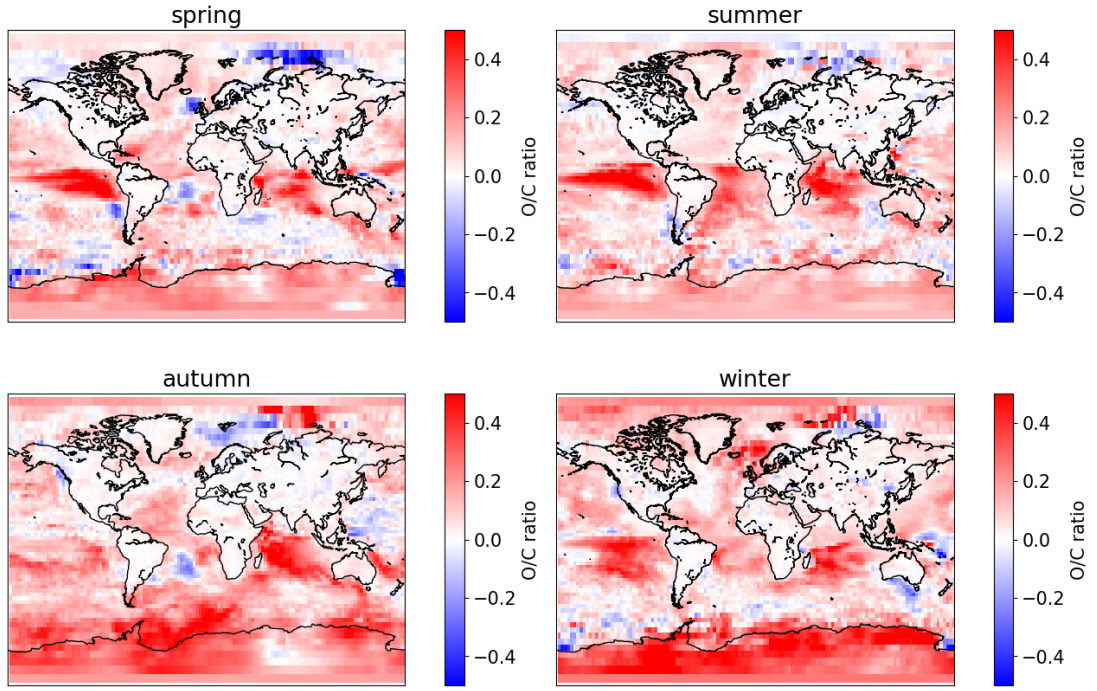

Figure 7.9: Seasonal difference between the ground-level O/C ratio in hydrophilic SOA between the MOM+ and MOM simulation

7.2 Estimated Henry's law solubility constants and temperature dependencies

The Henry's law constant tables in this section were previously published in Wieser et al. [2024].

Table 7.1: Newly implemented Henry's law solubility constants H_s estimated by GROMHE, and the temperature-dependence factor $B = \mathrm{d}\ln H_s/\mathrm{d}(1/T)$ calculated with the method of Kühne et al. [2005]. Compounds are characterized by their SMILES string and InChIKey. Only the first block of the InChIKey is shown in the table. As we do not consider stereochemistry here, the last part of the InChIKey is always "-UHFFFAOYSA-N" (excluded for better readability).

compound	SMILES	InChIKey	H_s / M/atm	$\mathrm{d}\ln H_s/\mathrm{d}(1/T)$ / K
IEPOX + OH				
IEPOXO4 (LIEPOXO)	CC1(CO)OC1C=O	DNQIATHBSKHPLN	2.1E6	13700
DIEPOXO3 (LDIEPOXO)	CC1(C(=O)CO)CO1	QGQUFAZKBSHWQB	1.3E5	13700
IEPOX1CO3H (LIEPOXCO3H)	CC1(C(=O)OO)OC1O	DJPWYFXNRMHUNU	9.1E4	14400
ME1TRIOL (LTRIOL)	C(O)C(O)C=C(C)(O)	MTMASQITBHTGFW	4.9E9	11100
METHFDIOL	C1C(O)-O-C(O)C1(C)	UNAIOYXCADSMDR	9.1E7	10900
MEBUTETROL	C(O)C(O)C(C)(O)C(O)	HGVJFBSSLICXEM	6.2E12	13600
METRICO	C(O)C(C)(O)C(=O)C(O)	LCGBCDAYKOJPSO	7.4E8	11500
MEDICO4CO	C(=O)C(C)(O)C(=O)C(O)	GXKSWJOBVXKANI	3.1E8	12100
MEDICO1CO	C(=O)C(=O)C(O)(C)C(O)	RRXXDUUNVWXRFN	2.5E9	12100
Isoprene + NO_3				
ISOP1N4OOH (E/Z)	C/C(=C\COO)CON(=O)=O	IRFXVIPRKCCSLU	9.8E4	11400
ISOP1N4ONO2 (E/Z)	C/C(=C\CON(=O)=O)CON(=O)=O	JGJBVRGABXKDRR	2.6E2	9400
HC4CCHO (LHC4ACCHO)	CC(=CCO)C=O	GCHJBJOOADXJFT	1.2E5	10600
EPXISOPNONO2	CC(CON(=O)=O)(ON(=O)=O)C1CO1	UAFKAIYDADHRMX	5.4E3	12500
ISOP1N5ONO2	O=N(=O)OC/C(=C\CO)CON(=O)=O	WRGRJJOKHABEJT	5.9E6	13300
ISOP1N5OOH	O=N(=O)OC/C(=C/CO)COO	LLNBZHMZWYQLAS	2.3E9	14300
ISOP1N6CO	O=C/C(=C\CO)CON(=O)=O	XXORYENTKCFFSM	2.1E7	14000
ISOP1N2ONO2	C=CC(C)(CON(=O)=O)ON(=O)=O	FQSKJUXVWIFNKX	1.6E2	9400
ISOP1N23O4CO (LISOP1N23O4CO)	CC1(CON(=O)=O)OC1C=O	WBVYILWVTRBTDJ	1.5E5	12400
ISOP1N23O4ONO2 (LISOP1N23O4ONO2)	CC1(CON(=O)=O)OC1CON(=O)=O	FSZUIXLMCRZJMS	4.6E3	12500
Large Alkanes + OH				
C5H112ONO2	CC(ON(=O)(=O))CCC	RWRBSYOTDDOXKC	3.4E-1	6000
C5H112O2H	CC(OO)CCCCC(OO)CCC	AXIHYONNAPPFSO	1.4E2	7000
C5OHONO2	C(ON(=O)(=O))CCC(O)C	RIQPKERROQFFJK	2.1E3	9900
C5OHOOH	C(OO)CCC(O)C	GSRFGQMXWRCOMF	7.2E5	10900
C5OHCO	C(O)CCC(=O)C	JSHPTIGHEWEXRW	3.6E5	9800
C6H13ONO2	CC(ON(=O)(=O))CCCC	JLGBOJJVQLNMGV	3.1E-2	6300
C6H13O2H	CC(OO)CCCC	XWXUHAUZCICPHE	1.0E2	7300
C6OHONO2	CC(ON(=O)(=O))CCC(O)C	PAWWQEMXBSLVJC	1.6E3	10200
C6OHOOH	CC(OO)CCC(O)C	BVOYWPYSMMRYPX	5.5E5	11200
C6OHCO	CC(O)CCC(=O)C	ZSDLLTJVENEIDW	2.8E5	10100

Table 7.1: Newly implemented Henry's law constants estimated by GROMHE, and the temperature-dependence factor $B = \mathrm{d}\ln H_\mathrm{s}/\mathrm{d}(1/T)$ calculated with the method of Kühne et al. [2005]. Compounds are characterized by their SMILES string and InChIKey Only the first block of the InChIKey is shown in the table. As we do not consider stereochemistry here, the last part of the InChIKey is always "-UHFFFAOYSA-N" (excluded for better readability). (continued)

compound	SMILES	InChIKey	H_s / M/atm	$\mathrm{d}\ln H_\mathrm{s}/\mathrm{d}(1/T)$ / K
Large Alkanes + OH				
C7H15ONO2	CC(ON(=O)(=O))CCCCC	HHXLSUKHLTZWKR	2.3E-1	6600
C7H15O2H	CC(OO)CCCCC	FWELUXZVATZEMI	7.8E1	7600
C7OHONO2	CCC(ON(=O)(=O))CCC(O)C	MZJHMUSTUUJGSJ	1.2E3	10600
C7OHOOH	CCC(OO)CCC(O)C	KHWIBANUCNWWGW	4.2E5	11600
C72CO5OH (LC7OHCO)	CCC(O)CCC(=O)C	MQRALIJAASQPNT	2.1E5	10500
C8H17ONO2	CC(ON(=O)(=O))CCCCCC	QCOKASLKYUXYJH	6.9E2	7000
C8H17O2H	CC(OO)CCCCCC	NAXZMRYIZGEALQ	5.9E1	8000
C8OHONO2	CCCC(ON(=O)(=O))CCC(O)C	UEQWMROPIQKFIM	9.1E2	10900
C8OHOOH	CCCC(OO)CCC(O)C	QQTSMKQYSKGCOU	3.2E5	11900
C82CO5OH (LC8OHCO)	CCCC(O)CCC(=O)C	KZPPEBIAPHLFQD	1.6E5	10800
Limonene				
HOC2H4CHO	O=CCCO	AKXKFZDCRYJKTF	3.6E3	9900
C517OOH	CC(=O)C(CO)COO	OAFCGFSFCVGKSH	1.1E8	13400
HMVKBCHO	CC(=O)C(C=O)CO	XYGGNMZYIGPNCC	3.6E7	10800
CO2C4CHO	CC(=O)CCC=O	KEHNRUNQZGRQHU	5.6E4	8400
C519OOH	CC(=O)C(CCO)OO	RDSFTYTWLRHJGZ	1.7E7	13400
C517CHO	CC(=O)C(CO)CC=O	JGHPNZFTVGSLKF	9.6E4	12700
C622OOH	C=C(C)C(CO)COO	GWTGWFHICNOSTQ	1.3E6	12000
C519CHO	CC(=O)C(C=O)CCO	PVAHQKAVPKMXGV	2.8E8	11100
C622ONO2	C=C(C)C(CO)CON(=O)=O	UCAFMJJTBHTENA	3.5E3	11000
C622CHO	C=C(C)C(CO)CC=O	JWVBPJJNIHELFZ	5.9E5	11300
C728OOH	CC(CO)(OO)C(CO)CC=O	WJYXJQPIZCIBJO	5.4E12	18100
C727OOH	CC(=O)CCC(OO)C(C)=O	IMCLYNFQESJQRO	2.0E7	12700
C624CHO	C=C(C)C(C=O)CCO	AIMYSSDKEKDSEU	5.9E5	11300
C730OOH	CC(CO)(OO)C(C=O)CCO	YXKHJQXHKYJCPI	6.2E12	18100
C728ONO2	CC(CO)(ON(=O)=O)C(CO)CC=O	CDBHNFBQKSTCON	1.5E10	17100
C622CONO2	C=C(C)C(CO)CC(=O)ON(=O)=O	DJCVHBPUJHAWIU	1.0E5	13900
C730ONO2	CC(CO)(ON(=O)=O)C(C=O)CCO	RVWIAVBELSCRER	3.5E11	17100
C818CO	CC(=O)C(=O)CC(CO)C(C)=O	CRQAGKNTHDNGEW	6.6E8	15900
C816CO	C=C(C)C(=O)CCC(C)=O	FXXXYZSMIIVJDG	3.1E4	10200
C819OOH	CC(=O)CCC(=O)C(C)(CO)OO	JRXMSSDNDAZISI	2.1E9	17000
C817CO	CC(=O)CCC(C=O)C(C)=O	WSCYQCAMZDXSLH	3.1E7	12000
C817OOH	CC(=O)CCC(COO)C(C)=O	WQMXPSRLZZCZTO	1.2E8	13000
C818OOH	CC(=O)C(CO)CC(OO)C(C)=O	DLMBPALZQHFDOH	5.8E10	17000
C729CHO	C=C(C)C(CC=O)CC=O	MEGRLTONSLAOOM	8.1E4	10200
C822OOH	C=C(C)C(CC=O)CCOO	XWYULULFGKWPMD	8.9E5	11300

Table 7.1: Newly implemented Henry's law constants estimated by GROMHE, and the temperature-dependence factor $B = \mathrm{d}\ln H_\mathrm{s}/\mathrm{d}(1/T)$ calculated with the method of Kühne et al. [2005]. Compounds are characterized by their SMILES string and InChIKey Only the first block of the InChIKey is shown in the table. As we do not consider stereochemistry here, the last part of the InChIKey is always "-UHFFFAOYSA-N" (excluded for better readability). (continued)

compound	SMILES	InChIKey	H_s / M/atm	$\mathrm{d}\ln H_\mathrm{s}/\mathrm{d}(1/T)$ / K
Limonene				
C824OOH	C=C(C)C(CCO)C(C=O)OO	FGEKWAMEWUMQIL	8.5E8	15300
RO5R5	CC(C)(OC=O)C(CO)CC=O	MESHXYGXEHAFFE	1.3E7	17300
C819ONO2	CC(=O)CCC(=O)C(C)(CO)ON(=O)=O	XLUWXWLWQTYVOF	4.0E8	16000
C817ONO2	CC(=O)CCC(CON(=O)=O)C(C)=O	ZONZWPKPCIWKRN	4.0E6	12000
C822ONO2	C=C(C)C(CC=O)CCON(=O)=O	JWAJNALJDDSHOA	2.9E3	10300
C824ONO2	C=C(C)C(CCO)C(C=O)ON(=O)=O	YMYILPYDFNRVBZ	9.6E8	14300
C923OOH	C=C(C)C(CCC(C)=O)COO	ZSCOJLRNNZZYOH	1.1E6	11700
C923OH	C=C(C)C(CO)CCC(C)=O	VZYSLJNPEGILSI	5.4E5	12000
NORLIMAL	C=C(C)C(C=O)CCC(C)=O	WPNOYHDEEVPEJH	6.2E4	10600
C924OOH	C=C(C)C(CO)CC(OO)C(C)=O	BVODBOGLMHSHGK	3.0E8	15600
C924OH	C=C(C)C(CO)CC(O)C(C)=O	OXSRPARPRXNCEH	3.8E7	15900
LMLKET	CC(=O)CCC(CC=O)C(C)=O	CWEQHJLFCKMWEE	1.1E8	13000
LIMKET	CC1=CCC(C(C)=O)CC1	HOBBEYSRFFJETF	6.5E1	8000
C817CO3H	CC(=O)CCC(CC(=O)OO)C(C)=O	NVOUBBWYYUIRJW	3.4E9	15900
C822CO3H	C=C(C)C(CC=O)CCC(=O)OO	DRDXOQWGQPPQFG	1.7E6	14200
C822CO2H	C=C(C)C(CC=O)CCC(=O)O	ADULCIYKWVJSFE	4.5E6	14500
C91ONO2	C=C(C)C(CCC(C)=O)CON(=O)=O	JEWJQSHMOKPQHI	3.2E3	10700
NORLIMONO2	CC(=O)CCC(C=O)C(C)(CO)ON(=O)=O	MUTWZANDXPDWFF	3.8E10	16300
C92ONO2	C=C(C)C(CO)CC(ON(=O)=O)C(C)=O	PNFDSIMYWKOAKE	4.8E7	14600
C817CONO2	CC(=O)CCC(CC(=O)ON(=O)=O)C(C)=O	LHFXXFGIVAQFTO	1.2E7	14900
C822CONO2	C=C(C)C(CC=O)CCC(=O)ON(=O)=O	RVFLVBTUEWAABB	6.3E3	13200
BPINCOOH (LABPINCOOH)	CC1=CCC(C(C)(CO)OO)CC1	VVHMRXSQYYKNLC	3.6E6	13400
RO5R1O2H	CC1(C)OC2CC1CCC2(CO)OO	NSOHXIGSWKLSHV	1.0E8	16600
RO5R2O2H	CC1(C)OC(OO)CC1CCC(=O)CO	MFXJOKCSTDMZRM	1.8E9	19100
RO5R3O2H	CC(C)(OC=O)C(CCC(=O)CO)COO	IEPFJXDIWPQIRC	7.8E9	21600
RO5R4O2H	CC(C)(OC=O)C(CO)CC(OO)C(=O)CO	YORZXZYHORHTRW	3.6E12	24000
C923CO3H	C=C(C)C(CCC(C)=O)CC(=O)OO	JSHGCXGTVADTAK	2.2E6	14500
LIMONONIC	C=C(C)C(CCC(C)=O)CC(=O)O	NJOIWWRMLFSDTM	5.8E6	14900
LIMAL	C=C(C)C(CC=O)CCC(C)=O	OGCGCISRMFSLTC	4.1E4	10900
LIMALOOH	CC(=O)CCC(CC=O)C(C)(CO)OO	OQLBLHLZVAPRGN	4.4E12	17700
LIMALOH	CC(=O)CCC(CC=O)C(C)(O)CO	ISUQULRVPDSRIP	2.2E12	18000
LIMALAOOH	C=C(C)C(CC=O)CC(OO)C(C)=O	DVORBFWFCUOYLW	2.5E7	14500
LIMALAOH	C=C(C)C(CC=O)CC(O)C(C)=O	VNYSFQVUCPNMDZ	3.1E6	14900
LIMALACO	C=C(C)C(CC=O)CC(=O)C(C)=O	OXUPJDFJWCMZMO	4.4E6	13400
LIMALBOOH	C=C(C)C(CC=O)CCC(=O)COO	DCWLKDSHBWMMQU	2.4E7	14500
BPINCONO2 (LABPINCONO2)	CC1=CCC(C(C)(CO)(ON(=O)(=O)))CC1	ZELLOEPLERCREX	8.7E3	18800

Table 7.1: Newly implemented Henry's law constants estimated by GROMHE, and the temperature-dependence factor $B = \mathrm{d}\ln H_\mathrm{s}/\mathrm{d}(1/T)$ calculated with the method of Kühne et al. [2005]. Compounds are characterized by their SMILES string and InChIKey Only the first block of the InChIKey is shown in the table. As we do not consider stereochemistry here, the last part of the InChIKey is always "-UHFFFAOYSA-N" (excluded for better readability). (continued)

compound	SMILES	InChIKey	H_s / M/atm	$\mathrm{d}\ln H_\mathrm{s}/\mathrm{d}(1/T)$ / K
Limonene				
C9CONO2	C=C(C)C(CCC(C)=O)CC(=O)(ON(=O)(=O))	FNVMVXZLPDKVAS	8.1E3	19900
LIMALONO2	CC(=O)CCC(CC=O)C(C)(CO)(ON(=O)(=O))	FDBNDHKWTKEDSC	1.3E10	23000
LIMONO2	C=C(C)C(CC=O)CCC(=O)CON(=O)=O	DEKWHDOXDJNWRD	3.9E6	13500
LIMAB15ONO22 (LLIMABONO22)	CC(CO)(ON(=O)=O)C1CCC(C)(ON(=O)=O)C(O)C1	UNHNJOVXNACOSQ	3.1E9	18200
LIMAB15ONO2OOH (LLIMABONO2OOH)	CC(CO)(OO)C1CCC(C)(ON(=O)=O)C(O)C1	JBKULLYZCMWERK	5.1E11	19200
LIMAB15OOH2 (LLIMABOOH2)	CC(CO)(OO)C1CCC(C)(OO)C(O)C1	IRUZCTPAAZATQM	2.3E14	20200
LIMAB1ONO2 (LLIMABONO2)	C=C(C)C1CCC(C)(ON(=O)=O)C(O)C1	LZDKYYHMAURBIK	8.5E3	12400
LIMAB1OOH (LLIMABOOH)	C=C(C)C1CCC(C)(OO)C(O)C1	FPMDSGWWEURSNO	3.6E6	13400
ROO6R1ONO2	CC1(CO)OOC2CC1CCC2(C)ON(=O)=O	JOFCABYMPNXMIS	1.4E4	15200
ROO6R1OOH	CC1(CO)OOC2CC1CCC2(C)OO	GBBPAXKBVMQHIG	6.9E6	16300
ROO6R5ONO2	CC(=O)CCC(CC(=O)ON(=O)=O)OO	LNWOWXJMUJHMJJ	1.7E7	15300
ROO6R5OOH	CC(=O)CCC(CC(=O)OO)OO	RAASFOSVQCCDRJ	4.7E9	16300
ROO6R6ONO2	CC(=O)CCC(CON(=O)=O)OO	CRECMHNOVVIMCR	6.2E7	12400
ROO6R6OOH	CC(=O)CCC(COO)OO	QZPUZDFJKAEVLL	2.6E10	13500
ROO6R7ONO2	CC(=O)CCC(CO)ON(=O)=O	COKJDYWOSQONMU	7.6E6	12800
ROO6R7OOH	CC(=O)CCC(CO)OO	UPAWKBDHGPWUCG	3.3E9	13800
C52COCONO2	CC(=O)CCC(=O)ON(=O)=O	QJXLMYNMVOSKND	6.8E3	11000
C52COCO3H	CC(=O)CCC(=O)OO	COVHHGSUFOHLBW	1.9E6	12000
C624ONO2	C=C(COO)C(CO)(CO)ON(=O)=O	XYBUKFJLXVIRLY	2.0E12	18600
C518OOH	C=C(COO)C(=O)CO	PQEISBQMLHJHJQ	4.2E6	14200
C624OOH	C=C(COO)C(CO)(CO)OO	FUTSLQULSAKEJA	1.2E15	19600
C520ONO2	O=C(CO)C(CO)(COO)ON(=O)=O	ZSADVAXZKGJKSG	2.9E11	20800
BIACETOH2	O=C(CO)C(=O)CO	GJCZUCLKDGABDS	2.1E8	16700
C520OOH	O=C(CO)C(CO)(COO)OO	GRPDYNZWDDUILX	5.4E13	21800
Glyoxal oligomers				
GOLIG1	O=CC(O)-O-C(O)C=O	LEKXYOUPWKVTGM	1.5E14	18700
GOLIG2	O=CC(O)-O-C(O)C(O)O	GWSRJJGBNXJVPO	1.5E17	24000
GOLIG3	OC(O)C(O)-O-C(O)C(O)O	ADECTKUVLJSMDK	3.8E20	28600
Methyl glyoxal oligomers				
MGLYOXDA	CC(=O)C(O)-O-C(O)C(=O)C	QMSLRDMQAWWKIZ	2.0E10	15500
MGLYOXDB	CC(=O)C(O)-O-C(O)(C)C(O)(O)	IUHMFBWAUOLAFM	1.5E15	22400
MGLYFA	CC(=O)C(=O)-O-C(O)C(=O)C	NOUUUBJIFPBZMZ	4.5E6	15600
MGLYFB	CC(=O)C(=O)-O-C(O)(C)C(O)(O)	UCPBJDKPOQEXSQ	7.2E10	22500

7.3 Subset of the estimated saturation vapor pressures and infinity dilution activity coefficients

Table 7.2: Collection of a subset of the estimated saturation vapor pressures and infinity dilution activity coefficients for water as solvent. As we do not consider stereochemistry here, the last part of the InChIKey is always "-UHFFFAOYSA-N" (excluded for better readability). Note that the infinity dilution activity coefficients is in the natural logarithmic representation. This is done for better comparison to literature results.

compound	SMILES	InChIKey	p^* / Pa	$ln(\gamma^{\infty}_{H_2O})$
IEPOX + OH				
IEPOXO4 (LIEPOXO)	CC1(CO)OC1C=O	DNQIATHBSKHPLN	3.11E+1	1.46E+00
DIEPOXO3 (LDIEPOXO)	CC1(C(=O)CO)CO1	QGQUFAZKBSHWQB	5.28E+1	9.98E-01
IEPOX1CO3H (LIEPOXCO3H)	CC1(C(=O)OO)OC1O	DJPWYFXNRMHUNU	1.14E-1	7.72E-01
ME1TRIOL (LTRIOL)	C(O)C(O)C=C(C)(O)	MTMASQITBHTGFW	1.32E-3	9.86E-01
METHFDIOL	C1C(O)-O-C(O)C1(C)	UNAIOYXCADSMDR	3.52E+0	-2.12E-01
MEBUTETROL	C(O)C(O)C(C)(O)C(O)	HGVJFBSSLICXEM	6.18E-4	-9.21E-01
METRICO	C(O)C(C)(O)C(=O)C(O)	LCGBCDAYKOJPSO	2.76E-2	-1.16E+00
MEDICO4CO	C(=O)C(C)(O)C(=O)C(O)	GXKSWJOBVXKANI	1.19E+1	7.63E-01
MEDICO1CO	C(=O)C(=O)C(O)(C)C(O)	RRXXDUUNVWXRFN	3.26E+0	9.63E-01
Isoprene + NO_3				
ISOP1N4OOH (E/Z)	C/C(=C\COO)CON(=O)=O	IRFXVIPRKCCSLU	4.24E-1	3.44E+00
ISOP1N4ONO2 (E/Z)	C/C(=C\CON(=O)=O)CON(=O)=O	JGJBVRGABXKDRR	1.23E+0	6.30E+00
HC4CCHO (LHC4ACCHO)	CC(=CCO)C=O	GCHJBJOOADXJFT	2.44E+1	3.19E-01
EPXISOPNONO2	CC(CON(=O)=O)(ON(=O)=O)C1CO1	UAFKAIYDADHRMX	5.03E-1	5.38E+00
ISOP1N5ONO2	O=N(=O)OC/C(=C\CO)CON(=O)=O	WRGRJJOKHABEJT	1.08E-2	2.94E+00
ISOP1N5OOH	O=N(=O)OC/C(=C/CO)COO	LLNBZHMZWYQLAS	1.46E-3	2.13E+00
ISOP1N6CO	O=C/C(=C\CO)CON(=O)=O	XXORYENTKCFFSM	1.05E-1	2.78E+00
ISOP1N2ONO2	C=CC(C)(CON(=O)=O)ON(=O)=O	FQSKJUXVWIFNKX	3.07E+0	6.07E+00
ISOP1N23O4CO (LISOP1N23O4CO)	CC1(CON(=O)=O)OC1C=O	WBVYILWVTRBTDJ	2.00E+1	5.31E+00
ISOP1N23O4ONO2 (LISOP1N23O4ONO2)	CC1(CON(=O)=O)OC1CON(=O)=O	FSZUIXLMCRZJMS	5.03E-1	5.60E+00
Large Alkanes + OH				
C5H112ONO2	CC(ON(=O)(=O))CCC	RWRBSYOTDDOXKC	-	-
C5H112O2H	CC(OO)CCCCC(OO)CCC	AXIHYONNAPPFSO	1.56E+2	3.76E+00
C5OHONO2	C(ON(=O)(=O))CCC(O)C	RIQPKERROQFFJK	5.03E+0	2.39E+00
C5OHOOH	C(OO)CCC(O)C	GSRFGQMXWRCOMF	6.52E-1	6.20E-01
C5OHCO	C(O)CCC(=O)C	JSHPTIGHEWEXRW	2.18E+1	6.84E-02
C6H13ONO2	CC(ON(=O)(=O))CCCC	JLGBOJJVQLNMGV	1.47E+2	7.25E+00
C6H13O2H	CC(OO)CCCC	XWXUHAUZCICPHE	5.10E+1	4.56E+00
C6OHONO2	CC(ON(=O)(=O))CCC(O)C	PAWWQEMXBSLVJC	2.60E+0	2.91E+00
C6OHOOH	CC(OO)CCC(O)C	BVOYWPYSMMRYPX	3.37E-1	5.66E-01
C6OHCO	CC(O)CCC(=O)C	ZSDLLTJVENEIDW	2.45E+1	-4.13E-01

Table 7.2: Collection of a subset of the estimated saturation vapor pressures and infinity dilution activity coefficients for water as solvent. As we do not consider stereochemistry here, the last part of the InChIKey is always "-UHFFFAOYSA-N" (excluded for better readability). Note that the infinity dilution activity coefficients is in the natural logarithmic representation. This is done for better comparison to literature results (continued).

compound	SMILES	InChIKey	p^* / Pa	$ln(\gamma^{\infty}_{H_2O})$
Large Alkanes + OH				
C7H15ONO2	CC(ON(=O)(=O))CCCCC	HHXLSUKHLTZWKR	4.82E+1	7.92E+00
C7H15O2H	CC(OO)CCCCC	FWELUXZVATZEMI	1.67E+1	5.00E+00
C7OHONO2	CCC(ON(=O)(=O))CCC(O)C	MZJHMUSTUUJGSJ	8.52E-1	2.95E+00
C7OHOOH	CCC(OO)CCC(O)C	KHWIBANUCNWWGW	1.10E-1	9.93E-01
C72CO5OH (LC7OHCO)	CCC(O)CCC(=O)C	MQRALIJAASQPNT	8.00E+0	2.65E-02
C8H17ONO2	CC(ON(=O)(=O))CCCCCC	QCOKASLKYUXYJH	1.58E+1	8.20E+00
C8H17O2H	CC(OO)CCCCCC	NAXZMRYIZGEALQ	5.47E+0	5.71E+00
C8OHONO2	CCCC(ON(=O)(=O))CCC(O)C	UEQWMROPIQKFIM	2.79E-1	3.71E+00
C8OHOOH	CCCC(OO)CCC(O)C	QQTSMKQYSKGCOU	3.61E-2	1.46E+00
C82CO5OH (LC8OHCO)	CCCC(O)CCC(=O)C	KZPPEBIAPHLFQD	2.62E+0	4.53E-01
Limonene				
HOC2H4CHO	O=CCCO	AKXKFZDCRYJKTF	2.03E+2	5.47E-03
C517OOH	CC(=O)C(CO)COO	OAFCGFSFCVGKSH	1.59E-2	-1.30E-01
HMVKBCHO	CC(=O)C(C=O)CO	XYGGNMZYIGPNCC	5.72E+0	5.62E-01
CO2C4CHO	CC(=O)CCC=O	KEHNRUNQZGRQHU	2.07E+2	1.07E+00
C519OOH	CC(=O)C(CCO)OO	RDSFTYTWLRHJGZ	4.26E-2	2.82E-01
C517CHO	CC(=O)C(CO)CC=O	JGHPNZFTVGSLKF	5.52E-1	-8.59E-01
C622OOH	C=C(C)C(CO)COO	GWTGWFHICNOSTQ	8.13E-2	1.13E+00
C519CHO	CC(=O)C(C=O)CCO	PVAHQKAVPKMXGV	1.87E+0	-3.26E-01
C622ONO2	C=C(C)C(CO)CON(=O)=O	UCAFMJJTBHTENA	-	-
C622CHO	C=C(C)C(CO)CC=O	JWVBPJJNIHELFZ	3.69E+0	1.19E+00
C728OOH	CC(CO)(OO)C(CO)CC=O	WJYXJQPIZCIBJO	6.97E-6	-1.12E+00
C727OOH	CC(=O)CCC(OO)C(C)=O	IMCLYNFQESJQRO	1.72E-1	1.85E+00
C624CHO	C=C(C)C(C=O)CCO	AIMYSSDKEKDSEU	3.69E+0	8.78E-01
C730OOH	CC(CO)(OO)C(C=O)CCO	YXKHJQXHKYJCPI	6.97E-6	-1.35E+00
C728ONO2	CC(CO)(ON(=O)=O)C(CO)CC=O	CDBHNFBQKSTCON	-	-
C622CONO2	C=C(C)C(CO)CC(=O)ON(=O)=O	DJCVHBPUJHAWIU	5.76E+1	1.10E+00
C730ONO2	CC(CO)(ON(=O)=O)C(C=O)CCO	RVWIAVBELSCRER	-	-
C818CO	CC(=O)C(=O)CC(CO)C(C)=O	CRQAGKNTHDNGEW	2.37E-2	4.49E-01
C816CO	C=C(C)C(=O)CCC(C)=O	FXXXYZSMIIVJDG	5.40E+0	2.22E+00
C819OOH	CC(=O)CCC(=O)C(C)(CO)OO	JRXMSSDNDAZISI	1.90E-4	1.11E+00
C817CO	CC(=O)CCC(C=O)C(C)=O	WSCYQCAMZDXSLH	1.71E+0	1.97E+00
C817OOH	CC(=O)CCC(COO)C(C)=O	WQMXPSRLZZCZTO	1.71E-2	1.58E+00
C818OOH	CC(=O)C(CO)CC(OO)C(C)=O	DLMBPALZQHFDOH	1.42E-4	8.62E-01
C729CHO	C=C(C)C(CC=O)CC=O	MEGRLTONSLAOOM	1.15E+1	3.41E+00
C822OOH	C=C(C)C(CC=O)CCOO	XWYULULFGKWPMD	3.50E-1	2.97E+00

Table 7.2: Collection of a subset of the estimated saturation vapor pressures and infinity dilution activity coefficients for water as solvent. As we do not consider stereochemistry here, the last part of the InChIKey is always "-UHFFFAOYSA-N" (excluded for better readability). Note that the infinity dilution activity coefficients is in the natural logarithmic representation. This is done for better comparison to literature results (continued).

compound	SMILES	InChIKey	p^* / Pa	$ln(\gamma^{\infty}_{H_2O})$
Limonene				
C824OOH	C=C(C)C(CCO)C(C=O)OO	FGEKWAMEWUMQIL	2.36E-3	1.07E+00
RO5R5	CC(C)(OC=O)C(CO)CC=O	MESHXYGXEHAFFE	3.02E+0	-1.89E-01
C819ONO2	CC(=O)CCC(=O)C(C)(CO)ON(=O)=O	XLUWXWLWQTYVOF	4.00E-1	1.98E-01
C817ONO2	CC(=O)CCC(CON(=O)=O)C(C)=O	ZONZWPKPCIWKRN	-	-
C822ONO2	C=C(C)C(CC=O)CCON(=O)=O	JWAJNALJDDSHOA	-	-
C824ONO2	C=C(C)C(CCO)C(C=O)ON(=O)=O	YMYILPYDFNRVBZ	5.12E+0	9.18E-02
C923OOH	C=C(C)C(CCC(C)=O)COO	ZSCOJLRNNZZYOH	1.14E-1	3.40E+00
C923OH	C=C(C)C(CO)CCC(C)=O	VZYSLJNPEGILSI	3.95E-1	1.11E+00
NORLIMAL	C=C(C)C(C=O)CCC(C)=O	WPNOYHDEEVPEJH	3.76E+0	3.01E+00
C924OOH	C=C(C)C(CO)CC(OO)C(C)=O	BVODBOGLMHSHGK	7.74E-4	1.64E+00
C924OH	C=C(C)C(CO)CC(O)C(C)=O	OXSRPARPRXNCEH	8.34E-3	-1.15E-01
LMLKET	CC(=O)CCC(CC=O)C(C)=O	CWEQHJLFCKMWEE	1.76E-1	8.27E-01
LIMKET	CC1=CCC(C(C)=O)CC1	HOBBEYSRFFJETF	4.85E+1	3.62E+00
C817CO3H	CC(=O)CCC(CC(=O)OO)C(C)=O	NVOUBBWYYUIRJW	7.58E-3	2.58E+00
C822CO3H	C=C(C)C(CC=O)CCC(=O)OO	DRDXOQWGQPPQFG	1.55E-1	3.07E+00
C822CO2H	C=C(C)C(CC=O)CCC(=O)O	ADULCIYKWVJSFE	1.87E-2	1.00E+00
C91ONO2	C=C(C)C(CCC(C)=O)CON(=O)=O	JEWJQSHMOKPQHI	-	-
NORLIMONO2	CC(=O)CCC(C=O)C(C)(CO)ON(=O)=O	MUTWZANDXPDWFF	6.30E-2	5.48E-02
C92ONO2	C=C(C)C(CO)CC(ON(=O)=O)C(C)=O	PNFDSIMYWKOAKE	1.68E+0	1.39E+00
C817CONO2	CC(=O)CCC(CC(=O)ON(=O)=O)C(C)=O	LHFXXFGIVAQFTO	3.76E+0	1.55E+00
C822CONO2	C=C(C)C(CC=O)CCC(=O)ON(=O)=O	RVFLVBTUEWAABB	7.67E+1	1.47E+00
BPINCOOH (LABPINCOOH)	CC1=CCC(C(C)(CO)OO)CC1	VVHMRXSQYYKNLC	-	-
RO5R1O2H	CC1(C)OC2CC1CCC2(CO)OO	NSOHXIGSWKLSHV	3.57E-4	5.44E-01
RO5R2O2H	CC1(C)OC(OO)CC1CCC(=O)CO	MFXJOKCSTDMZRM	3.87E-5	8.27E-01
RO5R3O2H	CC(C)(OC=O)C(CCC(=O)CO)COO	IEPFJXDIWPQIRC	5.36E-4	1.16E+00
RO5R4O2H	CC(C)(OC=O)C(CO)CC(OO)C(=O)CO	YORZXZYHORHTRW	2.78E-6	2.05E-02
C923CO3H	C=C(C)C(CCC(C)=O)CC(=O)OO	JSHGCXGTVADTAK	5.06E-2	3.33E+00
LIMONONIC	C=C(C)C(CCC(C)=O)CC(=O)O	NJOIWWRMLFSDTM	6.13E-3	1.38E+00
LIMAL	C=C(C)C(CC=O)CCC(C)=O	OGCGCISRMFSLTC	1.23E+0	3.76E+00
LIMALOOH	CC(=O)CCC(CC=O)C(C)(CO)OO	OQLBLHLZVAPRGN	9.79E-6	9.85E-01
LIMALOH	CC(=O)CCC(CC=O)C(C)(O)CO	ISUQULRVPDSRIP	4.38E-4	-5.55E-01
LIMALAOOH	C=C(C)C(CC=O)CC(OO)C(C)=O	DVORBFWFCUOYLW	9.56E-3	2.99E+00
LIMALAOH	C=C(C)C(CC=O)CC(O)C(C)=O	VNYSFQVUCPNMDZ	9.31E-2	4.92E-01
LIMALACO	C=C(C)C(CC=O)CC(=O)C(C)=O	OXUPJDFJWCMZMO	4.94E-1	2.55E+00
LIMALBOOH	C=C(C)C(CC=O)CCC(=O)COO	DCWLKDSHBWMMQU	6.04E-3	3.05E+00
BPINCONO2 (LABPINCONO2)	CC1=CCC(C(C)(CO)(ON(=O)(=O)))CC1	ZELLOEPLERCREX	-	-

Table 7.2: Collection of a subset of the estimated saturation vapor pressures and infinity dilution activity coefficients for water as solvent. As we do not consider stereochemistry here, the last part of the InChIKey is always "-UHFFFAOYSA-N" (excluded for better readability). Note that the infinity dilution activity coefficients is in the natural logarithmic representation. This is done for better comparison to literature results (continued).

compound	SMILES	InChIKey	p^* / Pa	$ln(\gamma^{\infty}_{H_2O})$
Limonene				
C9CONO2	C=C(C)C(CCC(C)=O)CC(=O)(ON(=O)(=O))	FNVMVXZLPDKVAS	2.51E+1	2.87E+00
LIMALONO2	CC(=O)CCC(CC=O)C(C)(CO)(ON(=O)(=O))	FDBNDHKWTKEDSC	-	-
LIMONO2	C=C(C)C(CC=O)CCC(=O)CON(=O)=O	DEKWHDOXDJNWRD	4.05E+0	1.64E+00
LIMAB15ONO22 (LLIMABONO22)	CC(CO)(ON(=O)=O)C1CCC(C)(ON(=O)=O)C(O)C1	UNHNJOVXNACOSQ	3.45E-7	3.91E+00
LIMAB15ONO2OOH (LLIMABONO2OOH)	CC(CO)(OO)C1CCC(C)(ON(=O)=O)C(O)C1	JBKULLYZCMWERK	3.32E-8	1.70E+00
LIMAB15OOH2 (LLIMABOOH2)	CC(CO)(OO)C1CCC(C)(OO)C(O)C1	IRUZCTPAAZATQM	2.40E-9	9.65E-01
LIMAB1ONO2 (LLIMABONO2)	C=C(C)C1CCC(C)(ON(=O)=O)C(O)C1	LZDKYYHMAURBIK	-	-
LIMAB1OOH (LLIMABOOH)	C=C(C)C1CCC(C)(OO)C(O)C1	FPMDSGWWEURSNO	-	-
ROO6R1ONO2	CC1(CO)OOC2CC1CCC2(C)ON(=O)=O	JOFCABYMPNXMIS	1.51E-3	3.53E+00
ROO6R1OOH	CC1(CO)OOC2CC1CCC2(C)OO	GBBPAXKBVMQHIG	1.47E-4	1.54E+00
ROO6R5ONO2	CC(=O)CCC(CC(=O)ON(=O)=O)OO	LNWOWXJMUJHMJJ	1.07E+0	3.92E+00
ROO6R5OOH	CC(=O)CCC(CC(=O)OO)OO	RAASFOSVQCCDRJ	7.33E-4	-
ROO6R6ONO2	CC(=O)CCC(CON(=O)=O)OO	CRECMHNOVVIMCR	1.41E-2	3.78E+00
ROO6R6OOH	CC(=O)CCC(COO)OO	QZPUZDFJKAEVLL	1.69E-3	1.55E+00
ROO6R7ONO2	CC(=O)CCC(CO)ON(=O)=O	COKJDYWOSQONMU	6.31E-2	2.89E+00
ROO6R7OOH	CC(=O)CCC(CO)OO	UPAWKBDHGPWUCG	6.95E-3	-5.65E-01
C52COCONO2	CC(=O)CCC(=O)ON(=O)=O	QJXLMYNMVOSKND	4.23E+3	3.15E+00
C52COCO3H	CC(=O)CCC(=O)OO	COVHHGSUFOHLBW	-	-
C624ONO2	C=C(COO)C(CO)(CO)ON(=O)=O	XYBUKFJLXVIRLY	1.23E-6	1.35E+00
C518OOH	C=C(COO)C(=O)CO	PQEISBQMLHJHJQ	2.36E-2	1.84E+00
C624OOH	C=C(COO)C(CO)(CO)OO	FUTSLQULSAKEJA	1.08E-7	4.51E-01
C520ONO2	O=C(CO)C(CO)(COO)ON(=O)=O	ZSADVAXZKGJKSG	1.72E-6	6.86E-01
BIACETOH2	O=C(CO)C(=O)CO	GJCZUCLKDGABDS	-	-
C520OOH	O=C(CO)C(CO)(COO)OO	GRPDYNZWDDUILX	1.52E-7	-3.00E-01
Glyoxal oligomers				
GOLIG1	O=CC(O)-O-C(O)C=O	LEKXYOUPWKVTGM	5.47E+0	6.60E-01
GOLIG2	O=CC(O)-O-C(O)C(O)O	GWSRJJGBNXJVPO	1.16E-3	-8.30E-01
GOLIG3	OC(O)C(O)-O-C(O)C(O)O	ADECTKUVLJSMDK	3.71E-7	-1.23E+00
Methyl glyoxal oligomers				
MGLYOXDA	CC(=O)C(O)-O-C(O)C(=O)C	QMSLRDMQAWWKIZ	5.86E-1	1.50E+00
MGLYOXDB	CC(=O)C(O)-O-C(O)(C)C(O)(O)	IUHMFBWAUOLAFM	9.35E-4	-3.15E-01
MGLYFA	CC(=O)C(=O)-O-C(O)C(=O)C	NOUUUBJIFPBZMZ	2.58E+0	1.86E+00
MGLYFB	CC(=O)C(=O)-O-C(O)(C)C(O)(O)	UCPBJDKPOQEXSQ	3.35E-4	-2.27E-01

Acronyms

AMS aerosol mass spectrometer

AN alkylnitrate

BrC brown carbon

BVOC biogenic volatile organic compounds

CCN cloud condensation nuclei

COPD chronic obstructive pulmonary disease

ESM Earth System Model

GMXe Global Modal-aerosol eXtension

IEPOX isoprene-derived epoxydiols

IVOC intermediate volatile organic compounds

JAMOC Jülich Aqueous-phase Mechanism of Organic Chemistry

KPP Kinetic PreProcessor

LIF laser-induced fluorescence

LVOC low volatile organic compounds

LWC liquid water content

MCM Master Chemical Mechanism

MEBUTETROL methylbutane-1,2,3,4-tetrol

MESSy Modular Earth Submodel System

MOM Mainz Organic Mechanism

NMVOC non methane volatile organic compound

O/C oxygen-to-carbon

OA organic aerosol

ORACLE Organic Aerosol Composition and Evolution in the Atmosphere

OVOC oxidized volatile organic compounds

PAN peroxy acetyl nitrate

PBL planetary boundary layer

POA primary organic aerosol

SARs structure-activity relationships

SOA secondary organic aerosol

SVOC semi volatile organic compounds

VBS volatility basis set

VCPs volatile chemical products

VOCs volatile organic compounds

Chapter 8

Bibliography

A. C. Aiken, P. F. DeCarlo, J. H. Kroll, D. R. Worsnop, J. A. Huffman, K. S. Docherty, I. M. Ulbrich, C. Mohr, J. R. Kimmel, D. Sueper, et al. O/c and om/oc ratios of primary, secondary, and ambient organic aerosols with high-resolution time-of-flight aerosol mass spectrometry. *Environmental science & technology*, 42(12):4478–4485, 2008. doi: 10.1021/es703009q.

D. Aljawhary, A. Lee, and J. Abbatt. High-resolution chemical ionization mass spectrometry (tof-cims): application to study soa composition and processing. *Atmospheric Measurement Techniques*, 6(11):3211–3224, 2013. doi: 10.5194/amt-6-3211-2013.

D. Aljawhary, R. Zhao, A. K. Lee, C. Wang, and J. P. Abbatt. Kinetics, mechanism, and secondary organic aerosol yield of aqueous phase photo-oxidation of a-pinene oxidation products. *The Journal of Physical Chemistry A*, 120(9):1395–1407, 2016. doi: 10.1021/acs.jpca.5b06237. URL `https://doi.org/10.1021/acs.jpca.5b06237`.

M. O. Andreae, A. Afchine, R. Albrecht, B. A. Holanda, P. Artaxo, H. M. J. Barbosa, S. Borrmann, M. A. Cecchini, A. Costa, M. Dollner, D. Fütterer, E. Järvinen, T. Jurkat, T. Klimach, T. Konemann, C. Knote, M. Krämer, T. Krisna, L. A. T. Machado, S. Mertes, A. Minikin, C. Pöhlker, M. L. Pöhlker, U. Pöschl, D. Rosenfeld, D. Sauer, H. Schlager, M. Schnaiter, J. Schneider, C. Schulz, A. Spanu, V. B. Sperling, C. Voigt, A. Walser, J. Wang, B. Weinzierl, M. Wendisch, and H. Ziereis. Aerosol characteristics and particle production in the upper troposphere over the amazon basin. *Atmospheric Chemistry and Physics*, 18(2):921–961, 2018. doi: 10.5194/acp-18-921-2018. URL `https://acp.copernicus.org/articles/18/921/2018/`.

T. Anttila, A. Kiendler-Scharr, R. Tillmann, and T. F. Mentel. On the reactive uptake of gaseous compounds by organic-coated aqueous aerosols: Theoretical analysis and application to the heterogeneous hydrolysis of n2o5. *The Journal of Physical Chemistry A*, 110(35):10435–10443, 2006. doi: 10.1021/jp062403c.

P. Atkins. *Physical chemistry*. 2006. ISBN 0-7167-8759-8.

R. Atkinson. Kinetics and mechanisms of the gas-phase reactions of the hydroxyl radical with organic compounds under atmospheric conditions. *Chemical Reviews*, 86(1):69–201, 1986. doi: 10.1021/cr00071a004.

R. Atkinson, J. Arey, and S. M. Aschmann. Atmospheric chemistry of alkanes: Review and recent developments. *Atmospheric Environment*, 42(23):5859–5871, 2008. doi: 10.1016/j.atmosenv.2007.08.040.

B. Aumont, S. Szopa, and S. Madronich. Modelling the evolution of organic carbon during its gas-phase tropospheric oxidation: development of an explicit model based on a self generating approach. *Atmospheric Chemistry and Physics*, 5(9):2497–2517, 2005. doi: 10.5194/acp-5-2497-2005.

B. Aumont, R. Valorso, C. Mouchel-Vallon, M. Camredon, J. Lee-Taylor, and S. Madronich. Modeling soa formation from the oxidation of intermediate volatility n-alkanes. *Atmospheric Chemistry and Physics*, 12(16):7577–7589, 2012. doi: 10.5194/acp-12-7577-2012.

B. Ayres, H. Allen, D. Draper, S. Brown, R. Wild, J. Jimenez, D. Day, P. Campuzano-Jost, W. d. Hu, J. De Gouw, et al. Organic nitrate aerosol formation via no 3+ biogenic volatile organic compounds in the southeastern united states. *Atmospheric Chemistry and Physics*, 15(23):13377–13392, 2015. doi: 10.5194/acp-15-13377-2015.

M. Barley and G. McFiggans. The critical assessment of vapour pressure estimation methods for use in modelling the formation of atmospheric organic aerosol. *Atmospheric Chemistry and Physics*, 10(2):749–767, 2010. doi: 10.5194/acp-10-749-2010.

A. P. Bateman, S. A. Nizkorodov, J. Laskin, and A. Laskin. Photolytic processing of secondary organic aerosols dissolved in cloud droplets. *Physical Chemistry Chemical Physics*, 13(26):12199–12212, 2011. doi: 10.1039/C1CP20526A.

K. H. Bates, J. D. Crounse, J. M. St. Clair, N. B. Bennett, T. B. Nguyen, J. H. Seinfeld, B. M. Stoltz, and P. O. Wennberg. Gas phase production and loss of isoprene epoxydiols. *The Journal of Physical Chemistry A*, 118(7):1237–1246, 2014. doi: 10.1021/jp4107958.

W. Bloss, J. Lee, D. Heard, R. A. Salmon, S.-B. Bauguitte, H. Roscoe, and A. Jones. Observations of oh and ho 2 radicals in coastal antarctica. *Atmospheric Chemistry and Physics*, 7(16):4171–4185, 2007. doi: 10.5194/acp-7-4171-2007.

Q. Bourgeois, A. M. Ekman, and R. Krejci. Aerosol transport over the andes from the amazon basin to the remote pacific ocean: A multiyear caliop assessment. *Journal of Geophysical Research: Atmospheres*, 120(16):8411–8425, 2015. doi: 10.1002/2015JD023254.

A. A. Boyd, P.-M. Flaud, N. Daugey, and R. Lesclaux. Rate constants for ro2+ ho2 reactions measured under a large excess of ho2. *The Journal of Physical Chemistry A*, 107(6):818–821, 2003. doi: 10.1021/jp026581r.

C. M. Boyd, J. Sanchez, L. Xu, A. J. Eugene, T. Nah, W. Y. Tuet, M. I. Guzman, and N. L. Ng. Secondary organic aerosol formation from the β-pinene+no_3 system: effect of humidity and peroxy radical fate. *Atmospheric Chemistry and Physics*, 15(13):7497–7522, 2015. doi: 10.5194/acp-15-7497-2015. URL `https://acp.copernicus.org/articles/15/7497/2015/`.

P. Bräuer, C. Mouchel-Vallon, A. Tilgner, A. Mutzel, O. Böge, M. Rodigast, L. Poulain, D. van Pinxteren, R. Wolke, B. Aumont, and H. Herrmann. Development of a protocol for the auto-generation of explicit aqueous-phase oxidation schemes of organic compounds. *Atmospheric Chemistry and Physics*, 19(14):9209–9239, 2019. doi: 10.5194/acp-19-9209-2019. URL `https://acp.copernicus.org/articles/19/9209/2019/`.

T. Brouwer and B. Schuur. Model performances evaluated for infinite dilution activity coefficients prediction at 298.15 k. *Industrial & Engineering Chemistry Research*, 58(20): 8903–8914, 2019. doi: 10.1021/acs.iecr.9b00727.

B. Brownwood, A. Turdziladze, T. Hohaus, R. Wu, T. F. Mentel, P. T. Carlsson, E. Tsiligiannis, M. Hallquist, S. Andres, L. Hantschke, et al. Gas-particle partitioning and soa yields of organonitrate products from no3-initiated oxidation of isoprene under varied chemical regimes. *ACS earth and space chemistry*, 5(4):785–800, 2021. doi: 10.1021/acsearthspacechem.0c00311.

M. Brueggemann, R. Xu, A. Tilgner, K. C. Kwong, A. Mutzel, H. Y. Poon, T. Otto, T. Schaefer, L. Poulain, M. N. Chan, et al. Organosulfates in ambient aerosol: state of knowledge and future research directions on formation, abundance, fate, and importance. *Environmental Science & Technology*, 54(7):3767–3782, 2020. doi: 10.1021/acs.est.9b06751.

S. Budisulistiorini, X. Li, S. Bairai, J. Renfro, Y. Liu, Y. Liu, K. McKinney, S. Martin, V. McNeill, H. Pye, et al. Examining the effects of anthropogenic emissions on isoprene-derived secondary organic aerosol formation during the 2013 southern oxidant and aerosol study (soas) at the look rock, tennessee ground site. *Atmospheric Chemistry and Physics*, 15(15):8871–8888, 2015. doi: 10.5194/acp-15-8871-2015.

S. H. Budisulistiorini, A. Nenes, A. G. Carlton, J. D. Surratt, V. F. McNeill, and H. O. Pye. Simulating aqueous-phase isoprene-epoxydiol (iepox) secondary organic aerosol production during the 2013 southern oxidant and aerosol study (soas). *Environmental science & technology*, 51(9):5026–5034, 2017. doi: 10.1021/acs.est.6b05750.

D. Cabrera-Perez, D. Taraborrelli, R. Sander, and A. Pozzer. Global atmospheric budget of simple monocyclic aromatic compounds. *Atmospheric Chemistry and Physics*, 16(11): 6931–6947, 2016. doi: 10.5194/acp-16-6931-2016.

M. Canagaratna, J. Jimenez, J. Kroll, Q. Chen, S. Kessler, P. Massoli, L. Hildebrandt Ruiz, E. Fortner, L. Williams, K. Wilson, et al. Elemental ratio measurements of organic compounds using aerosol mass spectrometry: characterization, improved calibration, and implications. *Atmospheric Chemistry and Physics*, 15(1):253–272, 2015. doi: 10.5194/acp-15-253-2015.

C. D. Cappa, E. R. Lovejoy, and A. R. Ravishankara. Evidence for liquid-like and nonideal behavior of a mixture of organic aerosol components. *Proceedings of the National Academy of Sciences*, 105(48):18687–18691, 2008. doi: 10.1073/pnas.0802144105.

P. T. Carlsson, L. Vereecken, A. Novelli, F. Bernard, S. S. Brown, B. Brownwood, C. Cho, J. N. Crowley, P. Dewald, P. M. Edwards, et al. Comparison of isoprene chemical mechanisms under atmospheric night-time conditions in chamber experiments: evidence of hydroperoxy aldehydes and epoxy products from no 3 oxidation. *Atmospheric chemistry and physics*, 23(5):3147–3180, 2023. doi: 10.5194/acp-23-3147-2023.

N. Carslaw. A mechanistic study of limonene oxidation products and pathways following cleaning activities. *Atmospheric Environment*, 80:507–513, 2013. doi: 10.1016/j.atmosenv.2013.08.034.

W. P. Carter, J. Jiang, J. J. Orlando, and K. C. Barsanti. Derivation of atmospheric reaction mechanisms for volatile organic compounds by the saprc mechanism generation system (mechgen). *EGUsphere*, 2023:1–65, 2023. doi: 10.5194/egusphere-2023-2343.

H. Chen, S. Wang, and L. Wang. Reaction of the acetyl peroxy radical and oh radical as a source of acetic acid in the atmosphere. *ACS Earth and Space Chemistry*, 2024. doi: 10.1021/acsearthspacechem.4c00211.

J. D. Cope, K. A. Abellar, K. H. Bates, X. Fu, and T. B. Nguyen. Aqueous photochemistry of 2-methyltetrol and erythritol as sources of formic acid and acetic acid in the atmosphere. *ACS Earth and Space Chemistry*, 5(6):1265–1277, 2021. doi: 10.1021/acsearthspacechem.1c00107.

T. Cui, H. S. Green, P. W. Selleck, Z. Zhang, R. E. O'Brien, A. Gold, M. Keywood, J. H. Kroll, and J. D. Surratt. Chemical characterization of isoprene-and monoterpene-derived secondary organic aerosol tracers in remote marine aerosols over a quarter century. *ACS Earth and Space Chemistry*, 3(6):935–946, 2019. doi: 10.1021/acsearthspacechem.9b00061.

E. L. D'Ambro, S. Schobesberger, C. J. Gaston, F. D. Lopez-Hilfiker, B. H. Lee, J. Liu, A. Zelenyuk, D. Bell, C. D. Cappa, T. Helgestad, Z. Li, A. Guenther, J. Wang, M. Wise, R. Caylor, J. D. Surratt, T. Riedel, N. Hyttinen, V.-T. Salo, G. Hasan, T. Kurtén, J. E. Shilling, and J. A. Thornton. Chamber-based insights into the factors controlling epoxydiol (iepox) secondary organic aerosol (soa) yield, composition, and volatil-

ity. *Atmospheric Chemistry and Physics*, 19(17):11253–11265, 2019. doi: 10.5194/acp-19-11253-2019. URL https://acp.copernicus.org/articles/19/11253/2019/.

A. I. Darer, N. C. Cole-Filipiak, A. E. O'Connor, and M. J. Elrod. Formation and stability of atmospherically relevant isoprene-derived organosulfates and organonitrates. *Environmental Science & Technology*, 45(5):1895–1902, 2011. doi: 10.1021/es103797z. URL https://doi.org/10.1021/es103797z.

K. E. Daumit, A. J. Carrasquillo, R. A. Sugrue, and J. H. Kroll. Effects of condensed-phase oxidants on secondary organic aerosol formation. *The Journal of Physical Chemistry A*, 120(9):1386–1394, 2016. doi: 10.1021/acs.jpca.5b06160.

A. De Meij, A. Pozzer, K. Pringle, H. Tost, and J. Lelieveld. Emac model evaluation and analysis of atmospheric aerosol properties and distribution with a focus on the mediterranean region. *Atmospheric research*, 114:38–69, 2012. doi: 10.1016/j.atmosres.2012.05.014.

S. Dietmüller, P. Jöckel, H. Tost, M. Kunze, C. Gellhorn, S. Brinkop, C. Frömming, M. Ponater, B. Steil, A. Lauer, and J. Hendricks. A new radiation infrastructure for the modular earth submodel system (messy, based on version 2.51). *Geoscientific Model Development*, 9(6):2209–2222, 2016. doi: 10.5194/gmd-9-2209-2016. URL https://gmd.copernicus.org/articles/9/2209/2016/.

N. M. Donahue, A. L. Robinson, C. O. Stanier, and S. N. Pandis. Coupled Partitioning, Dilution, and Chemical Aging of Semivolatile Organics. *Environmental Science & Technology*, 40(8):2635–2643, Apr. 2006. ISSN 0013-936X. doi: 10.1021/es052297c. URL https://doi.org/10.1021/es052297c.

N. M. Donahue, S. Epstein, S. N. Pandis, and A. L. Robinson. A two-dimensional volatility basis set: 1. organic-aerosol mixing thermodynamics. *Atmospheric Chemistry and Physics*, 11(7):3303–3318, 2011. doi: 10.5194/acp-11-3303-2011.

N. M. Donahue, J. Kroll, S. N. Pandis, and A. L. Robinson. A two-dimensional volatility basis set–part 2: Diagnostics of organic-aerosol evolution. *Atmospheric Chemistry and Physics*, 12(2):615–634, 2012. doi: 10.5194/acp-12-615-2012.

J.-F. Doussin and A. Monod. Structure–activity relationship for the estimation of oh-oxidation rate constants of carbonyl compounds in the aqueous phase. *Atmospheric Chemistry and Physics*, 13(23):11625–11641, 2013. doi: 10.5194/acp-13-11625-2013.

R. Dreger, T. Kirfel, A. Pozzer, S. Rosanka, R. Sander, and D. Taraborrelli. Optimized step size control within the rosenbrock solvers for stiff chemical ode systems in kpp version 2.2.3rs4. *Geoscientific Model Development Discussions*, 2025:1–30, 2025. doi: 10.5194/gmd-2024-166. URL https://gmd.copernicus.org/preprints/gmd-2024-166/.

E. L. D'Ambro, K. H. Møller, F. D. Lopez-Hilfiker, S. Schobesberger, J. Liu, J. E. Shilling, B. H. Lee, H. G. Kjaergaard, and J. A. Thornton. Isomerization of second-generation isoprene peroxy radicals: Epoxide formation and implications for secondary organic aerosol yields. *Environmental science & technology*, 51(9):4978–4987, 2017. doi: 10.1021/acs.est.7b00460.

P. G. Eger, L. Vereecken, R. Sander, J. Schuladen, N. Sobanski, H. Fischer, E. Karu, J. Williams, V. Vakkari, T. Petäjä, J. Lelieveld, A. Pozzer, and J. N. Crowley. Impact of pyruvic acid photolysis on acetaldehyde and peroxy radical formation in the boreal forest: theoretical calculations and model results. *Atmospheric Chemistry and Physics*, 21(18): 14333–14349, 2021. doi: 10.5194/acp-21-14333-2021. URL `https://acp.copernicus.org/articles/21/14333/2021/`.

EPA. Clean air status and trends network (castnet). www.epa.gov/castnet.

B. Ervens. Modeling the processing of aerosol and trace gases in clouds and fogs. *Chemical reviews*, 115(10):4157–4198, 2015. doi: 10.1021/cr5005887.

B. Ervens, B. Turpin, and R. Weber. Secondary organic aerosol formation in cloud droplets and aqueous particles (aqsoa): a review of laboratory, field and model studies. *Atmospheric Chemistry and Physics*, 11(21):11069–11102, 2011. doi: 10.5194/acp-11-11069-2011.

B. Ervens, A. Sorooshian, Y. B. Lim, and B. J. Turpin. Key parameters controlling oh-initiated formation of secondary organic aerosol in the aqueous phase (aqsoa). *Journal of Geophysical Research: Atmospheres*, 119(7):3997–4016, 2014. doi: 10.1002/2013JD021021.

D. K. Farmer, E. K. Boedicker, and H. M. DeBolt. Dry deposition of atmospheric aerosols: Approaches, observations, and mechanisms. *Annual Review of Physical Chemistry*, 72(Volume 72, 2021):375–397, 2021. doi: 10.1146/annurev-physchem-090519-034936. URL `https://www.annualreviews.org/content/journals/10.1146/annurev-physchem-090519-034936`.

C. Fountoukis and A. Nenes. Isorropia ii: a computationally efficient thermodynamic equilibrium model for k+–ca 2+–mg 2+–nh 4+–na+–so 4 2—no 3—cl—h 2 o aerosols. *Atmospheric Chemistry and Physics*, 7(17):4639–4659, 2007. doi: 10.5194/acp-7-4639-2007.

B. Franco, T. Blumenstock, C. Cho, L. Clarisse, C. Clerbaux, P.-F. Coheur, M. De Mazière, I. De Smedt, H.-P. Dorn, T. Emmerichs, H. Fuchs, G. Gkatzelis, D. W. T. Griffith, S. Gromov, J. W. Hannigan, F. Hase, T. Hohaus, N. Jones, A. Kerkweg, A. Kiendler-Scharr, E. Lutsch, E. Mahieu, A. Novelli, I. Ortega, C. Paton-Walsh, M. Pommier, A. Pozzer, D. Reimer, S. Rosanka, R. Sander, M. Schneider, K. Strong, R. Tillmann,

M. Van Roozendael, L. Vereecken, C. Vigouroux, A. Wahner, and D. Taraborrelli. Ubiquitous atmospheric production of organic acids mediated by cloud droplets. *Nature*, 593(7858):233–237, 2021. ISSN 1476-4687. doi: 10.1038/s41586-021-03462-x. URL https://www.nature.com/articles/s41586-021-03462-x.

J. Fry, A. Kiendler-Scharr, A. Rollins, T. Brauers, S. Brown, H.-P. Dorn, W. Dubé, H. Fuchs, A. Mensah, F. Rohrer, et al. Soa from limonene: role of no 3 in its generation and degradation. *Atmospheric chemistry and physics*, 11(8):3879–3894, 2011. doi: 10.5194/acp-11-3879-2011.

H. Fuchs, A. Novelli, C. Cho, F. Rohrer, R. Tillmann, D. Reimer, T. Hohaus, A. Turdziladze, P. Dewald, J. M. Liebmann, N. Friedrich, J. Shenolikar, J. Schuladen, J. Crowley, S. S. Brown, F. Bernard, L. Zhou, T. Mentel, R. Wu, and J. F. Hamilton. Atmospheric simulation chamber study: isoprene + no3 - gas-phase oxidation - product study - 2018-08-13 (version 1.0) [data set], 2018.

M. I. García, B. L. Van Drooge, S. Rodríguez, and A. Alastuey. Speciation of organic aerosols in the saharan air layer and in the free troposphere westerlies. *Atmospheric Chemistry and Physics*, 17(14):8939–8958, 2017. doi: 10.5194/acp-17-8939-2017.

C. J. Gaston, T. P. Riedel, Z. Zhang, A. Gold, J. D. Surratt, and J. A. Thornton. Reactive Uptake of an Isoprene-Derived Epoxydiol to Submicron Aerosol Particles. *Environmental Science & Technology*, 48(19):11178–11186, Oct. 2014a. ISSN 0013-936X. doi: 10.1021/es5034266. URL https://doi.org/10.1021/es5034266.

C. J. Gaston, J. A. Thornton, and N. L. Ng. Reactiv uptake of N_2O_5 to internally mixed inorganic and organic particles: the role of organic carbon oxidation state and inferred organic phase separations. *Atmospheric Chemistry and Physics*, 14(11):5693–5707, June 2014b. ISSN 1680-7316. doi: 10.5194/acp-14-5693-2014. URL https://acp.copernicus.org/articles/14/5693/2014/.

G. I. Gkatzelis, R. Tillmann, T. Hohaus, M. Müller, P. Eichler, K.-M. Xu, P. Schlag, S. H. Schmitt, R. Wegener, M. Kaminski, et al. Comparison of three aerosol chemical characterization techniques utilizing ptr-tof-ms: a study on freshly formed and aged biogenic soa. *Atmospheric Measurement Techniques*, 11(3):1481–1500, 2018. doi: 10.5194/amt-11-1481-2018.

B. G. Glover and T. A. Miller. Near-ir cavity ringdown spectroscopy and kinetics of the isomers and conformers of the butyl peroxy radical. *The Journal of Physical Chemistry A*, 109(49):11191–11197, 2005. doi: 10.1021/jp054838q.

A. Guenther, T. Karl, P. Harley, C. Wiedinmyer, P. I. Palmer, and C. Geron. Estimates of global terrestrial isoprene emissions using megan (model of emissions of gases and aerosols

from nature). *Atmospheric Chemistry and Physics*, 6(11):3181–3210, 2006. doi: 10.5194/acp-6-3181-2006. URL https://acp.copernicus.org/articles/6/3181/2006/.

I. Gultepe and G. Isaac. Liquid water content and temperature relationship from aircraft observations and its applicability to gcms. *Journal of Climate*, 10(3):446–452, 1997. doi: 10.1175/1520-0442(1997)010⟨0446:LWCATR⟩2.0.CO;2.

C. L. Heald, H. Coe, J. L. Jimenez, R. J. Weber, R. Bahreini, A. M. Middlebrook, L. M. Russell, M. Jolleys, T.-M. Fu, J. D. Allan, K. N. Bower, G. Capes, J. Crosier, W. T. Morgan, N. H. Robinson, P. I. Williams, M. J. Cubison, P. F. DeCarlo, and E. J. Dunlea. Exploring the vertical profile of atmospheric organic aerosol: comparing 17 aircraft field campaigns with a global model. *Atmospheric Chemistry and Physics*, 11(24):12673–12696, 2011. doi: 10.5194/acp-11-12673-2011. URL https://acp.copernicus.org/articles/11/12673/2011/.

W. Henry. Experiments on the quantity of gases absorbed by water, at different temperatures, and under different pressures. *Philosophical Transactions of the Royal Society of London*, (93):29–274, 1803. doi: 10.1098/rstl.1803.0004.

H. Herrmann, A. Tilgner, P. Barzaghi, Z. Majdik, S. Gligorovski, L. Poulain, and A. Monod. Towards a more detailed description of tropospheric aqueous phase organic chemistry: Capram 3.0. *Atmospheric Environment*, 39(23):4351–4363, 2005. ISSN 1352-2310. doi: 10.1016/j.atmosenv.2005.02.016. URL https://www.sciencedirect.com/science/article/pii/S1352231005001937.

A. Hodzic, B. Aumont, C. Knote, J. Lee-Taylor, S. Madronich, and G. Tyndall. Volatility dependence of henry's law constants of condensable organics: Application to estimate depositional loss of secondary organic aerosols. *Geophysical Research Letters*, 41(13):4795–4804, 2014. doi: 10.1002/2014GL060649.

A. Hodzic, P. S. Kasibhatla, D. S. Jo, C. D. Cappa, J. L. Jimenez, S. Madronich, and R. J. Park. Rethinking the global secondary organic aerosol (soa) budget: stronger production, faster removal, shorter lifetime. *Atmospheric Chemistry and Physics*, 16(12):7917–7941, 2016.

K. S. Hu, A. I. Darer, and M. J. Elrod. Thermodynamics and kinetics of the hydrolysis of atmospherically relevant organonitrates and organosulfates. *Atmospheric Chemistry and Physics*, 11(16):8307–8320, 2011. doi: 10.5194/acp-11-8307-2011. URL https://acp.copernicus.org/articles/11/8307/2011/.

Q.-H. Hu, Z.-Q. Xie, X.-M. Wang, H. Kang, Q.-F. He, and P. Zhang. Secondary organic aerosols over oceans via oxidation of isoprene and monoterpenes from arctic to antarctic. *Scientific reports*, 3(1):2280, 2013. doi: 10.1038/srep02280.

W. Hu, P. Campuzano-Jost, B. Palm, D. Day, A. Ortega, P. Hayes, J. Krechmer, Q. Chen, M. Kuwata, Y. Liu, et al. Characterization of a real-time tracer for isoprene epoxydiols-derived secondary organic aerosol (iepox-soa) from aerosol mass spectrometer measurements. *Atmospheric Chemistry and Physics*, 15(20):11807–11833, 2015. doi: 10.5194/acp-15-11807-2015.

X. Huang, Z. Wang, and A. Ding. Impact of aerosol-pbl interaction on haze pollution: Multiyear observational evidences in north china. *Geophysical Research Letters*, 45(16): 8596–8603, 2018. doi: 10.1029/2018GL079239. URL `https://agupubs.onlinelibrary.wiley.com/doi/abs/10.1029/2018GL079239`.

N. Hyttinen, I. Pullinen, A. Nissinen, S. Schobesberger, A. Virtanen, and T. Yli-Juuti. Comparison of saturation vapor pressures of α-pinene + O_3 oxidation products derived from cosmo-rs computations and thermal desorption experiments. *Atmospheric Chemistry and Physics*, 22(2):1195–1208, 2022. doi: 10.5194/acp-22-1195-2022. URL `https://acp.copernicus.org/articles/22/1195/2022/`.

N. Hyttinen, L. Li, M. Hallquist, and C. Wu. Machine learning model to predict saturation vapor pressures of atmospheric aerosol constituents. *ACS ES&T Air*, 1(9):1156–1163, 2024. doi: 10.1021/acsestair.4c00113. URL `https://doi.org/10.1021/acsestair.4c00113`.

M. I. Jacobs, W. J. Burke, and M. J. Elrod. Kinetics of the reactions of isoprene-derived hydroxynitrates: gas phase epoxide formation and solution phase hydrolysis. *Atmospheric Chemistry and Physics*, 14(17):8933–8946, 2014. doi: 10.5194/acp-14-8933-2014. URL `https://acp.copernicus.org/articles/14/8933/2014/`.

V. Jain, S. N. Tripathi, N. Tripathi, L. K. Sahu, S. Gaddamidi, A. K. Shukla, D. Bhattu, and D. Ganguly. Seasonal variability and source apportionment of non-methane vocs using ptr-tof-ms measurements in delhi, india. *Atmospheric Environment*, 283:119163, 2022. doi: 10.1016/j.atmosenv.2022.119163.

M. Jenkin, S. M. Saunders, and M. J. Pilling. The tropospheric degradation of volatile organic compounds: A protocol for mechanism development. *Atmos. Environ.*, 31:81–104, 1997. doi: 10.1016/S1352-2310(96)00105-7.

G.-R. Jeong and I. N. Sokolik. Effect of mineral dust aerosols on the photolysis rates in the clean and polluted marine environments. *Journal of Geophysical Research: Atmospheres*, 112(D21), 2007. doi: 10.1029/2007JD008442. URL `https://agupubs.onlinelibrary.wiley.com/doi/abs/10.1029/2007JD008442`.

P. Jöckel, R. Sander, A. Kerkweg, H. Tost, and J. Lelieveld. The modular earth submodel system (messy)-a new approach towards earth system modeling. *Atmospheric Chemistry and Physics*, 5(2):433–444, 2005. doi: 1680-7324/acp/2005-5-433.

P. Jöckel, H. Tost, A. Pozzer, C. Brühl, J. Buchholz, L. Ganzeveld, P. Hoor, A. Kerkweg, M. Lawrence, R. Sander, et al. The atmospheric chemistry general circulation model echam5/messy1: consistent simulation of ozone from the surface to the mesosphere. *Atmospheric Chemistry and Physics*, 6(12):5067–5104, 2006. doi: 10.5194/acp-6-5067-2006.

P. Jöckel, A. Kerkweg, A. Pozzer, R. Sander, H. Tost, H. Riede, A. Baumgaertner, S. Gromov, and B. Kern. Development cycle 2 of the modular earth submodel system (messy2). *Geoscientific Model Development*, 3(2):717–752, 2010. doi: 10.5194/gmd-3-717-2010. URL `https://gmd.copernicus.org/articles/3/717/2010/`.

P. Jöckel, H. Tost, A. Pozzer, M. Kunze, O. Kirner, C. A. M. Brenninkmeijer, S. Brinkop, D. S. Cai, C. Dyroff, J. Eckstein, F. Frank, H. Garny, K.-D. Gottschaldt, P. Graf, V. Grewe, A. Kerkweg, B. Kern, S. Matthes, M. Mertens, S. Meul, M. Neumaier, M. Nützel, S. Oberländer-Hayn, R. Ruhnke, T. Runde, R. Sander, D. Scharffe, and A. Zahn. Earth system chemistry integrated modelling (escimo) with the modular earth submodel system (messy) version 2.51. *Geoscientific Model Development*, 9(3):1153–1200, 2016. doi: 10.5194/gmd-9-1153-2016. URL `https://gmd.copernicus.org/articles/9/1153/2016/`.

J. W. Kaiser, A. Heil, M. O. Andreae, A. Benedetti, N. Chubarova, L. Jones, J.-J. Morcrette, M. Razinger, M. G. Schultz, M. Suttie, and G. R. van der Werf. Biomass burning emissions estimated with a global fire assimilation system based on observed fire radiative power. *Biogeosciences*, 9(1):527–554, 2012. doi: 10.5194/bg-9-527-2012. URL `https://bg.copernicus.org/articles/9/527/2012/`.

M. Kanakidou, J. H. Seinfeld, S. N. Pandis, I. Barnes, F. J. Dentener, M. C. Facchini, R. Van Dingenen, B. Ervens, A. Nenes, C. J. Nielsen, E. Swietlicki, J. P. Putaud, Y. Balkanski, S. Fuzzi, J. Horth, G. K. Moortgat, R. Winterhalter, C. E. L. Myhre, K. Tsigaridis, E. Vignati, E. G. Stephanou, and J. Wilson. Organic aerosol and global climate modelling: a review. *Atmospheric Chemistry and Physics*, 5(4):1053–1123, 2005. doi: 10.5194/acp-5-1053-2005. URL `https://acp.copernicus.org/articles/5/1053/2005/`.

M. Karl, H.-P. Dorn, F. Holland, R. Koppmann, D. Poppe, L. Rupp, A. Schaub, and A. Wahner. Product study of the reaction of oh radicals with isoprene in the atmosphere simulation chamber saphir. *Journal of atmospheric chemistry*, 55:167–187, 2006. doi: 10.1007/s10874-006-9034-x.

A. Kerkweg, J. Buchholz, L. Ganzeveld, A. Pozzer, H. Tost, and P. Jöckel. Technical note: An implementation of the dry removal processes dry deposition and sedimentation in the modular earth submodel system (messy). *Atmospheric Chemistry and Physics*, 6(12): 4617–4632, 2006a. doi: 10.5194/acp-6-4617-2006. URL `https://acp.copernicus.org/articles/6/4617/2006/`.

A. Kerkweg, R. Sander, H. Tost, and P. Jöckel. Technical note: Implementation of prescribed (offlem), calculated (onlem), and pseudo-emissions (tnudge) of chemical species in the modular earth submodel system (messy). *Atmospheric Chemistry and Physics*, 6 (11):3603–3609, 2006b. doi: 10.5194/acp-6-3603-2006. URL https://acp.copernicus.org/articles/6/3603/2006/.

A. Kerkweg, T. Kirfel, D. H. Do, S. Griessbach, P. Jöckel, and D. Taraborrelli. The messy dwarf (based on messy v2.55.2). *Geoscientific Model Development Discussions*, 2024:1–30, 2024. doi: 10.5194/gmd-2024-117. URL https://gmd.copernicus.org/preprints/gmd-2024-117/.

A. Klamt. Conductor-like screening model for real solvents: a new approach to the quantitative calculation of solvation phenomena. *The Journal of Physical Chemistry*, 99(7): 2224–2235, 1995. doi: 10.1021/j100007a062.

R. Kluger. Decarboxylation, co2 and the reversion problem. *Accounts of Chemical Research*, 48(11):2843–2849, 2015. doi: 10.1021/acs.accounts.5b00306. URL https://doi.org/10.1021/acs.accounts.5b00306.

C. Knote, A. Hodzic, and J. Jimenez. The effect of dry and wet deposition of condensable vapors on secondary organic aerosols concentrations over the continental us. *Atmospheric Chemistry and Physics*, 15(1):1–18, 2015. doi: 10.5194/acp-15-1-2015.

K. Kojima, S. Zhang, and T. Hiaki. Measuring methods of infinite dilution activity coefficients and a database for systems including water. *Fluid Phase Equilibria*, 131 (1):145–179, 1997a. ISSN 0378-3812. doi: 10.1016/S0378-3812(96)03210-4. URL https://www.sciencedirect.com/science/article/pii/S0378381296032104.

K. Kojima, S. Zhang, and T. Hiaki. Measuring methods of infinite dilution activity coefficients and a database for systems including water. *Fluid Phase Equilibria*, 131(1-2): 145–179, 1997b. doi: 10.1016/S0378-3812(96)03210-4.

D. Krause and P. Thörnig. Jureca: general-purpose supercomputer at jülich supercomputing centre. *Journal of large-scale research facilities JLSRF*, 2:A62–A62, 2016. doi: 10.17815/jlsrf-2-121.

U. Kuhn, M. O. Andreae, C. Ammann, A. Araújo, E. Brancaleoni, P. Ciccioli, T. Dindorf, M. Frattoni, L. V. Gatti, L. Ganzeveld, et al. Isoprene and monoterpene fluxes from central amazonian rainforest inferred from tower-based and airborne measurements, and implications on the atmospheric chemistry and the local carbon budget. *Atmospheric Chemistry and Physics*, 7(11):2855–2879, 2007. doi: 10.5194/acp-7-2855-2007.

R. Kühne, R.-U. Ebert, and G. Schüürmann. Prediction of the temperature dependency of henry's law constant from chemical structure. *Environmental science & technology*, 39 (17):6705–6711, 2005. doi: 10.1021/es050527h.

E. S. Kwok and R. Atkinson. Estimation of hydroxyl radical reaction rate constants for gas-phase organic compounds using a structure-reactivity relationship: An update. *Atmospheric Environment*, 29(14):1685–1695, 1995. doi: 10.1016/1352-2310(95)00069-B.

R. Kühne, R.-U. Ebert, and G. Schüürmann. Prediction of the temperature dependency of henry's law constant from chemical structure. *Environmental Science & Technology*, 39(17):6705–6711, 2005. doi: 10.1021/es050527h. URL `https://doi.org/10.1021/es050527h`.

A. Lambe, T. Onasch, P. Massoli, D. Croasdale, J. Wright, A. Ahern, L. Williams, D. Worsnop, W. Brune, and P. Davidovits. Laboratory studies of the chemical composition and cloud condensation nuclei (ccn) activity of secondary organic aerosol (soa) and oxidized primary organic aerosol (opoa). *Atmospheric Chemistry and Physics*, 11 (17):8913–8928, 2011. doi: 10.5194/acp-11-8913-2011.

J. Landgraf and P. Crutzen. An efficient method for online calculations of photolysis and heating rates. *Journal of the Atmospheric Sciences*, 55(5):863–878, 1998. doi: 10.1175/1520-0469(1998)055⟨0863:AEMFOC⟩2.0.CO;2.

T. E. Lane, N. M. Donahue, and S. N. Pandis. Simulating secondary organic aerosol formation using the volatility basis-set approach in a chemical transport model. *Atmospheric Environment*, 42(32):7439–7451, 2008. ISSN 1352-2310. doi: 10.1016/j.atmosenv.2008.06.026. URL `https://www.sciencedirect.com/science/article/pii/S1352231008005840`.

A. Laskin, J. Laskin, and S. A. Nizkorodov. Chemistry of Atmospheric Brown Carbon. *Chemical Reviews*, 115(10):4335–4382, 2015. ISSN 0009-2665. doi: 10.1021/cr5006167. URL `https://doi.org/10.1021/cr5006167`.

K. Lau, T. Rogers, and D. Zei. Modeling the temperature dependence of the henry's law constant of organic solutes in water. *Fluid Phase Equilibria*, 290(1):166–180, 2010. ISSN 0378-3812. doi: 10.1016/j.fluid.2009.11.020. URL `https://www.sciencedirect.com/science/article/pii/S0378381209004737`.

M. Lawrence, P. Jöckel, and R. Von Kuhlmann. What does the global mean oh concentration tell us? *Atmospheric Chemistry and Physics*, 1(1):37–49, 2001. doi: 10.5194/acp-1-37-2001.

J. Lelieveld. Clean air in the anthropocene. *Faraday discussions*, 200:693–703, 2017.

Y. Li, U. Pöschl, and M. Shiraiwa. Molecular corridors and parameterizations of volatility in the chemical evolution of organic aerosols. *Atmospheric Chemistry and Physics*, 16 (5):3327–3344, 2016. doi: 10.5194/acp-16-3327-2016.

Y. Lim, Y. Tan, and B. Turpin. Chemical insights, explicit chemistry, and yields of secondary organic aerosol from oh radical oxidation of methylglyoxal and glyoxal in the aqueous phase. *Atmospheric Chemistry and Physics*, 13(17):8651–8667, 2013.

G. Lin, J. E. Penner, M. G. Flanner, S. Sillman, L. Xu, and C. Zhou. Radiative forcing of organic aerosol in the atmosphere and on snow: Effects of soa and brown carbon. *Journal of Geophysical Research: Atmospheres*, 119(12):7453–7476, 2014. doi: 10.1002/2013JD021186.

D. Liu, Y. Zhang, S. Zhong, S. Chen, Q. Xie, D. Zhang, Q. Zhang, W. Hu, J. Deng, L. Wu, et al. Large differences of highly oxygenated organic molecules (homs) and low volatile species in soa formed from ozonolysis of β-pinene and limonene. *Atmospheric Chemistry and Physics Discussions*, 2022:1–29, 2022. doi: 10.5194/acp-23-8383-2023.

S. Lou, M. Shrivastava, R. C. Easter, Y. Yang, P.-L. Ma, H. Wang, M. J. Cubison, P. Campuzano-Jost, J. L. Jimenez, Q. Zhang, P. J. Rasch, J. E. Shilling, A. Zelenyuk, M. Dubey, P. Cameron-Smith, S. T. Martin, J. Schneider, and C. Schulz. New soa treatments within the energy exascale earth system model (e3sm): Strong production and sinks govern atmospheric soa distributions and radiative forcing. *Journal of Advances in Modeling Earth Systems*, 12(12):e2020MS002266, 2020. doi: 10.1029/2020MS002266. URL `https://agupubs.onlinelibrary.wiley.com/doi/abs/10.1029/2020MS002266`.

Z. Lu, D. G. Streets, E. Winijkul, F. Yan, Y. Chen, T. C. Bond, Y. Feng, M. K. Dubey, S. Liu, J. P. Pinto, and G. R. Carmichael. Light absorption properties and radiative effects of primary organic aerosol emissions. *Environmental Science & Technology*, 49(8):4868–4877, 2015. doi: 10.1021/acs.est.5b00211. URL `https://doi.org/10.1021/acs.est.5b00211`.

X. Mao, H. Gao, T. Huang, L. Zhang, and J. Ma. Modeling global persistent organic chemicals in clouds. *Atmospheric Environment*, 96:345–352, 2014. doi: 10.1016/j.atmosenv.2014.05.081.

C. Marcolli, B. Luo, and T. Peter. Mixing of the organic aerosol fractions: Liquids as the thermodynamically stable phases. *The Journal of Physical Chemistry A*, 108(12):2216–2224, 2004. doi: 10.1021/jp036080l.

M. Martinez, H. Harder, D. Kubistin, M. Rudolf, H. Bozem, G. Eerdekens, H. Fischer, T. Klüpfel, C. Gurk, R. Königstedt, et al. Hydroxyl radicals in the tropical troposphere over the suriname rainforest: airborne measurements. *Atmospheric Chemistry and Physics*, 10(8):3759–3773, 2010. doi: 10.5194/acp-10-3759-2010.

P. Massoli, H. Stark, M. R. Canagaratna, J. E. Krechmer, L. Xu, N. L. Ng, R. L. Mauldin III, C. Yan, J. Kimmel, P. K. Misztal, et al. Ambient measurements of highly oxidized gas-phase molecules during the southern oxidant and aerosol study (soas) 2013.

ACS Earth and Space Chemistry, 2(7):653–672, 2018. doi: 10.1021/acsearthspacechem.8b00028.

W. M. Meylan and P. H. Howard. Bond contribution method for estimating henry's law constants. *Environmental Toxicology and Chemistry*, 10(10):1283–1293, 1991. ISSN 1552-8618. doi: 10.1002/etc.5620101007. URL https://onlinelibrary.wiley.com/doi/abs/10.1002/etc.5620101007.

D. Minakata, K. Li, P. Westerhoff, and J. Crittenden. Development of a group contribution method to predict aqueous phase hydroxyl radical (ho•) reaction rate constants. *Environmental Science & Technology*, 43(16):6220–6227, 2009. doi: 10.1021/es900956c. URL https://doi.org/10.1021/es900956c.

J. M. Moch, E. Dovrou, L. J. Mickley, F. N. Keutsch, Y. Cheng, D. J. Jacob, J. Jiang, M. Li, J. W. Munger, X. Qiao, et al. Contribution of hydroxymethane sulfonate to ambient particulate matter: A potential explanation for high particulate sulfur during severe winter haze in beijing. *Geophysical Research Letters*, 45(21):11–969, 2018. doi: 10.1029/2018GL079309.

A. Monod and J. Doussin. Structure-activity relationship for the estimation of oh-oxidation rate constants of aliphatic organic compounds in the aqueous phase: alkanes, alcohols, organic acids and bases. *Atmospheric Environment*, 42(33):7611–7622, 2008a. ISSN 1352-2310. doi: 10.1016/j.atmosenv.2008.06.005. URL https://www.sciencedirect.com/science/article/pii/S1352231008005712.

A. Monod and J. Doussin. Structure-activity relationship for the estimation of oh-oxidation rate constants of aliphatic organic compounds in the aqueous phase: alkanes, alcohols, organic acids and bases. *Atmospheric Environment*, 42(33):7611–7622, 2008b. doi: 10.1016/j.atmosenv.2008.06.005.

C. Mouchel-Vallon, L. Deguillaume, A. Monod, H. Perroux, C. Rose, G. Ghigo, Y. Long, M. Leriche, B. Aumont, L. Patryl, et al. Cleps 1.0: A new protocol for cloud aqueous phase oxidation of voc mechanisms. *Geoscientific Model Development*, 10(3):1339–1362, 2017. doi: 10.5194/gmd-10-1339-2017.

Y. Nannoolal, J. Rarey, D. Ramjugernath, and W. Cordes. Estimation of pure component properties: Part 1. estimation of the normal boiling point of non-electrolyte organic compounds via group contributions and group interactions. *Fluid Phase Equilibria*, 226:45–63, 2004. doi: 10.1016/j.fluid.2004.09.001.

Y. Nannoolal, J. Rarey, and D. Ramjugernath. Estimation of pure component properties: Part 3. estimation of the vapor pressure of non-electrolyte organic compounds via group contributions and group interactions. *Fluid Phase Equilibria*, 269(1-2):117–133, 2008. doi: 10.1016/j.fluid.2008.04.020.

M. J. Newland, A. R. Rickard, T. Sherwen, M. J. Evans, L. Vereecken, A. Muñoz, M. Ródenas, and W. J. Bloss. The atmospheric impacts of monoterpene ozonolysis on global stabilised criegee intermediate budgets and so_2 oxidation: experiment, theory and modelling. *Atmospheric Chemistry and Physics*, 18(8):6095–6120, 2018. doi: 10.5194/acp-18-6095-2018. URL https://acp.copernicus.org/articles/18/6095/2018/.

N. Ng, J. Kroll, A. Chan, P. Chhabra, R. Flagan, and J. Seinfeld. Secondary organic aerosol formation from m-xylene, toluene, and benzene. *Atmospheric Chemistry and Physics*, 7 (14):3909–3922, 2007. doi: 10.5194/acp-7-3909-2007.

T. Nguyen, M. Petters, S. Suda, H. Guo, R. Weber, and A. Carlton. Trends in particle-phase liquid water during the southern oxidant and aerosol study. *Atmospheric Chemistry and Physics*, 14(20):10911–10930, 2014. doi: 10.5194/acp-14-10911-2014.

N. Ni and S. H. Yalkowsky. Prediction of setschenow constants. *International Journal of Pharmaceutics*, 254(2):167–172, 2003. ISSN 0378-5173. doi: 10.1016/S0378-5173(03)00008-5. URL https://www.sciencedirect.com/science/article/pii/S0378517303000085.

A. Novelli, C. Cho, H. Fuchs, A. Hofzumahaus, F. Rohrer, R. Tillmann, A. Kiendler-Scharr, A. Wahner, and L. Vereecken. Experimental and theoretical study on the impact of a nitrate group on the chemistry of alkoxy radicals. *Physical Chemistry Chemical Physics*, 23(9):5474–5495, 2021. doi: 10.1039/D0CP05555G.

N. M. O'Boyle, M. Banck, C. A. James, C. Morley, T. Vandermeersch, and G. R. Hutchison. Open babel: An open chemical toolbox. *Journal of cheminformatics*, 3:1–14, 2011. doi: 10.1186/1758-2946-3-33.

M. Octaviani, M. Shrivastava, R. A. Zaveri, A. Zelenyuk, Y. Zhang, Q. Z. Rasool, D. M. Bell, M. Riva, M. Glasius, and J. D. Surratt. Modeling the Size Distribution and Chemical Composition of Secondary Organic Aerosols during the Reactive Uptake of Isoprene-Derived Epoxydiols under Low-Humidity Condition. *ACS Earth and Space Chemistry*, 5(11):3247–3257, Nov. 2021. doi: 10.1021/acsearthspacechem.1c00303. URL https://doi.org/10.1021/acsearthspacechem.1c00303.

J. R. Odum. *Secondary organic aerosol formation and gas/aerosol partitioning*. California Institute of Technology, 1998.

J. J. Orlando and G. S. Tyndall. Laboratory studies of organic peroxy radical chemistry: an overview with emphasis on recent issues of atmospheric significance. *Chem. Soc. Rev.*, 41:6294–6317, 2012. doi: 10.1039/C2CS35166H. URL http://dx.doi.org/10.1039/C2CS35166H.

T. Otto, B. Stieger, P. Mettke, and H. Herrmann. Tropospheric aqueous-phase oxidation of isoprene-derived dihydroxycarbonyl compounds. *The Journal of Physical Chemistry A*, 121(34):6460–6470, 2017. doi: 10.1021/acs.jpca.7b05879.

M. Paglione, D. C. Beddows, A. Jones, T. Lachlan-Cope, M. Rinaldi, S. Decesari, F. Manarini, M. Russo, K. Mansour, R. M. Harrison, et al. Simultaneous organic aerosol source apportionment at two antarctic sites reveals large-scale and eco-region specific components. *Atmospheric Chemistry and Physics*, 24(10):6305–6322, 2024. doi: 10.5194/acp-24-6305-2024.

B. B. Palm, Q. Peng, C. D. Fredrickson, B. H. Lee, L. A. Garofalo, M. A. Pothier, S. M. Kreidenweis, D. K. Farmer, R. P. Pokhrel, Y. Shen, S. M. Murphy, W. Permar, L. Hu, T. L. Campos, S. R. Hall, K. Ullmann, X. Zhang, F. Flocke, E. V. Fischer, and J. A. Thornton. Quantification of organic aerosol and brown carbon evolution in fresh wildfire plumes. *Proceedings of the National Academy of Sciences*, 117(47):29469–29477, 2020. doi: 10.1073/pnas.2012218117. URL `https://www.pnas.org/doi/abs/10.1073/pnas.2012218117`.

J. Y. S. Pang, A. Novelli, M. Kaminski, I.-H. Acir, B. Bohn, P. T. M. Carlsson, C. Cho, H.-P. Dorn, A. Hofzumahaus, X. Li, A. Lutz, S. Nehr, D. Reimer, F. Rohrer, R. Tillmann, R. Wegener, A. Kiendler-Scharr, A. Wahner, and H. Fuchs. Investigation of the limonene photooxidation by oh at different no concentrations in the atmospheric simulation chamber saphir (simulation of atmospheric photochemistry in a large reaction chamber). *Atmospheric Chemistry and Physics*, 22(13):8497–8527, 2022. doi: 10.5194/acp-22-8497-2022. URL `https://acp.copernicus.org/articles/22/8497/2022/`.

J. F. Pankow. An absorption model of the gas/aerosol partitioning involved in the formation of secondary organic aerosol. *Atmospheric Environment*, 28(2):189–193, 1994. ISSN 1352-2310. doi: 10.1016/1352-2310(94)90094-9. URL `https://www.sciencedirect.com/science/article/pii/1352231094900949`.

F. Paulot, J. D. Crounse, H. G. Kjaergaard, A. Kürten, J. M. St. Clair, J. H. Seinfeld, and P. O. Wennberg. Unexpected epoxide formation in the gas-phase photooxidation of isoprene. *science*, 325(5941):730–733, 2009. doi: 10.1126/science.1172910.

J. Peeters, W. Boullart, V. Pultau, S. Vandenberk, and L. Vereecken. Structure activity relationship for the addition of oh to (poly)alkenes: Site-specific and total rate constants. *The Journal of Physical Chemistry A*, 111(9):1618–1631, 2007. doi: 10.1021/jp066973o.

S. S. Petters, D. Pagonis, M. S. Claflin, E. J. T. Levin, M. D. Petters, P. J. Ziemann, and S. M. Kreidenweis. Hygroscopicity of organic compounds as a function of carbon chain length and carboxyl, hydroperoxy, and carbonyl functional groups. *The Journal of Physical Chemistry A*, 121(27):5164–5174, 2017. doi: 10.1021/acs.jpca.7b04114. URL `https://doi.org/10.1021/acs.jpca.7b04114`.

S. S. Petters, T. Cui, Z. Zhang, A. Gold, V. F. McNeill, J. D. Surratt, and B. J. Turpin. Organosulfates from dark aqueous reactions of isoprene-derived epoxydiols under cloud and fog conditions: Kinetics, mechanism, and effect of reaction environment on regioselectivity of sulfate addition. *ACS Earth and Space Chemistry*, 5(3):474–486, 2021. doi: 10.1021/acsearthspacechem.0c00293?ref=pdf.

I. R. Piletic and T. E. Kleindienst. Rates and yields of unimolecular reactions producing highly oxidized peroxy radicals in the oh-induced autoxidation of α-pinene, β-pinene, and limonene. *The Journal of Physical Chemistry A*, 126(1):88–100, 2022. doi: 10.1021/acs.jpca.1c07961.

M. L. Pöhlker, C. Pöhlker, J. Quaas, J. Mülmenstädt, A. Pozzer, M. O. Andreae, P. Artaxo, K. Block, H. Coe, B. Ervens, et al. Global organic and inorganic aerosol hygroscopicity and its effect on radiative forcing. *Nature communications*, 14(1):6139, 2023. doi: 10.1038/s41467-023-41695-8.

A. Pozzer, P. Jöckel, R. Sander, J. Williams, L. Ganzeveld, and J. Lelieveld. Technical note: The messy-submodel airsea calculating the air-sea exchange of chemical species. *Atmospheric Chemistry and Physics*, 6(12):5435–5444, 2006. doi: 10.5194/acp-6-5435-2006. URL `https://acp.copernicus.org/articles/6/5435/2006/`.

A. Pozzer, S. F. Reifenberg, V. Kumar, B. Franco, M. Kohl, D. Taraborrelli, S. Gromov, S. Ehrhart, P. Jöckel, R. Sander, V. Fall, S. Rosanka, V. Karydis, D. Akritidis, T. Emmerichs, M. Crippa, D. Guizzardi, J. W. Kaiser, L. Clarisse, A. Kiendler-Scharr, H. Tost, and A. Tsimpidi. Simulation of organics in the atmosphere: evaluation of emacv2.54 with the mainz organic mechanism (mom) coupled to the oracle (v1.0) submodel. *Geoscientific Model Development*, 15(6):2673–2710, 2022. doi: 10.5194/gmd-15-2673-2022. URL `https://gmd.copernicus.org/articles/15/2673/2022/`.

A. Pozzer, S. C. Anenberg, S. Dey, A. Haines, J. Lelieveld, and S. Chowdhury. Mortality attributable to ambient air pollution: A review of global estimates. *GeoHealth*, 7(1):e2022GH000711, 2023. doi: 10.1029/2022GH000711. URL `https://agupubs.onlinelibrary.wiley.com/doi/abs/10.1029/2022GH000711`.

K. J. Pringle, H. Tost, S. Message, B. Steil, D. Giannadaki, A. Nenes, C. Fountoukis, P. Stier, E. Vignati, and J. Lelieveld. Description and evaluation of gmxe: a new aerosol submodel for global simulations (v1). *Geoscientific Model Development*, 3(2):391–412, 2010. doi: 10.5194/gmd-3-391-2010. URL `https://gmd.copernicus.org/articles/3/391/2010/`.

H. Pye, A. Chan, M. Barkley, and J. Seinfeld. Global modeling of organic aerosol: the importance of reactive nitrogen (no x and no 3). *Atmospheric Chemistry and Physics*, 10(22):11261–11276, 2010. doi: 10.5194/acp-10-11261-2010.

H. O. Pye, B. N. Murphy, L. Xu, N. L. Ng, A. G. Carlton, H. Guo, R. Weber, P. Vasilakos, K. W. Appel, S. H. Budisulistiorini, et al. On the implications of aerosol liquid water and phase separation for organic aerosol mass. *Atmospheric Chemistry and Physics*, 17 (1):343–369, 2017. doi: 10.5194/acp-17-343-2017.

H. O. Pye, A. Nenes, B. Alexander, A. P. Ault, M. C. Barth, S. L. Clegg, J. L. Collett Jr, K. M. Fahey, C. J. Hennigan, H. Herrmann, et al. The acidity of atmospheric particles and clouds. *Atmospheric chemistry and physics*, 20(8):4809–4888, 2020a. doi: 10.5194/acp-20-4809-2020.

H. O. T. Pye, A. Nenes, B. Alexander, A. P. Ault, M. C. Barth, S. L. Clegg, J. L. Collett Jr., K. M. Fahey, C. J. Hennigan, H. Herrmann, M. Kanakidou, J. T. Kelly, I.-T. Ku, V. F. McNeill, N. Riemer, T. Schaefer, G. Shi, A. Tilgner, J. T. Walker, T. Wang, R. Weber, J. Xing, R. A. Zaveri, and A. Zuend. The acidity of atmospheric particles and clouds. *Atmospheric Chemistry and Physics*, 20(8):4809–4888, 2020b. doi: 10.5194/acp-20-4809-2020. URL `https://acp.copernicus.org/articles/20/4809/2020/`.

M. Qin, Y. Hu, X. Wang, P. Vasilakos, C. M. Boyd, L. Xu, Y. Song, N. L. Ng, A. Nenes, and A. G. Russell. Modeling biogenic secondary organic aerosol (bsoa) formation from monoterpene reactions with no3: A case study of the soas campaign using cmaq. *Atmospheric Environment*, 184:146–155, 2018.

K. Rajeev, V. Ramanathan, and J. Meywerk. Regional aerosol distribution and its long-range transport over the indian ocean. *Journal of Geophysical Research: Atmospheres*, 105(D2):2029–2043, 2000. doi: 10.1029/1999JD900414.

T. Raventos-Duran, M. Camredon, R. Valorso, C. Mouchel-Vallon, and B. Aumont. Structure-activity relationships to estimate the effective henry's law constants of organics of atmospheric interest. *Atmospheric Chemistry and Physics*, 10(16):7643–7654, 2010. doi: 10.5194/acp-10-7643-2010.

A. M. J. Rickards, R. E. H. Miles, J. F. Davies, F. H. Marshall, and J. P. Reid. Measurements of the sensitivity of aerosol hygroscopicity and the κ parameter to the o/c ratio. *The Journal of Physical Chemistry A*, 117(51):14120–14131, 2013. doi: 10.1021/jp407991n. URL `10.1021/jp407991n`.

T. Riedel, Y.-H. Lin, Z. Zhang, K. Chu, J. Thornton, W. Vizuete, A. Gold, and J. Surratt. Constraining condensed-phase formation kinetics of secondary organic aerosol components from isoprene epoxydiols. *Atmospheric Chemistry and Physics*, 16(3):1245–1254, 2016. doi: 10.5194/acp-16-1245-2016.

M. P. Rissanen, T. Kurten, M. Sipila, J. A. Thornton, J. Kangasluoma, N. Sarnela, H. Junninen, S. Jørgensen, S. Schallhart, M. K. Kajos, et al. The formation of highly oxidized multifunctional products in the ozonolysis of cyclohexene. *Journal of the American Chemical Society*, 136(44):15596–15606, 2014. doi: 10.1021/ja507146s.

E. Roeckner, G. Bäuml, L. Bonaventura, R. Brokopf, M. Esch, M. Giorgetta, S. Hagemann, I. Kirchner, L. Kornblueh, E. Manzini, et al. The atmospheric general circulation model echam 5. part i: Model description. 2003.

F. Rohrer, B. Bohn, T. Brauers, D. Brüning, F.-J. Johnen, A. Wahner, and J. Kleffmann. Characterisation of the photolytic hono-source in the atmosphere simulation chamber saphir. *Atmospheric Chemistry and Physics*, 5(8):2189–2201, 2005. doi: 10.5194/acp-5-2189-2005.

S. Rosanka, R. Sander, B. Franco, C. Wespes, A. Wahner, and D. Taraborrelli. Oxidation of low-molecular-weight organic compounds in cloud droplets: global impact on tropospheric oxidants. *Atmospheric Chemistry and Physics*, 21(12):9909–9930, 2021a. doi: 10.5194/acp-21-9909-2021. URL `https://acp.copernicus.org/articles/21/9909/2021/`.

S. Rosanka, R. Sander, A. Wahner, and D. Taraborrelli. Oxidation of low-molecular-weight organic compounds in cloud droplets: development of the jülich aqueous-phase mechanism of organic chemistry (jamoc) in caaba/mecca (version 4.5.0). *Geoscientific Model Development*, 14(6):4103–4115, 2021b. doi: 10.5194/gmd-14-4103-2021. URL `https://gmd.copernicus.org/articles/14/4103/2021/`.

S. Rosanka, H. Tost, R. Sander, P. Jöckel, A. Kerkweg, and D. Taraborrelli. How non-equilibrium aerosol chemistry impacts particle acidity: the gmxe aerosol chemistry (gmxe–aerchem, v1.0) sub-submodel of messy. *Geoscientific Model Development*, 17(7): 2597–2615, 2024. doi: 10.5194/gmd-17-2597-2024. URL `https://gmd.copernicus.org/articles/17/2597/2024/`.

A. Ruggaber, R. Dlugi, A. Bott, R. Forkel, H. Herrmann, and H.-W. Jacobi. Modelling of radiation quantities and photolysis frequencies in the aqueous phase in the troposphere. *Atmospheric Environment*, 31(19):3137–3150, 1997. ISSN 1352-2310. doi: 10.1016/S1352-2310(97)00058-7. URL `https://www.sciencedirect.com/science/article/pii/S1352231097000587`.

A. Rusumdar, R. Wolke, A. Tilgner, and H. Herrmann. Treatment of non-ideality in the spaccim multiphase model–part 1: Model development. *Geoscientific Model Development*, 9(1):247–281, 2016. doi: 10.5194/gmd-9-247-2016.

A. J. Rusumdar, A. Tilgner, R. Wolke, and H. Herrmann. Treatment of non-ideality in the spaccim multiphase model–part 2: Impacts on the multiphase chemical processing in deliquesced aerosol particles. *Atmospheric Chemistry and Physics*, 20(17):10351–10377, 2020. doi: 10.5194/acp-20-10351-2020.

H. Saathoff, K.-H. Naumann, O. Möhler, Å. M. Jonsson, M. Hallquist, A. Kiendler-Scharr, T. F. Mentel, R. Tillmann, and U. Schurath. Temperature dependence of yields of

secondary organic aerosols from the ozonolysis of α-pinene and limonene. *Atmospheric Chemistry and Physics*, 9(5):1551–1577, 2009. doi: 10.5194/acp-9-1551-2009.

T. Sakulyanontvittaya, T. Duhl, C. Wiedinmyer, D. Helmig, S. Matsunaga, M. Potosnak, J. Milford, and A. Guenther. Monoterpene and sesquiterpene emission estimates for the united states. *Environmental science & technology*, 42(5):1623–1629, 2008. doi: 10.1021/es702274e.

S. Sanap and G. Pandithurai. Inter-annual variability of aerosols and its relationship with regional climate over indian subcontinent. *International Journal of Climatology*, 35(5), 2015. doi: 10.1002/joc.4037.

R. Sander. Modeling atmospheric chemistry: Interactions between gas-phase species and liquid cloud/aerosol particles. *Surveys in Geophysics*, 20:1–31, 1999. doi: 10.1023/A:1006501706704.

R. Sander. Compilation of henry's law constants (version 4.0) for water as solvent. *Atmospheric Chemistry and Physics*, 15(8):4399–4981, 2015.

R. Sander. Compilation of henry's law constants (version 5.0.0) for water as solvent. 23:10901–12440, 2023. doi: 10.5194/ACP-23-10901-2023.

R. Sander, A. Kerkweg, P. Jöckel, and J. Lelieveld. The new comprehensive atmospheric chemistry module mecca. *Atmospheric Chemistry and Physics*, 5(2):445–450, 2005. doi: 10.5194/acp-5-445-2005.

R. Sander, A. Baumgaertner, S. Gromov, H. Harder, P. Jöckel, A. Kerkweg, D. Kubistin, E. Regelin, H. Riede, A. Sandu, et al. The atmospheric chemistry box model caaba/mecca-3.0. *Geoscientific Model Development*, 4(2):373–380, 2011. doi: 10.5194/gmd-4-373-2011.

R. Sander, P. Jöckel, O. Kirner, A. T. Kunert, J. Landgraf, and A. Pozzer. The photolysis module jval-14, compatible with the messy standard, and the jval preprocessor (jvpp). *Geoscientific Model Development*, 7(6):2653–2662, 2014a. doi: 10.5194/gmd-7-2653-2014. URL `https://gmd.copernicus.org/articles/7/2653/2014/`.

R. Sander, P. Jöckel, O. Kirner, A. T. Kunert, J. Landgraf, and A. Pozzer. The photolysis module JVAL-14, compatible with the MESSy standard, and the JVal PreProcessor (JVPP). *Geosci. Model Dev.*, 7:2653–2662, 2014b. doi: 10.5194/GMD-7-2653-2014.

R. Sander, A. Baumgaertner, D. Cabrera-Perez, F. Frank, S. Gromov, J.-U. Grooß, H. Harder, V. Huijnen, P. Jöckel, V. A. Karydis, et al. The community atmospheric chemistry box model caaba/mecca-4.0. *Geoscientific model development*, 12(4):1365–1385, 2019. doi: 10.5194/gmd-12-1365-2019.

R. Sander, W. E. Acree Jr, A. De Visscher, S. E. Schwartz, and T. J. Wallington. Henry's law constants (iupac recommendations 2021). *Pure and applied chemistry*, 94(1):71–85, 2022. doi: 10.1515/pac-2020-0302.

A. Sandu and R. Sander. Simulating chemical systems in fortran90 and matlab with the kinetic preprocessor kpp-2.1. *Atmospheric Chemistry and Physics*, 6(1):187–195, 2006. doi: 10.5194/acp-6-187-2006.

A. Sandu, J. Verwer, J. Blom, E. Spee, G. Carmichael, and F. Potra. Benchmarking stiff ode solvers for atmospheric chemistry problems ii: Rosenbrock solvers. *Atmospheric environment*, 31(20):3459–3472, 1997. doi: 10.1016/S1352-2310(97)83212-8.

N. Sareen, A. G. Carlton, J. D. Surratt, A. Gold, B. Lee, F. D. Lopez-Hilfiker, C. Mohr, J. A. Thornton, Z. Zhang, Y. B. Lim, et al. Identifying precursors and aqueous organic aerosol formation pathways during the soas campaign. *Atmospheric Chemistry and Physics*, 16 (22):14409–14420, 2016. doi: 10.5194/acp-16-14409-2016.

S. M. Saunders, M. E. Jenkin, R. G. Derwent, and M. J. Pilling. Protocol for the development of the master chemical mechanism, mcm v3 (part a): tropospheric degradation of non-aromatic volatile organic compounds. *Atmospheric Chemistry and Physics*, 3 (1):161–180, 2003. doi: 10.5194/acp-3-161-2003. URL `https://acp.copernicus.org/articles/3/161/2003/`.

E. Schlosser, B. Bohn, T. Brauers, H.-P. Dorn, H. Fuchs, R. Häseler, A. Hofzumahaus, F. Holland, F. Rohrer, L. O. Rupp, et al. Intercomparison of two hydroxyl radical measurement techniques at the atmosphere simulation chamber saphir. *Journal of atmospheric chemistry*, 56:187–205, 2007. doi: 10.1007/s10874-006-9049-3.

J. Schmale, J. Schneider, G. Ancellet, B. Quennehen, A. Stohl, H. Sodemann, J. F. Burkhart, T. Hamburger, S. R. Arnold, A. Schwarzenboeck, et al. Source identification and airborne chemical characterisation of aerosol pollution from long-range transport over greenland during polarcat summer campaign 2008. *Atmospheric Chemistry and Physics*, 11(19):10097–10123, 2011. doi: 10.5194/acp-11-10097-2011.

S. Schmitt. *Formation of Secondary Organic Aerosol from Photo-Oxidation of Benzene: a Chamber Study*, volume 412. 2018.

T. Schmitz, D. Hassel, and F.-J. Weber. Determination of voc-components in the exhaust of gasoline and diesel passenger cars. *Atmospheric environment*, 34(27):4639–4647, 2000. doi: 10.1016/S1352-2310(00)00303-4.

L. Schöne and H. Herrmann. Kinetic measurements of the reactivity of hydrogen peroxide and ozone towards small atmospherically relevant aldehydes, ketones and organic acids in aqueous solutions. *Atmospheric Chemistry and Physics*, 14(9):4503–4514, 2014. doi:

10.5194/acp-14-4503-2014. URL https://acp.copernicus.org/articles/14/4503/2014/.

M. K. Schueneman, B. A. Nault, P. Campuzano-Jost, D. S. Jo, D. A. Day, J. C. Schroder, B. B. Palm, A. Hodzic, J. E. Dibb, and J. L. Jimenez. Aerosol ph indicator and organosulfate detectability from aerosol mass spectrometry measurements. *Atmospheric Measurement Techniques*, 14(3):2237–2260, 2021. doi: 10.5194/amt-14-2237-2021. URL https://amt.copernicus.org/articles/14/2237/2021/.

C. Schulz, J. Schneider, B. Amorim Holanda, O. Appel, A. Costa, S. S. de Sá, V. Dreiling, D. Fütterer, T. Jurkat-Witschas, T. Klimach, C. Knote, M. Krämer, S. T. Martin, S. Mertes, M. L. Pöhlker, D. Sauer, C. Voigt, A. Walser, B. Weinzierl, H. Ziereis, M. Zöger, M. O. Andreae, P. Artaxo, L. A. T. Machado, U. Pöschl, M. Wendisch, and S. Borrmann. Aircraft-based observations of isoprene-epoxydiol-derived secondary organic aerosol (iepox-soa) in the tropical upper troposphere over the amazon region. *Atmospheric Chemistry and Physics*, 18(20):14979–15001, 2018. doi: 10.5194/acp-18-14979-2018. URL https://acp.copernicus.org/articles/18/14979/2018/.

A. Schumpe. The estimation of gas solubilities in salt solutions. *Chemical engineering science*, 48(1):153–158, 1993. doi: 10.1016/0009-2509(93)80291-W.

J. Setschenow. Über die konstitution der salzlösungen auf grund ihres verhaltens zu kohlensäure. *Zeitschrift für Physikalische Chemie*, 4U(1):117–125, 1889. doi: doi: 10.1515/zpch-1889-0409. URL https://doi.org/10.1515/zpch-1889-0409.

J. E. Shilling, R. A. Zaveri, J. D. Fast, L. Kleinman, M. L. Alexander, M. R. Canagaratna, E. Fortner, J. M. Hubbe, J. T. Jayne, A. Sedlacek, A. Setyan, S. Springston, D. R. Worsnop, and Q. Zhang. Enhanced soa formation from mixed anthropogenic and biogenic emissions during the cares campaign. *Atmospheric Chemistry and Physics*, 13(4):2091–2113, 2013. doi: 10.5194/acp-13-2091-2013. URL https://acp.copernicus.org/articles/13/2091/2013/.

M. Shiraiwa, K. Ueda, A. Pozzer, G. Lammel, C. J. Kampf, A. Fushimi, S. Enami, A. M. Arangio, J. Fröhlich-Nowoisky, Y. Fujitani, A. Furuyama, P. S. J. Lakey, J. Lelieveld, K. Lucas, Y. Morino, U. Pöschl, S. Takahama, A. Takami, H. Tong, B. Weber, A. Yoshino, and K. Sato. Aerosol health effects from molecular to global scales. *Environmental Science & Technology*, 51(23):13545–13567, 2017. doi: 10.1021/acs.est.7b04417. URL https://doi.org/10.1021/acs.est.7b04417.

M. K. Shrivastava, T. E. Lane, N. M. Donahue, S. N. Pandis, and A. L. Robinson. Effects of gas particle partitioning and aging of primary emissions on urban and regional organic aerosol concentrations. *Journal of Geophysical Research: Atmospheres*, 113(D18), 2008. doi: 10.1029/2007JD009735.

P. Sicard. Ground-level ozone over time: an observation-based global overview. *Current Opinion in Environmental Science & Health*, 19:100226, 2021. doi: 10.1016/j.coesh.2020.100226.

M. Simmel and S. Wurzler. Condensation and activation in sectional cloud microphysical models. *Atmospheric research*, 80(2-3):218–236, 2006. doi: 10.1016/j.atmosres.2005.08.002.

K. Sindelarova, C. Granier, I. Bouarar, A. Guenther, S. Tilmes, T. Stavrakou, J.-F. Müller, U. Kuhn, P. Stefani, and W. Knorr. Global data set of biogenic voc emissions calculated by the megan model over the last 30 years. *Atmospheric Chemistry and Physics*, 14(17):9317–9341, 2014. doi: 10.5194/acp-14-9317-2014.

R. Sivaramakrishnan and J. Michael. Rate constants for oh with selected large alkanes: shock-tube measurements and an improved group scheme. *The Journal of Physical Chemistry A*, 113(17):5047–5060, 2009. doi: 10.1021/jp810987u.

J. M. St. Clair, J. C. Rivera-Rios, J. D. Crounse, H. C. Knap, K. H. Bates, A. P. Teng, S. Jørgensen, H. G. Kjaergaard, F. N. Keutsch, and P. O. Wennberg. Kinetics and products of the reaction of the first-generation isoprene hydroxy hydroperoxide (isopooh) with oh. *The Journal of Physical Chemistry A*, 120(9):1441–1451, 2016. doi: 10.1021/acs.jpca.5b06532.

J. Staudinger and P. V. Roberts. A critical compilation of henry's law constant temperature dependence relations for organic compounds in dilute aqueous solutions. *Chemosphere*, 44(4):561–576, 2001. ISSN 0045-6535. doi: 10.1016/S0045-6535(00)00505-1. URL `https://www.sciencedirect.com/science/article/pii/S0045653500005051`.

M. I. Stefan and J. R. Bolton. Reinvestigation of the acetone degradation mechanism in dilute aqueous solution by the uv/h2o2 process. *Environmental Science & Technology*, 33(6):870–873, 1999. doi: 10.1021/es9808548. URL `https://doi.org/10.1021/es9808548`.

D. Taraborrelli. *Isoprene oxidation and its impacts on the atmospheric composition*. PhD thesis, Citeseer, 2010.

D. Taraborrelli, M. Lawrence, T. Butler, R. Sander, and J. Lelieveld. Mainz isoprene mechanism 2 (mim2): an isoprene oxidation mechanism for regional and global atmospheric modelling. *Atmospheric Chemistry and Physics*, 9(8):2751–2777, 2009. doi: 10.5194/acp-9-2751-2009.

D. Topping, M. Barley, M. K. Bane, N. Higham, B. Aumont, N. Dingle, and G. McFiggans. Umansysprop v1. 0: an online and open-source facility for molecular property prediction and atmospheric aerosol calculations. *Geoscientific Model Development*, 9(2):899–914, 2016. doi: 10.5194/gmd-9-899-2016.

H. Tost, P. Jöckel, A. Kerkweg, R. Sander, and J. Lelieveld. Technical note: A new comprehensive scavenging submodel for global atmospheric chemistry modelling. *Atmospheric Chemistry and Physics*, 6(3):565–574, 2006a. doi: 10.5194/acp-6-565-2006. URL `https://acp.copernicus.org/articles/6/565/2006/`.

H. Tost, P. Jöckel, A. Kerkweg, R. Sander, and J. Lelieveld. A new comprehensive scavenging submodel for global atmospheric chemistry modelling. *Atmospheric Chemistry and Physics*, 6(3):565–574, 2006b. doi: 1680-7375/acpd/2005-5-11157.

H. Tost, P. Jöckel, and J. Lelieveld. Lightning and convection parameterisations; uncertainties in global modelling. *Atmospheric Chemistry and Physics*, 7(17):4553–4568, 2007. doi: 10.5194/acp-7-4553-2007. URL `https://acp.copernicus.org/articles/7/4553/2007/`.

A. Tsimpidi, V. Karydis, A. Pozzer, S. Pandis, and J. Lelieveld. Oracle (v1. 0): module to simulate the organic aerosol composition and evolution in the atmosphere. *Geoscientific Model Development*, 7(6):3153–3172, 2014. doi: 10.5194/gmd-7-3153-2014.

A. P. Tsimpidi, V. A. Karydis, A. Pozzer, S. N. Pandis, and J. Lelieveld. Oracle 2-d (v2.0): an efficient module to compute the volatility and oxygen content of organic aerosol with a global chemistry–climate model. *Geoscientific Model Development*, 11(8):3369–3389, 2018. doi: 10.5194/gmd-11-3369-2018. URL `https://gmd.copernicus.org/articles/11/3369/2018/`.

US-EPA. Estimation programs interface suite™ for microsoft® windows, v 4.11, 2012. United States Environmental Protection Agency, Washington, DC, USA.

H. Vehkamäki, M. Kulmala, I. Napari, K. E. Lehtinen, C. Timmreck, M. Noppel, and A. Laaksonen. An improved parameterization for sulfuric acid–water nucleation rates for tropospheric and stratospheric conditions. *Journal of Geophysical Research: Atmospheres*, 107(D22):AAC–3, 2002. doi: 10.1029/2002JD002184.

L. Vereecken. Reaction mechanisms for the atmospheric oxidation of monocyclic aromatic compounds. In *Advances in Atmospheric Chemistry: Volume 2: Organic Oxidation and Multiphase Chemistry*, pages 377–527. World Scientific, 2019. doi: 10.1142/9789813271838_0006.

L. Vereecken and B. Nozière. H migration in peroxy radicals under atmospheric conditions. *Atmospheric chemistry and physics*, 20(12):7429–7458, 2020. doi: 10.5194/acp-20-7429-2020.

L. Vereecken and J. Peeters. Nontraditional (per) oxy ring-closure paths in the atmospheric oxidation of isoprene and monoterpenes. *The Journal of Physical Chemistry A*, 108(24):5197–5204, 2004. doi: 10.1021/jp049219g.

L. Vereecken and J. Peeters. A theoretical study of the oh-initiated gas-phase oxidation mechanism of β-pinene (c 10 h 16): first generation products. *Physical Chemistry Chemical Physics*, 14(11):3802–3815, 2012. doi: 10.1039/c2cp23711c.

L. Vereecken, P. Carlsson, A. Novelli, F. Bernard, S. Brown, C. Cho, J. Crowley, H. Fuchs, W. Mellouki, D. Reimer, et al. Theoretical and experimental study of peroxy and alkoxy radicals in the no 3-initiated oxidation of isoprene. *Physical Chemistry Chemical Physics*, 23(9):5496–5515, 2021. doi: 10.1039/D0CP06267G.

E. Vignati, J. Wilson, and P. Stier. M7: An efficient size-resolved aerosol microphysics module for large-scale aerosol transport models. *Journal of Geophysical Research: Atmospheres*, 109(D22), 2004. doi: 10.1029/2003JD004485.

P. W. Villalta, E. R. Lovejoy, and D. R. Hanson. Reaction probability of peroxyacetyl radical on aqueous surfaces. *Geophysical research letters*, 23(14):1765–1768, 1996. doi: 10.1029/96GL01286.

E. von Schneidemesser, J. J. Schauer, G. S. Hagler, and M. H. Bergin. Concentrations and sources of carbonaceous aerosol in the atmosphere of summit, greenland. *Atmospheric Environment*, 43(27):4155–4162, 2009. doi: 10.1016/j.atmosenv.2009.05.043.

C. Wang, T. Yuan, S. A. Wood, K.-U. Goss, J. Li, Q. Ying, and F. Wania. Uncertain henry's law constants compromise equilibrium partitioning calculations of atmospheric oxidation products. *Atmospheric Chemistry and Physics*, 17(12):7529–7540, 2017. doi: 10.5194/acp-17-7529-2017.

L. Wang, R. Wu, and C. Xu. Atmospheric oxidation mechanism of benzene. fates of alkoxy radical intermediates and revised mechanism. *The Journal of Physical Chemistry A*, 117 (51):14163–14168, 2013. doi: 10.1021/jp4101762.

S. Wang, Y. Zhao, A. W. Chan, M. Yao, Z. Chen, and J. P. Abbatt. Organic peroxides in aerosol: key reactive intermediates for multiphase processes in the atmosphere. *Chemical Reviews*, 123(4):1635–1679, 2023. doi: 10.1021/acs.chemrev.2c00430.

E. M. Waxman, K. Dzepina, B. Ervens, J. Lee-Taylor, B. Aumont, J. L. Jimenez, S. Madronich, and R. Volkamer. Secondary organic aerosol formation from semi-and intermediate-volatility organic compounds and glyoxal: Relevance of o/c as a tracer for aqueous multiphase chemistry. *Geophysical Research Letters*, 40(5):978–982, 2013. doi: 10.1002/grl.50203.

W. Wei, S. Wang, S. Chatani, Z. Klimont, J. Cofala, and J. Hao. Emission and speciation of non-methane volatile organic compounds from anthropogenic sources in china. *Atmospheric Environment*, 42(20):4976–4988, 2008. doi: 10.1016/j.atmosenv.2008.02.044.

F. Wieser, R. Sander, C. Cho, H. Fuchs, T. Hohaus, A. Novelli, R. Tillmann, and D. Taraborrelli. Development of a multiphase chemical mechanism to improve secondary organic aerosol formation in caaba/mecca (version 4.7. 0). *Geoscientific Model Development*, 17(10):4311–4330, 2024. doi: 10.5194/gmd-17-4311-2024.

B. Winter, C. Winter, J. Schilling, and A. Bardow. A smile is all you need: predicting limiting activity coefficients from smiles with natural language processing. *Digital Discovery*, 1(6):859–869, 2022. doi: 10.1039/D2DD00058J.

L. Xu, S. Suresh, H. Guo, R. J. Weber, and N. L. Ng. Aerosol characterization over the southeastern united states using high-resolution aerosol mass spectrometry: spatial and seasonal variation of aerosol composition and sources with a focus on organic nitrates. *Atmospheric Chemistry and Physics*, 15(13):7307–7336, 2015. doi: 10.5194/acp-15-7307-2015.

L. Xu, K. H. Møller, J. D. Crounse, H. G. Kjaergaard, and P. O. Wennberg. New insights into the radical chemistry and product distribution in the oh-initiated oxidation of benzene. *Environmental Science & Technology*, 54(21):13467–13477, 2020. doi: 10.1021/acs.est.0c04780.

P. J. Young, A. T. Archibald, K. W. Bowman, J.-F. Lamarque, V. Naik, D. S. Stevenson, S. Tilmes, A. Voulgarakis, O. Wild, D. Bergmann, P. Cameron-Smith, I. Cionni, W. J. Collins, S. B. Dalsøren, R. M. Doherty, V. Eyring, G. Faluvegi, L. W. Horowitz, B. Josse, Y. H. Lee, I. A. MacKenzie, T. Nagashima, D. A. Plummer, M. Righi, S. T. Rumbold, R. B. Skeie, D. T. Shindell, S. A. Strode, K. Sudo, S. Szopa, and G. Zeng. Pre-industrial to end 21st century projections of tropospheric ozone from the atmospheric chemistry and climate model intercomparison project (accmip). *Atmospheric Chemistry and Physics*, 13 (4):2063–2090, 2013. doi: 10.5194/acp-13-2063-2013. URL `https://acp.copernicus.org/articles/13/2063/2013/`.

P. J. Young, V. Naik, A. M. Fiore, A. Gaudel, J. Guo, M. Lin, J. Neu, D. Parrish, H. Rieder, J. Schnell, et al. Tropospheric ozone assessment report: Assessment of global-scale model performance for global and regional ozone distributions, variability, and trends. *Elem Sci Anth*, 6:10, 2018. doi: 10.1016/j.coesh.2020.100226.

K. E. Yttri, A. Bäcklund, F. Conen, S. Eckhardt, N. Evangeliou, M. Fiebig, A. Kasper-Giebl, A. Gold, H. Gundersen, C. L. Myhre, et al. Composition and sources of carbonaceous aerosol in the european arctic at zeppelin observatory, svalbard (2017 to 2020). *Atmospheric Chemistry and Physics*, 24(4):2731–2758, 2024. doi: 10.1021/acsearthspacechem.9b00061.

A. Zare, K. M. Fahey, G. Sarwar, R. C. Cohen, and H. O. Pye. Vapor-pressure pathways initiate but hydrolysis products dominate the aerosol estimated from organic nitrates.

ACS Earth and Space Chemistry, 3(8):1426–1437, 2019. doi: 10.1021/acsearthspacechem.9b00067.

M. A. Zawadowicz, B. H. Lee, M. Shrivastava, A. Zelenyuk, R. A. Zaveri, C. Flynn, J. A. Thornton, and J. E. Shilling. Photolysis controls atmospheric budgets of biogenic secondary organic aerosol. *Environmental Science & Technology*, 54(7):3861–3870, 2020. doi: 10.1021/acs.est.9b07051.

Q. Zhang, J. L. Jimenez, M. R. Canagaratna, I. M. Ulbrich, N. L. Ng, D. R. Worsnop, and Y. Sun. Understanding atmospheric organic aerosols via factor analysis of aerosol mass spectrometry: a review. *Analytical and bioanalytical chemistry*, 401:3045–3067, 2011. doi: 10.1007/s00216-011-5355-y.

X. Zhang, Z. M. Chen, and Y. Zhao. Laboratory simulation for the aqueous oh-oxidation of methyl vinyl ketone and methacrolein: significance to the in-cloud soa production. *Atmospheric Chemistry and Physics*, 10(19):9551–9561, 2010. doi: 10.5194/acp-10-9551-2010. URL `https://acp.copernicus.org/articles/10/9551/2010/`.

Y. Zhang, D. J. Jacob, J. D. Maasakkers, M. P. Sulprizio, J.-X. Sheng, R. Gautam, and J. Worden. Monitoring global tropospheric oh concentrations using satellite observations of atmospheric methane. *Atmospheric Chemistry and Physics*, 18(21):15959–15973, 2018. doi: 10.5194/acp-18-15959-2018.

W. Zheng, F. Flocke, G. Tyndall, A. Swanson, J. Orlando, J. Roberts, L. Huey, and D. Tanner. Characterization of a thermal decomposition chemical ionization mass spectrometer for the measurement of peroxy acyl nitrates (pans) in the atmosphere. *Atmospheric Chemistry and Physics*, 11(13):6529–6547, 2011. doi: 10.5194/acp-11-6529-2011.

Y. Zhu, A. Tilgner, E. H. Hoffmann, H. Herrmann, K. Kawamura, L. Yang, L. Xue, and W. Wang. Multiphase mcm–capram modeling of the formation and processing of secondary aerosol constituents observed during the mt. tai summer campaign in 2014. *Atmospheric Chemistry and Physics*, 20(11):6725–6747, 2020. doi: 10.5194/acp-20-6725-2020. URL `https://acp.copernicus.org/articles/20/6725/2020/`.

Acknowledgements

Zuallererst möchte ich mich bei Domenico Taraborrelli dafür danken, dass er mir die Chance gegeben hat die Doktorarbeit in der Modellierung am ICE-3 (oder eher dem IEK-8) durchführen zu können. Im Hinblick auf meine vorangegangenen Abschlussarbeiten in der Femtosekunden-spektroskopie (OLED-Farbstoffe) und der Synthese und Charakterisierung von Kolloiden (Oberflächenfunktionalisierung von Silica Partikeln), war nicht allgemein abzusehen, ob ich das nötige Rüstzeug für die Arbeit an der Modellierung von Atmosphärenchemie mitbringe. Deshalb bedanke ich mich für das vorgestreckte Vertrauen und die gute Betreuung während meiner Arbeit am Institut!

Ebenfalls bedanke ich mich bei Prof. Peter Wiesen für die Betreuung der Arbeit an der Universität Wuppertal. Gleichermaßen möchte ich mich bei Prof. Astrid Kiendler-Scharr und Prof. Hendrik Fuchs für die Übernahme des Zweitgutachtens bedanken.

Weiterer Dank gilt sowohl Timo Kirfel, als auch Astrid Kerkweg. Beide haben mir über die drei Jahre verteilt in zahlreichen Situationen geholfen etwaige Technische- und Programmierprobleme zu lösen und meine Fähigkeiten in beidem zu verbessern. Ohne diese Hilfe wären die meisten Probleme weitaus schwerer (wenn überhaupt) zu lösen gewesen.

Für die experimentellen Daten, welche ich in meiner Publikation verwendet habe, Danke ich allen beteiligten Experimentatoren sowie Betreibern der Atmosphärenkammer SAPHIR. Ebenso bedanke ich mich bei Rolf Sander für die Hilfe beim Umgang mit CAABA/MECCA und die Unterstützung bei der Implementierung der neuen Chemie. Bei Alexandra Tsimpidi möchte ich mich für die Hilfe bei der Visualisierung des Vergleiches zwischen den Modellergebnissen und den Messstationen bedanken.

Zusätzlich möchte ich mich bei den „Mitbewohnern“ meines Büros für die angenehme Arbeitsatmosphäre bedanken. Vor allem Hoang Duong Do Danke ich für die gemeinsam gelösten Probleme und die zahlreichen Kaffee-, sowie Schokoladenspezialitäten aus Vietnam. Der Kokos-Cappuccino bleibt auf meiner Liste für einen potenziellen Vietnam Urlaub.

Natürlich möchte ich mich auch bei meiner Familie für die Unterstützung bedanken. Egal

was anfällt, ich habe mich mein Leben lang immer auf euch verlassen können. Ob ich frühmorgens einen Taxiservice nach Aachen brauche, wertvolle Tipps zur Verbesserung der Doktorarbeit benötige, innerhalb von zwei Tagen eine komplette Wohnung streichen muss oder Verpflegung für einen kompletten Umzug brauche, auf euch ist Verlass. Ich danke euch für jegliche Hilfe in den letzten Jahren und Jahrzehnten!

Zuletzt möchte ich mich noch bei Lea bedanken. Wir haben unseren akademischen Werdegang nahezu komplett gemeinsam beschritten (Chemiestudium und Promotion) und haben uns stets gegenseitig in allen Lebenslagen unterstützt. Dabei haben wir uns beide über die Jahre weiterentwickelt und sind zu dem Team geworden, welches wir heute sind. Danke, dass du in meinem Leben bist und mit mir gekonnt die Herausforderungen des Lebens meisterst!

Declaration of Authorship

Hiermit erkläre ich, dass ich die vorliegende Arbeit mit dem Titel

"Formation and fate of secondary organic aerosol components in the atmosphere: explicit modeling at global scale"

selbständig verfasst und keine anderen als die gekennzeichneten Hilfsmittel und Quellen verwendet habe.

Die vorliegende Arbeit wurde weder in der gegenwärtigen noch einer früheren Fassung bereits einer anderen Hochschule zur Erlangung eines akademischen Grades vorgelegt.

Alle Methoden, Daten und Arbeitsschritte wurden wahrheitsgemäß dokumentiert und keinerlei Daten manipuliert.

Ort, Datum	Unterschrift